**Evaluation of volume holographic optical elements in dichromated gelatin**



by

Loudon Thomas Blair
Hertford College, Oxford

A THESIS
SUBMITTED FOR THE DEGREE OF
DOCTOR OF PHILOSOPHY
AT THE UNIVERSITY OF OXFORD
MICHAELMAS TERM 1989

Department of Engineering Science
Parks Road, Oxford

# *Abstract*

*Loudon Thomas Blair*
*Hertford College*

*Thesis submitted for D. Phil. degree*
*Michaelmas Term, 1989*

**Evaluation of volume holographic optical elements in dichromated gelatin**

The use of dichromated gelatin (DCG) for the formation of holographic optical elements is investigated. In particular, a study is made of the possible sources of spurious recording and replay in such diffracting media. The formation of spurious gratings due to boundary mismatch, when recording a transmission grating in air, is investigated. Experimental results are treated using a simple linear theory which is capable of predicting the relative modulation strengths of each of six recorded gratings. The efficiencies of each of these gratings is related to Fresnel's Laws of reflection and therefore the beam ratio. A brief experimental study of the beam ratio is made. It is found that linear theories do not explain replay of gratings recorded at high exposure energies. This is because DCG exhibits a saturating recording characteristic. A theoretical model is developed to verify experimental results of modulation versus exposure energy for the recording of single and double exposure transmission gratings and their subsequent harmonics. This gives good agreement for most cases, however, it does not explain fully the replay of a difference grating formed due to nonlinearities in the double exposure hologram. A coupled wave theory is therefore developed to take account of both multiple grating interactions between the two primary recordings and the recording of a third grating with a spatial frequency equal to the difference of the two fundamental frequencies. The model gives good agreement with experimental results for varying replay angles and wavelengths. DCG is finally used as a tool to investigate the formation of noise gratings in silver halide emulsions. In particular, results are presented for experiments which were performed to study the effect of high angular scatter upon the selectivity of the noise grating and the recording of reflection noise gratings.

# *Acknowledgments*

I would like to express my sincere thanks to everyone who has made this thesis possible.

In particular, I owe much gratitude to my supervisor *Laszlo Solymar*.

I would like to thank the Science and Engineering Research Council of the U.K. for a postgraduate studentship. The studentship has been complimented technically and financially with a C.A.S.E. Award by Pilkington Research Laboratories Ltd., Lathom. Many thanks to *Andrew Ramsbottom, David Sheel* and *Colin Wilson*. I would also like to thank National Physical Laboratories at Teddington for their supply of optical flat substrates. May I also thank the S.E.R.C., the Department of Engineering Science and Hertford College for financial assistance to attend conferences in Paris and Bath.

I am deeply thankful to the attention of *Jeno Takacs, Andrew Ward* and *David Webb*. Early discussions with *Chris Newell, Don Erbschloe* and *Gerson Riddy* have also proved most useful. Thanks must go to fellow students: *Paul Hubel, Sean Sheridan, Peter Galloway* and *David Jones*. Good luck for the future. I cannot forget *Grahame Faulkner* and *Cliff Brindley* for their excellent technical and 'vocal' support. Thank you *Lynn Murphy* for your wonderful cakes and *Rachael Nieto* and *John Sharpe* for proof reading the text. Thank you *Steve Barnett* for keeping me off the streets.

I would like to acknowledge the educational enlightenment gained at the Friday Seminar Group sessions.

Finally, I would like to acknowledge the contribution to my education by *Mr. R. Smith* of Loudoun Academy, Galston who first introduced me to holography and *Mr. B. Lawrenson* of Dundee University whose enthusiasm kept my interest.

*To Mum and Dad*

# Contents

Page

## Chapter 1 : Introduction



## Chapter 2 : Dichromated gelatin

# Chapter 1

# Introduction

## 1.1 Basic principles

A hologram is a device which is capable of reconstructing both the amplitude and phase of a recorded wavefront.

To form the hologram, we require two mutually coherent waves which we will call the reference wave $U_{ref}$ and the object wave $U_{obj}$. These are illustrated in Figure 1.1. We may regard $U_{obj}$ as being light scattered from the surface of an object. When $U_{ref}$ and $U_{obj}$ interfere in space, the phase difference between the two wavefronts will form standing waves. We may record a hologram by placing a photosensitive material into this area of interference. The hologram will then store a copy of the intensity fluctuations of the standing wave electric field pattern. We can represent the time averaged intensity variation ($I$), and therefore the transmittance, of the hologram as being proportional to the following:-

$$\begin{aligned} I &= |U_{ref} + U_{obj}|^2 \\ &= U_{ref}U_{ref}^* + U_{obj}U_{obj}^* + U_{ref}U_{obj}^* + U_{obj}U_{ref}^* \end{aligned} \tag{1.1}$$

To replay the hologram we rely on a fundamental wave property known as *diffraction*.

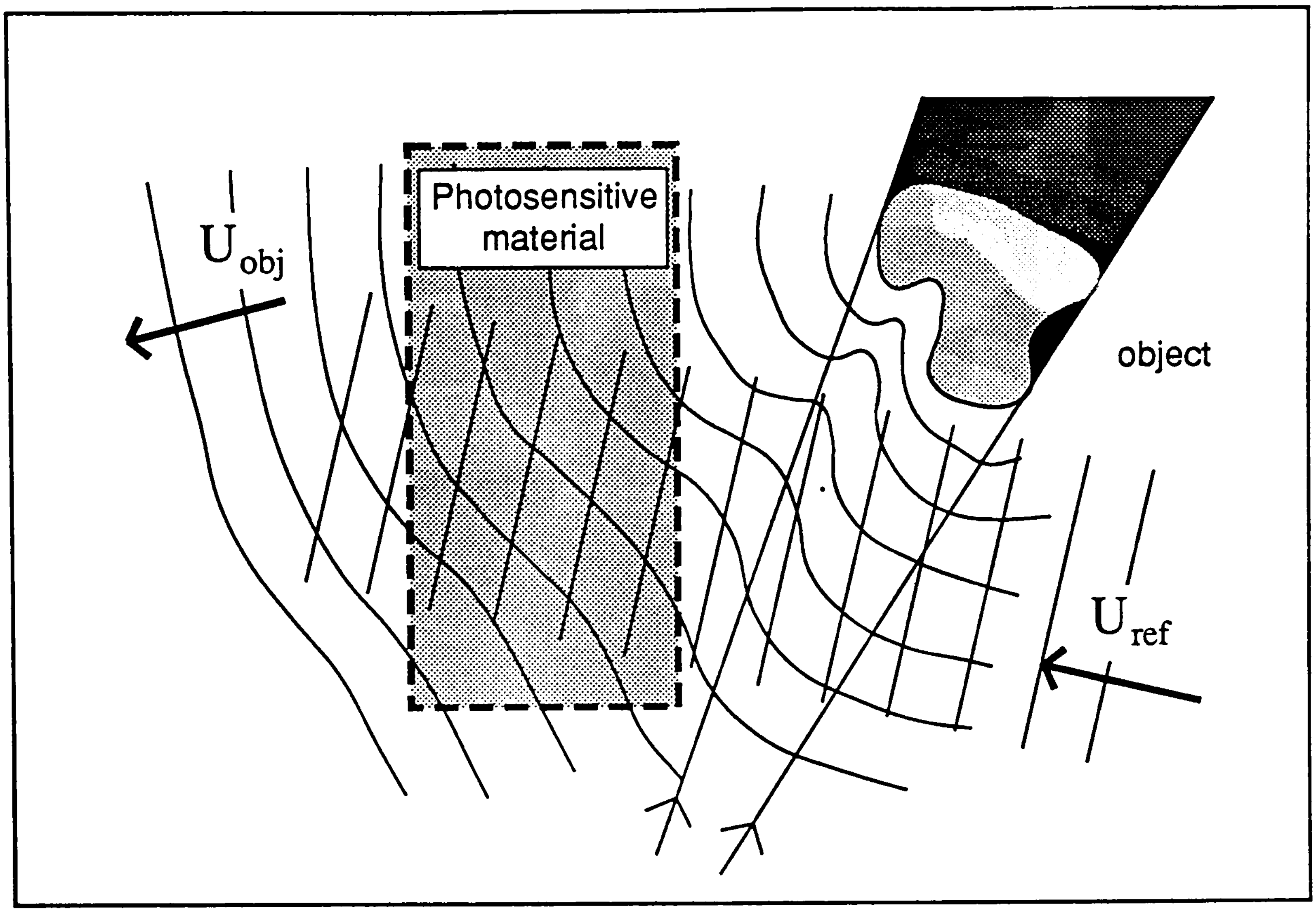


Figure 1.1 Recording configuration for a simple transmission hologram

The plate is placed in the path of a replay wave $U_{rep}$ which is similar in nature to the recording reference wave $U_{ref}$ such that:-

$$U_{rep} = cU_{ref} \tag{1.2}$$

where $c$ is a constant.

As $U_{rep}$ passes through the hologram it aquires similar amplitude and phase characteristics as the original electric field. The output wave $U_{out}$ can be described as the input multiplied by the hologram transmittance and will therefore take the form:-

$$U_{out} = c\left[\underbrace{U_{ref}\left(|U_{ref}|^2 + |U_{obj}|^2\right)}_{\text{(i)}} + \underbrace{U_{ref}^2 U_{obj}^*}_{\text{(ii)}} + \underbrace{U_{obj}\,|U_{ref}|^2}_{\text{(iii)}}\right] \tag{1.3}$$

Equation (1.3) contains three terms:-

(i) This is proportional to $U_{ref}$ and describes the undiffracted replay beam.

(ii) This describes replay of the conjugate object beam.

(iii) This final term describes replay of the original object beam illustrating the fact that if $U_{rep} = U_{ref}$ then the object wave will be reconstructed exactly.

If a hologram is sufficiently thick (for definition see [Sol81]), it may be said to have *volume* characteristics. Wave interactions in a volume medium may be described by Bragg's Law [Bra12]. This states that for a simple volume hologram where a single frequency grating with sinusoidal varying permittivity has been formed, the amplitude of diffracted light will be a maximum whenever the following condition is met:-

$$\lambda = 2d\sin\theta \tag{1.4}$$

where $\lambda$ is the replay wavelength, $d$ is the grating period, and $\theta$ is the angle corresponding to the incident and diffracted waves of an unslanted grating.

Many books are now available which give excellent reviews of holography and the theory of diffraction. I will therefore present only a brief introduction to the subject and refer the reader to the following texts for further information [Col71b] [Cau79] [Sol81] [Hut82] [Har84] [Sym89].

## 1.2 Historical background

The invention of holography has been accredited to Denis Gabor [Gab48] [Gab49] who, for his early pioneering work, received a Nobel Prize in 1971. His work of the late 1940's was originally aimed at a method of improving the resolution and reducing the spherical aberrations inherent in the electron microscope at that time. He reasoned that if he could record the scattered field of an illuminated object as a diffraction pattern he could regenerate the image at optical frequencies and hence correct for aberrations via a compensating lens design, i.e. a two step process. To prove his theory he tested both steps at optical wavelengths forming an image of the original object which he called a *hologram* (after the Greek for 'whole record'). However, his method did suffer from a few limitations. The light source / pinhole combination displayed poor monochromaticity, temporal and spatial coherence properties; the set up was "on-axis" (in line) so when viewing at replay the observer saw both the real and conjugate image overlapping at equal distances either side of the hologram plane; the recording materials at that time were absorption type bearing low efficiencies. Holography remained at this level of understanding for about the next fifteen years. In 1960 the first laser was built, promising high coherence and monochromatic properties; ideal for holography. However, before this became a practical tool, the next significant advance occurred in 1962. In this year both Leith and Upatnieks [Lei62] [Lei63] [Lei64] and Denisyuk [Den62] [Den63] [Den65] proposed recording geometries which eliminated the deficiencies of Gabor's method and moved holography into a practical era. Using a mercury arc lamp, Leith and Upatnieks, whilst working on communications theory for radar, separated the reference and object waves from a single axis and produced the off axis transmission hologram. This was found to separate spatially the diffracted orders and avoid the ghosting so apparent in Gabor's imaging. Also, around this time Denisyuk, following a technique described by Lippman in 1894 [Lip94], recorded volume type *reflection* holograms with beams incident from opposite sides of the plate. This produced a higher spatial frequency of fringing within the emulsion allowing high spectral selectivity and monochromatic replay by white light illumination. Shortly after these discoveries holography was applied to information storage by van Heerden [Van63a] [Van63b], closely followed in 1965 by the introduction of holographic interferometry [Pow65] [Hai65].

In early experiments, the recording material used was silver halide emulsion which produced absorption type holograms capable of a maximum diffraction efficiency around 3%. Several holographic recording materials have since emerged to improve upon efficiency and quality. Using a method known as *bleaching* Cathey [Cat65] found that he could greatly increase the efficiency of silver halide absorption holograms by converting absorption modulation to that of phase. In 1968 Shankoff [Sha68a] [Sha68b] discovered that dichromated gelatin could be used as a means of recording extremely high diffraction efficiencies. More recently, attention has been paid to the dynamic recording of real time holographic gratings in photorefractive materials [Kuk77].

## 1.3 Applications

Nowadays many applications exist for the hologram. The most obvious and common is display holography [Sym89]. This is probably the most popular area of holography, because of its ability to recreate three dimensional images of objects. Because of this, many workers are attempting to improve the resolution, contrast and brightness of the display hologram. Due to an improvement in available recording materials, true colour holograms are now being developed [Hub89b]. The holographic principle has found several other useful and exciting applications. Holographic interferometry [Mol89] is now a standard method capable of measuring faults and deformations. In the medical field, for example, much work is presently being concentrated on holographic endoscopy [Von88] [Bje89]. Von Bally [Von86] gives an excellent review of holography in medicine. Recently, with the rise in interest of neural networks [Abu87], holography is being applied to the principles of pattern recognition [Van64] and the area of holographic interconnects are considered [Goo84]. Another popular branch is *Holographic Optical Elements* which will be reviewed in more detail below.

### 1.3.1 *Holographic Optical Elements (HOEs)*

Volume holography, in the shape of Volume Holographic Optical Elements (VHOEs), offers a means of forming optical beams by means of diffraction as opposed to refraction and reflection in the case of conventional elements [Sch67] [Cha68] [Col73] [Cha80a] [Sch85]. Transmission gratings may take the role of prisms or lenses [Ric74] [Che87] and reflection gratings may compete with mirrors [Min75] [Gup77] [Rao80] [Mag85]. In addition, HOEs are capable of performing functions beyond the scope of classical elements. HOEs may be recorded using one of three techniques:-

(i) using two independent beams with the desired replay wavefronts.

(ii) a conventional element may be placed in the path of one of the incident beams. For example, a holographic mirror may be formed by index matching a mirror to the back surface of a holographic plate. The incident beam (reference wave) may then pass through the plate and reflect off of the mirror forming the subject wave.

(iii) the HOE may be copied from a master holographic element [Van78] [Bla89c].

HOEs have several advantages and disadvantages over conventional elements. Advantages include the following:-

(i) Because of their diffractive properties HOEs are dispersive. They can therefore be tuned to a specific narrowband frequency range for use in monochromatic optical systems.

(ii) They are formed via a photographic process, therefore are more reproducible and more simply fabricated than their conventional counterpart. Because of this...

(iii) ...it is possible to produce an HOE on any shaped substrate surface (curved or flat) [Woo85] [Wel73a] [Wel73b].

(iv) ...it is possible to produce lightweight, easily stackable elements.

(v) ...HOEs may be produced more cheaply than conventional elements.

(vi) ...multi-functional HOEs may be produced reducing the overall size and complexity of an optical system.

However several of these advantages may also be disadvantages for different applications:-

(i) Because of the dispersive quality of diffractive elements, they cannot be used in white light, but only in a narrow frequency band.

(ii) The angular / wavelength (Bragg) selectivity leads to aberrations if replay is not at recording conditions.

(iii) Off axis HOEs usually have larger aberrations than their conventional counterparts.

It is understood that HOEs will never fully replace conventional optical elements, but will complement them where conventional elements are not particularly practical. Because of their diffractive properties HOEs have even found new applications (apart from copying existing elements). Such applications are displays [McC73], for example, the Head Up Display (HUD) used in military aircraft [Woo83] [Per85] and currently being developed for the motor car [Eva89], or the Laser Scanner which is currently in use as a bar code reader in supermarkets [Dic89]. The exceptional efficiency of the modern HUD has only been made possible through the advancement of diffractive optics. Other applications for HOEs range from its use as a simple grating for hologram analysis [Sol81] to complex multiple gratings such as optical interconnects [Goo84].

## 1.4 Recording materials

An ideal holographic recording material must be capable of truly representing the variation in intensity of the standing wave pattern that it is attempting to record. This means that it should posses a linear recording characteristic, very high resolution (capable of sampling to less than half the wavelength of light), with low scatter and high sensitivity over a wide spectral range. This, of course, has not yet been achieved in practice.

The are many photosensitive materials available which are capable of recording optical holograms, and each has its own special merit. However, no one material can be said to be *ideal*. Popular materials include silver halide emulsions [Jam77], dichromated gelatin [New87], photopolymers [Col71a] [Smo89], photochromics [Ker71] and photorefractive crystals [Gün87]. For general reviews of the range of holographic recording materials in use see References [Smi77] and [Sol81].

In this thesis I will be concerned mainly with recording in the material *Dichromated Gelatin (DCG)*. This is a homogeneous material which is particularly suitable for volume phase recording. It displays many of the above mentioned properties of an ideal recording medium. For example, over the optical spectrum, it exhibits low scatter, high resolution, a capacity for high index modulation, a high signal to noise ratio and low absorption. These advantages coupled with an ability to coat varying thicknesses of gelatin make DCG suitable for high efficiency recording. DCG, however, is only sensitive to a limited range of the electromagnetic spectrum. It is primarily sensitive to ultra violet, blue and green radiation but insensitive to red, although it may be sensitised to red wavelengths by using methylene blue [Kub76]. DCG has a relatively low sensitivity compared with other materials (a typical exposure energy for DCG is approximately one thousand times that of silver halide emulsions) and the difficulty of reproducing DCG holograms is a major disadvantage. They are extremely sensitive to humidity and temperature fluctuations. Humidity should be kept low (less than 40% r. h.) and temperature should be kept constant around room temperature (25°C). In order for DCG holograms to maintain consistency outwith this environment they should be hermetically encapsulated, usually with epoxy resin and a coverplate of glass. The subject of dichromated gelatin recording will be dealt with in more detail in Chapter 2.

A second material to be used in the course of this work is silver halide emulsion ($AgH^+$). This is the most common commercially available recording material for holography. Many types are available with different levels of resolution, sensitivity and scatter and it is available for use at all visible wavelengths. In this thesis, I will concern myself only with $AgH^+$ as a scattering device [Hub89a] so a detailed discussion concerning the processing of this material will be referred to [Coo84]. The process by which interference is recorded is the same as a photograph in that during processing exposed silver halide (usually silver bromide) crystals turn to silver when developed, i.e. the interference pattern is recorded at a sampling rate determined by the resolution of the silver halide particles [Fer84]. This procedure forms absorption type holograms with a maximum possible efficiency around 3.7% [Kog69]. By bleaching [Phi80] it is possible to create phase holograms which allows a vast improvement in efficiency [Lam72]. However, because of its inhomogeneous nature, $AgH^+$ exhibits high scattering both at recording [Sym82b] [Sym83b] and replay [Goo68]. At recording, this leads to the construction of noise gratings [Rid88]. In Chapter 7, I will discuss in more detail the recording of these gratings and simulate their replay in DCG.

## 1.5 Theory

As we have already discussed, the formation of a hologram in a photosensitive material is a complex process which comprises of two steps. (i) A latent image of a diffraction pattern is recorded in the medium due to the interference of two sets of waves. (ii) The next step is to process the latent information and generate a device capable of replay at high efficiencies. The hologram is now fixed as a diffraction pattern.

When we come to replay the hologram we have to model the interaction of light waves with a diffraction pattern which is fixed in some complicated variation of the complex permittivity within the medium.

Several theories have been derived to model the replay of holograms. References [Gay82] and [Gay85] give excellent reviews for both rigorous and approximate models. However, throughout this thesis, I will refer to and use an approximate model first introduced by Raman and Nath [Ram35a] [Ram35b] when studying the scattering of light by ultrasonic waves in liquids. This coupled wave theory was later applied to holographic gratings by Kogelnik [Kog69]. I chose this model because, in spite of its relative simplicity, it gives good results for volume diffraction. Kogelnik's model assumes the recording of the simplest type of hologram, i.e. a sinusoidal grating formed between two ideal, collimated plane waves. It gives a one dimensional analysis of only two interacting waves close to the Bragg condition, the incoming replay wave ($0^{th}$ order) and the outgoing signal wave ($-1^{st}$ order). The theory uses coupled differential equations to mathematically model a continuous exchange of energy between waves propagating inside a hologram which are coupled together by a grating. It is capable of giving good approximation to the replay of both amplitude and phase type volume holograms. Since its introduction to holography, other authors have adapted the theory for more complex geometries (see [Sol81]).

### 1.5.1 *Recording*

In order to study mathematically the recording and replay conditions of a hologram, it is necessary to look at the most simple case, and build from there towards more complex recording. The fundamental study is the recording and replay of a single, sinusoidal grating formed by interference between two coherent monochromatic waves. When the plane waves are linearly polarised, we can describe them as a function of Maxwell's equations [Sol76] and assume solutions of the scalar wave equation:-

$$\nabla^2 E + \gamma^2 E = 0 \tag{1.5}$$

where $E$ represents the electric field strength

and $\gamma$ is a constant related to the variation of conductivity and permittivity within the propagating medium.

We may assume solutions for the recording waves as:-

$$E_r = A_r e^{-j(\overline{\sigma}_r.\bar{r} - \omega t + \phi_r)}$$

and

$$E_s = A_s e^{-j(\overline{\sigma}_s.\bar{r} - \omega t + \phi_s)} \tag{1.6}$$

where $\bar{r}$ is the position vector and $\omega$ is the angular frequency. $E_r$ and $E_s$ represent the electric field, $A_r$ and $A_s$ are the amplitudes, $\overline{\sigma}_r$ and $\overline{\sigma}_s$ are the wave vectors, and $\phi_r$ and $\phi_s$ are the relative phase terms of the reference and signal waves respectively.

At recording, the total electric field $E_{tot}$ takes the form:-

$$E_{tot} = E_r + E_s \tag{1.7}$$

However, since the recording medium responds only to the intensity ($I$) of the electric field [Wie90], we can let:-

$$\begin{aligned} I &\propto E_{tot}E_{tot}^* \\ &\propto (E_r + E_s)(E_r + E_s)^* \\ &\propto A_r^2 + A_s^2 + 2A_rA_s\cos(\overline{\mathrm{K}}.\overline{\mathrm{r}} + \phi_{diff}) \end{aligned} \tag{1.8}$$

where $\phi_{diff}$ is a relative phase term. $\overline{\mathrm{K}} = \overline{\sigma}_r - \overline{\sigma}_s$ is the grating vector whose modulus is inversely related to the spatial frequency of the grating i.e.

$$|\overline{\mathrm{K}}| = \frac{2\pi}{\Lambda} \tag{1.9}$$

where $\Lambda$ = the period of the recorded grating.

Thus, a small grating vector represents a grating with a large period and a long grating vector represents a grating with high spatial frequency.

The intensity variation manifests itself in the processed hologram as a variation in permittivity ( $\varepsilon_r$ ) and / or conductivity ( $\sigma_r$ ) as:

$$\begin{aligned} \varepsilon_r &= \varepsilon_{ro} + \varepsilon_{r1}\cos(\overline{\mathrm{K}}.\overline{\mathrm{r}} + \phi_{diff}) \\ \sigma_r &= \sigma_{ro} + \sigma_{r1}\cos(\overline{\mathrm{K}}.\overline{\mathrm{r}} + \phi_{diff}) \end{aligned} \tag{1.10}$$

If a hologram is described solely in terms of permittivity it is referred to as a phase hologram, whereas if it is described by a variation in conductivity it is referred to as an absorption hologram.

There is a useful tool available which allows us to visualise geometrically the recording conditions for simple periodic gratings. This is known as the Ewald sphere [Jam48] and simply describes diffraction by using vectors in reciprocal space. For our analysis, we need only describe a circle since we will limit our theory to two dimensions. Figure 1.2 shows the Ewald circle representation for the recording of (a) a transmission grating and (b) a reflection grating. In (a) we observe a typical transmission geometry with both beams incident from the same side of the plate. We observe that the grating vector is perpendicular to the recorded fringes and therefore lies with a vertical orientation. Conversely, we see that the reflection grating has fringes lying parallel to the hologram surface indicating a $\overline{K}$ vector lying in the horizontal plane.

The radius of the circle is given by the propagation constant $\beta$ which is related to a monochromatic temporal frequency $\omega$, i.e.

$$\beta = \frac{2\pi n}{\lambda} \tag{1.11}$$

where $n$ = the refractive index of the medium

$\lambda$ = the recording wavelength in air

Thus, for the same refractive index, a small circle represents a large recording wavelength and a large circle represents a low recording wavelength.

### 1.5.2 *Replay*

At replay we must make some initial assumptions regarding the recorded grating. Referring to Figure 1.2, we will assume a two dimensional coordinate system where the parallel boundaries of the hologram are perpendicular to x - axis. We will assume that it has a thickness $d$ in the x direction and infinitely long in the y direction. We will neglect any variation in fringe formation in the z direction.

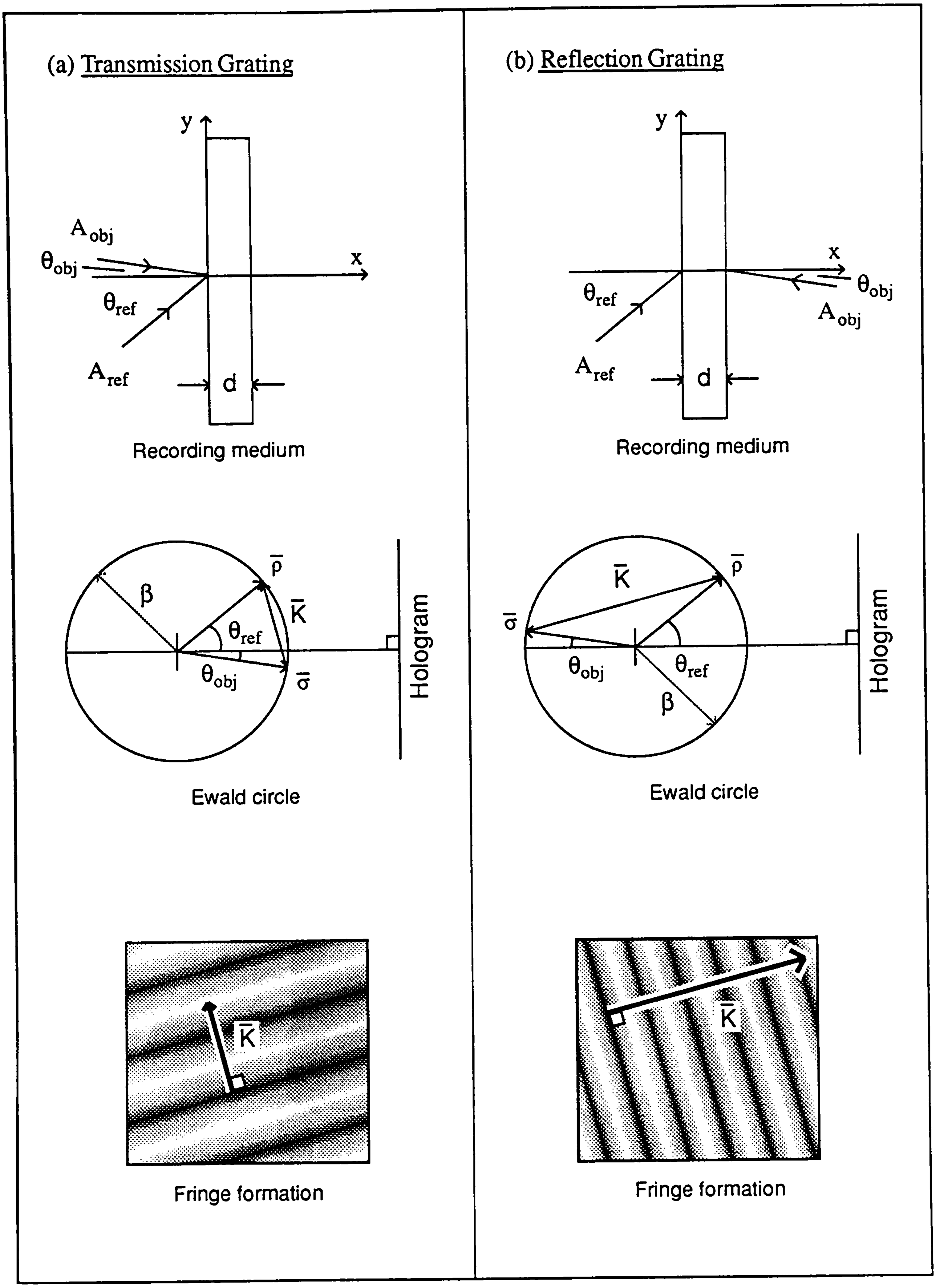


Figure 1.2 Recording geometry, Ewald circle and fringe formation for (a) transmission and (b) reflection gratings.

The recorded grating is a slowly varying periodic structure which can therefore be represented by a Fourier series. From equation (1.10) we are able to assume the dielectric constant $\varepsilon_r(\bar{r})$ inside the material takes the following complex form:-

$$\begin{aligned}\varepsilon_r(\bar{r}) &= \varepsilon_r'(\bar{r}) - j\varepsilon_r''(\bar{r}) \\ &= \left[\varepsilon_{ro}'(\bar{r}) - j\varepsilon_{ro}''(\bar{r})\right] + \sum_{i=1}^{\infty}\left\{\varepsilon_{ri}'(\bar{r})\cos(i\bar{K}.\bar{r}+\phi_i) - j\varepsilon_{r1}''(\bar{r})\cos(i\bar{K}.\bar{r}+\phi_i)\right\} \qquad (1.12)\end{aligned}$$

The real component of this equation describes a refractive index variation in permittivity whilst the complex term describes absorption modulation in terms of conductivity.

However, since we are assuming the recording of a pure sinusoidal grating, we may neglect higher spatial orders and simplify the expression to:-

$$\varepsilon_r(\bar{r}) = \left[\varepsilon_{ro}'(\bar{r}) - j\varepsilon_{ro}''(\bar{r})\right] + \left[\varepsilon_{r1}'(\bar{r}) - j\varepsilon_{r1}''(\bar{r})\right]\cos(\bar{K}.\bar{r}+\phi) \qquad (1.13)$$

At the hologram boundaries, we are required to satisfy the condition that the tangential components of a propagating electric field $E$ are conserved. This complicates replay by having to include multiple diffraction by waves reflected at the boundaries. To simplify the mathematics, we can neglect spectral reflections by making the assumption that the average permittivity is the same inside and outside the hologram (e.g. replay within an index matching medium). We will also assume replay by a coherent wave which is polarised perpendicularly to the x - axis. This allows us to describe the electric field $E$ within the hologram by the time independent scalar wave equation:-

$$\nabla^2 E + k^2 E = 0 \qquad (1.14)$$

where
$$\begin{aligned}k^2 &= \frac{\omega^2}{c^2}\left[\varepsilon_r'(\bar{r}) - j\varepsilon_r''(\bar{r})\right] \\ &= \left[\alpha + j\beta\right]^2 \qquad (1.15)\end{aligned}$$

$c$ is the speed of light in a vacuum, $\alpha$ represents absorption and $\beta$ represents the propagation constant.

However, by making the assumption that absorption is small (i.e. $\alpha << \beta$), we may rewrite the wave equation as:-

$$\nabla^2 E + \left[\beta^2 - 2j\alpha\beta + 4\kappa\beta\cos(\bar{K}.\bar{r} + \phi)\right]E = 0 \tag{1.16}$$

where the propagation constant $\beta$ and absorption constant $\alpha$ take the following forms:-

$$\beta = \frac{\omega}{c}\sqrt{\varepsilon'_{ro}} \qquad \text{and} \qquad \alpha = \frac{\omega^2}{2\beta c^2}\varepsilon''_{ro} \tag{1.17}$$

and we introduce a coupling constant ($\kappa$) defined as:-

$$\kappa = \beta\left[\frac{\varepsilon'_{r1} - j\varepsilon''_{r1}}{4\varepsilon'_{ro}}\right] \tag{1.18}$$

For practical purposes we can define the average refractive index $n_0$ as:-

$$n_o = \sqrt{\varepsilon'_{ro}} \tag{1.19}$$

and, if we can assume that the refractive index modulation $n_1$ is small (i.e. $n_1 << n_o$), then we can let:-

$$n_1 = \frac{\varepsilon'_{r1}}{2\sqrt{\varepsilon'_{ro}}} \tag{1.20}$$

To solve equation (1.16) we will assume replay by an incident wave given by:-

$$E(\bar{r}) = A_o \exp\{-j\bar{\sigma}_o.\bar{r}\} \tag{1.21}$$

$A_o$ is the amplitude and $\bar{\sigma}_o$ is the wave vector of the replay wave within the hologram. A general solution, taking account of diffracted waves, may be described by:-

$$E(\bar{r}) = \sum_{n=-\infty}^{\infty} A_n(x)\exp\{-j\bar{\sigma}_n.\bar{r}\} \tag{1.22}$$

where $A_n(x)$ is the amplitude and $\bar{\sigma}_n$ is the wave vector of the $n^{th}$ diffraction order.

In his analysis Kogelnik described $\bar{\sigma}_n$ by the relation

$$\bar{\sigma}_n = \bar{\sigma}_o + n\bar{K} \tag{1.23}$$

where the modulus of $\bar{\sigma}_n$ is only equal to $\beta$ for the *on-Bragg* condition. This technique, known as *K vector closure*, is illustrated using Ewald circle representation in Figure 1.3(a).

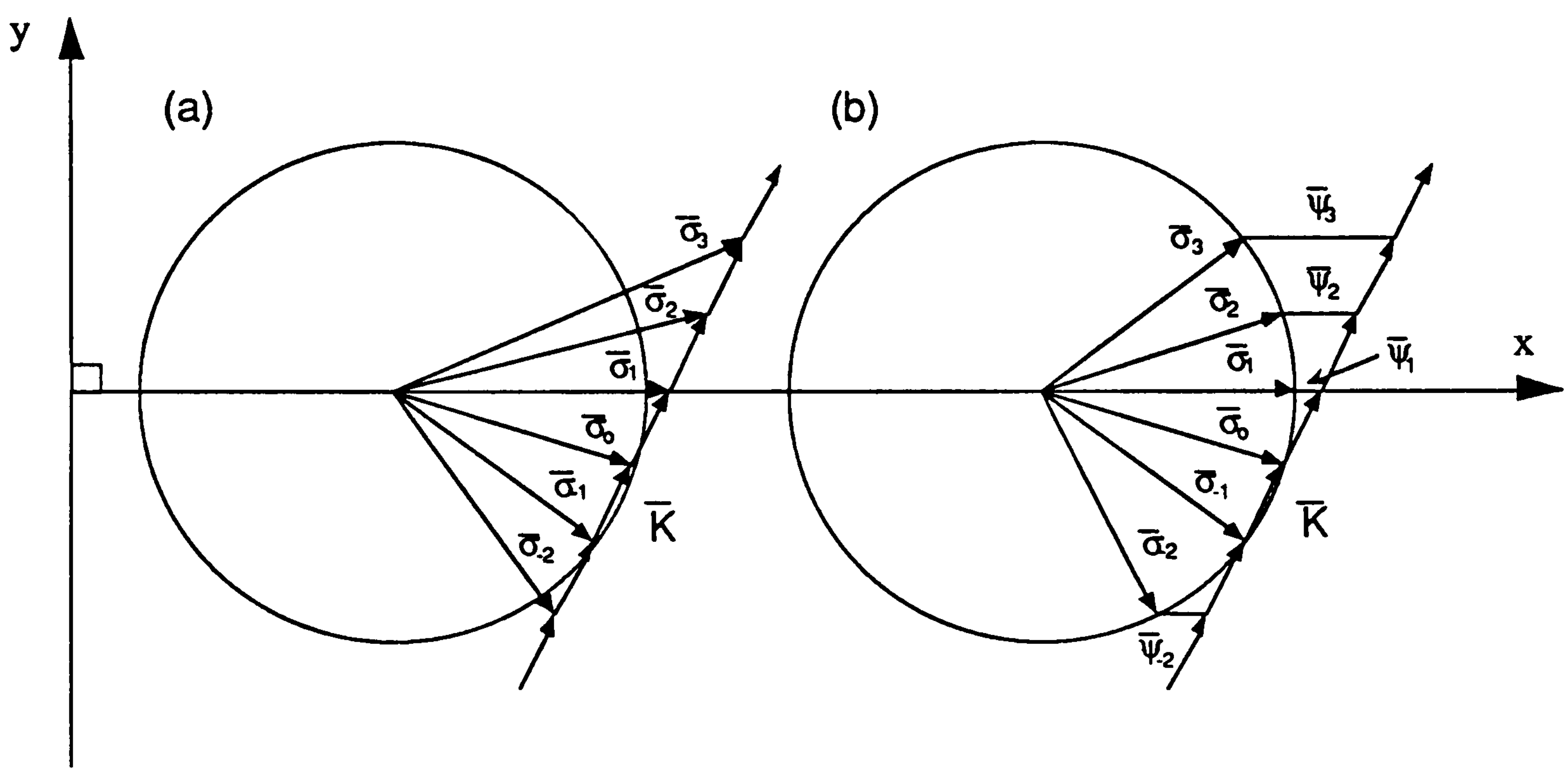


Figure 1.3 Ewald circles illustrating diffracted orders by (a) $\bar{K}$ - vector closure theory and (b) $\beta$ - valued theory

Here, we see that if a diffracted wave is not replaying on the Bragg condition it does not touch the circle. This leads to a decrease in the amplitude of that wave which is dependent on the coupling strength ($\kappa$) of the grating and the thickness ($d$) of the emulsion.

The vector $\bar{\sigma}_n$ may also be represented by the *$\beta$-valued* condition where all the wave vectors lie on the Ewald circle :-

$$|\bar{\sigma}_n| = \beta \tag{1.24}$$

and $$\overline{\sigma}_n = \overline{\sigma}_o + n\overline{K} - \overline{\psi}_n \tag{1.25}$$

Figure 1.3(b) illustrates this relationship and shows how the diffracted wave vectors are related to the replay wave by means of the grating vector $\overline{K}$ and an dephasing parameter $\overline{\psi}_n$ . This is assumed always perpendicular to the hologram surface [Uch73] and therefore may be written as a scalar $\psi_n$ which is function of x. Thus, we are able to write:-

$$\sigma_{nx} = \sigma_{ox} + nK_x - \psi_n \tag{1.26}$$

As we leave the Bragg condition, the dephasing parameter increases causing a reduction in diffracted energy to that order. Thus, the coupling power between diffraction orders is significant when the dephasing parameter is small.

For the on - Bragg condition and when the modulus of the diffracted wave vector is close to $\beta$, both the $\overline{K}$ vector closure and the $\beta$ - value assumptions agree to first order approximations. However, as we replay further off - Bragg, the $\beta$ - valued theory has been shown [Sym82a] to give better agreement with experimental results in an index matching tank. For this reason the $\beta$ - valued assumption will be used in this thesis. We must note here that the situation may arise where the y component of the diffracted wave $\sigma_{ny}$ is greater than $\beta$. For this case $\psi_n$ will not touch the Ewald circle and we cannot obtain a real solution for $\sigma_{nx}$. When this situation occurs, $\psi_n$ will usually be large allowing us to neglect any power transfer to the wave in question.

By substituting the general solution (1.22) into the scalar wave equation (1.16) we obtain the expression:-

$$\sum_{n=-\infty}^{\infty} \exp\{-j\overline{\sigma}_n.\overline{r}\}\left[\frac{d^2A_n}{dx^2} + 2j\sigma_{nx}\frac{dA_n}{dx} + \left[\left(\beta^2 - \sigma_n^2\right) - 2j\alpha\beta\right]A_n + 2\kappa\beta\left(e^{-j\overline{K}.\overline{r}} + e^{+j\overline{K}.\overline{r}}\right)\right] \tag{1.27}$$

However, if we assume that energy exchange between the diffracted orders is slow with respect to the electric field fluctuations, we can neglect the second order derivatives.

By substituting for $\overline{\mathrm{K}}$ using the *β-valued* expression (1.26), the term $\left(\beta^2 - \sigma_n^2\right)$ reduces to zero. Then, by equating the coefficients of the exponential terms to zero, it is possible to obtain the following set of differential equations:-

$$\sum_{n=-\infty}^{\infty}\left\{\frac{\sigma_{nx}}{\beta}\frac{dA_n}{dx} + \alpha A_n + j\kappa\left[A_{n+1}e^{j(\psi_{n+1}-\psi_n)x} + A_{n-1}e^{j(\psi_{n-1}-\psi_n)x}\right]\right\} = 0 \qquad (1.28)$$

These equations describe an infinite set of coupled waves where the amplitude of $A_n$ is related to the amplitudes of adjacent diffraction orders n - 1 and n + 1 by the coupling constant $\kappa$ as the incident wave passes through the grating.

The equations may now be solved by imposing initial boundary conditions. For transmission gratings we assume that the incident wave starts at x = 0 with an amplitude of one. All diffracted orders travelling in the same direction start at x = 0 with amplitudes of zero, i.e. as the incident wave passes through the hologram, energy is coupled into higher orders. For reflection gratings, we make the same assumption for the incident beam but assume that diffracted waves which travel in the opposite direction will be zero at the far boundary of x = *d*.

If a hologram is described as being optically thick or volume it is possible to simplify the above series of differential equations. The amplitudes of each diffracted order are dependent upon the exponential terms shown in (1.28). As the dephasing parameter $\psi_n$ or the depth $x$ become large then the exponential term will reduce in magnitude allowing us to neglect that order. Eventually, we will reach a stage where it is possible to neglect the amplitudes of higher diffracted orders and assume only zeroth and first order diffraction.

There have been several theories considered to define when a hologram is optically *thin* or *thick* [Kle66] [Mag78] [Moh78] [Gay81]. We can assume a dimensionless parameter Ω [Sol81] which we can define as:-

$$\Omega = \frac{|\mathrm{K}|^2}{2\beta\kappa} \qquad (1.29)$$

It has been shown that if $\Omega$ is large (i.e. $\Omega > 20$) then the hologram may be considered as volume and higher orders may be neglected, leaving a simple two wave solution. Equation (1.28) may then be rewritten as:-

$$\frac{\sigma_{ox}}{\beta}\frac{dA_o}{dx} + \alpha A_o + j\kappa A_{-1}\,e^{+j\psi_{-1}x} = 0$$

$$\frac{\sigma_{-1x}}{\beta}\frac{dA_{-1}}{dx} + \alpha A_{-1} + j\kappa A_o\,e^{+j\psi_{-1}x} = 0 \qquad (1.30)$$

These equations assume that only two waves with amplitudes $A_o$ and $A_{-1}$ exist and are coupled together throughout the depth of the hologram by the coupling constant $\kappa$, assuming a constant attenuation $\alpha$. We may then define the diffraction efficiency as the fraction of the incident power which is diffracted into the signal waves at the output of the hologram.

It is possible to solve these simple equations analytically for both the reflection and transmission cases [Hea85a,b] [Sym82a], however once we start to complicate the situation by adding further gratings and additional interactions it becomes necessary to resort to numerical techniques. The results may then be compared to experimental data in a fashion similar to that described by Syms and Solymar [Sym83a].

## 1.6 Experimental techniques

Much of the work discussed in this thesis was experimental. This section gives a brief resume of the necessary requirements for recording holograms in DCG and the techniques used for analysis.

### 1.6.1 *Thickness measurement*

The thickness of gelatin before and after exposure was measured using a Michelson interferometer, with a white light tungsten source and a Mercury lamp. A slit was cut in the gelatin to form a discontinuity. The thickness could then be related to the number of green mercury fringes between the two sets of white light fringes using the equation:-

$$d = \frac{N\lambda_{Hg}}{2} \tag{1.31}$$

where $N$ is the number of fringes and $\lambda_{Hg}$ is the wavelength of the Mercury source (546.1 nm).

### 1.6.2 *Measurement of average refractive index*

The average refractive index of dichromated gelatin before exposure was measured using an Abbe refractometer. This measures the surface refractive index of the gelatin. However, after exposure, the average refractive index is volume dependent and cannot be measured simply as a surface parameter. Nevertheless, if the thickness at recording and replay and the recording refractive index are known, then it is possible to calculate the replay refractive index from the replay Bragg conditions of a recorded grating.

### 1.6.3 *Recording*

Because DCG is sensitive to high humidity levels or changes in room temperature the environmental conditions of the laboratory had to be controlled. In order to maintain consistency throughout the recording stage, the relative humidity of the laboratory was kept at a value equal to or less than 40%, and the temperature was kept constant at 25°C. The light source used was an Innova argon ion continuous wave laser running at $TEM_{00}$ mode and a wavelength of 514.5 nm with an output power of 2 Watts. This power level compensated for the relative insensitivity of DCG at 514.5 nm compared to other materials and allowed exposure times of up to 120 seconds. A large coherence length (of several meters) was achieved by operating in single frequency mode with the aid of an etalon. Finally, the optical table used was an Anaspec Zero-G floating on Anaspec legs in order to isolate the experimental apparatus from any external physical vibrations.

### 1.6.4 *Replay*

The majority of results presented in this thesis are derived from the analytical technique shown in Figure 1.4 (see Reference [Sym82c]).

The set-up measures the transmitted beam intensity of a holographic plate. A pencil thin beam of white light passes through an aperture and is polarised perpendicular to the plane of incidence of the plate. The plate is immersed in an index matching tank in order to reduce boundary reflections at replay [Owe83]. This contains an index matching oil with a refractive index similar to that of glass (n ~ 1.5). The beam passes through the tank and enters the input slit of the spectrometer where the appropriate replay wavelength is selected by a diffraction grating. The transmitted intensity at that wavelength is measured by a photomultiplier and normalised against the white light source to compensate for any spurious fluctuations in input intensity. Data acquisition is controlled by a 380Z microcomputer.

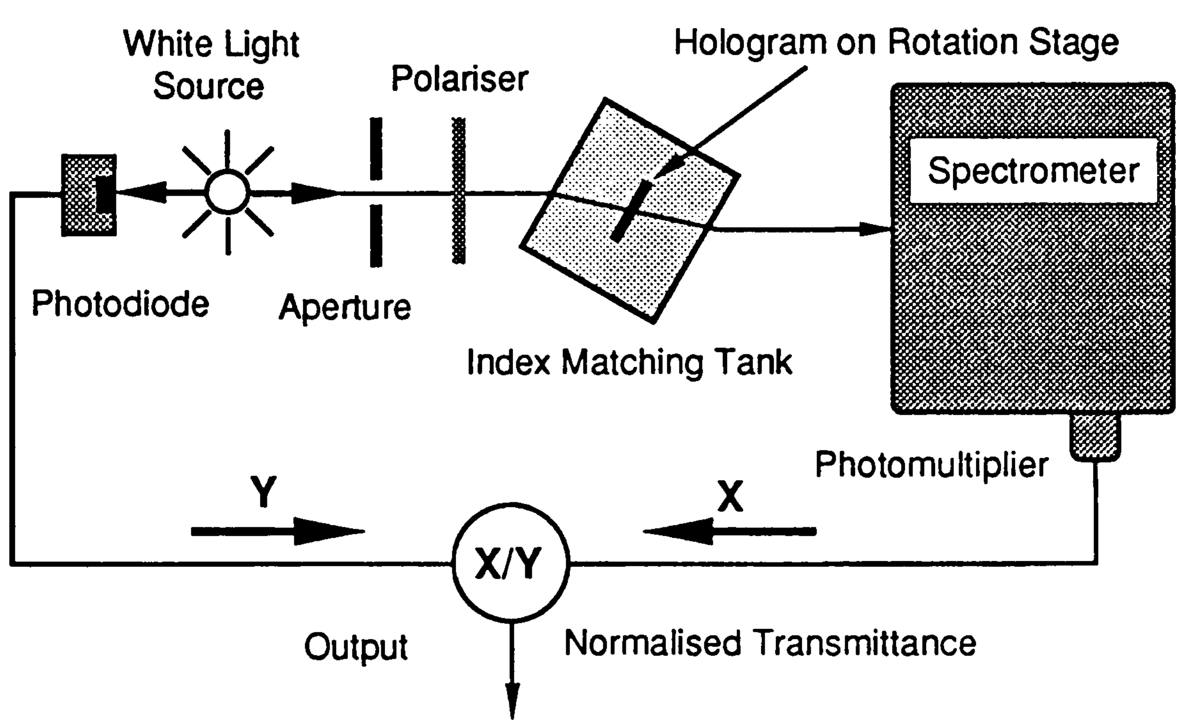


Figure 1.4 The set up used to analyse volume gratings.

This set-up was used to measure (i) a spectral (wavelength) characteristic of a hologram at one particular replay angle or (ii) angular information when replayed at one particular wavelength.

(i) The hologram is placed in the index matching tank and kept stationary at the particular angle of replay. The spectrometer then scans through the selected range of replay wavelengths supplying information to the computer about the transmitted beam intensity at each increment. After the scan is complete the plate is removed and the scan repeated in order to provide normalising values for the acquired data.

(ii) Here, the replay wavelength remains constant and the hologram rotates under computer control. At each angle the transmitted intensity is measured. These angular transmission measurements are normalised against a single transmission result after the plate has been removed from the tank.

Because this measuring technique is only capable of measuring the energy depleted from the incident wave, it is suitable for measuring the first order diffraction by thick DCG gratings. Volume type DCG gratings show low absorption at replay and reduced higher orders. However, the same cannot be said for other recording materials (e.g. silver halide) where the thickness may be much less and the attenuation and scatter at replay is much larger.

## 1.7 Thesis summary

Since this thesis is concerned primarily with dichromated gelatin as a recording material, I will start in Chapter 2 with a more detailed look at DCG and its properties. I will discuss the effects of sensitisation and processing upon replay and examine the importance of the quality of the substrate and coverplate.

Chapter 3 looks at the problem of non matching boundary conditions when attempting to record a transmission grating in air. A simple linear theory is described to predict the relative strengths of six recorded gratings. The simple coupled wave theory described earlier is extended to cope with the multiple replay of both reflection and transmission gratings.

From the linear study in the previous chapter, Chapter 4 takes a look at the nonlinear recording characteristic of dichromated gelatin. A theory is described which takes account of material saturation effects and predicts the modulation strengths of harmonic gratings formed at high exposures. This theory is used to match experimental data for single and double exposure transmission gratings.

Chapter 5 follows on from the combined results of Chapters 3 and 4. In this short chapter the beam ratio is investigated at different recording angles using the back surface of the holographic plate to provide the object wave. Thus, it is possible to investigate the strength of spurious gratings recorded due to boundary mismatch at different recording angles. The nonlinear theory developed in Chapter 4 is used to match results of modulation versus exposure energy of both reflection and transmission gratings at varying beam ratios.

In Chapter 6, I look at the combined effect of grating interactions and material nonlinearities when replaying double exposure transmission gratings. A coupled wave approach is taken to account for the recording of a nonlinear difference grating at high exposures. Multiple grating interactions between all three gratings are included at replay and the results are compared with experimental results for differing exposure energies, recording angles and replay wavelengths.

Chapter 7 departs from direct analysis of DCG itself and uses DCG as a tool to investigate the scattering phenomenon apparent in silver halide emulsions. Different silver halide emulsions are investigated for comparison.

# Chapter 2

# Dichromated Gelatin

## 2.1 Background

Dichromated gelatin (DCG) has been used as a photosensitive medium since the 1800's when it was introduced as a photoresist in the printing industry [Kos65]. In 1968, Shankoff [Sha68a] used its photosensitive properties to periodically harden the gelatin by exposing it to a varying interference pattern of intensity. It was then processed to construct a high efficiency surface relief hologram which varied as a function of refractive index. In addition, its volume properties were discovered which led to the use of DCG for holographic recording purposes.

### 2.1.1 *Gelatin*

Gelatin is a transparent medium from protein collagen. The primary sources for this are generally cattle hide and bones. The gelatin molecules may be described by the following general description of a polypeptide chain in Figure 2.1, where R represents an amino acid.

The chemical composition and the choice of amino acid is dependent upon the source. For a detailed description of gelatin for use in photosensitive systems see James [Jam77].

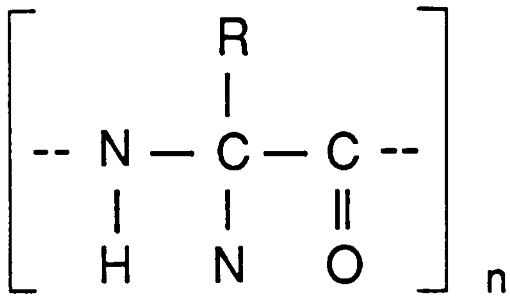

Figure 2.1 Chemical composition of gelatin molecule

The gelatin matrix has the ability to soak up large quantities of water and hence chemicals in a soluble form. This allows the impregnation by photosensitive particles, such as silver halide, used in photographic film. However, it also has the ability to swell to several hundred percent due to strong hydrogen bonding between water molecules and polar regions of the gelatin. We find that this is an extremely useful property when we come to use gelatin as an actively photosensitised medium, instead of its conventional role as a passive support for silver halide. The gelatin may be actively photosensitised using the dichromate ion to form dichromated gelatin.

### 2.1.2 *Photochemistry*

The dichromate ion ($Cr_2O_7^{2-}$) may be introduced into the gelatin by soaking in an aqueous solution of ammonium dichromate [$(NH_4)_2Cr_2O_7$]. Other dichromate solutions are available for use (e.g. potassium or sodium dichromate), however, ammonium dichromate is easily soluble, offering the capability of high dichromate concentrations and hence greater sensitivity.

When a photon of sufficient energy is incident on the sensitised gelatin, the hexavalent cromium ion ($Cr^{6+}$) is reduced to the trivalent ($Cr^{3+}$) state directly or via several intermediate chromium compounds. Several photochemical reactions have been proposed [Kos65]. Figure 2.2 shows how this acts to crosslink the carboxyl groups of neighbouring gelatin molecules at areas of exposure. The extent of crosslinking is related to the incident energy such that high energies will cause greater crosslinking and hence greater hardening than at lower energies. This hardening process is extremely stable and reduces the ability of gelatin to absorb water.

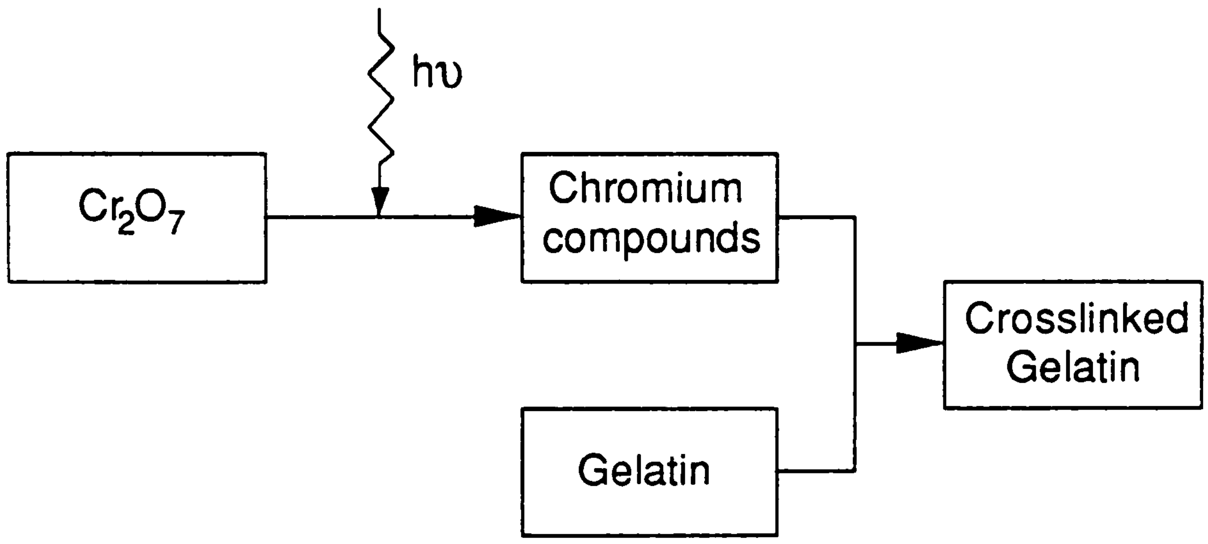


Figure 2.2 Mechanism of the crosslinking of gelatin

## 2.2 Dichromated gelatin for holography

### 2.2.1 *Hologram formation*

We have just described how DCG hardens with exposure energy. When a DCG plate is placed in a periodic spatial intensity variation of optical frequency, such as a standing wave interference pattern, it will respond in the above manner. At areas of high intensity, crosslinking will cause it to harden more than at areas of low intensity. This creates a periodic hardness differential throughout the volume of the gelatin, and describes the recording of a latent image of the intensity distribution. We note here that the recording mechanism is homogeneous leading to the capability of high resolution (> 5000 lines $mm^{-1}$). Calixto [Cal84] and Newell *et al* [New85] have studied the replay of these weak absorption type gratings in their study of real time DCG holograms.

By processing the DCG plate we can amplify the latent image to allow high efficiency replay. The processing steps will be described later in some detail, however, this involves the swelling of the exposed plate with water and then a rapid dehydration using an alcohol such as isopropanol. This changes the hardness differential to one of refractive index, giving the gelatin phase properties.

If the gelatin is soft the areas of low exposure will wash away in the water bath and a surface relief grating will be recorded [Sha68a] [Mey71]. However, if the average hardness of the gelatin is increased then the gelatin will not dissolve leaving the material to vary in hardness throughout its volume. The actual mechanism by which we obtain volume refractive index variation is not clear. Many authors have proposed theories to describe the modulation mechanism although it appears that DCG will respond differently depending upon the amount of hardening of the gelatin.

Initially, in 1970, Curran and Shankoff [Cur70] described the large refractive index variation as being air filled voids between areas of strong crosslinking. They believed that these were cracks introduced along the fringe planes due to the strain of shrinking the gelatin rapidly and removing water from the gelatin matrix. This explained the high modulation values achieved perhaps with a soft gelatin, however did not explain the absence of scatter for low exposure gratings. In 1972 Meyerhofer [Mey72] described the large refractive index modulation as being caused by the binding of isopropanol molecules to chromium atoms at the crosslinked sites, however this was unable to explain why water has a significant effect on the efficiency of a DCG hologram before and after the isopropanol processing steps. In 1976 Case and Alferness [Cas76] attempted to model the method of fringe formation by assuming the formation of small air filled vacuoles. Instead of a small number of large separations between gelatin strands, they proposed the existence of a large number of voids ($<< \lambda$) of density in volume. This would then explain the low scatter of DCG since a periodic waveform could now be sampled more accurately. In 1980, Chang [Cha80a] and Samoilovich *et al* [Sam80] attempted to explain several experimental observations which the other models could not describe. They proposed a rearrangement of the gelatin molecules being dependent upon the exposure level, i.e. a higher exposure would lead to a higher density of gelatin. At the swelling stage, this more dense volume would not then swell as much as areas of less exposure. In 1981, Sjölinder [Sjö81] dismissed hardening to be the main reason for change in refractive index. He proposed that volume modulation formation is due to the refractive index variation of a compound of the $Cr^{3+}$ ion, gelatin and isopropanol.

### 2.2.2 *Preparation of plates*

Reliable, high quality dichromated gelatin plates are not commercially available. This is because of the low lifetime of sensitised gelatin and because of the fact that DCG is not environmentally stable. The majority of plates used throughout the course of this thesis were kindly supplied by Pilkington Research Plc. in the form of high quality plane gelatin coated on 3 mm thick float glass substrates. The standard thickness of gelatin supplied was nominally 22 μm. Although the average thickness varied from batch to batch, the variation of thickness on each 8" x 10" plate was very low to a tolerance of approximately 5%.

A simple method of obtaining plane gelatin plates has been suggested by Lin [Lin69]. By removing the silver halide and dyes from commercial photographic plates (e.g. Kodak 649F) it is possible to obtain a reasonably uniform gelatin coating of commercial quality [Oli84] [Cha71]. There are several methods available to coat gelatin on to glass substrates. After treating the glass substrate with acetic acid to obtain greater adhesion, the gelatin may be applied by spinning or dipcoating [Bra69], casting [Sjö81] or pouring [Cul82]. Others have suggested the doctor blade method [Bra69] and the coating of non planar substrates [McC73]. The drying of these films plays an important role in obtaining high quality coatings. Chang [Cha71] suggested an optimum temperature just below the melting point. Duncan *et al* [Dun85] have also described the problem of drying induced stress and discussed how these can be reduced by controlling carefully the drying process.

### 2.2.3 *Processing*

The processing stages of dichromated gelatin holograms play a critical role in determining the final quality at replay. Several authors have suggested different formulae for hologram processing [Gue79] [Cha79] [Sam80] [Geo87], however they all tend to follow the basic steps of *wash* and *dehydrate*. In particular, we are required to closely control the processing times, pH and temperatures. The variation of these parameters at each step allows close control over the modulation and thickness of a hologram enabling variation of replay efficiency, bandwidth and wavelength [Cha79] [Cul82]. We will therefore take some time looking in detail at the whole processing procedure. A table containing the processing conditions for the holograms in this thesis is outlined and followed by a brief explanation of each stage.

2.2.3.1 *Table of processing procedure*

Table 2.1 outlines the whole process used in this thesis to record holograms in dichromated gelatin. It is similar to that described by Newell [New89] giving details of temperature, processing time and the solutions used at each step.

| | Step | Temp. | Time | Solution |
|---|---|---|---|---|
| *Sensitisation:* | 1. | 20°C | 5 min. | 2% ammonium dichromate + 0.5% photoflo. |
| | 2. | 20°C | 3 hrs. | Dry in rapidly circulating dry air. |
| | 3. | | | Remove crystalised ammonium dichromate from rear of glass substrate. |
| *Exposure:* | 4. | | | Expose at a wavelength of 514.5 nm. |
| | 5. | 25°C | 5 min. | Wash off index matching fluid with propanol. |
| *Bias hardening:* | 6. | 25°C | 5 min. | 0.5% ammonium dichromate. |
| | 7. | 25°C | 5 min. | 25% Agfa structurix fixer + 1% hardner. |
| *Wash:* | 8. | 25°C | 5 min. | Distilled Water. |
| *Dehydration:* | 9. | 25°C | 5 min. | 50% propanol + 50% distilled water. |
| | 10. | 25°C | 5 min. | 100% propanol. |
| | 11. | 40°C | 12 hrs. | Dry overnight in rapidly circulating dry air. |
| *Encapsulation:* | 12. | | | Coverplate with glass using optical quality epoxy resin (Epo-tek 301). |

Table 2.1 Processing procedure used for dichromated gelatin holograms

### 2.2.3.2 *Sensitisation*

Plane gelatin plates were sensitised by bathing in a solution of 2% / weight ammonium dichromate (20 grammes / litre) plus 0.5% wetting agent (Photoflo). Ammonium dichromate [$(NH_4)_2Cr_2O_7$] was chosen because of its high solubility in water and high sensitivity, however it is also possible to use other dichromates (e.g. potassium dichromate). The wetting agent used was photoflo, the purpose of which is to improve uniform diffusion of $(NH_4)_2Cr_2O_7$ throughout the gelatin matrix.

It is possible to sensitise using much higher concentrations of $(NH_4)_2Cr_2O_7$ than 2%. This increases the sensitivity of the DCG leading to a reduction in necessary exposure energy and an increase in available modulation. However, it also leads to an increase in absorption at recording, causing greater attenuation of the recording beams. We then obtain a higher degree of nonuniformity and an increase in bandwidth.

Varying the sensitisation also leads to a change in average refractive index and thickness. Newell [New87] has made a comprehensive study of these parameters. He has shown that both the refractive index and thickness of sensitised gelatin (before exposure) increase with a rise in sensitiser concentration. After processing, he found that the refractive index, relative to the pre - exposure values, reduced at different rates for different sensitisation concentrations. Also, he found that the relative thickness of the DCG increased more at lower sensitisations. This is due to the fact that high $(NH_4)_2Cr_2O_7$ concentrations occupy a larger volume within the gelatin than lower concentrations. During the processing stage most of the dichromate is washed out resulting in a difference in replay Bragg condition. Because of these changes in dimension and refractive index, we would expect the replay wavelength of a grating to vary with sensitisation and exposure energy.

Figure 2.3 shows a plot of replay wavelength versus exposure energy at three levels of sensitiser concentration (5%, 6.5% and 8%) for single reflection gratings recorded at 514.5 nm. Each was replayed at the recording angle of 20° in the index matching tank. This illustrates how the sensitiser concentration affects the replay Bragg condition. At low exposures, the 5% case shows replay at longer wavelengths than recording showing swelling, the 6.5% case replays around 514.5 nm and the 8% case replays at a shorter wavelength than recording indicating shrinkage. This plot also shows how the Bragg condition is affected by varying degrees of exposure energy. At low energies, we obtain less hardening and thus replay at a longer wavelength than the same hologram at a higher energy. Of course, this plot is dependent upon the angle of the grating vector within the gelatin. A reflection grating will be affected by a far greater extent by swelling than a transmission grating, simply because reflection planes are parallel to the direction of swelling or shrinkage.

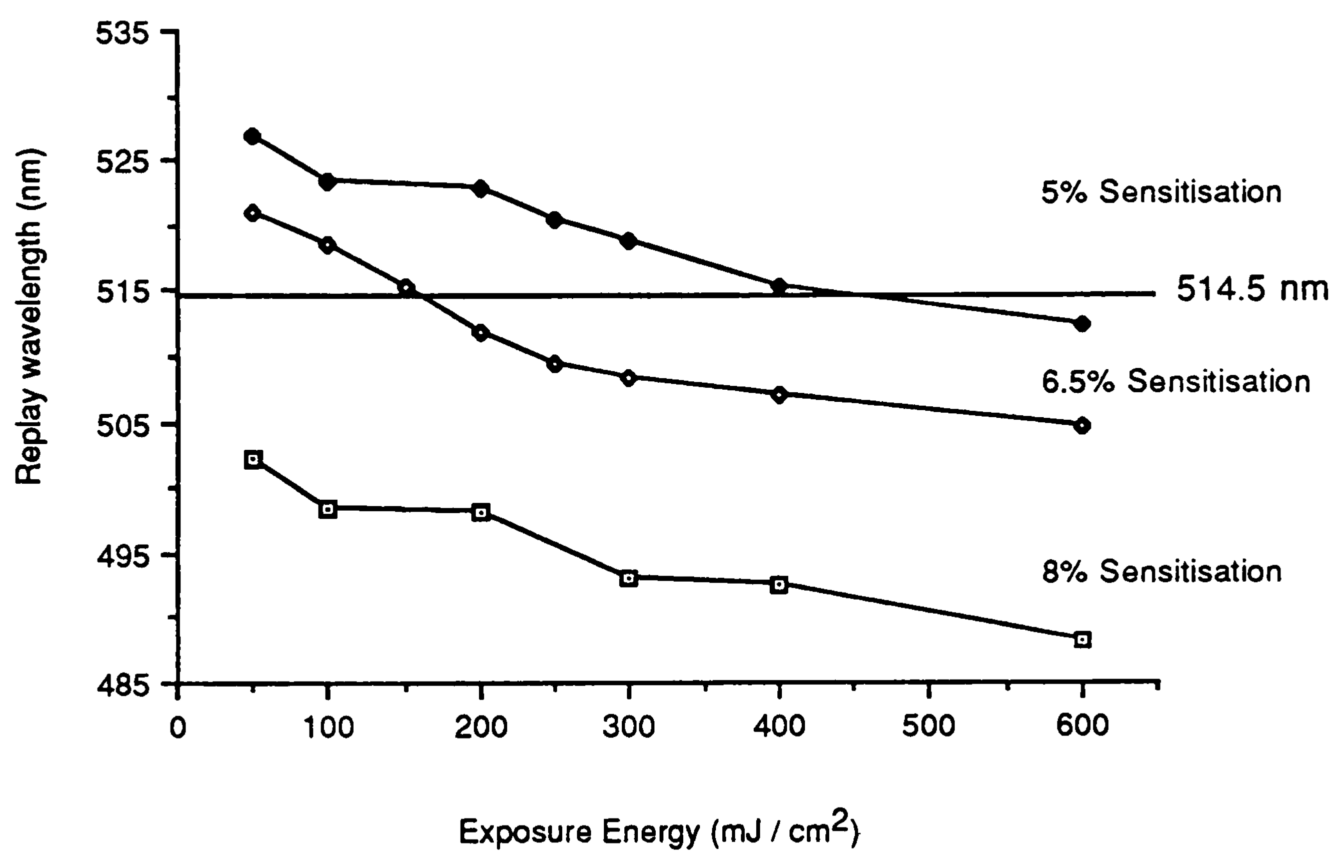


Figure 2.3 Bragg replay wavelength versus exposure energy for varying degrees of sensitisation

After sensitisation, the plates were dried in a low humidity oven in rapidly circulating dry air at room temperature. A humidity level less than 40% is necessary since the plates are now highly sensitive to moisture. After three hours the plates are taken out and $(NH_4)_2Cr_2O_7$ which has crystalised on the rear of the substrate is removed.

For consistency of results, all exposures were taken within four hours of this step. This is because after sensitisation a *dark reaction* takes place which slowly hardens the DCG (as if constantly exposed to a low, uniform intensity) [Kos65] [Cha79]. This may result in a change in modulation if plates are recorded after a different period of time. It is believed that this dark reaction is due to the slow reduction of the dichromate ion, and continues after exposure until processing. Chang [Cha80a] has shown that gratings left for over two days before processing may double in modulation strength.

### 2.2.3.3 *Exposure*

An ideal exposure energy for DCG sensitised at 2% ammonium dichromate is in the region of 200 to 800 mJ / cm$^2$.

The exposure energy required for a DCG hologram is primarily dependent upon the level of sensitisation and the absorption spectra of ammonium dichromate. Figure 2.4 shows a plot of transmittance versus replay wavelength for sensitised DCG plates for two concentrations (2% and 10%) of ammonium dichromate.

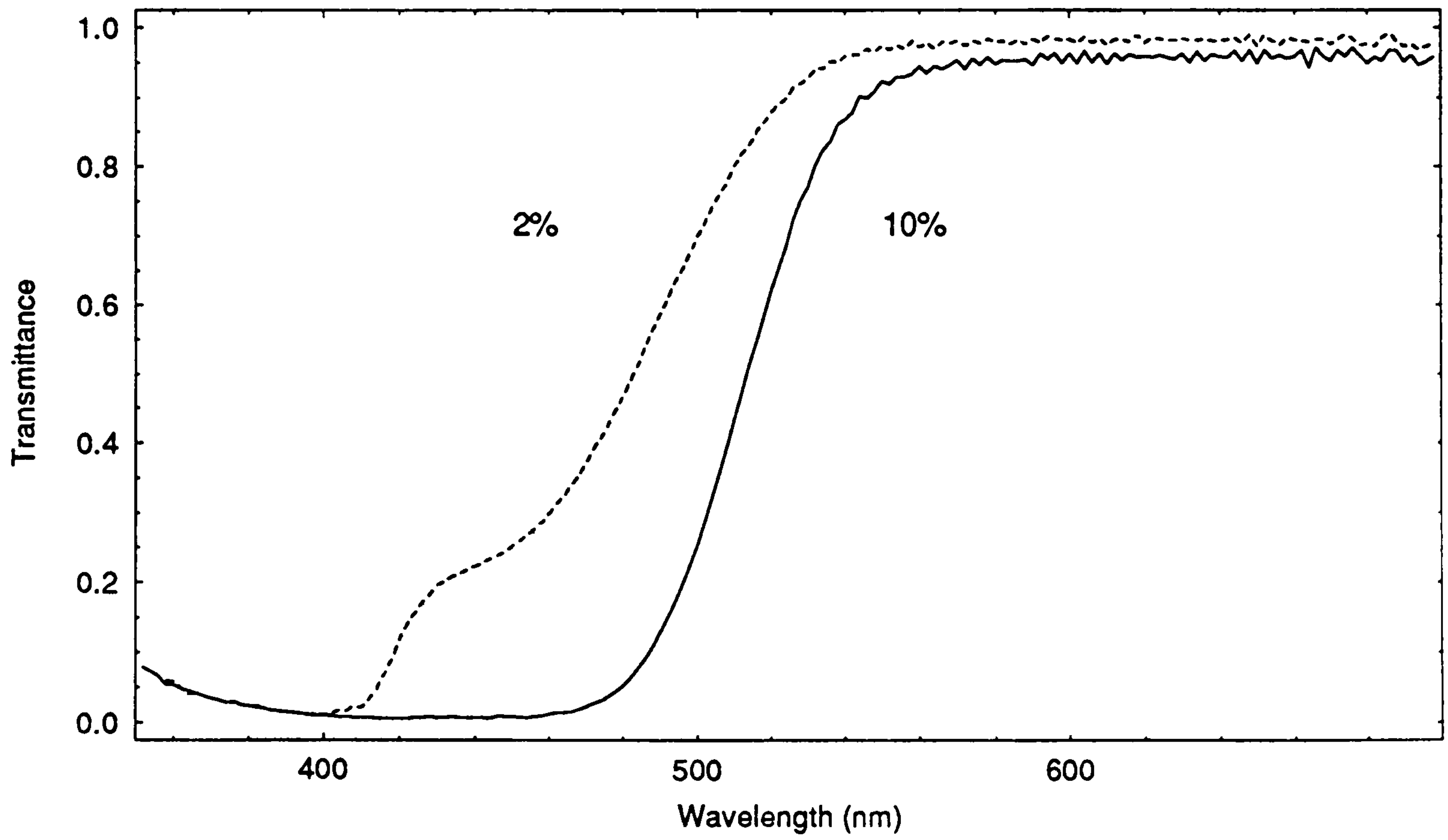


Figure 2.4 Plot of transmittance versus incident wavelength for 2% and 10% concentrations of ammonium dichromate.

Each plot is normalised to an unsensitised gelatin plate. For both cases it shows high absorption (little transmittance) at short wavelengths, however it shows very little absorption at wavelengths above 540 nm. This means that DCG is insensitive to long wavelengths. However, Sosnowski and Kogelnik [Sos70] have described the recording of holograms at ultra violet wavelengths. We can see that the 10% case is about two times more sensitive than the 2% case at 514.5 nm. Also, we can see that the gelatin is now about five times more sensitive at 488 nm than 514.5 nm when sensitised with 10% solution.

Sensitivity at longer wavelengths may be achieved by adding dyes to the gelatin [Kub79a] [Kub79b] [Cha86] [Cha88]. However, the concentration of these dyes tends to be high and leads to an increase in absorption and scatter. Solano *et al* [Sol85] have been able to record gratings with red wavelengths without the addition of dyes, but this required extremely high exposure energies which are not feasible for normal recording.

One method of obtaining a panchromatic response and increasing the light sensitivity is to record a hologram in silver halide emulsion and then form phase holograms by means of silver halide sensitised gelatin (SHG) processing [Pen71] [Gra80] [Har86] [Maz82a,b]. A major disadvantage of this technique is that the resolution of recording is limited by the grain size of the silver halide grains in the emulsion. This will limit the response at high spatial frequencies.

The exposure required for a particular result, is also dependent upon the gelatin type, fringe structure and the processing method used. The temperature, pH and concentrations of solutions all play a critical part in modulation formation [Cul82].

After exposure the plates were processed immediately. However, if index matching oil had been used during exposure it was washed off using a solvent such as propanol.

#### 2.2.3.4 *Bias hardening*

As we discussed earlier, the hardness of gelatin before the swelling stage is very important. If it is relatively soft, the water will dissolve too much gelatin creating cracks and fractures. This will result in a noisy hologram with high scatter. If the gelatin is too hard, there will not be enough relative swelling between the exposed and unexposed regions to form a large modulation. However, the scatter will be reduced.

The hardness level of the gelatin may be controlled by following Lin [Lin69]. He was first to suggest soaking the plate in a low concentration of ammonium dichromate and then hardening it by using fixer. This procedure adds a uniform level of dichromate ions to the exposed hologram, then the fixer reduces the $Cr^{6+}$ to the $Cr^{3+}$ state increasing the bias hardness of the gelatin.

Once the gelatin is in the fixer bath it is no longer photosensitive.

2.2.3.5 *Swelling*

The washing step softens the gelatin and causes it to swell to a thickness governed by its hardness. During this step all unwanted chemicals are removed to avoid scatter and noise in the final hologram. The amount of swelling, and thus the replay Bragg condition, are not only controlled by the hardness of the gelatin after exposure, but are critically dependent upon temperature and the pH of the water. As the temperature increases, the gelatin softens and we obtain greater swelling. This manifests itself in the final hologram as an increase in replay wavelength and an increase in modulation. However, we must be careful not to make the gelatin too soft otherwise we will introduce scattering [Bra69]. Of course, a transmission type grating will resist swelling more than a reflection grating due to the orientation of its fringes [Cha79].

2.2.3.6 *Dehydration*

Dehydration is the most crucial step in the processing procedure. During this stage the gelatin is dehydrated rapidly using an alcohol such as propanol, forcing it to replace the volume once occupied by water with air. A number of water and propanol mixtures have been discussed [Cul82], however, in this thesis two stages were performed. That was 50% water : 50% propanol bath followed by 100% propanol.

The number of dehydration steps influences the spectral bandwidth of the final hologram. Several steps of increasing propanol to water ratio have been found to reduce the bandwidth. This is because the propanol is allowed to diffuse slowly through the gelatin creating a more uniform grating, however, this may lead to a lower modulation.

#### 2.2.3.7 *Drying*

After the dehydration step the gelatin plate is extremely sensitive to humidity. The plates were therefore dried and hardened in an oven at 40° C and low humidity. If the plates were exposed to higher humidities they would absorb water causing an increase in thickness and a reduction in modulation. After drying they were then coverplated with 2 mm thick float glass and an optical quality epoxy.

#### 2.2.3.8 *Post processing*

Before coverplating it is possible to test the hologram and measure its replay characteristics. If these are not suitable it is then possible to reprocess the gelatin under slightly different conditions [Cha76a]. The hologram may be placed back in the water bath and dehydrated afterwards, once more at different temperature or pH values. The amount of dehydration steps may also be altered. Thus, we can alter the thickness and modulation offering control over replay wavelength, angle, efficiency and bandwidth.

## 2.3 Shifting the spectral response

We have seen that DCG is not sensitive at long wavelengths unless dyes are added to the gelatin. However, the adding of dyes to DCG films introduces a large absorption at recording which is not ideal for the recording of reflection gratings. Under certain sensitising and processing conditions, DCG will swell causing a reflection grating which has been recorded at 514.5 nm to replay around 550 nm. However, we are unable to obtain much more swelling by the simple process. Coleman and Magariños [Col81] have shown that by the introduction of certain *inorganic hardeners* to the processing stage can cause the gelatin to resist returning to its original thickness. This allowed them to replay the same hologram at a wavelength as high as 680 nm. Unfortunately, they did not describe the chemicals used.

In this section I will describe some experiments carried out with the chemical Ilfoshift IP8710/23 [Ilf89] to perform a similar type of experiment. Ilfoshift is a swelling agent supplied by Ilford for use with silver halide emulsions. It is believed to act on the gelatin matrix when swollen and not allow it to shrink back to its original thickness.

### 2.3.1 *Experiments*

Single unslanted reflection gratings were recorded in an index matching tank (filled with Xylene) at incident angles of +20° and +160° using a mirror attached to the back surface of the plate. The exposure energy used was 1000 mJ / cm$^2$ and the recording wavelength was 514.5 nm. Figure 2.5 shows the recording geometry.

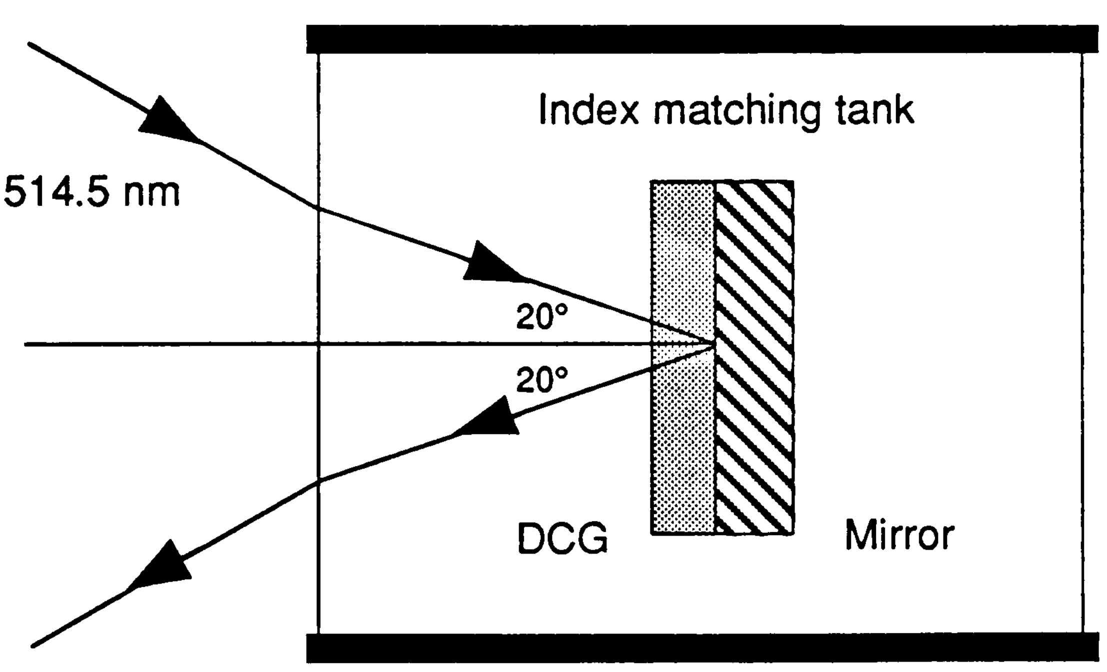


Figure 2.5 Recording geometry for swelling experiments

The plates were then processed using the above technique, however, different concentrations of Ilfoshift were used at the swelling stage. For this case, the temperature was maintained at 25° C, however the wash time was extended to 9 minutes. Table 2.2 shows the gratings recorded and the associated swelling stage. Grating 2.1 was washed in water for the full 9 minutes as an example of the standard processing technique. Gratings 2.2, 2.3 and 2.4 were washed in water for 2 minutes + Ilfoshift for 5 minutes + water again for 2 minutes using increasing Ilfoshift concentrations of 5%, 10% and 20% respectively. The pH was kept constant at 6.5. Then, to observe the effect of pH, Gratings 2.5 and 2.6 were processed using a pH value of 10. Grating 2.5 was washed solely in water and Grating 2.6 was washed using 10% Ilfoshift.

| Grating | Swelling stage | pH |
|---|---|---|
| 2.1 | 9 min $H_20$ | 6.5 |
| 2.2 | 2 min $H_20$ | 6.5 |
| | 5 min 5% Ilfoshift | 6.5 |
| | 2 min $H_20$ | 6.5 |
| 2.3 | 2 min $H_20$ | 6.5 |
| | 5 min 10% Ilfoshift | 6.5 |
| | 2 min $H_20$ | 6.5 |
| 2.4 | 2 min $H_20$ | 6.5 |
| | 5 min 20% Ilfoshift | 6.5 |
| | 2 min $H_20$ | 6.5 |
| 2.5 | 9 min $H_20$ | 10 |
| 2.6 | 2 min $H_20$ | 10 |
| | 5 min 10% Ilfoshift | 10 |
| | 2 min $H_20$ | 10 |

Table 2.2 Processing for Ilfoshift tests

### 2.3.2 *Results*

The gratings were characterised using the spectral transmittance measuring technique described in Chapter 1. Figures 2.6 and 2.7 show the results of replaying at the recording angle of +20° in the index matching tank.

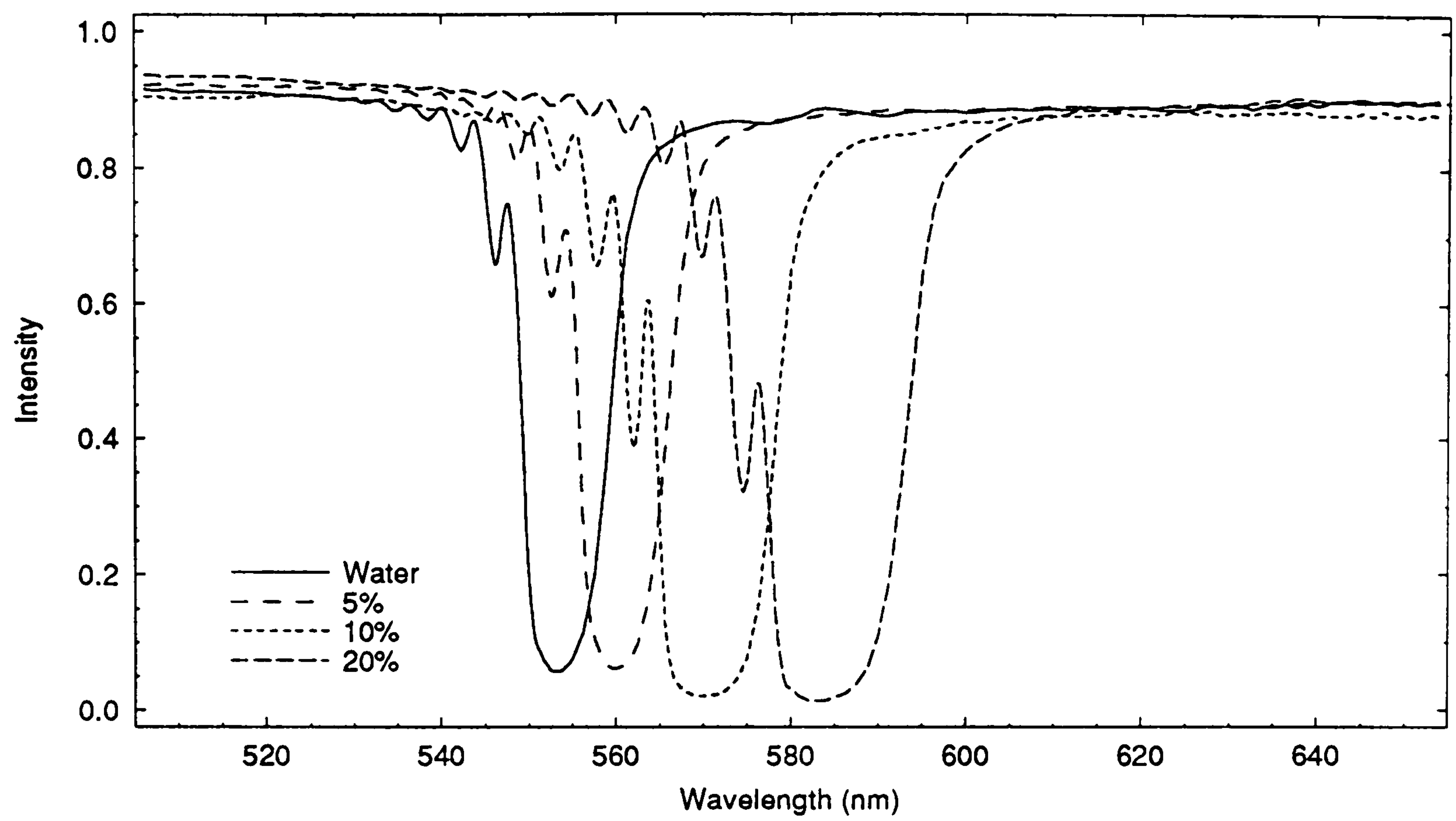


Figure 2.6 Effect of processing with pH = 6.5.

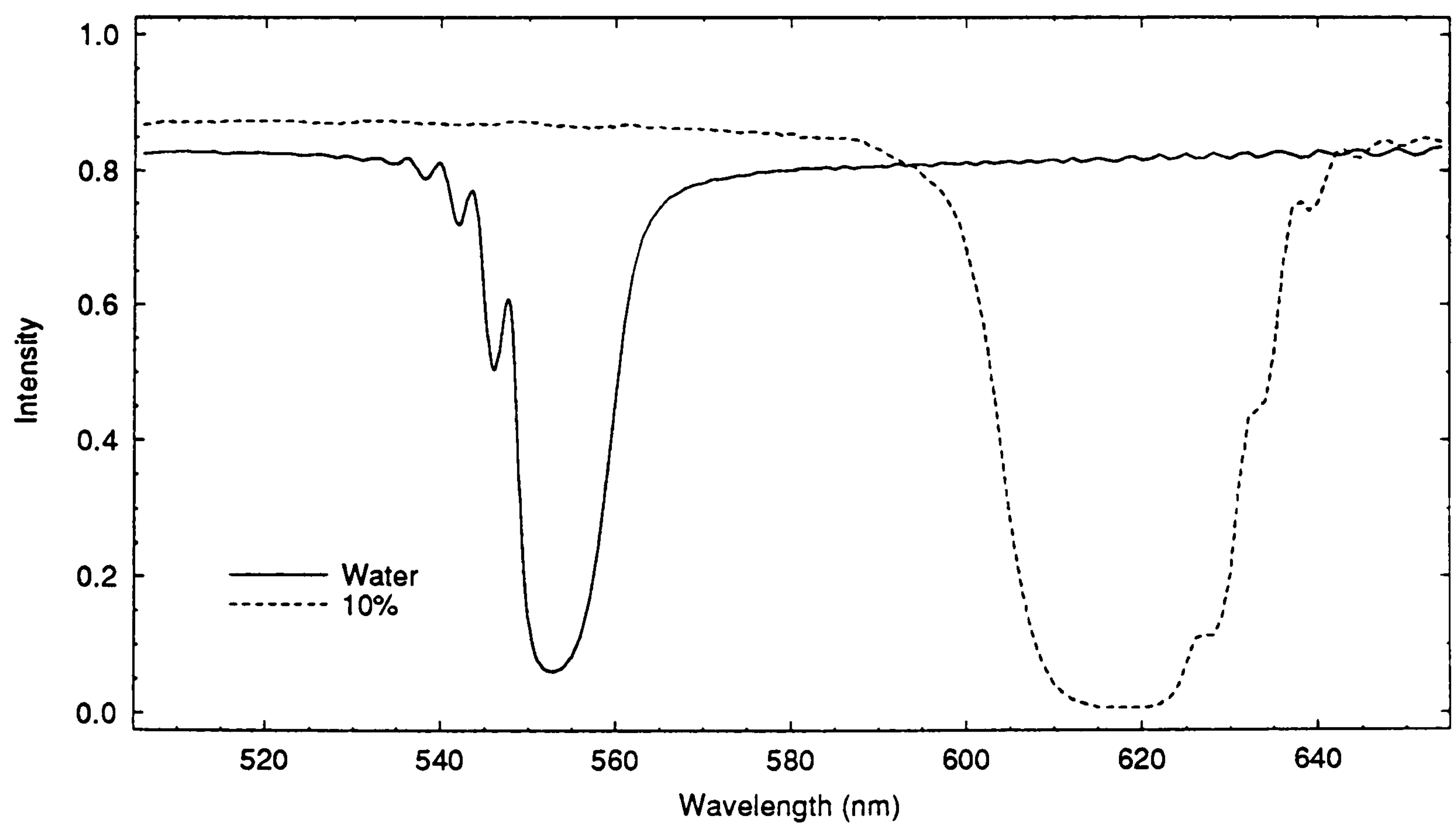


Figure 2.7 Effect of processing with pH = 10.

In Figure 2.6, as the concentration of Ilfoshift is increased from 0% to 20% we observe an increase in replay wavelength from 552 nm to 584 nm corresponding to swelling of 18% and 25% respectively. We also observe an increase in half power spectral bandwidth from 100 nm to 170 nm and an increase in modulation ($n_1$) from about 0.0135 to approximately 0.0195.

Figure 2.7 shows the effect of increasing the pH in the swelling stage. By using only water we find replay occurring once more around 552 nm, however, we see now that the 10% solution of Ilfoshift at the greater pH has caused the grating to replay at a wavelength around 620 nm (i.e. a swelling of 32%) with a half power bandwidth of 300 nm. In this case, the measured modulation ($n_1$) values increased from 0.0135 to 0.021.

Thus, we can conclude that greater concentrations of Ilfoshift are causing the gelatin to harden to greater levels at the swelling stage causing it to restrict shrinkage during dehydration. This is leading to a greater final thickness which causes a larger replay wavelength and an increase in modulation. If we increase the pH in the swelling stage, we find that the grating replays at an even higher wavelength.

## 2.4 Substrate and coverplate quality

When recording holograms and, in particular, Holographic Optical Elements in dichromated gelatin, it is important to note that the quality and optical performance are not solely dependent on the properties of the recording medium, but are also influenced by other factors such as the optical and opto - mechanical properties of the substrate and coverplate. It is desirable therefore to investigate these components to assess their influence individually on the performance of the final product. This section takes an inquisitive, experimental look at their effect on a simple reflection grating. Prime consideration was given to the effect of the flatness of the various plane surfaces in the element, namely the external face of the substrate, the face of the gelatin before sensitisation and the faces of the coverplate used for encapsulation.

### 2.4.1 *Experiments*

Planar reflection gratings were recorded in 22 μm thick DCG on two different substrates. One grating was recorded using an ordinary 3 mm thick float glass substrate (as supplied by Pilkington) and a second was recorded on gelatin on a 10 mm thick optical flat. The unslanted reflection gratings were recorded at 514.5 nm at normal incidence (0° and 180°). To minimise swelling and increase sensitivity, we used an exposure energy of 250 mJ / $cm^2$ and a sensitisation concentration of 6% ammonium dichromate. The flatness and quality of the substrate and gelatin surfaces were then measured and compared to the reconstructed wavefront.

### 2.4.2 *Results*

To measure surface flatness and the uniformity of wavefronts we used a Fiseau type Interferometer supplied by Specac Plc. Figure 2.8 shows the basic arrangement for such a device.

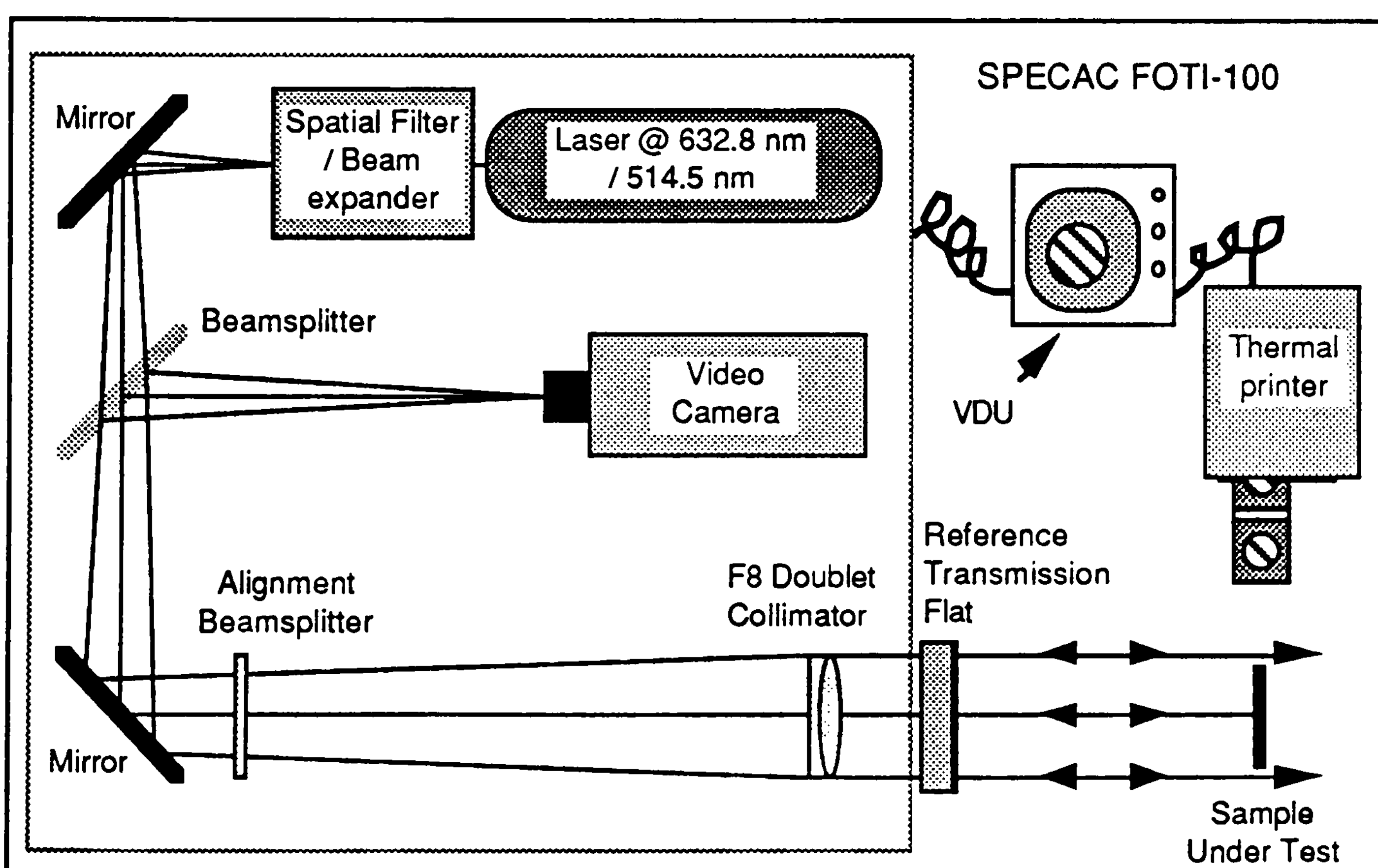


Figure 2.8 Fiseau interferometer for measuring reflected wavefronts.

Essentially, a collimated beam from a coherent source is reflected from a sample and compared with the flatness of a reference transmission flat. This information is selected by a beamsplitter and displayed on a VDU screen in the form of an interference pattern which can then be recorded. A flat sample will therefore produce a low number of straight fringes. The deviation from straightness indicates the extent of flatness according to the equation [Mal78]:-

$$\text{error} = \frac{k\lambda}{2d} \tag{2.1}$$

where $k$ is the peak deviation from straightness and $d$ is the fringe spacing. For the following measurements, we used a $\lambda/20$ flat transmission element as a reference, supplied by Specac.

Figure 2.9 shows an interferogram of a float glass substrate. We clearly see a wood grain type contour pattern corresponding to the uneven surface flatness of the plate. Figure 2.10 shows the interferogram of the gelatin coating on a similar substrate, and in this case we see that the coated gelatin has similar contours. This illustrates that it has followed the flatness of the substrate. Similarly Figures 2.11 and 2.12 show the interferograms for an optical flat substrate. This time we observe straight fringes corresponding to a flatness of approximately $\lambda/10$.

Figure 2.13 shows an interferogram of the optically flat mirror used to record the reflection gratings. Again, measurements on the fringe spacing and straightness illustrate a flatness of approximately $\lambda/10$.

After processing the recorded reflection gratings were replayed in the interferometer to measure the quality of the replayed wavefront in comparison with the master mirror. Figure 2.14 shows the result of a grating recorded using a float glass substrate. Here, we observe straight fringes showing that the grating is replaying a wavefront close to that of the master. If we look at the reflection grating recorded on an optical flat substrate (see Figure 2.15), we see similar straight fringes corresponding to a flatness of $\lambda/8$ to $\lambda/10$. Therefore, we can conclude that we are able to reconstruct high quality wavefronts using DCG gratings.

Figure 2.9 Interferogram of float glass substrate (633 nm)

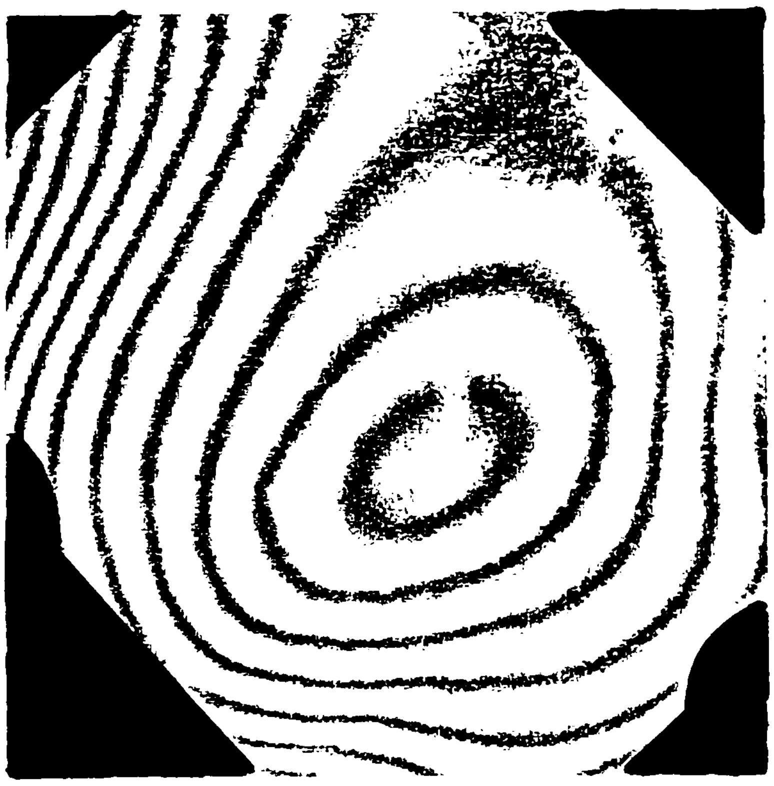

Figure 2.10 Interferogram of gelatin coated on float glass substrate (633 nm)

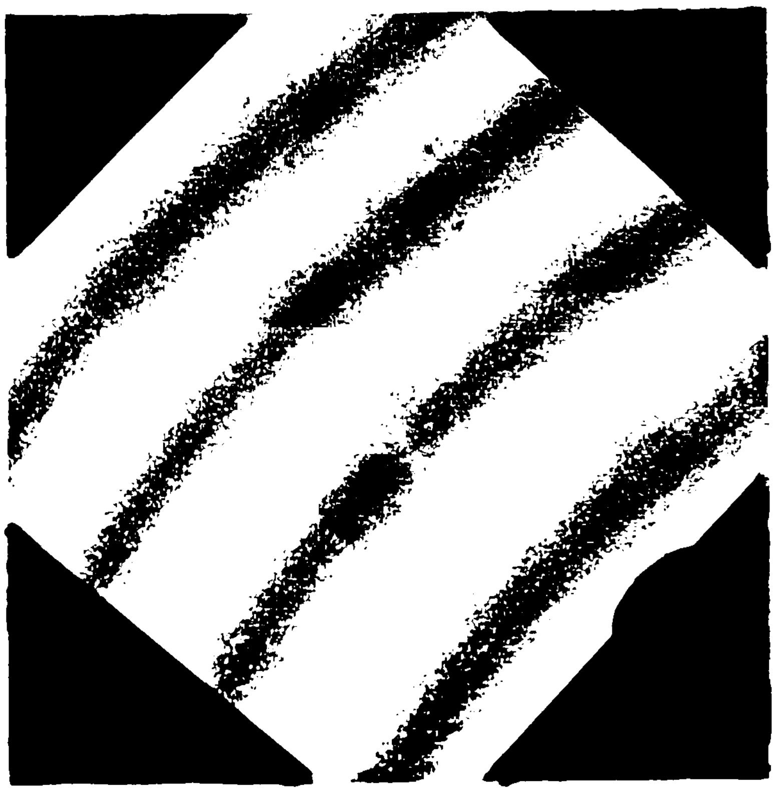

Figure 2.11 Interferogram of flat glass substrate (633 nm)

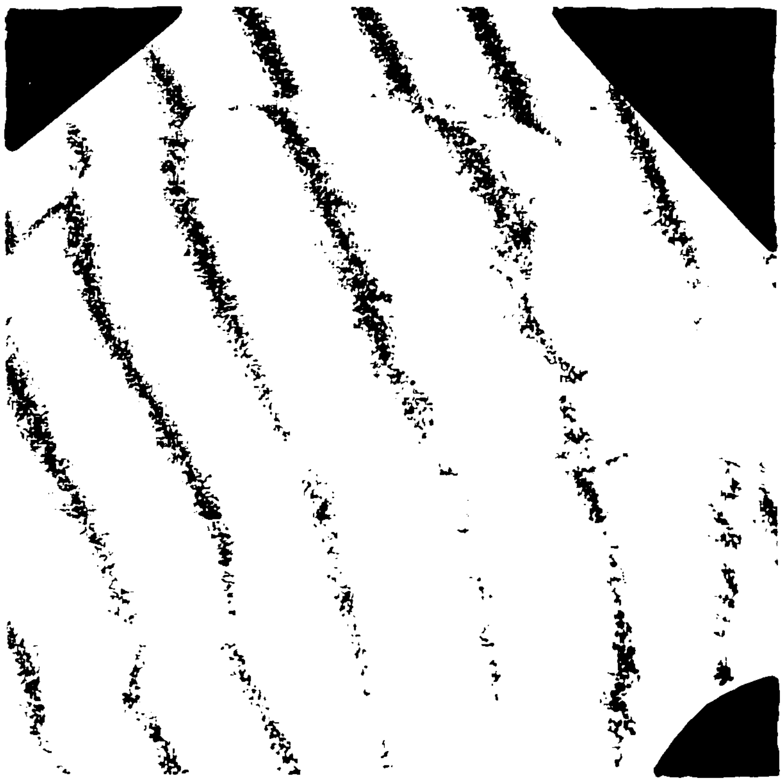

Figure 2.12 Interferogram of gelatin coated on flat glass substrate (633 nm)

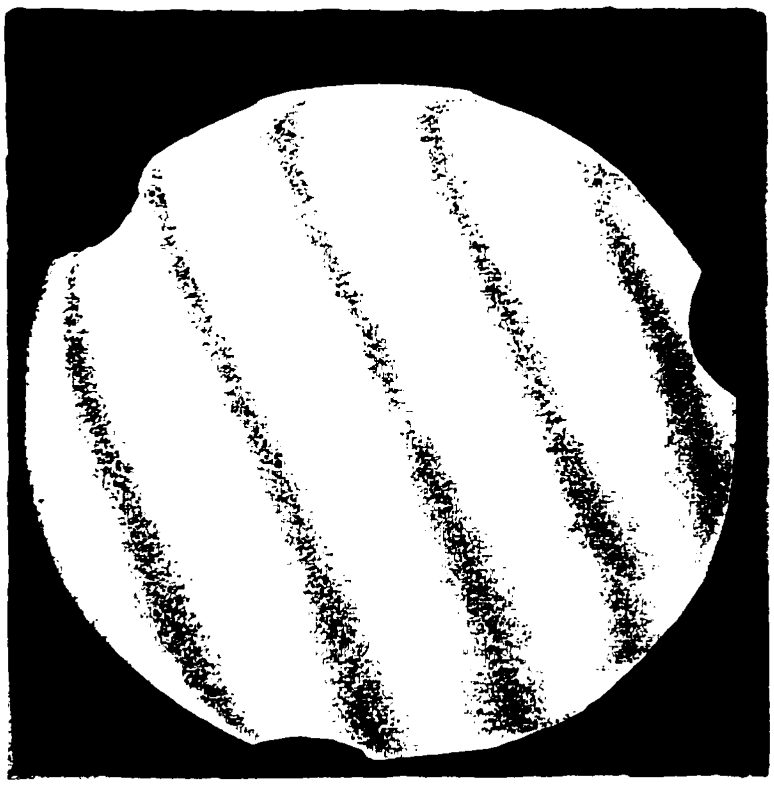

Figure 2.13 Interferogram of mirror used for recordings (633 nm)

Figure 2.14 Diffraction using float glass substrate - no coverplate (514.5 nm)

Figure 2.15 Diffraction using flat glass substrate - no coverplate (514.5 nm)

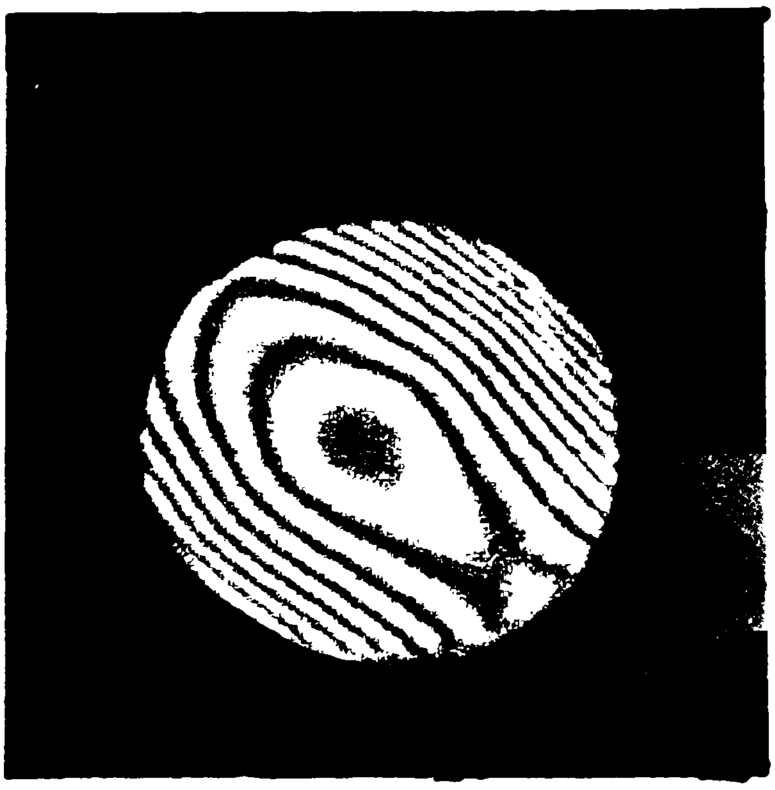

Figure 2.16 Diffraction using float glass substrate - with coverplate (514.5 nm)

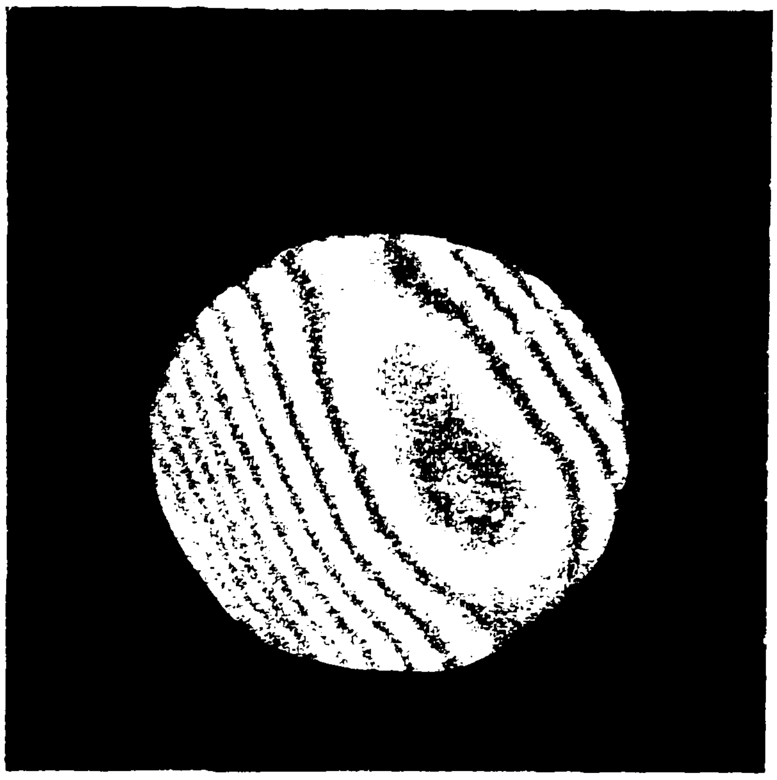

Figure 2.17 Diffraction using flat glass substrate - with coverplate (514.5 nm)

Figure 2.18 Interferogram showing surface irregularities before sensitisation (633 nm)

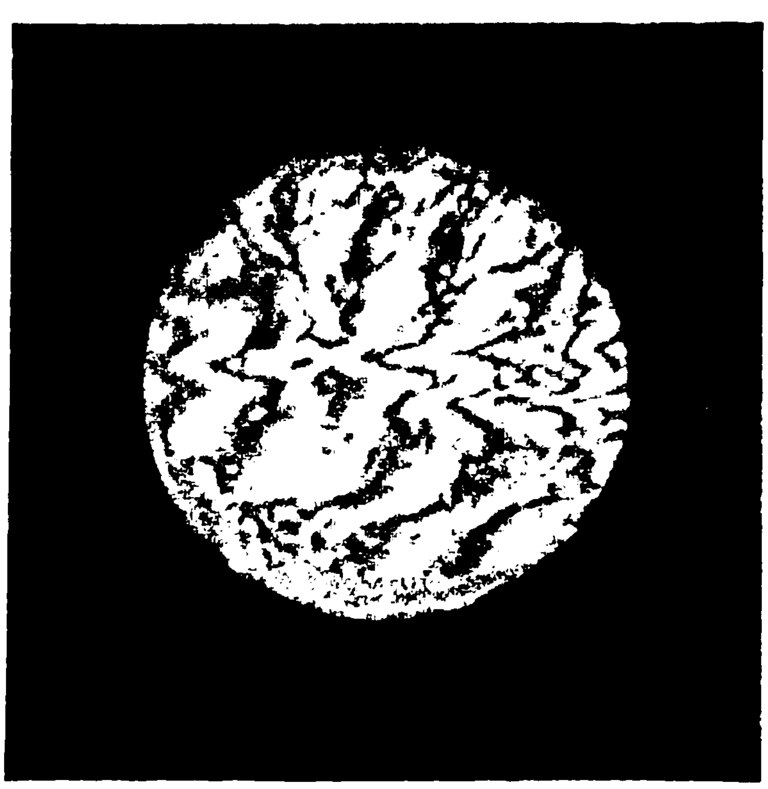

Figure 2.19 Diffraction using irregular gelatin (633 nm)

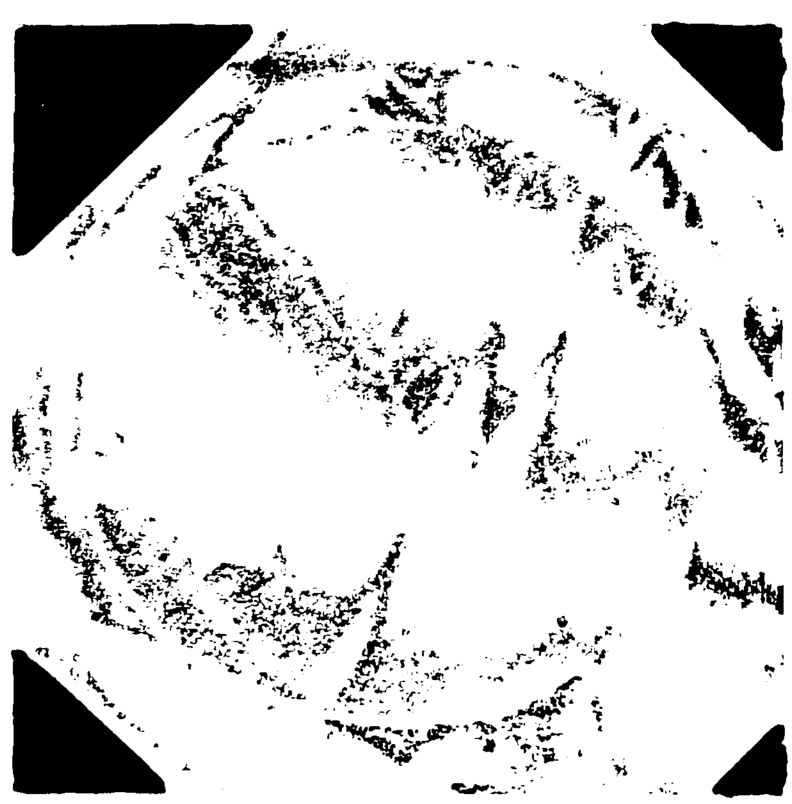

Figure 2.20 Interferogram of gelatin after processing (633 nm)

What happens now if we coverplate the DCG grating? If we use a typical float glass coverplate then its interferogram is similar to Figure 2.9 above. Figures 2.16 and 2.17 show the results of coverplating the holograms recorded on float glass and flat glass substrates respectively. If we compare these to Figure 2.14 and 2.15 and, in particular the master (Figure 2.13), we can clearly see greater distortion of the fringes caused by the introduction of the coverplate on the surface. In fact the contour pattern is extremely similar to the result of the individual coverplate.

Wavefront distortion may be caused by other factors. Figure 2.18 shows an interferogram of gelatin where defects have been introduced during the coating process. There appear to be surface irregularities combined with cracks running along the surface.

When a grating is recorded in this gelatin layer we find that the diffracted fringe pattern is distorted by the irregularities (see Figure 2.19). Figure 2.20 shows replay at 633 nm. This wavelength is too large to be diffracted by the grating, allowing us to observe the effect of exposure upon the gelatin. We see a discontinuity around the circumference of exposure indicating a difference in thickness of refractive index. However, we also see severe distortion of the fringes due to irregularities in the gelatin.

## 2.5 Hologram properties

### 2.5.1 *Quality*

In the preceding section we have outlined some of the factors which influence the final quality of DCG holograms, i.e. the quality of the substrate, coverplate and DCG coating must be considered when recording high quality elements. However, setting aside their influence, DCG is still a superior holographic recording material. Because of its homogeneity, it is capable of recording high frequency reflection holograms of extremely high resolution (> 5000 lines $mm^{-1}$). This leads to negligible scatter, reducing the level of noise at both recording and replay. It exhibits extremely low absorption allowing gratings to be recorded with efficiencies very close to the theoretical maximum of 100%. Because of these properties DCG holograms may be formed in very thick gelatin coatings (200 μm say) producing high efficiencies with high selectivity and low spectral bandwidths. The material is not perfect in that it has a saturating response to exposure energy. This may lead to the formation of nonsinusoidal fringe formation and hence the creation of higher harmonics. Nevertheless, it has a large linear recording range which means a large modulation capability.

### 2.5.2 *Nonlinearity*

At low exposure energies, the recording response of DCG is linear and follows the intensity distribution of interfering waves. However, at higher energies, the recording characteristic becomes nonlinear and it saturates. This leads to the replay of nonsinusoidal modulation profiles which act to replay spatial harmonic and intermodulation gratings (see Chapter 4). The exposure energy and modulation at which saturation occurs are dependent upon the sensitiser concentration and pH of the processing solutions. Increasing the concentration of sensitisation increases the modulation and reduces the exposure energy of saturation. Increasing the pH of processing reduces the sensitivity of DCG but also increases the rate of the dark reaction. Chang [Cha79] has suggested that the level of saturation is due to the availability of active sites in the gelatin as opposed to the amount of cromium ions available for the photochemical reaction.

### 2.5.3 *Nonuniformities*

The fringe structure of a DCG grating is subject to nonuniformities. This simply means that the recorded gratings may not be regarded as having constant modulation and being of a single spatial frequency throughout the depth of the gelatin. These nonuniformities arise because of several reasons. If the gelatin has been sensitised with a high concentration of ammonium dichromate then it will have a relatively large attenuation constant at recording. This will lead to a variation of modulation which is dependent upon the hologram depth. Also, if the recording beams are not truly collimated then there will be a variation in the spatial frequency of the grating leading to a broadening of the spectral bandwidth. Perhaps the main cause of nonuniformities is the processing procedure. During the dehydration step the propanol is only capable of entering the gelatin from one side. Therefore we can expect the process to take place more efficiently nearer the gelatin surface than the gelatin / substrate boundary. This forms a *chirped* grating of varying spatial frequency and modulation throughout the gelatin depth. These effects can lead to an increase in bandwidth and an alteration of the sidelobe structure. Mathematical models have been developed which take account of these effects in both transmission [Au87] and reflection gratings [New89].

# *Chapter 3*

# *Spurious gratings due to boundary reflections at recording*

## 3.1 Introduction

It is very often the case, in practical applications of holographic optical elements, that the boundaries of the recording medium cannot be index matched. Therefore, at recording, when an incident light wave of intensity $I_i$ and phase $\theta_i$ impinges upon an interface of differing refractive index, some of its energy will be transmitted and some reflected according to Fresnel's laws [Hec87]. Thus, multiple gratings can arise in the recording medium, due to reflections when matched boundary conditions are not satisfied. Indeed, superposition of as many as six gratings is inevitable if a planar transmission grating is recorded when boundary reflections are not negligible. Figure 3.1 shows how four beams (A, B, C and D) may propagate within a dichromated gelatin (DCG) plate when simply attempting to record a single transmission grating. Beams B and C are waves introduced due to reflections at the air / substrate boundary. In this chapter I study this phenomenon and its contribution to multiple reflection and transmission gratings when recording a dichromated gelatin hologram in air.

Multiple holographic gratings have been the focus of attention for many authors for over twenty five years.

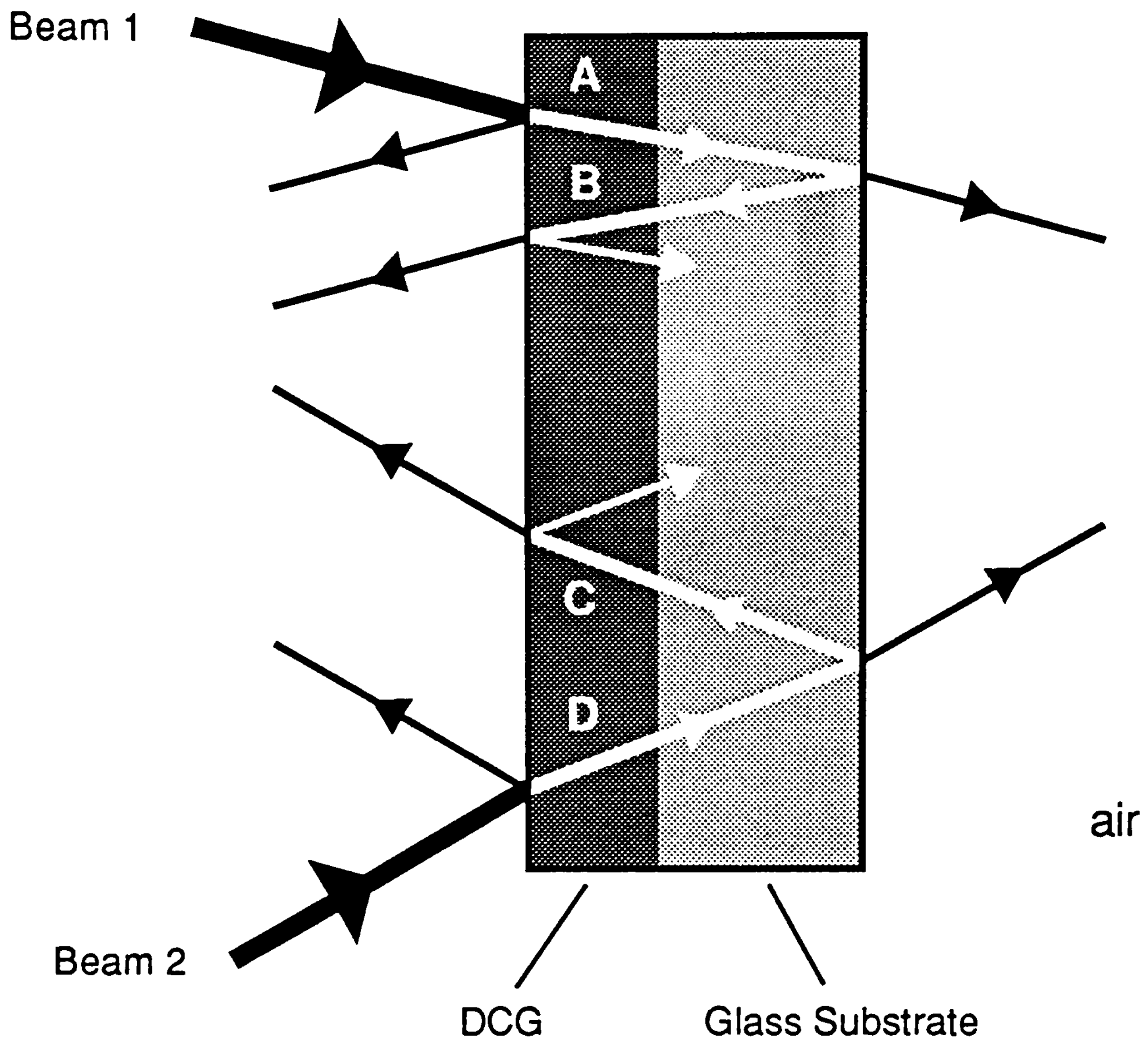


Figure 3.1 Propagation of four beams within a DCG plate at recording.

Multiple recordings in the form of holographic data storage were discussed as early as 1963 by van Heerden [Van63a] [Van63b]. Groh [Gro68], in 1968, looked at the possibility of recording multiple holograms in silver halide emulsion to replay simultaneously a number of images of a single object. Further work with $AgH^+$ has been discussed by LaMacchia and White [LaM68a] who, in 1968, stored over 1000 superimposed holograms of a point source, and Akahori and Sakurai [Aka71] who recorded an array of 100 recordings. In 1972, Meyerhoffer [Mey72] showed that DCG is capable of recording at least twenty efficient superimposed holographic lenses, and Bartolini *et al* [Bar76] succeeded in storing 550 recordings in campharquinone. In 1975 Staebler *et al* [Sta75] showed that lithium niobate is capable of high density recording by storing 500 holograms, while recently, Strasser *et al* [Str89] reported the experimental storage and recall of more than twenty holograms with equal diffraction efficiency. Theoretical investigations of multiple recordings include studies in 1975 by Case [Cas75] and Alferness and Case [Alf75] when experimenting with the sequential superposition of two transmission gratings in DCG. In 1978 Kowarschik looked at the case of sequential recordings in both transmission [Kow78a] and reflection [Kow78b] geometries. In 1986, using a numerical approach, Kostuk *et al* [Kos86] modelled both sequentially and simultaneously recorded reflection and transmission gratings, which had been recorded in bleached photographic emulsions. More recently Slinger and co-workers [Sli86] [Sli87] have published a more comprehensive model of multiple transmission gratings, giving comparisons between theoretical and experimental results in silver halide emulsion for sequentially and simultaneously recorded cases.

The recording of additional spurious gratings due to internal specular reflections is a problem which has been recognised for some time. At replay the spurious waves can cause false readings of diffraction efficiency and, in the case of reflection type elements, introduce dispersive transmission gratings. In 1967 Kogelnik [Kog67] first took account of multiple internal reflections in a hologram by assuming an unslanted sinusoidal transmission grating with a change of average refractive index at the boundaries. Using an algebraic summation and relevant reflectances he derived a simple formula to describe the diffraction efficiency at replay. Cornish and Young [Cor75] in 1975 studied the effect of boundary reflections upon the measurement of diffraction efficiency at replay. By expanding Kogelnik's result they were able to compensate for thermal expansion of lithium niobate due to absorption. In 1976 Ctyroky [Cty76] again studied multiple internal reflections when replaying a similar thick sinusoidal grating. However, he generalised Kogelnik's result by producing an analytical solution to diffraction efficiency for both on and off Bragg cases using a coupled wave theory. Konstantinov *et al* explained a mismatch between theoretical and experimental results by allowing for the back reflection of light from the medium / air boundary at replay [Kon79] and later attributed a discrepancy in calculated values to the formation of *secondary structures* during the recording process as a result of interference between the transmitted and reflected waves within the emulsion [Kon82]. In 1984 Sjölinder [Sjö84] used dichromated gelatin to study the formation of unwanted secondary holograms. In his report he index matched a prism to his plate in order to reduce spurious recordings. Owen *et al* [Owe83] in 1983 looked at the problem of multiple diffraction when a single, slanted reflection grating is replayed in air. Here they used a simple iterative coupled wave solution. Finally, Skochilov and Sattarov [Sko86] in 1986 treated theoretically the problem of replaying a fundamental plus four spurious secondary gratings using a coupled wave method.

I will describe some experiments designed to illustrate the effect of spurious recordings in thick dichromated gelatin. I will introduce an experimental technique to separate angularly the spurious gratings and hence identify each one individually. This differs from previous results in that it allows independent, non - interactive replay, and enables the study of each recording as a single volume grating. It is shown that experimental results of transmitted power against incident angle agree well with a simple, linear model. The model is based on the simple assumption that the modulation of a grating in a linear medium is proportional to the product of the amplitudes of each recording wave (see Eqn. 1.8). Therefore, using the Fresnel amplitude coefficients given below, we are able to find the amplitude ratio of each recorded grating within the hologram. By calculating the modulation of the main, strong grating by modelling the experimental dip with coupled wave theory we are then able to estimate the modulation strengths of all other recordings [Bla89a].

For recording with waves parallel to the plane of incidence we can let the amplitude reflection $r_{||}$ and transmission $t_{||}$ coefficients be [Bor80]:-

$$r_{||} = \frac{\left(\frac{n_2}{n_1}\right)^2 \cos\phi_i - \sqrt{\left(\frac{n_2}{n_1}\right)^2 - \sin^2\phi_i}}{\left(\frac{n_2}{n_1}\right)^2 \cos\phi_i + \sqrt{\left(\frac{n_2}{n_1}\right)^2 - \sin^2\phi_i}} \tag{3.1}$$

$$t_{||} = \frac{2\frac{n_2}{n_1}\cos\phi_i}{\left(\frac{n_2}{n_1}\right)^2 \cos\phi_i + \sqrt{\left(\frac{n_2}{n_1}\right)^2 - \sin^2\phi_i}} \tag{3.2}$$

In the case of polarisation perpendicular to the plane of incidence, $\mathbf{r}_\perp$ and $\mathbf{t}_\perp$ are given as:-

$$\mathbf{r}_\perp = \frac{\cos\phi_i - \sqrt{\left(\frac{n_2}{n_1}\right)^2 - \sin^2\phi_i}}{\cos\phi_i + \sqrt{\left(\frac{n_2}{n_1}\right)^2 - \sin^2\phi_i}} \tag{3.3}$$

$$\mathbf{t}_\perp = \frac{2\cos\phi_i}{\cos\phi_i + \sqrt{\left(\frac{n_2}{n_1}\right)^2 - \sin^2\phi_i}} \tag{3.4}$$

where $\phi_i$ is the angle of incidence of a wave at a boundary with refractive indices of $n_1$ and $n_2$. A coupled wave theory capable of modelling sequential multiple transmission and reflection gratings was used to fit experimental data enabling the parameters of each grating to be found. It solves the following set of differential equations:-

$$\sum_{l=1}^{L}\left\{\frac{dA_l}{dx} - \left(\frac{\alpha}{\cos\theta_l} + j\psi_l\right)A_l - j\frac{\kappa_l}{\cos\theta_l}R_o\right\} = 0$$

$$\sum_{i=-1,1}\sum_{n=1}^{N}\left\{\frac{dB_n^{(i)}}{dx} - \left(\frac{\alpha}{\cos\phi_n^{(i)}} + j\psi_n^{(i)}\right)B_n^{(i)} - j\frac{\kappa_n}{\cos\phi_n^{(i)}}R_o\right\} = 0$$

$$\cos\theta_o\frac{dR_o}{dx} - \alpha R_o - j\sum_{l=1}^{L}\kappa_l A_l - j\sum_{i=-1,1}\sum_{n=1}^{N}\kappa_n B_n^{(i)} = 0 \tag{3.5}$$

where
$$\kappa_m = \frac{\varepsilon_m\beta}{4\varepsilon_o} \qquad \cos\theta_o = \frac{\rho_{ox}}{\beta}$$

$$A_l = S_l e^{+j\psi_l.x} \qquad \cos\theta_l = \frac{\sigma_{lx}}{\beta}$$

$$B_n^{(i)} = Q_n^{(i)}e^{+j\psi_n.x} \qquad \cos\phi_n^{(i)} = \frac{\mu_{nx}^{(i)}}{\beta}$$

$R_o$ is the amplitude of the incident replay beam, $S_l$ and $Q_n{}^{(i)}$ are the amplitudes of the beams diffracted by the $l^{\text{th}}$ reflection and the $n^{\text{th}}$ transmission grating respectively. Also, $\bar{\rho}_o$, $\bar{\sigma}_l$ and $\bar{\mu}_n^{(i)}$ are the wave vectors of the replay beam, of the beams diffracted by the $l^{\text{th}}$ reflection, and of those diffracted by the $n^{\text{th}}$ transmission grating respectively.

This provides the solution to the diffraction problem for N superimposed uniform phase gratings which may be any combination of transmission and reflection gratings and allows a direct comparison between experimental and theoretical diffraction, taking account of all recording and replay conditions. This is discussed in more detail in Appendix I.

## 3.2 Experiments

In order to illustrate the effect of non matching boundary conditions upon the recording of a hologram the following experiments were performed. Single, planar transmission gratings were formed both (i) inside an index matching tank and (ii) in air. All recordings were carried out using nominally 22 μm thick dichromated gelatin plates on a 3 mm float glass substrate. Each was sensitised with 6% ammonium dichromate since this had previously been found to help minimise optical path changes in the emulsion and hence allow optimum replay around the recording wavelength (514.5 nm). The total exposure energy used was 210 mJ / $cm^2$ and the measured beam power ratios were kept constant at 1:1. The plates were processed using the procedure outlined in Chapter 2. The characteristics of the recorded gratings were determined by measuring the transmitted beam intensity; a technique also discussed in Chapter 2. These transmission measurements were normalised to readings taken at the respective wavelengths after the plate had been removed from the system.

### 3.2.1 *Transmission gratings recorded in an index matching tank*

Transmission gratings were formed within an index matching tank to reduce any boundary mismatch and therefore attenuate any reflected wave. The recording geometry is shown in Figure 3.2. Here we can see two collimated beams representing plane waves incident on the DCG surface at recording angles of +30° and -16° (+50° and -25° in air) respectively in transmission geometry. The angles +50° and -25° were chosen to give the grating sufficient slant so as to separate the gratings recorded by boundary interference. Since 50° is close to the Brewster angle [Bor80] for an air / glass boundary, a polarisation horizontal to the plane of incidence was chosen in an attempt to reduce any power loss at the tank or hologram / air surface. The Index matching liquid used was Di-n-butylephalate with a refractive index of 1.497.

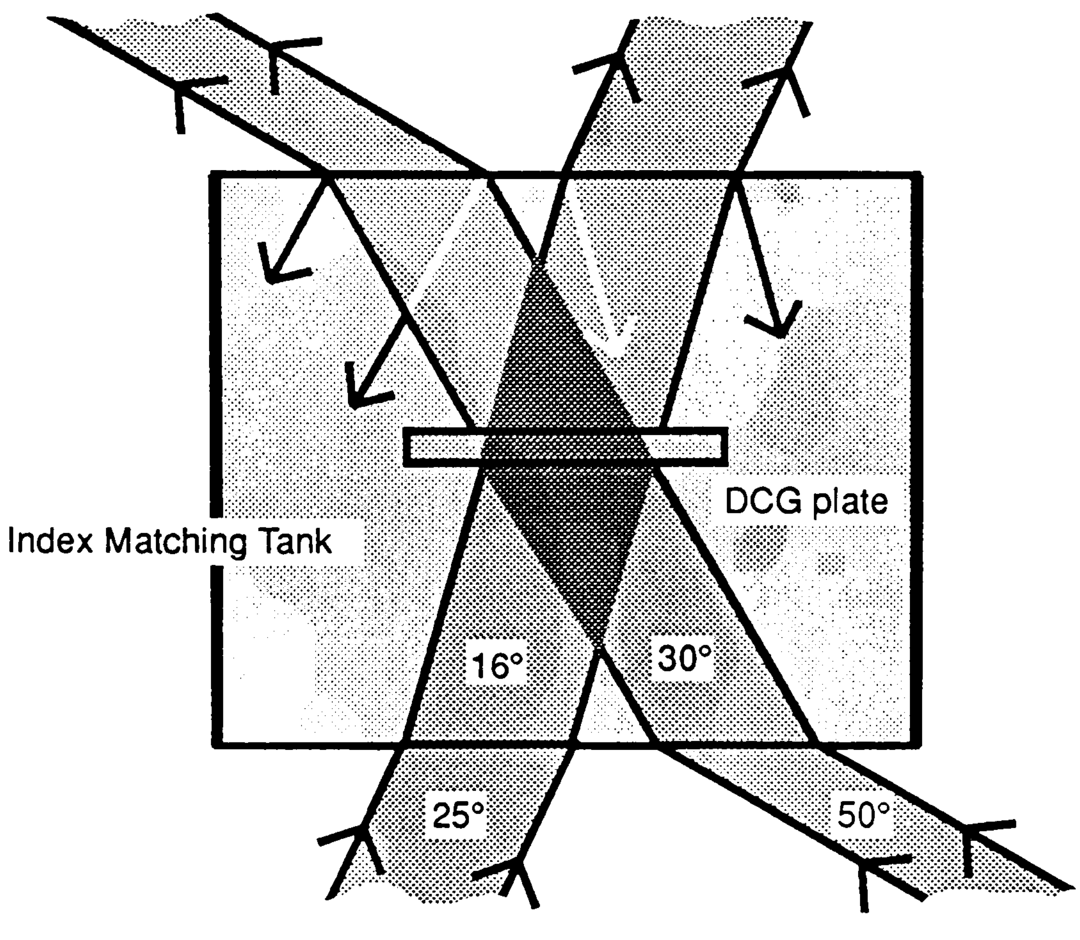


Figure 3.2 Recording geometry for single grating experiments.

Figure 3.3 (a) and (b) show angular transmittance scans of a plate replayed in an index matching tank (a) at the recording wavelength and (b) at 460 nm. In each plot we can see only two dips in transmission corresponding to the replay Bragg angles of the single recorded transmission grating. However, no spurious diffraction is observed illustrating that recording within the index matching tank has succeeded in reducing boundary effects to the point where reflected intensities may be assumed negligible. The solid line in each figure is a theoretical fit of the transmission characteristic using the coupled wave model mentioned earlier. With a modulation ($n_1$) of 0.0073, the hologram was found to have swollen from a recording thickness of 22.1 μm to 23.3 μm, the average refractive index changed from 1.57 at recording to 1.505 and absorption ($\alpha$) was considered by assuming a constant attenuation factor of 3800 m$^{-1}$.

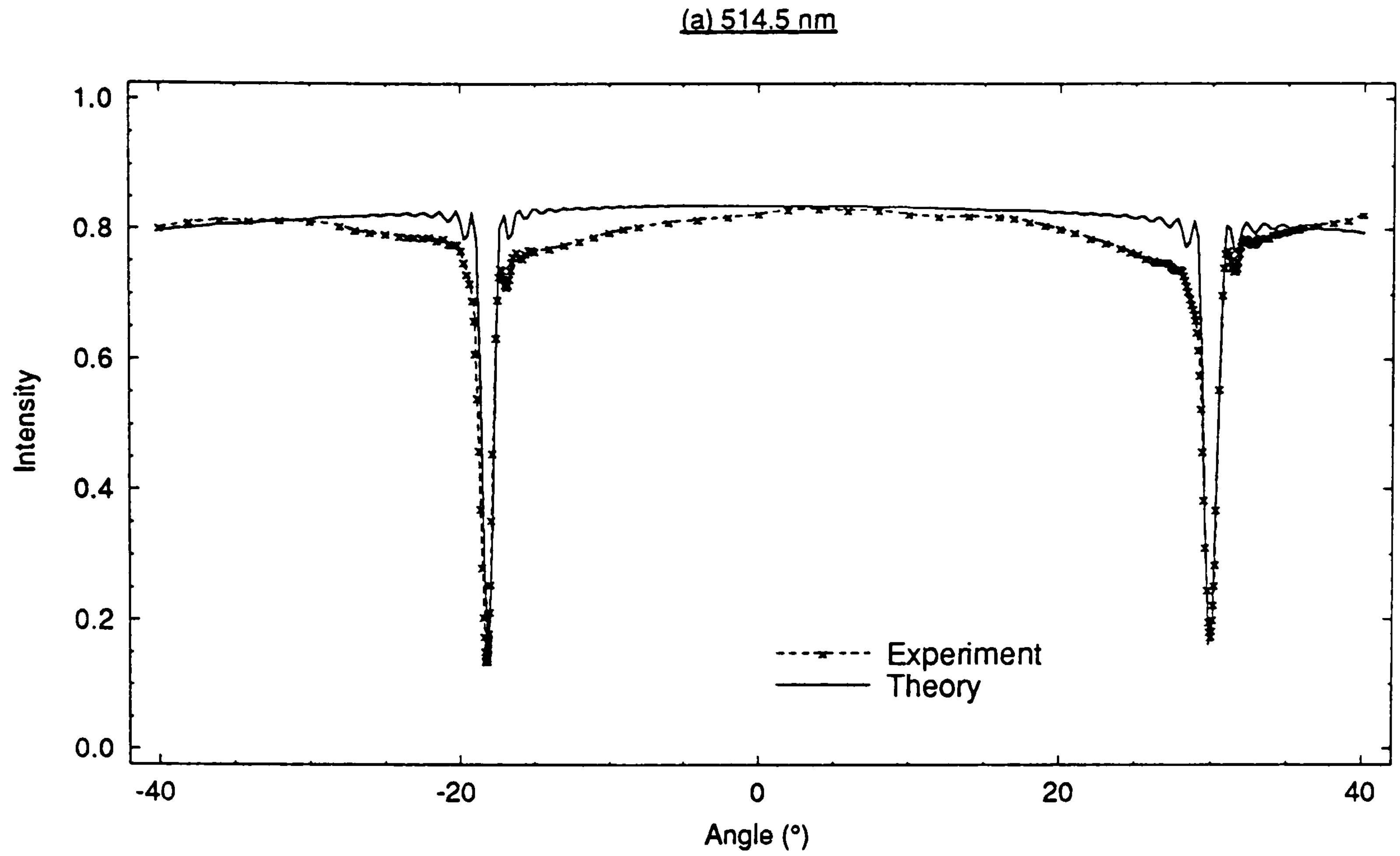


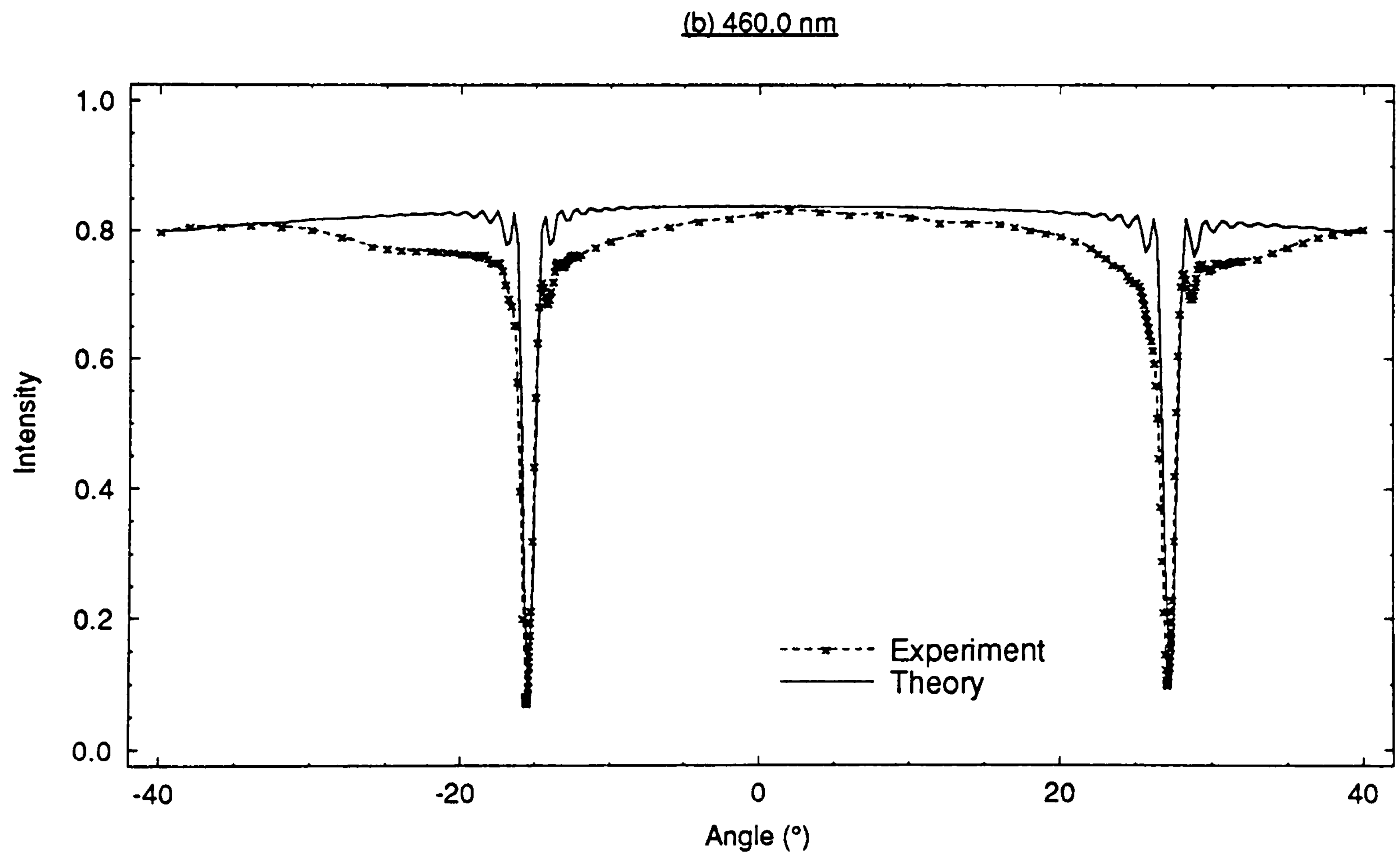


Figure 3.3 Plot of transmittance versus replay angle for a single transmission grating replayed at (a) 514.5 nm and (b) 460.0 nm.

There are some discrepancies between the theoretical and experimental plots. This is due to the fact that the theory used here is for a uniform grating and does not take account of chirp [Au87] [New89]. To model this is a complex problem which is outwith the scope of this study.

### 3.2.2 *Transmission gratings recorded in air*

In this case single transmission gratings were recorded using the recording geometry shown in Figure 3.4. This shows the construction of a planar single transmission grating in air, at a wavelength of 514.5 nm and recording angles of +50° and -25° (+30° and -16° in the gelatin) representing the reference and object beams R and S respectively. Recordings were made for both the cases with (i) polarisation parallel to the plane of incidence and (ii) polarisation perpendicular to the plane of incidence.

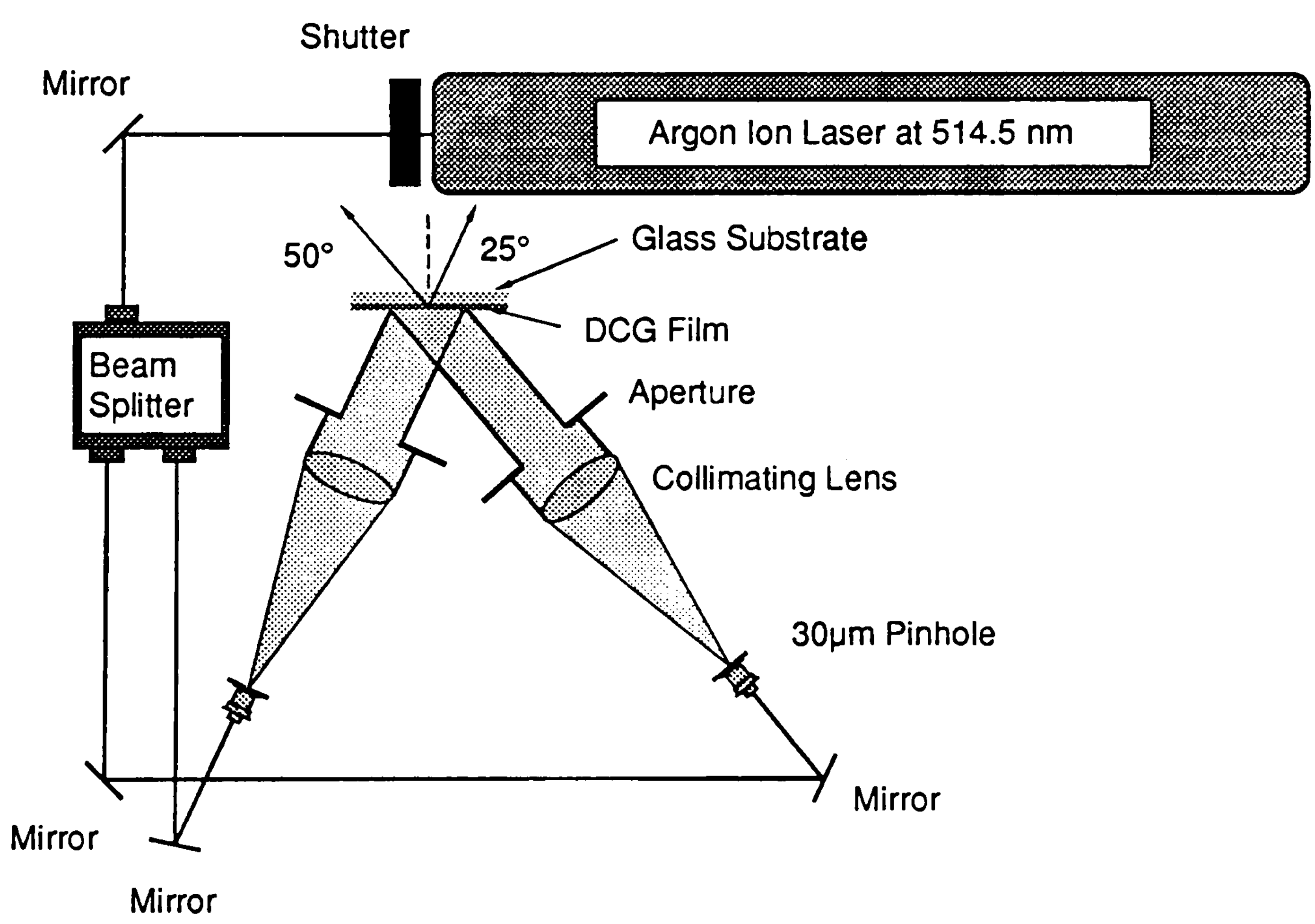


Figure 3.4 Recording geometry for transmission gratings in air.

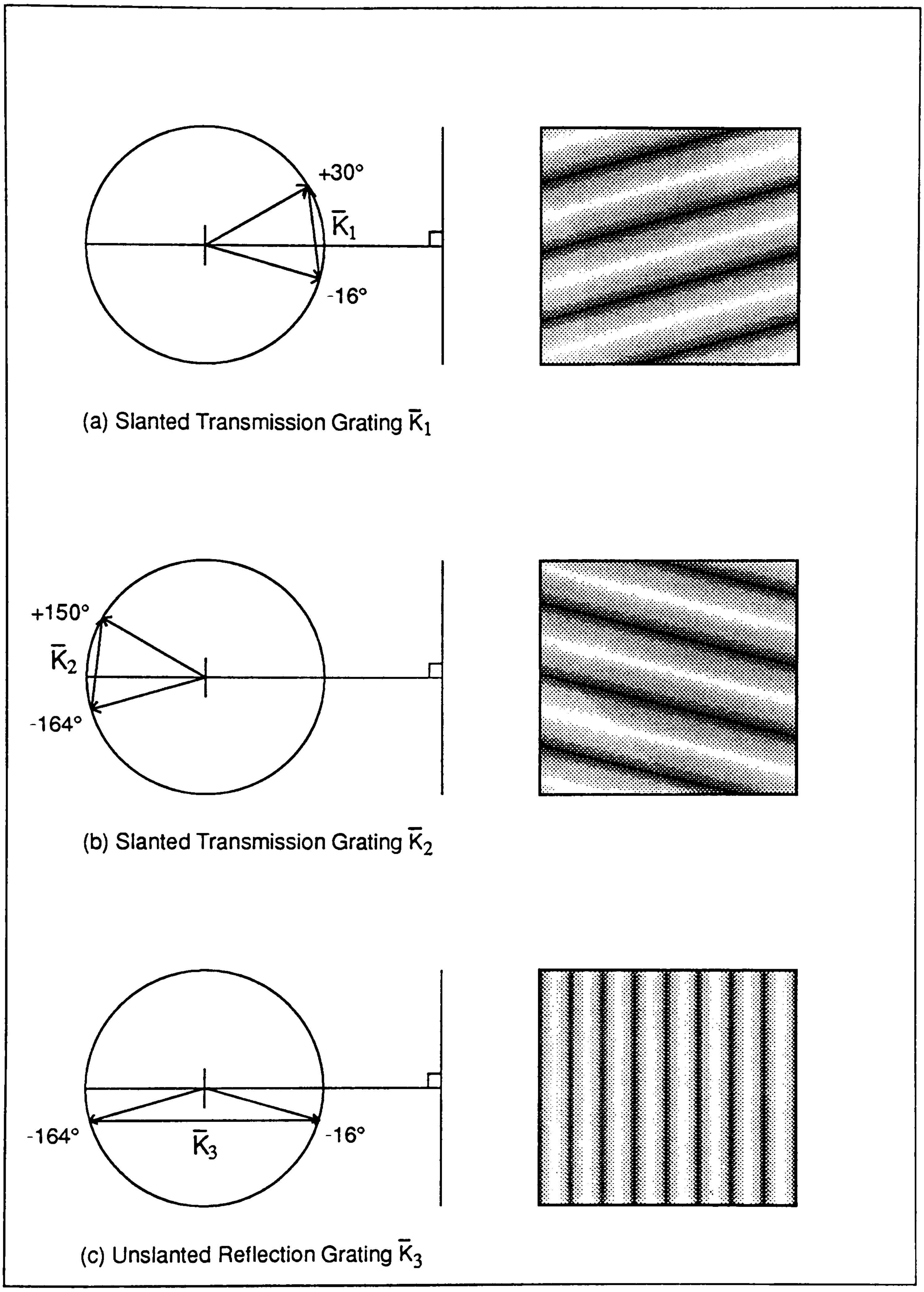


Figure 3.5 Recorded gratings due to boundary reflections.

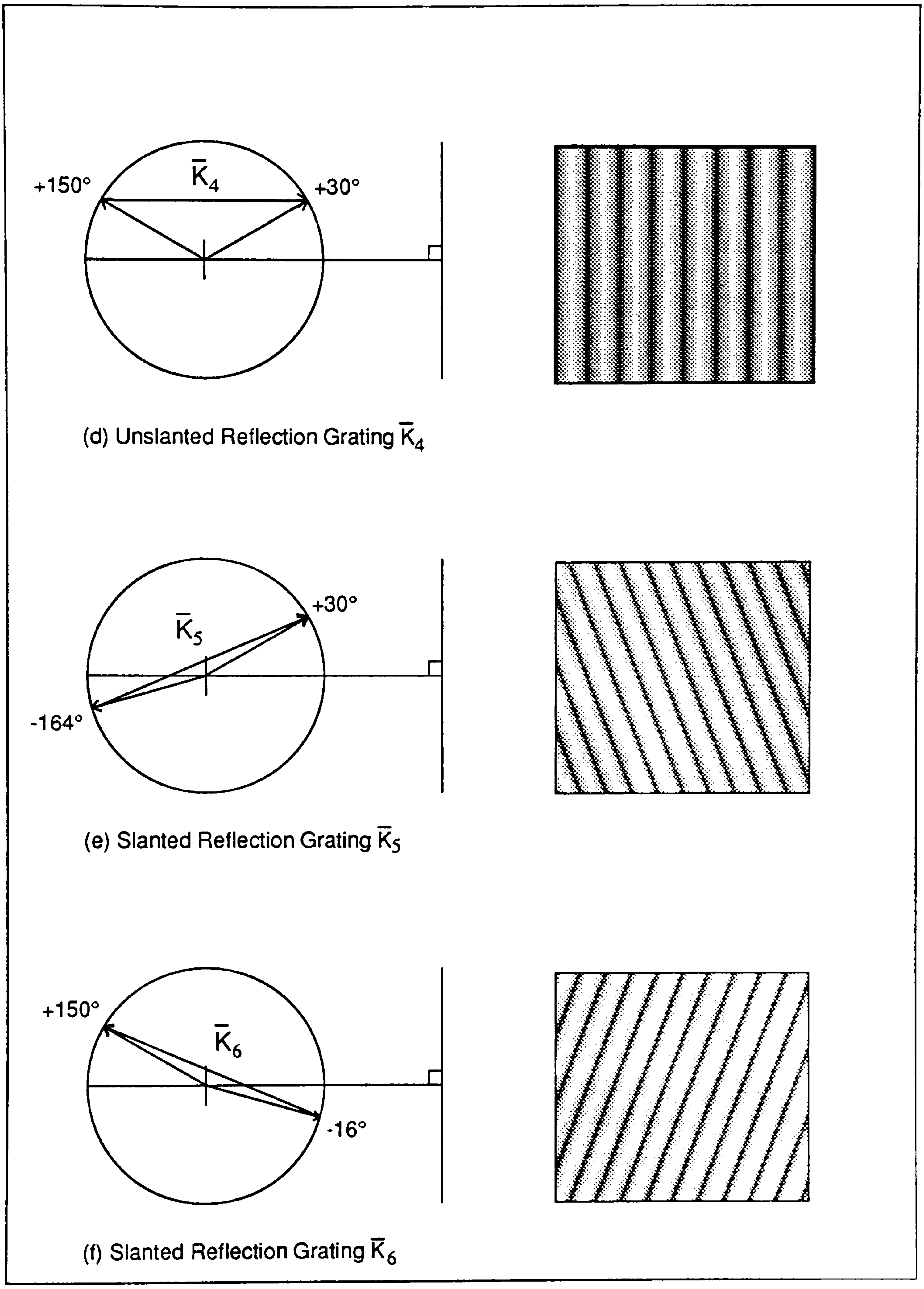


Figure 3.5 (continued).

Due to the characteristically low absorption of dichromated gelatin, it was expected that unwanted gratings may be formed in the emulsion by specular reflections of the main recording beams from the rear substrate / air interface. This, in effect, produces four recording beams. Figure 3.5 shows the Ewald circle representations of the six possible grating vectors expected to be formed inside the emulsion

Ideally, assuming no change in wavelength, thickness or average refractive index, the expected Ewald circle at replay (illustrated in Figure 3.6) shows that each Bragg dip represents the diffracted waves from three gratings at any one time.

i.e. $\overline{K}_1$ causes Bragg dips at -16° and +30°

$\overline{K}_2$ " " " " -30° and +16°

$\overline{K}_3$ " " " " -16° and +16°

$\overline{K}_4$ " " " " -30° and +30°

$\overline{K}_5$ " " " " -30° and +16°

$\overline{K}_6$ " " " " +30° and -16°

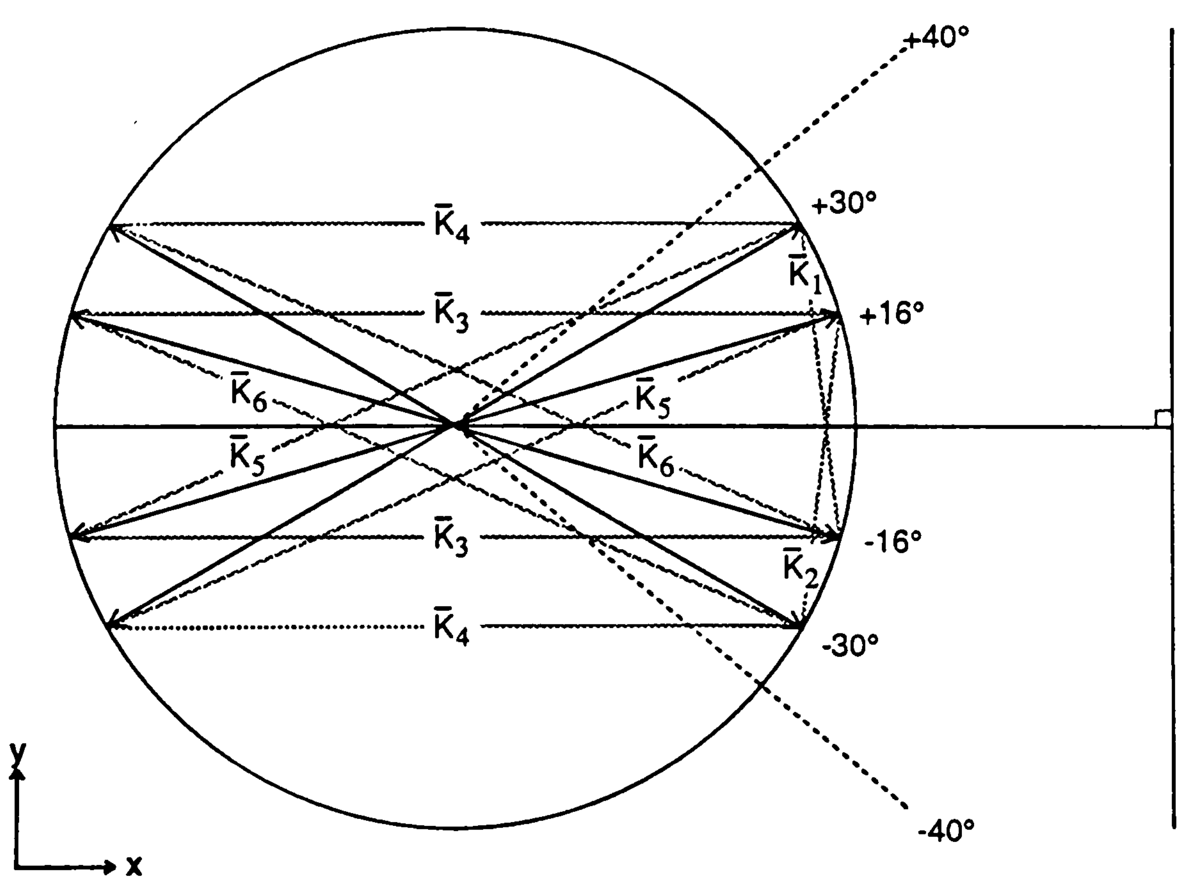


Figure 3.6 Ewald circle showing replay Bragg angles under ideal replay conditions at a wavelength of 514.5 nm.

This does not allow direct efficiency measurement of each individual grating due to the fact that the total modulation at any given angle is not linearly proportional to the sum of the individual modulations replayed at that angle [Sol81]. Admittedly Figure 3.6 is complex and difficult to comprehend, however this is necessary to illustrate fully the complicated replay conditions.

3.2.2.1 *Parallel Polarisation*

The hologram was initially scanned at the recording wavelength of 514.5 nm through the angles -40° to +40° whereupon five Bragg dips were found (see Figure 3.7).

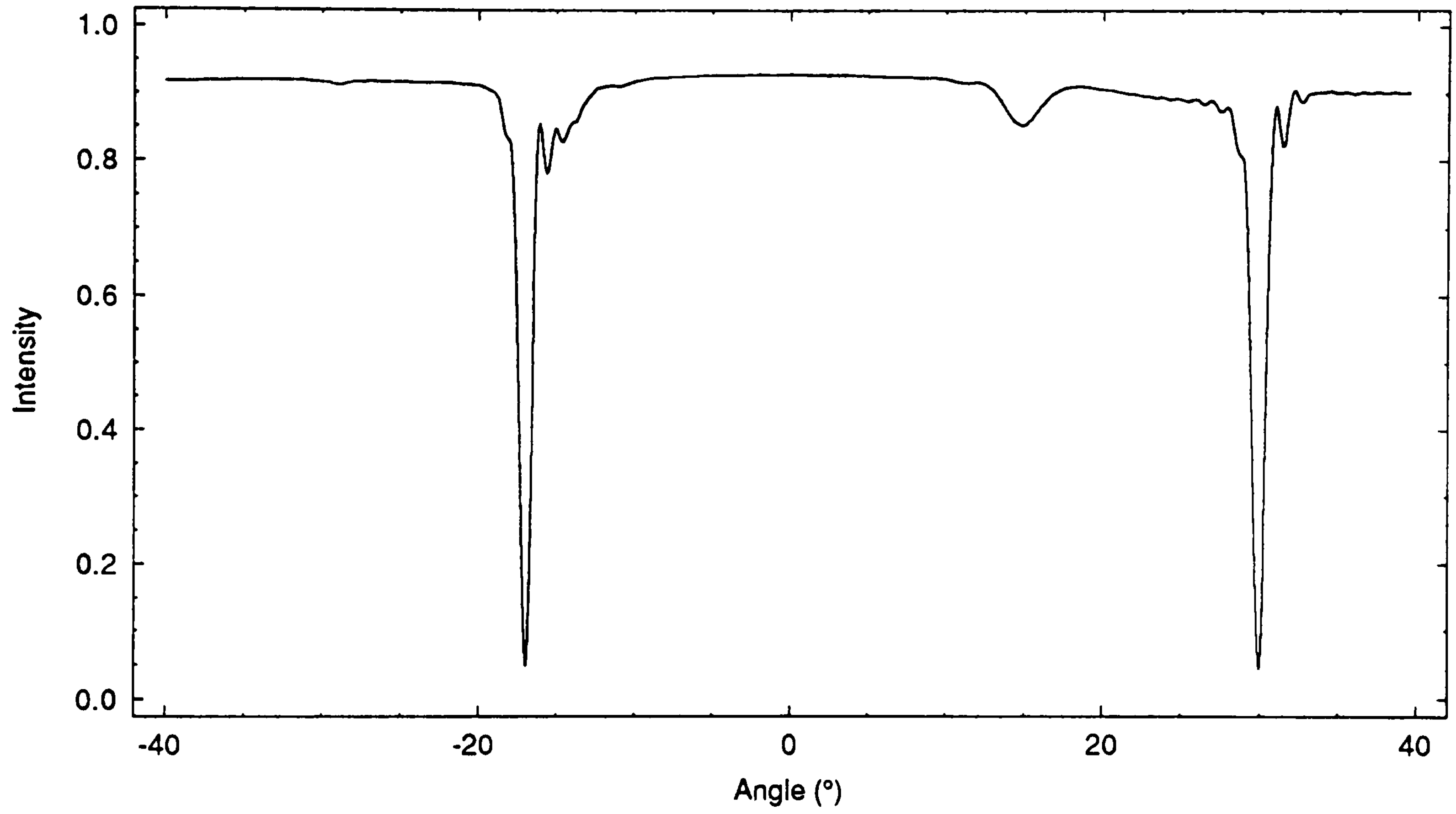


Figure 3.7 Experimental angular transmittance scan for a single transmission grating recorded in air with parallel polarisation (at 514.5 nm).

In comparison to Figure 3.3, this showed not only two highly efficient dips at -17° and +30° corresponding to the recording angles of the main grating ($G_1$), but also smaller dips at 15° and -15° (the latter one is not clearly resolved because of the sidelobes of $G_1$) and a hardly noticeable dip at -30°. These small deviations from the expected angles can be explained by the fact that both the thickness and the refractive index change relative to the recording conditions. The thickness at replay we measured to be 4% larger whereas the change in the average refractive index (from 1.57 to 1.505) was deduced from the measurement of the Bragg angle of one of the reflection gratings.

It is clear that in spite of the changes in material parameters the individual gratings are not resolved at this wavelength. We can, however, achieve the separation of the gratings by having a bigger Ewald sphere, i.e. by replaying at a shorter wavelength which we chose to be 460 nm. The resulting transmission versus angle curve is shown in Figure 3.8 for the range -60° to 60°.

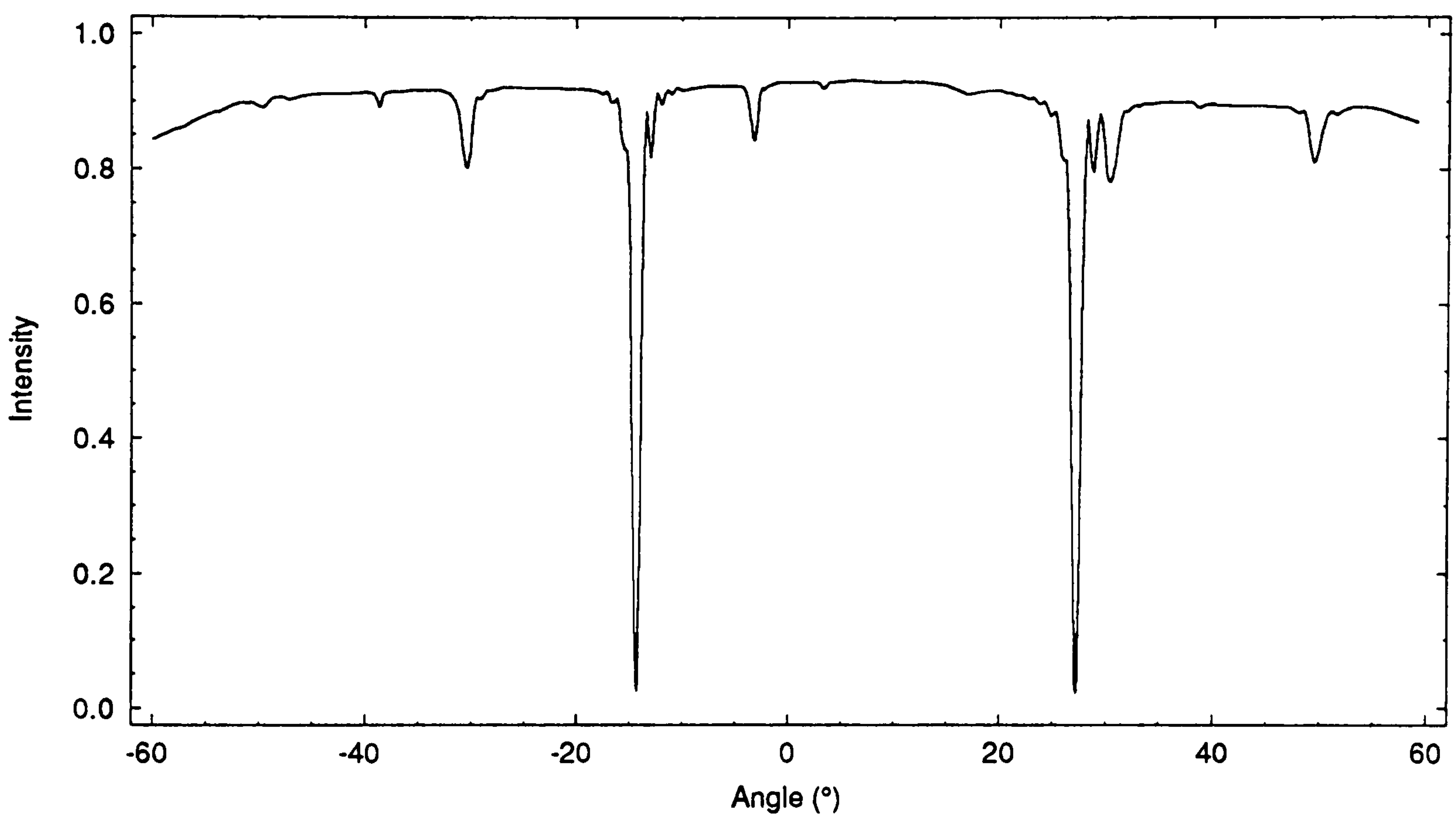


Figure 3.8 Experimental angular transmittance scan for a single transmission grating recorded in air with parallel polarisation (at 460.0 nm).

We may now distinguish as many as 12 dips. The expected positions of the dips, taking into account the changes in thickness (and the corresponding changes in the grating vectors) and in average refractive index may be deduced from the Ewald sphere construction shown in Figure 3.9.

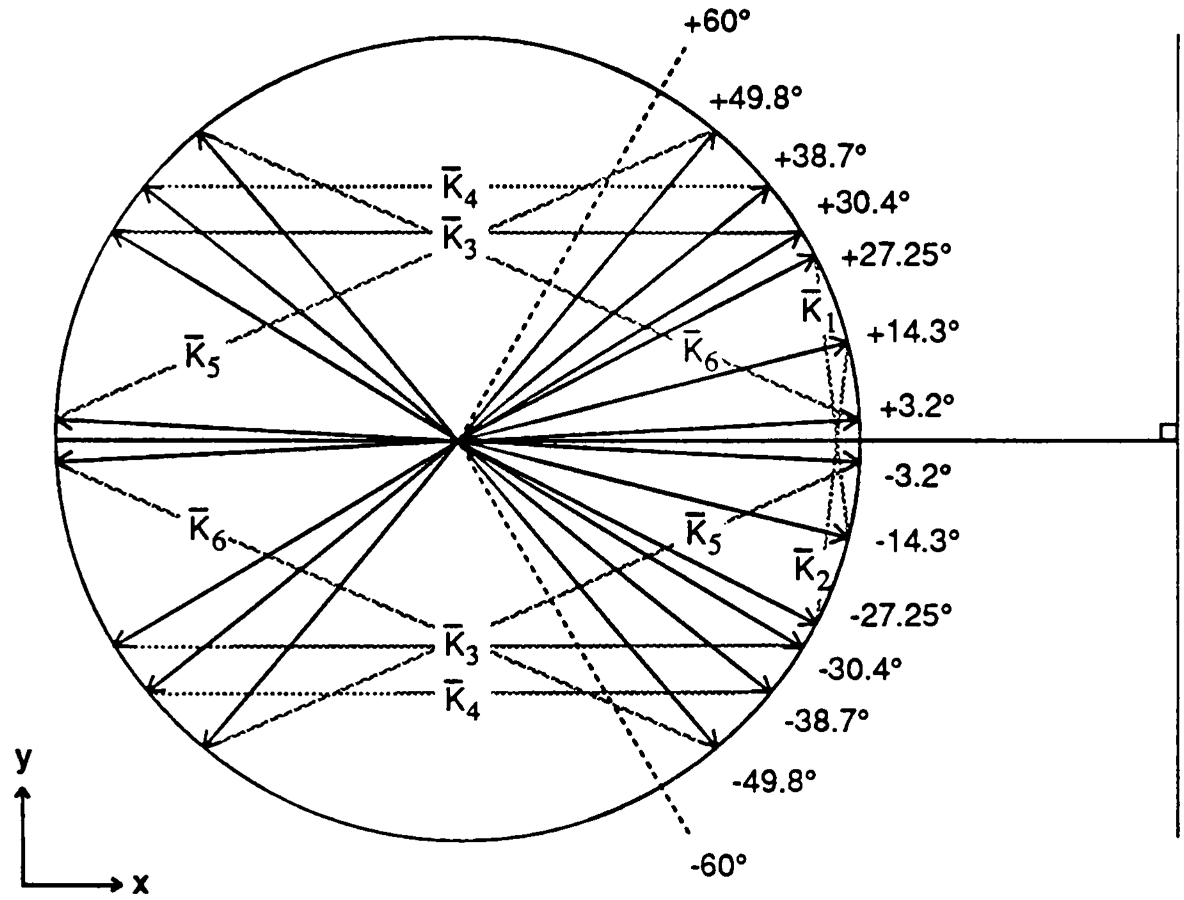


Figure 3.9 Ewald circle showing replay Bragg angles under actual replay conditions at a wavelength of 460.0 nm.

It may be seen that :-

| | | | | | | |
|---|---|---|---|---|---|---|
| $\overline{K}_1$ | causes | Bragg | dips | at | -14.3° and +27.3° |
| $\overline{K}_2$ | " | " | " | " | -27.3° and +14.3° |
| $\overline{K}_3$ | " | " | " | " | -30.3° and +30.3° |
| $\overline{K}_4$ | " | " | " | " | -38.5° and +38.5° |
| $\overline{K}_5$ | " | " | " | " | -49.6° and +3.2° |
| $\overline{K}_6$ | " | " | " | " | -3.2° and +49.6° |

These angles agree closely with the experimental dips found in Figure 3.8 at ±49.8°, ±38.7°, ±30.4°, ±27.3°, ±14.3° and ±3.2°.

3.2.2.2 *Perpendicular Polarisation*

Figures 3.10 and 3.11 again show angular transmittance scans of a hologram replayed at 514.5 nm and 460 nm respectively.

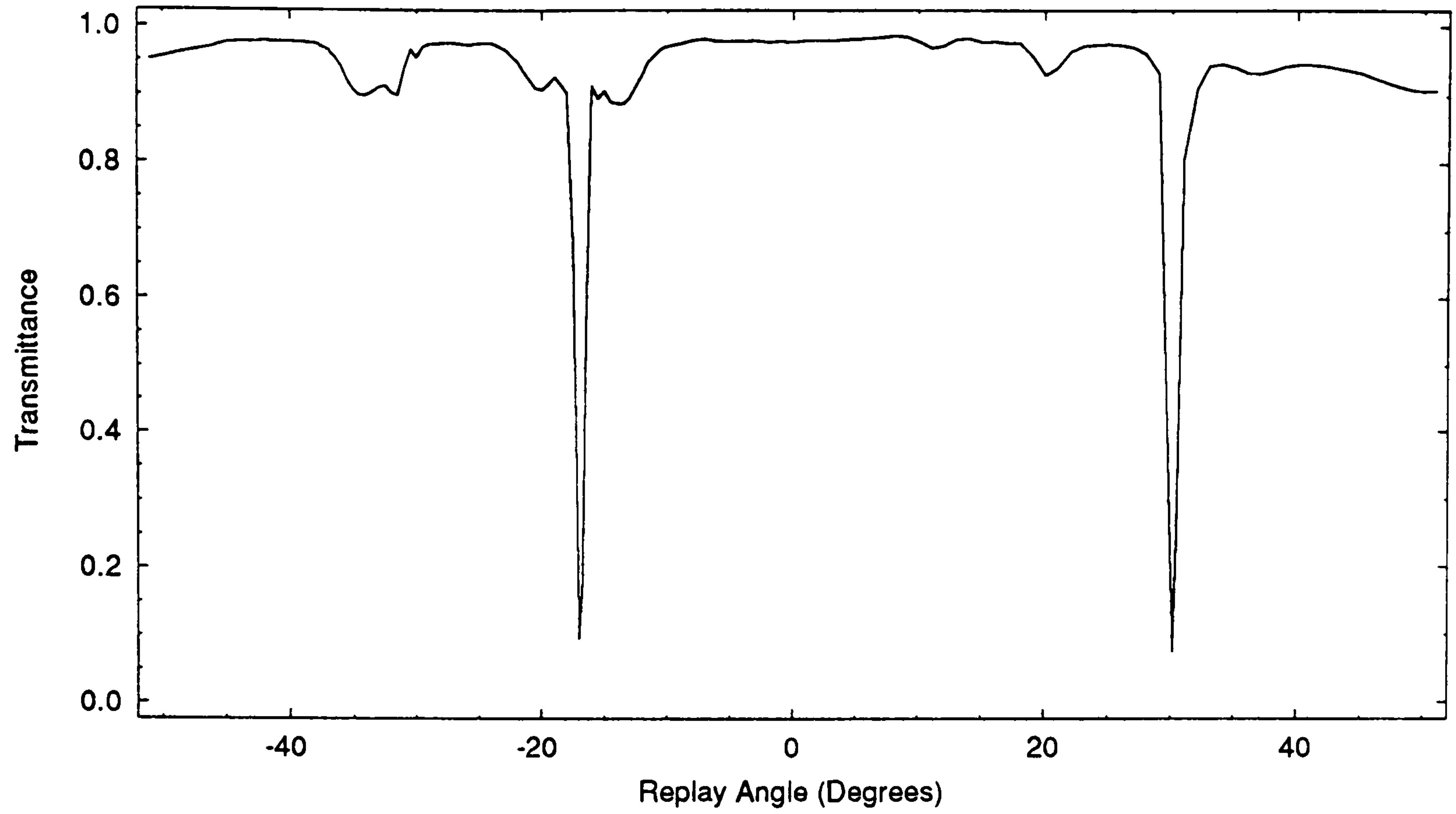


Figure 3.10 Experimental angular transmission scan for a single transmission grating recorded in air with perpendicular polarisation (at 514.5 nm).

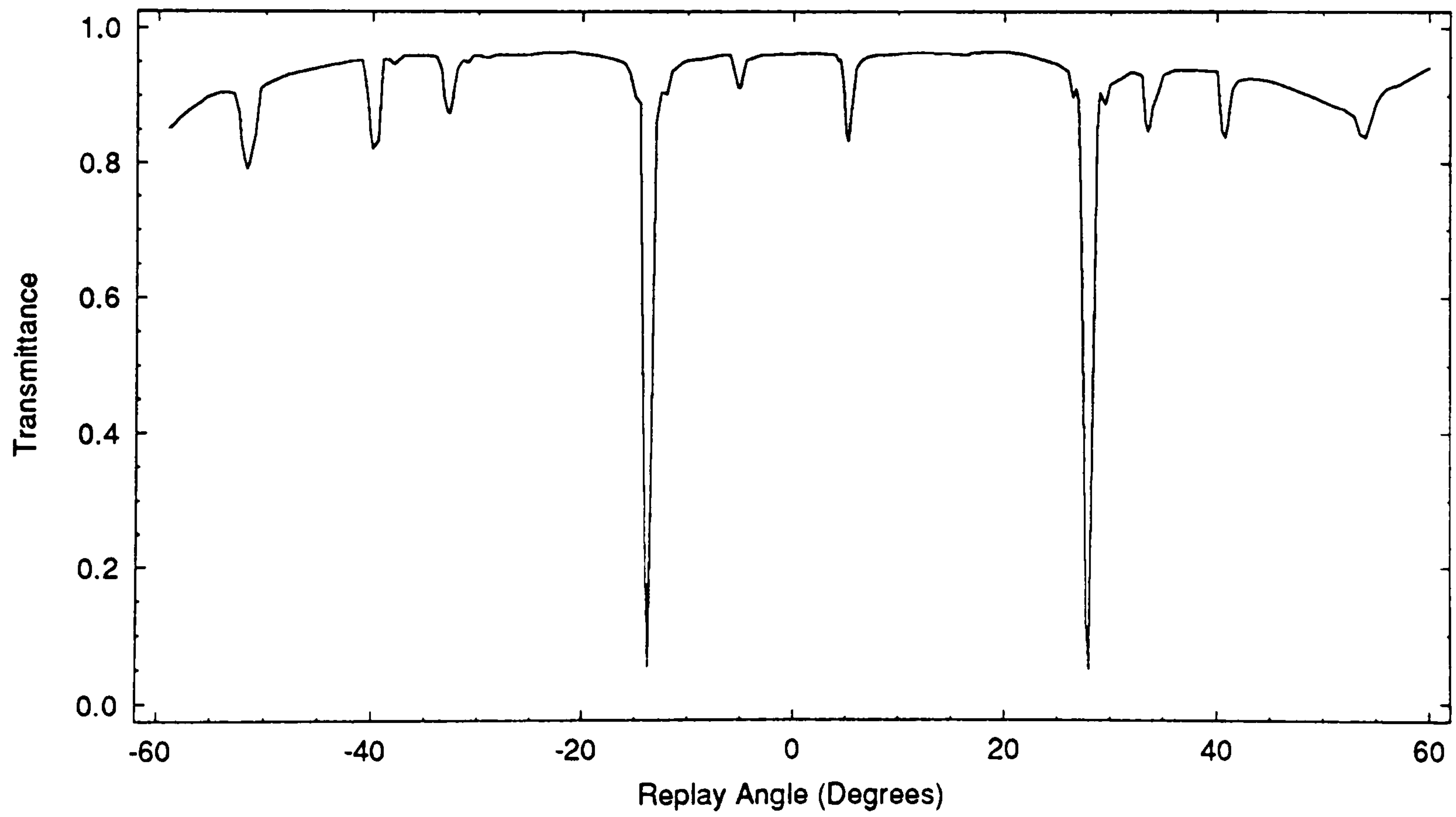


Figure 3.11 Experimental angular transmittance scan for a single transmission grating recorded in air with perpendicular polarisation (at 460.0 nm).

In this case the hologram was recorded with perpendicular polarisation. This time in Figure 3.10 we can see at least seven clear dips as opposed to five dips in the previous case. As before we observe two highly efficient Bragg dips at +30° and -17° corresponding to the recording angles of the main grating $G_1$, but we can also see dips appearing at -37°, -30°, -11°, +14° and+20°. To analyse these we need to look at Figure 3.11 for the scan at 460 nm. Now we can see as many as twelve Bragg dips. By visually comparing Figures 3.8 and 3.11 it is interesting to see that the change in polarisation has affected the strengths of the recorded gratings. For example, we can immediately spot that, for the case with perpendicular polarisation at recording, the dips are much larger at -50°, +4° and ±40°. This is due to the fact that one of the beams which contributes to the formation of these gratings ($G_6$ and $G_4$ respectively) is close to the Brewster angle. We would therefore expect little reflection from the boundary at this angle when recording with parallel polarisation.

## 3.3 Comparison between theory and experiments

### 3.3.1 *Parallel Polarisation*

In Figure 3.8 the Bragg dips are sufficiently far away from each other so that we can determine the parameters of each individual grating from its angular characteristics. It is possible, of course, to apply a more sophisticated model (see e.g. Ref. [New89]) in which refractive index modulation is nonuniform and the fringes are bent. We do not, however, need such a model here because our aim is limited to finding out whether we have all the expected gratings present and whether their modulation is approximately equal to those expected from the boundary reflections.

It is clear that we have the right number of gratings and the expected grating vectors. What we need to do next is to determine $n_{1i}$ the modulation of the $i^{th}$ grating. They may be deduced from the dips of Figure 3.8 by using the results of a theory [Kog69] which assumes a pure phase grating of constant amplitude in the background of uniform (space independent) attenuation. The attenuation coefficient may be determined from the known thickness (24.7

μm) of the grating and from the measured transmission at angles when all the gratings are far away from the Bragg condition. We obtain an absorption value of $\alpha = 1510$ m$^{-1}$. The modulations $n_{1i}$ determined from the depth of each Bragg dip are given by column 3 of Table 3.1. In each row the upper figure is obtained from the dip at negative angles and the lower figure from the positive angle dips. The two should be very close to each other and indeed they are, except for grating 4 where we can offer no explanation for the large discrepancy.

| Grating | Bragg Angle (degrees) | Experimental modulation | Theoretical modulation |
|---|---|---|---|
| 1 | -14.3 | 0.0077 | 0.0078 |
| | +27.3 | 0.0078 | |
| 2 | -27.3 | Not measurable | 0.000 098 |
| | +14.3 | | |
| 3 | -30.4 | 0.0019 | 0.001 61 |
| | +30.4 | 0.0020 | |
| 4 | -38.7 | 0.000 74 | 0.000 474 |
| | +38.7 | 0.000 34 | |
| 5 | -3.2 | 0.0015 | 0.001 44 |
| | +49.8 | 0.0015 | |
| 6 | -49.8 | 0.000 52 | 0.000 527 |
| | +3.2 | 0.000 45 | |

Table 3.1 Experimental and theoretical modulation values for a hologram recorded with parallel polarisation.

Next we shall determine the modulation of the gratings relying on the calculated reflection coefficients. We shall start by assuming that we have the correct value of modulation for the main grating $G_1$ and that a linear model is applicable in which the modulation is proportional to exposure, i.e. to the products of the amplitudes of the two recording waves. Therefore the modulation of the spurious gratings is determined by the amount of reflection suffered by the incident waves at the boundaries. The size of these reflections are determined by the Fresnel coefficients given in Equations 3.1 and 3.2. Thus, for example, the modulation of $G_3$ is determined by the following considerations. It is recorded by the wave incident at -16° and by its own reflected wave propagating at 196°. The corresponding Fresnel coefficient (for polarization in the plane of the grating) is equal to -0.177 hence the modulation of $G_3$ is $n_{13}$ = 0.00161. The modulation for each grating worked out with the aid of this method (which we shall call the theoretical modulation) is given by column 4 of Table 3.1. The agreement with the experimentally derived values listed in column 3 is quite good.

Finally, we shall take the values of modulation from column 3 and substitute them, together with the value of $\alpha$ found earlier, into the theory outlined in Appendix I. The experimental and theoretical curves are compared in Figures 3.12 (a) and (b) for replay at 460.0 nm and Figures 3.13 (a) and (b) for replay at 514.5 nm. The agreement is as good as may be expected. The position and depth of each Bragg dip is given quite accurately but not, of course, the angular width of the dips. The experimentally found widths are invariably wider indicating that, in contrast to the theoretical assumptions, the gratings are nonuniform.

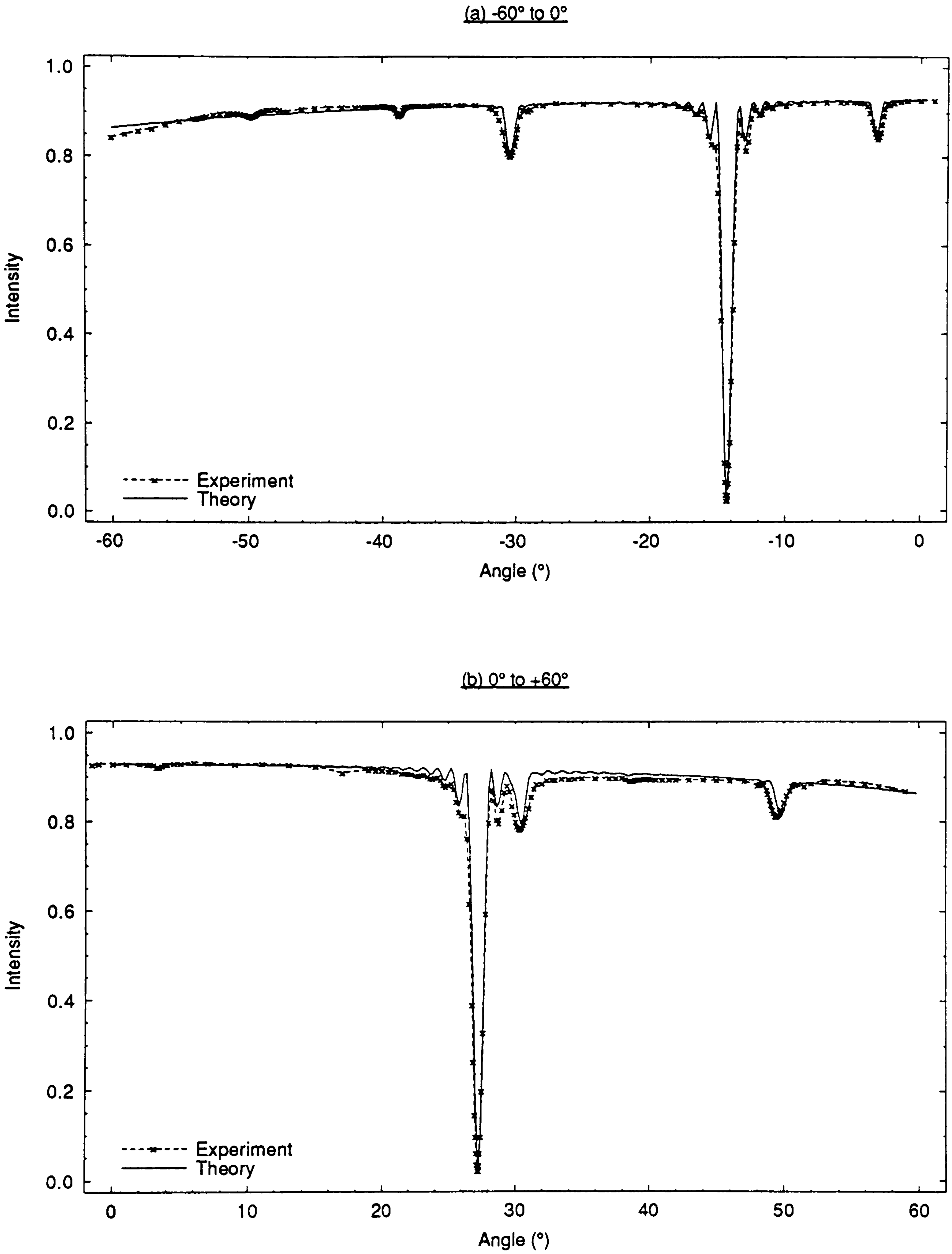


Figure 3.12 Parallel polarisation: Theoretical matching (solid line) of an experimental (dashed line) angular transmittance scan when replayed at 460.0 nm.
(a) -60° to 0° and (b) 0° to +60°.

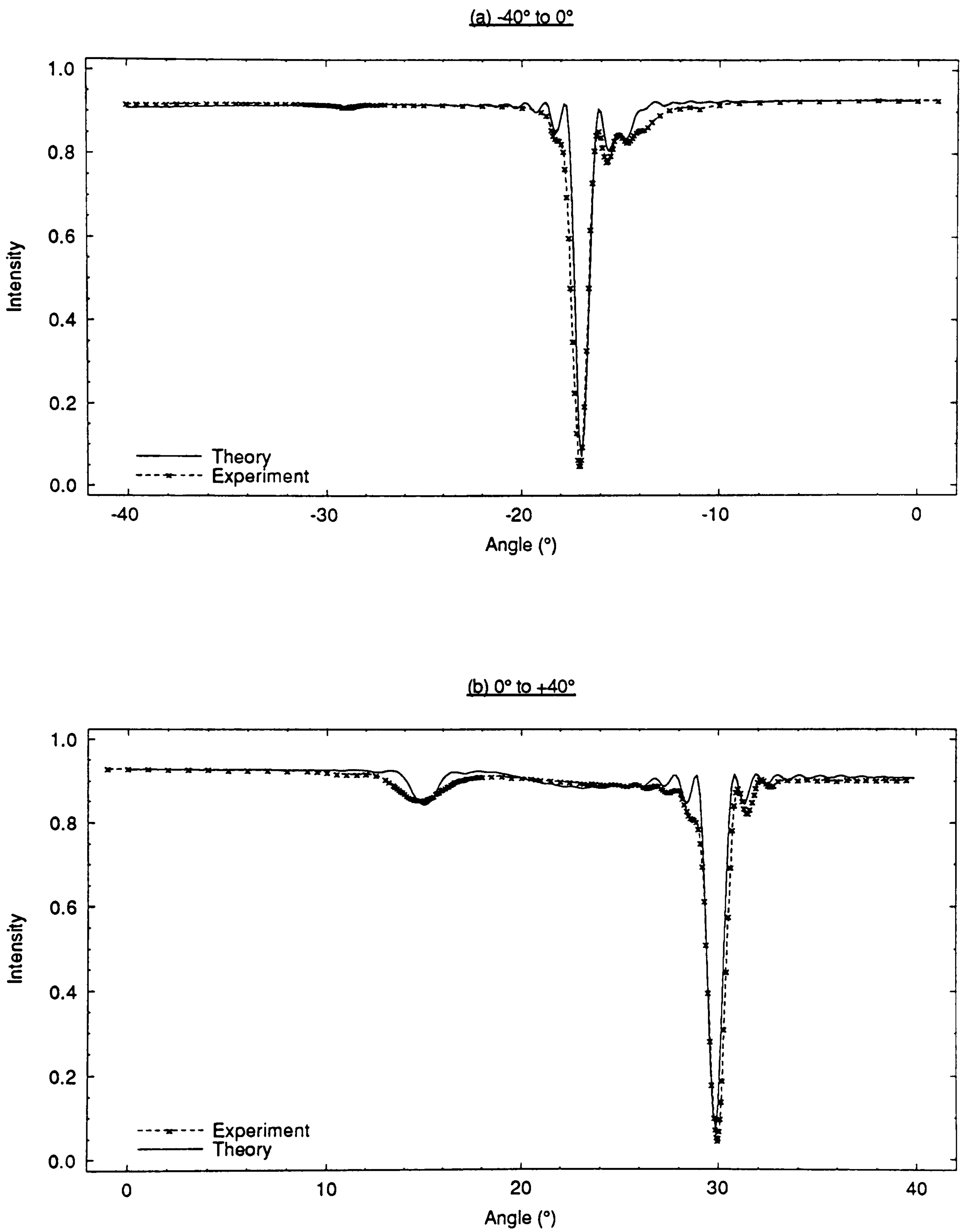


Figure 3.13 Parallel polarisation: Theoretical matching (solid line) of an experimental (dashed line) angular transmittance scan when replayed at 514.5 nm.
(a) -40° to 0° and (b) 0° to +40°.

### 3.3.2 *Perpendicular Polarisation*

Following the procedure outlined above we can model the case where polarisation is perpendicular to the plane of incidence. Table 3.2 shows a comparison between theoretically calculated modulations and values found by fitting experimental curves. Again, quite good agreement is found. Figures 3.14 and 3.15 show comparisons of experimental scans with theoretical models using the theoretically calculated modulations. In comparison to the parallel polarisation case we can see that higher modulations have been achieved by the spurious gratings due to higher reflection coefficients. It is noticeable, however, that all the theoretically calculated values are slightly larger than experimental ones. It is expected that this is due to absorption at exposure or material nonlinearities which are neglected in this simple theory.

| Grating | Bragg Angle (degrees) | Experimental modulation | Theoretical modulation |
|---|---|---|---|
| 1 | -14.3 | 0.0078 | 0.0078 |
| | +27.3 | 0.0078 | |
| 2 | -27.3 | Not measurable | 0.0006 |
| | +14.3 | | |
| 3 | -30.4 | 0.0018 | 0.00206 |
| | +30.4 | 0.0020 | |
| 4 | -38.7 | 0.0020 | 0.00225 |
| | +38.7 | 0.0019 | |
| 5 | -3.2 | 0.0013 | 0.00177 |
| | +49.8 | 0.0018 | |
| 6 | -49.8 | 0.0022 | 0.00261 |
| | +3.2 | 0.0021 | |

Table 3.2 Experimental and theoretical modulation values for a hologram recorded with perpendicular polarisation.

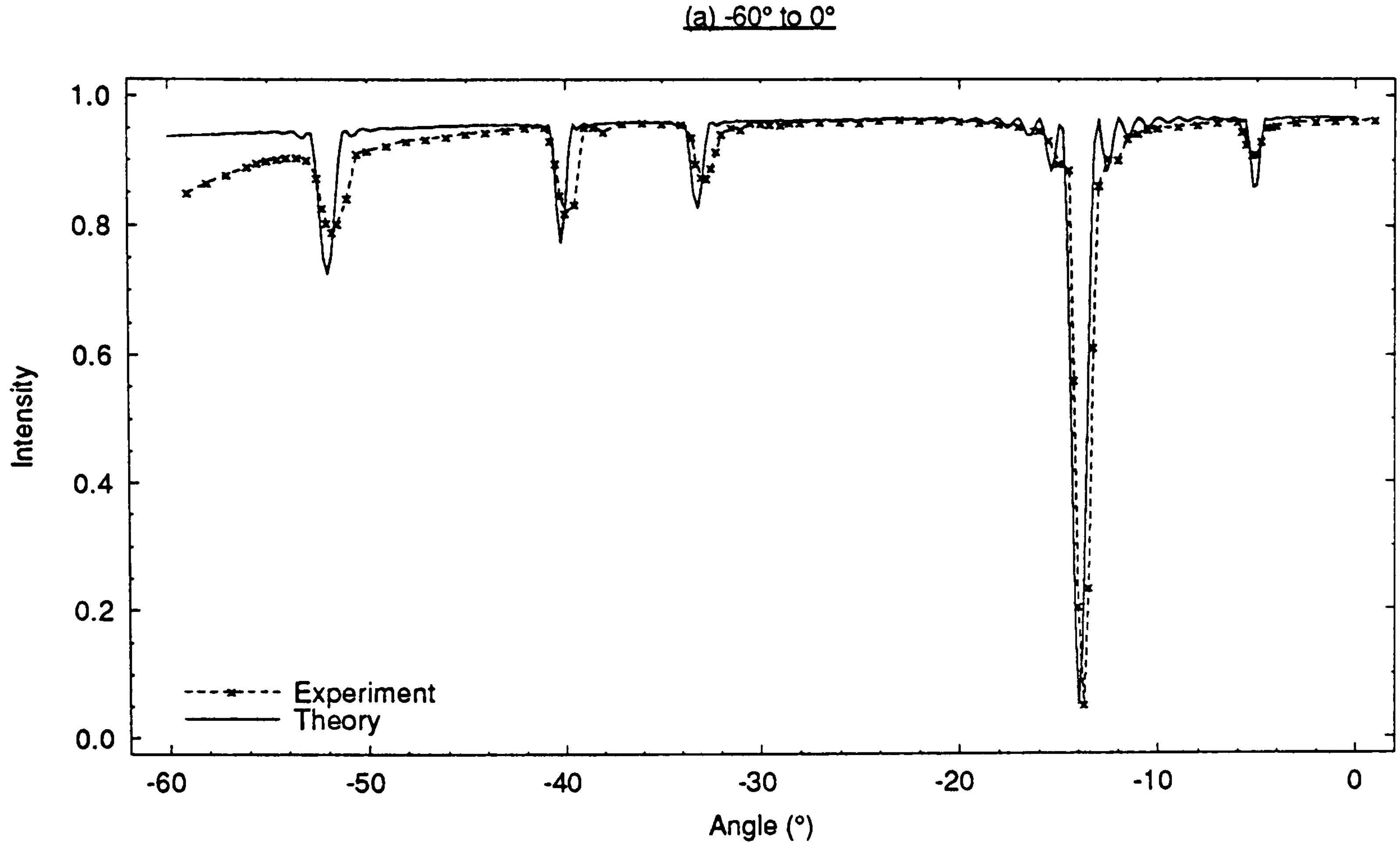


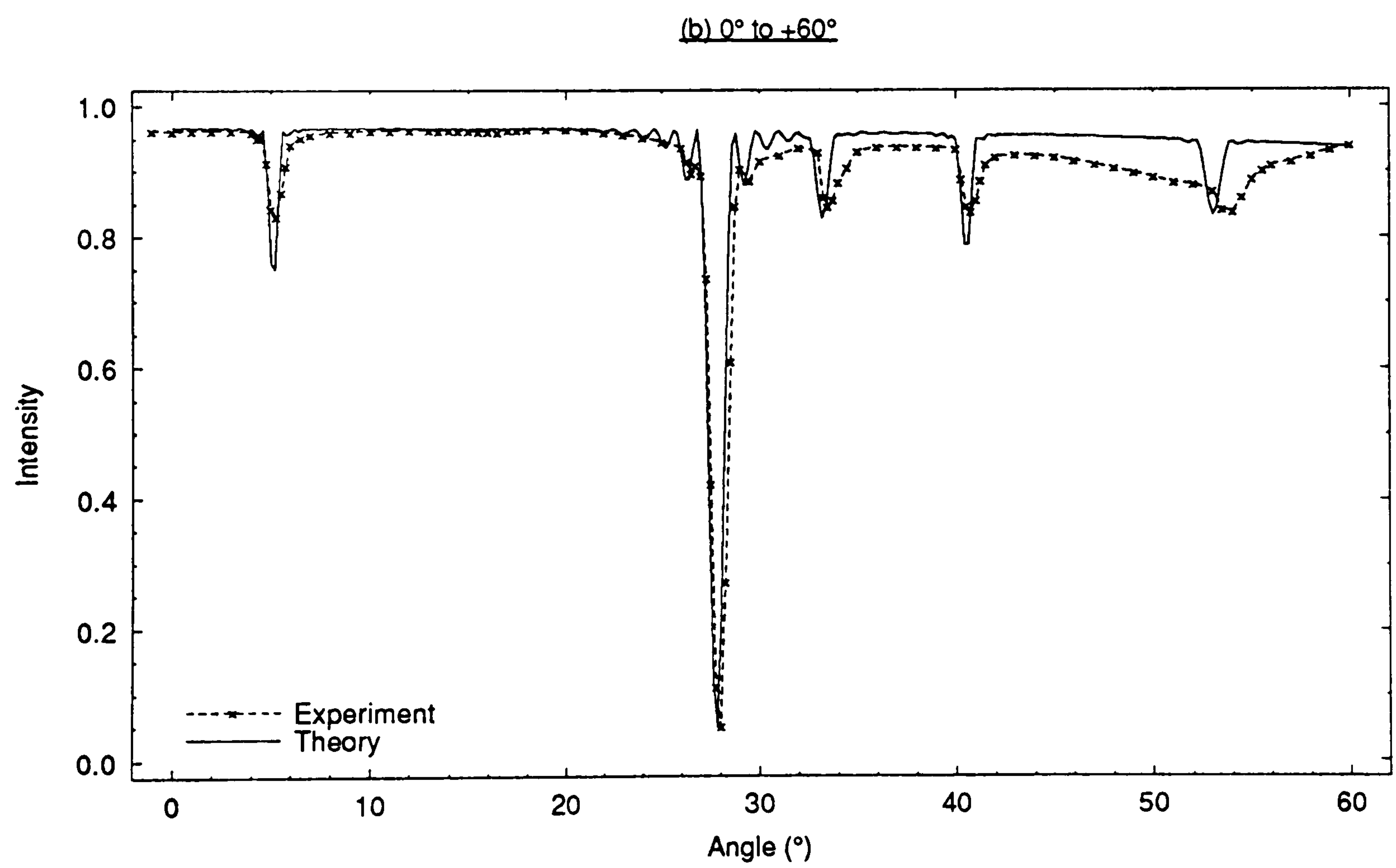


Figure 3.14 Perpendicular polarisation: Theoretical matching (solid line) of an experimental (dashed line) angular transmittance scan when replayed at 460.0 nm.
(a) -60° to 0° and (b) 0° to +60°.

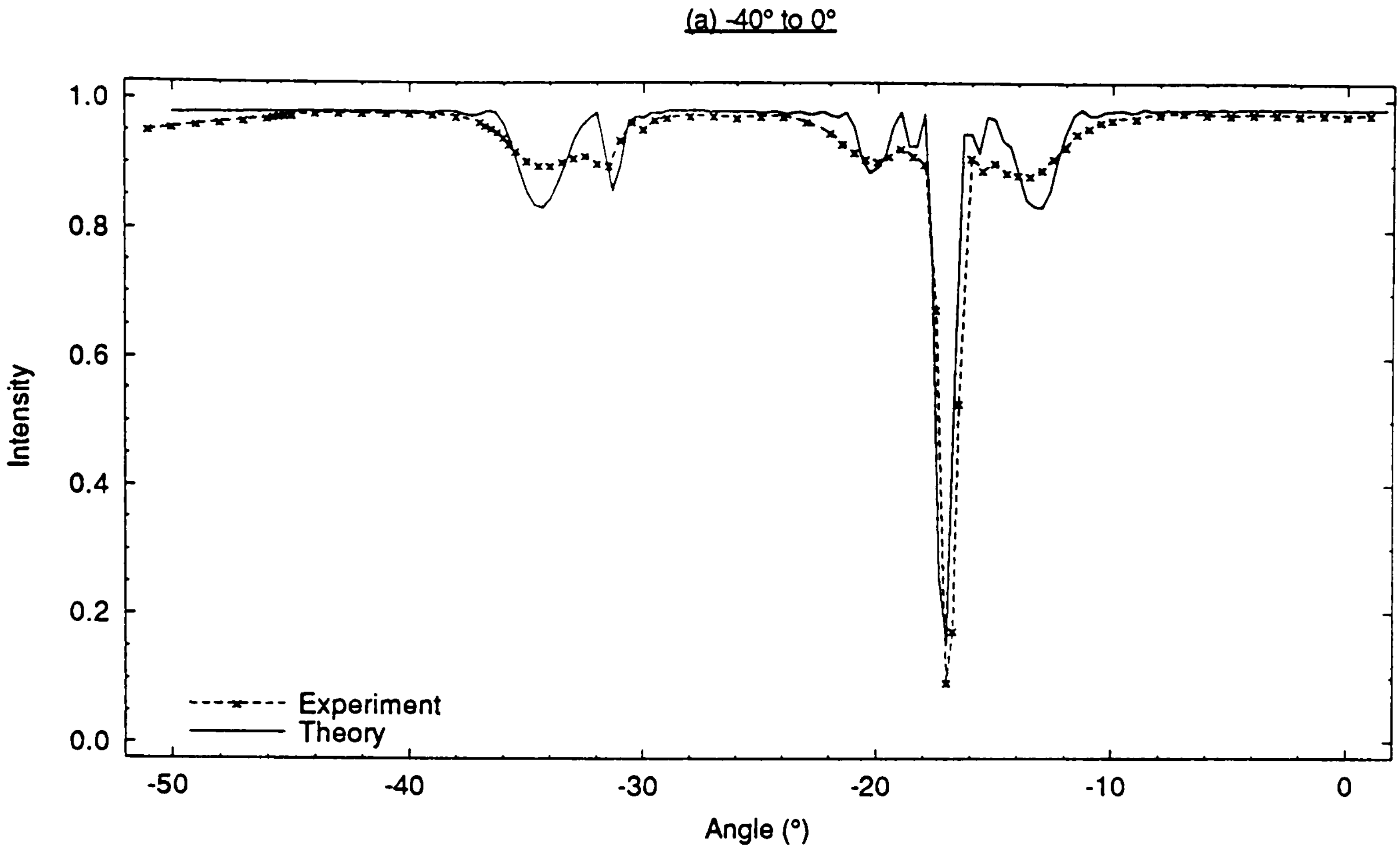


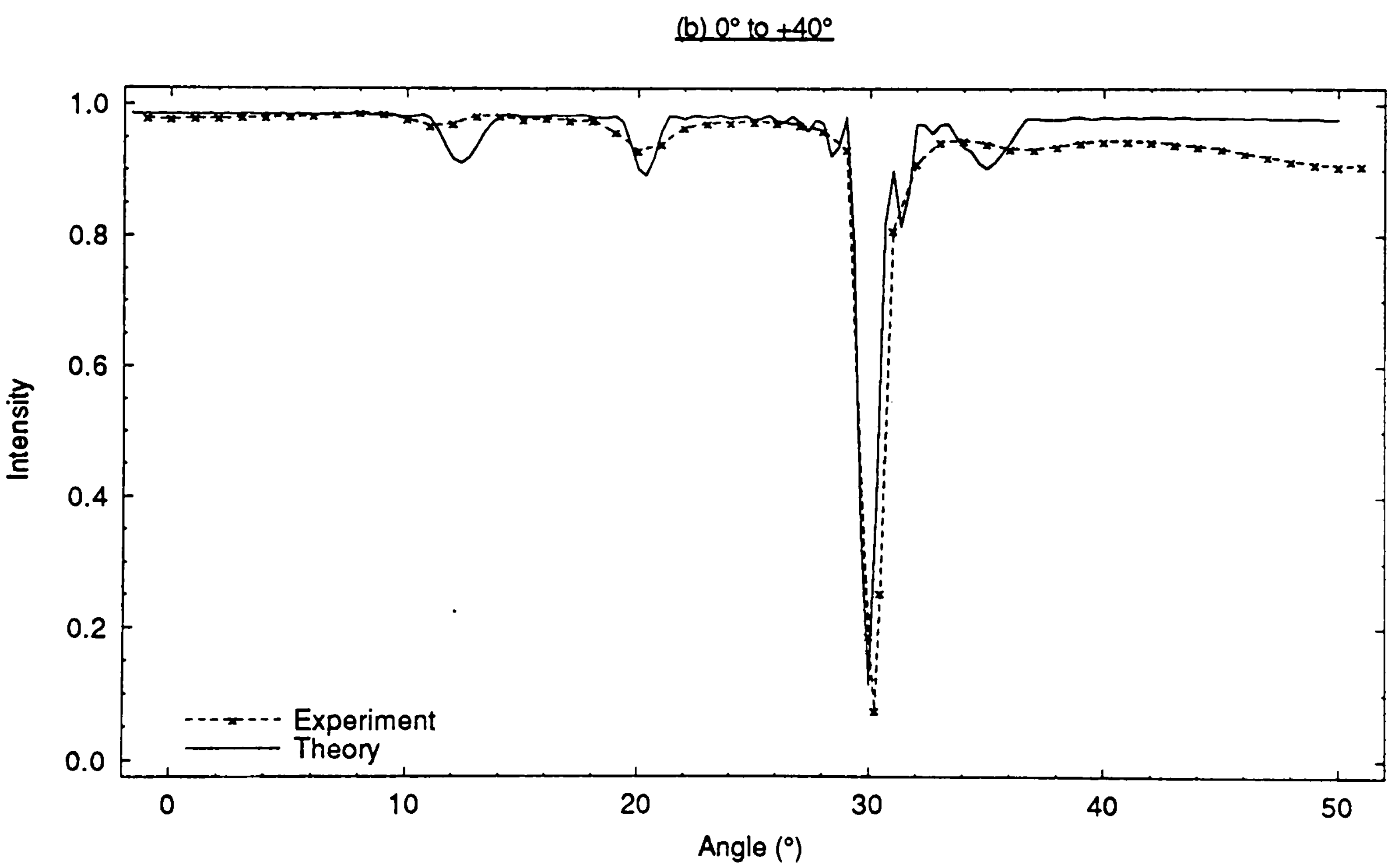


Figure 3.15 Perpendicular polarisation: Theoretical matching (solid line) of an experimental (dashed line) angular transmittance scan when replayed at 514.5 nm.
(a) -40° to 0° and (b) 0° to +40°.

## 3.4 Summary

A simple linear model has been presented which predicts the relative modulation strengths of multiple transmission and reflection gratings which have been recorded due to boundary reflections. It has been used to predict modulations for transmission gratings recorded in air with polarisations parallel and perpendicular to the plane of incidence of the hologram. By applying the theoretical modulation values to a multiple grating coupled wave theory, good agreement was found for angular transmission measurements of both cases.

# Chapter 4

# Nonlinear recording in dichromated gelatin

## 4.1 Introduction

The simple model described in the previous chapter was based on the assumption that dichromated gelatin has an ideal linear recording response to exposure energy. In practice this is not the case. Holographic recording materials all exhibit nonlinearities which limit the dynamic range of modulation formation.

An ideal holographic recording material is one which will form a faithful replica of the interference pattern in which it is placed. At low energy levels dichromated gelatin comes quite close to behaving in this manner. Unfortunately, at higher energies, the response of the gelatin saturates causing distortion in the modulation profile and hence forming spatial harmonic gratings. At replay this distorted grating structure will diffract multiple beams at frequencies corresponding to these spatial harmonics. This saturation effect is due to the limited range of hardening within the DCG causing a nonlinear response to increased exposure levels.

In 1976 Case and Alferness [Cas76] studied the effects of saturation and hardening in dichromated gelatin in order to consider the generation of spatial harmonics. In their model they assumed a saturating exponential function based on experimental observations.

Alferness [Alf76] in 1976 studied the double contribution to diffraction efficiency at the second Bragg angle of a single unslanted transmission grating by diffraction both by the fundamental and by the second spatial harmonic. In his publication he considers replay of the spatial harmonic grating at the Bragg condition for second order diffraction. Chang and Case [Cha76b] looked at the use of second harmonics for waveguide coupling. In 1979 Chang and Leonard [Cha79] published the results of a model, assuming nonlinear absorption of DCG, to compare experimental exposure characteristics with theory. More recently Newell [New85], describing the real time effects of DCG, showed how absorption saturates with an increase in exposure. The real time diffraction efficiency was also seen to saturate accordingly, illustrating the nonlinear response of DCG. He also recorded single reflection gratings to investigate the material nonlinearity [New87].

Nonlinear recording has not been limited to dichromated gelatin. In 1967 Friesem and Zelenka [Fri67] studied the effect of film nonlinearities in silver halide emulsions and the formation of 'false images' at replay. Bendall *et al* [Ben72] in 1972 also investigated nonlinear recording in thick amplitude holograms by extending Kogelnik's coupled wave theory to take account of higher order harmonic gratings when recording a single transmission grating. In 1980, theoretical work considering the replay of holograms recorded in the presence on nonlinearities was carried out by Zel'dovich and Yakovleva [Zel80] using a mode theory. More recently, in 1985, Slinger [Sli85a] and Slinger *et al* [Sli85b] investigated the effect of nonlinear recording in commercially available silver halide materials. They developed a general coupled wave theory to take account of higher harmonic gratings and obtained good comparisons with holograms recorded with different optical thickness.

The aim of this chapter is to examine the effect of nonlinearity on the performance of gratings recorded in dichromated gelatin for both single and double exposure transmission gratings [Bla89b]. Results are presented for plates which have been recorded over a wide energy range to illustrate the recording of spatial harmonic gratings. A theory is presented here capable of modelling the refractive index modulation versus exposure energy of both fundamental and harmonic gratings for both cases, as well as predicting the modulation profile of the recorded structure.

## 4.2 Experiments

To study the effect of nonlinear recording in dichromated gelatin, single and double exposure transmission holograms were recorded over a wide range of exposure energies and observed over a range of replay wavelengths. A large exposure range was chosen in order to look at the effect of recording within the linear and nonlinear regions of the exposure characteristic.

All recordings were made with 22 μm thick DCG plates sensitised by 2% ammonium dichromate and with beams polarised perpendicular to the plane of incidence. To avoid the recording of spurious gratings, due to interference with reflected waves at the boundaries, all recordings were made in an index matching tank. The index matching fluid used was Xylene with a refractive index of 1.497.

To be able to assume that the measured dips at different Bragg angles are solely the result of first order diffraction, recording angles were chosen so as to assume optically thick replay conditions, i.e. where $\Omega > 20$ (see Chapter 1).

For the single grating case the recording angles were chosen as +30° and -20° in air. By feeding these into equation (1.27) and assuming replay at 514.5 nm, an average refractive index of 1.5 and a maximum possible refractive index modulation of 0.016, we find that $\Omega_{30^\circ} \sim 43$ and $\Omega_{20^\circ} \sim 19$ which tells us that we are safely working in the volume domain. We are therefore able to neglect higher orders.

For the double exposure experiments the recording angles were chosen at ±35° and ±27°. These are sufficiently separated so as to reduce the effects of grating interactions [Alf75] and are large enough to obtain values of $\Omega_{35^\circ} \sim 53$ and $\Omega_{27^\circ} \sim 38$ using the same parameters as above. This again allows volume replay at 514.5 nm. We should note that these calculations were carried out for a large $n_1$ so any reduction in modulation is going to increase $\Omega$ further still and reinforce the decision to assume only first order diffraction.

### 4.2.1 *Single exposure transmission gratings*

The recording geometry use to record single exposure transmission gratings is shown in Figure 4.1. Here we can see two plane, collimated beams incident on the plate at angles +20° and -13°.

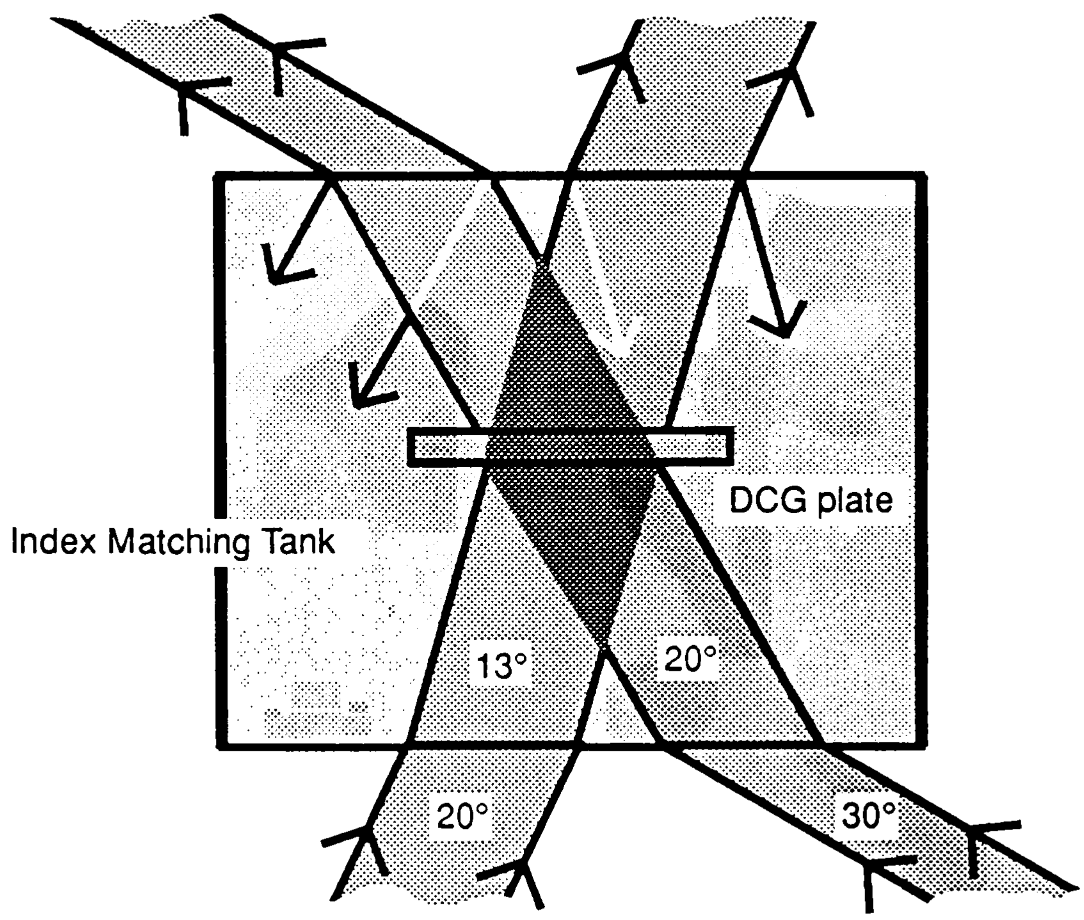


Figure 4.1 Recording geometry for single grating in an index matching tank

The plates were exposed over an energy range from 50 mJ / cm$^2$ to 2800 mJ / cm$^2$ and scanned at a short replay wavelength of 400 nm in order to enhance overmodulation and to allow replay of higher harmonic gratings. Figure 4.2 shows a comparison between (a) the recording and (b) the replay Ewald circles for this particular situation. Assuming realistic average refractive index values of $n_1$ = 1.57 and $n_2$ = 1.49, we see how reducing the replay wavelength increases the radius of the circle allowing replay of the higher harmonic grating with vector $3\overline{K}$ at large angles of incidence. Because of the drop in wavelength to 400 nm, we expect to observe dips around the angles (-10°, +16°), (-23°,+30°) and (-39°,+45°) corresponding to the replay in the index matching tank of the fundamental grating with vector $\overline{K}$ and the spatial harmonics $2\overline{K}$ and $3\overline{K}$ respectively. For simplicity we will name these gratings G, 2G and 3G.

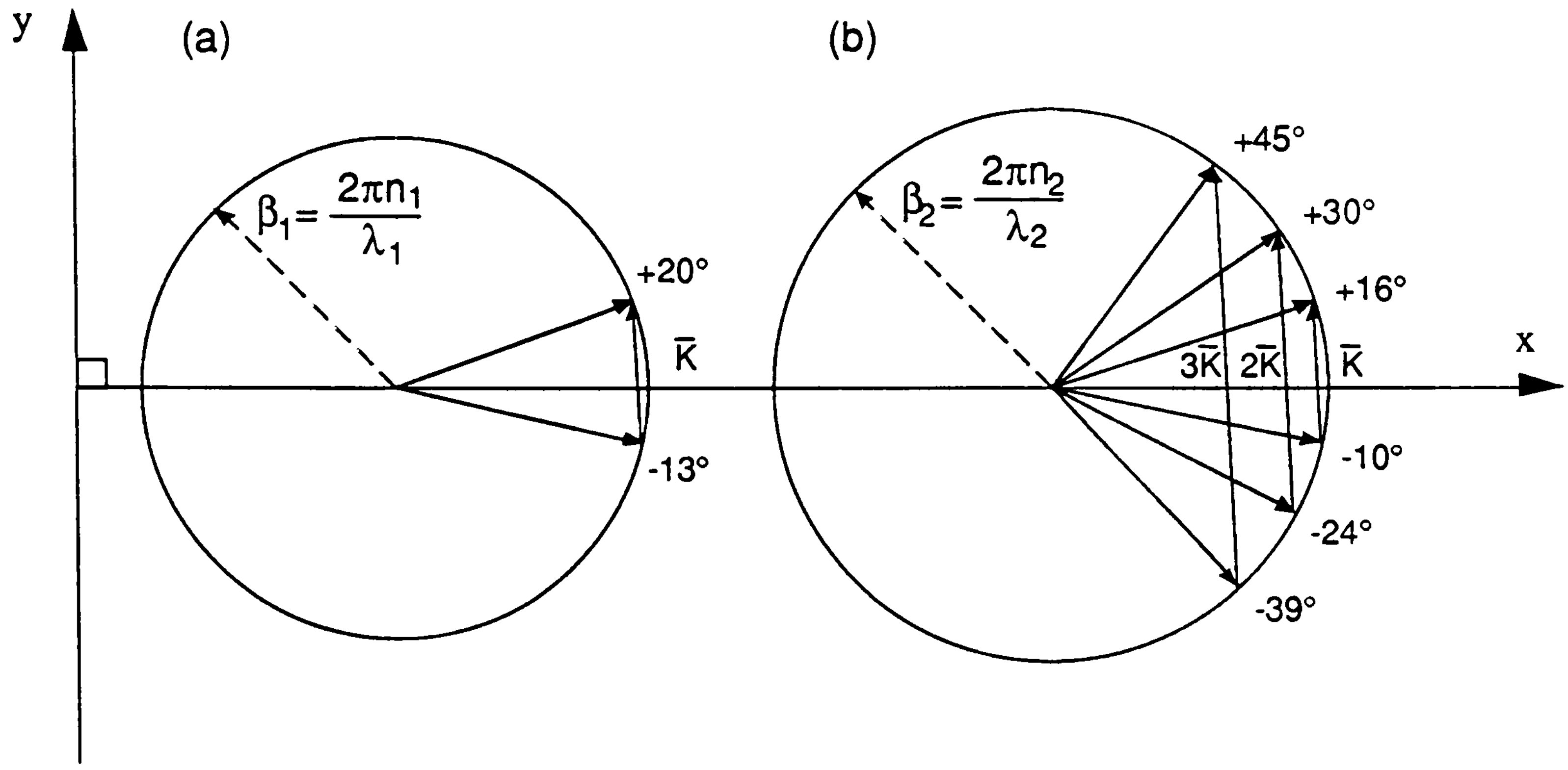


Figure 4.2 Ewald circles showing (a) recording at $\lambda_1$ = 514.5 nm and (b) replay at $\lambda_2$ = 400 nm.

Figure 4.3 shows angular transmittance scans of these plates as a function of exposure energy. At low energies (Diagrams (a) to (c)) we can observe the existence of only two Bragg dips at -10° and +16° corresponding to the recorded fundamental grating. As the exposure energy is increased we can clearly see the formation of dips at angles corresponding to the replay of gratings 2G and 3G. Figure 4.4 shows the variation of efficiency with exposure for the fundamental grating and second harmonic when replayed at the recording wavelength (514.5 nm). At low exposures we can see that the efficiency of the fundamental grating follows a sinusoidal characteristic as described by Kogelnik [Kog69], however as the exposure energy is increased, it reaches 95% efficiency before dropping off at 1000 mJ / cm$^2$. We notice that the second harmonic increases in strength as G falls and we can see that the efficiency of G does not fall to zero before increasing again. This gives us a clear indication that the material is behaving in a nonlinear manner at higher exposure levels.

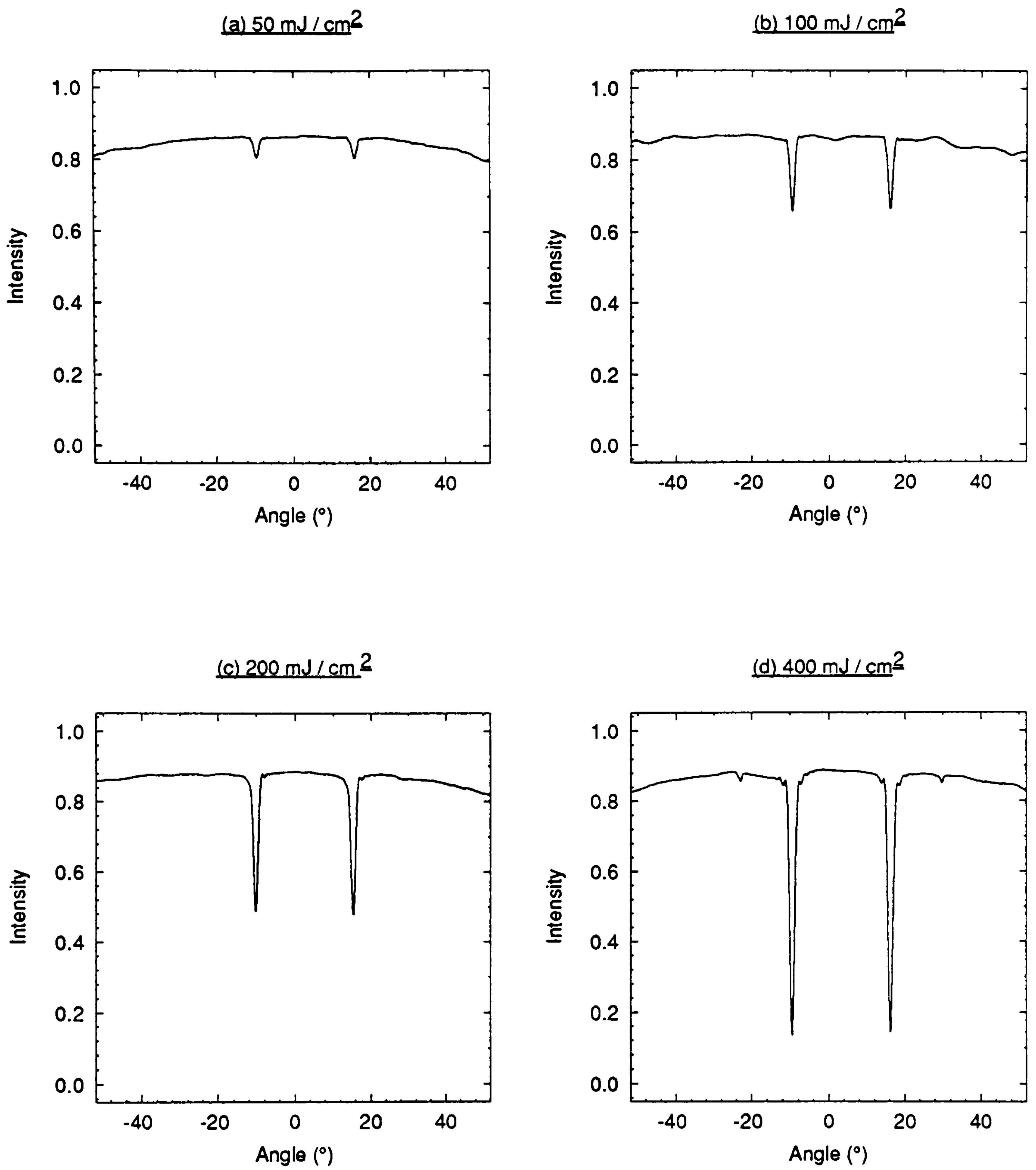


Figure 4.3 Experimental angular transmittance scans of a single transmission grating as a function of exposure energy (at 400 nm).

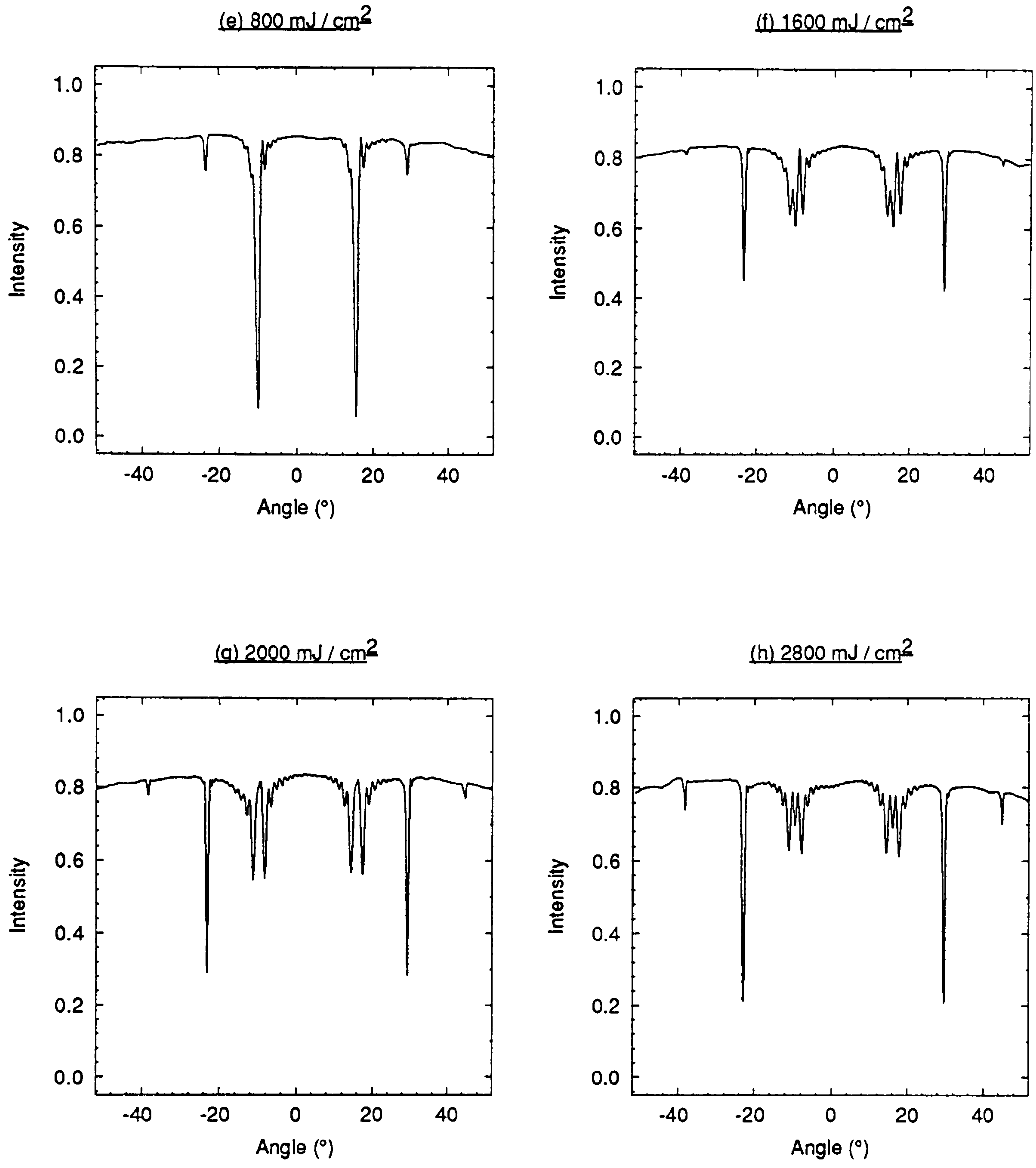


Figure 4.3 (Continued).

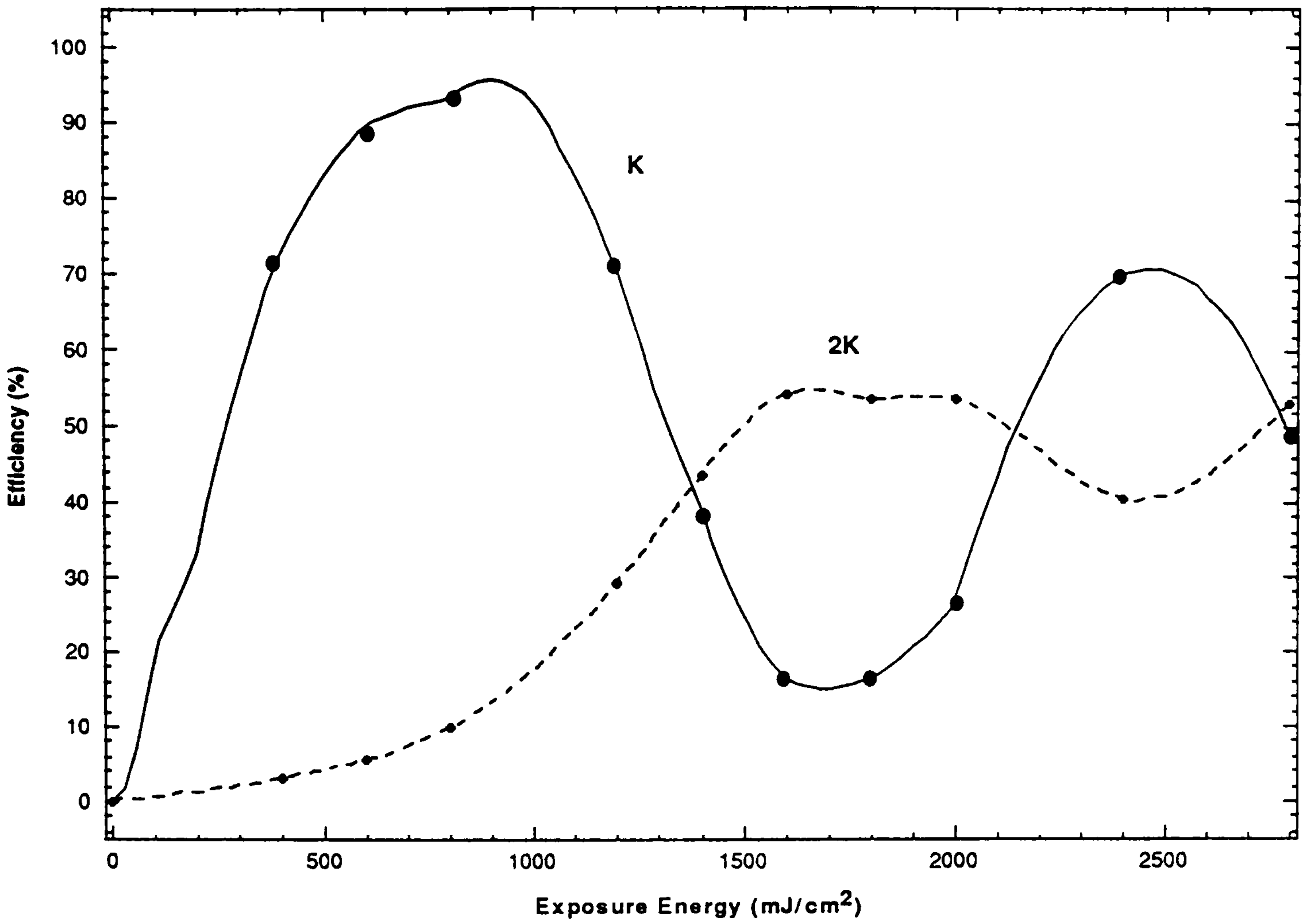


Figure 4.4 Experimental plot of efficiency versus exposure energy for the fundamental and second harmonic of a single transmission grating when replayed at 514.5 nm.

Figure 4.5 shows the replay of a plate exposed at 2000 mJ / cm$^2$ at wavelengths of 400 nm, 514.5 nm, 600 nm and 700 nm. As the replay wavelengths increase we observe the replay angles of all Bragg dips increasing according to Bragg's law.

*The effect of dispersion*

To measure the effect of dispersion, the efficiencies of each dip were measured over a range of replay wavelengths as above. By making the assumptions that the hologram is optically thick and of low absorption, we can let the efficiency $\eta$ take the form:-

$$\eta = 1 - \mathrm{T} \tag{4.1}$$

where T is the transmittance.

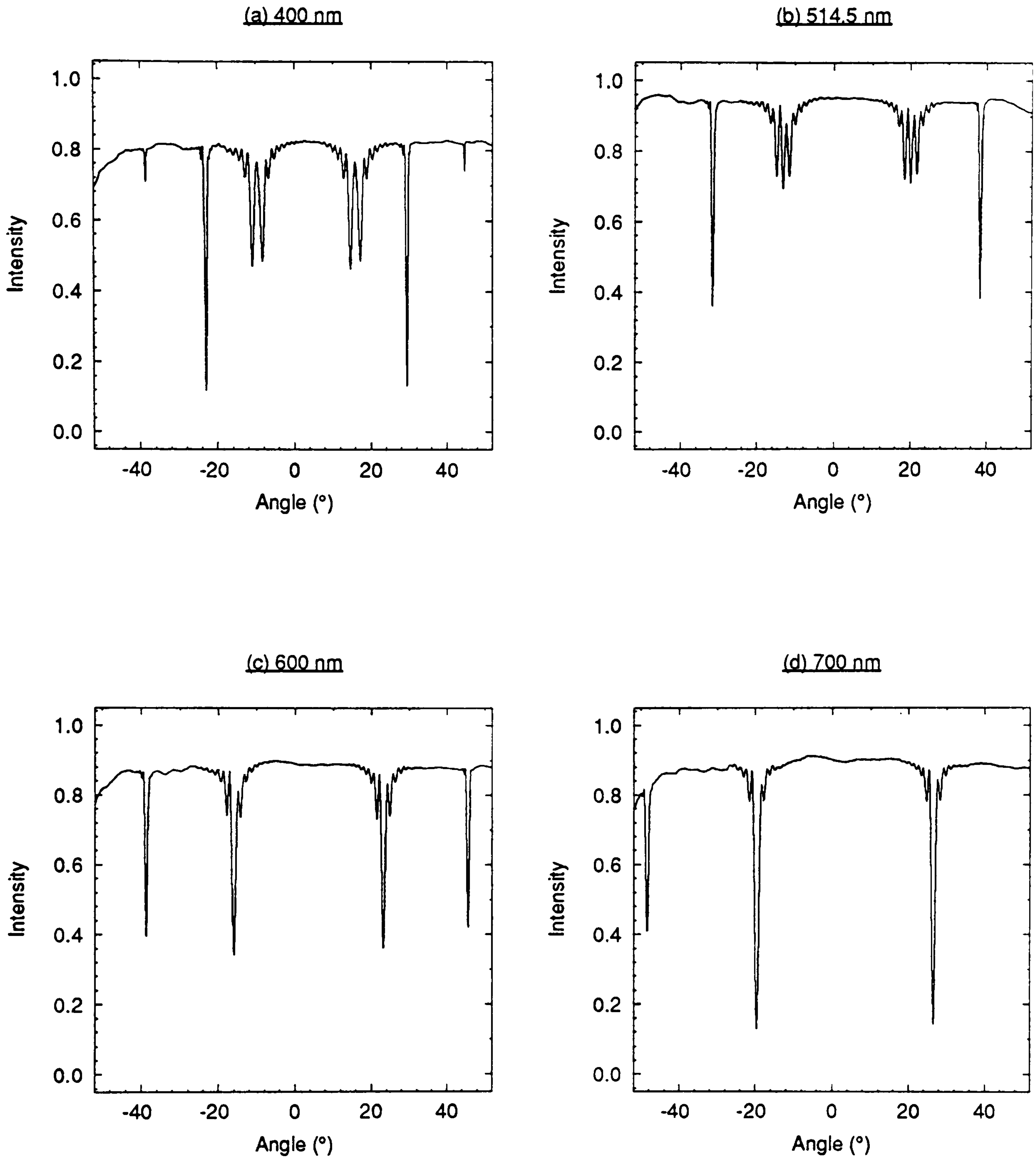


Figure 4.5 Experimental angular transmittance scans for a single grating at varying replay wavelengths.

Including the effect of constant absorption $\alpha$, which may be calculated by measuring transmittance ($T_\alpha$) away from the Bragg dips, i.e.

$$\alpha = \frac{-\cos\theta_\alpha \; ln\sqrt{T_\alpha}}{d} \tag{4.2}$$

where $\theta_\alpha$ is the angle and $d$ is the thickness at replay, it is possible to calculate the refractive index modulation ($n_1$) of each dip of a transmission hologram using a simple expression for efficiency taken from Kogelnik's paper [Kog69]:-

$$n_1 = \frac{\lambda\cos\theta_o}{\pi d}\cos^{-1}\left[\frac{\sqrt{T_o}}{e^{-\frac{\alpha d}{\cos\theta_o}}}\right] \tag{4.3}$$

where $T_o$ is the transmittance at the Bragg angle $\theta_0$ and $\lambda$ is the replay wavelength.

From these calculations we can observe the variation of refractive index modulation ($n_1$) with replay wavelength for a single recording. Figure 4.6 shows a graph of $n_1$ versus replay wavelength for a hologram recorded at 2000 mJ / cm$^2$.

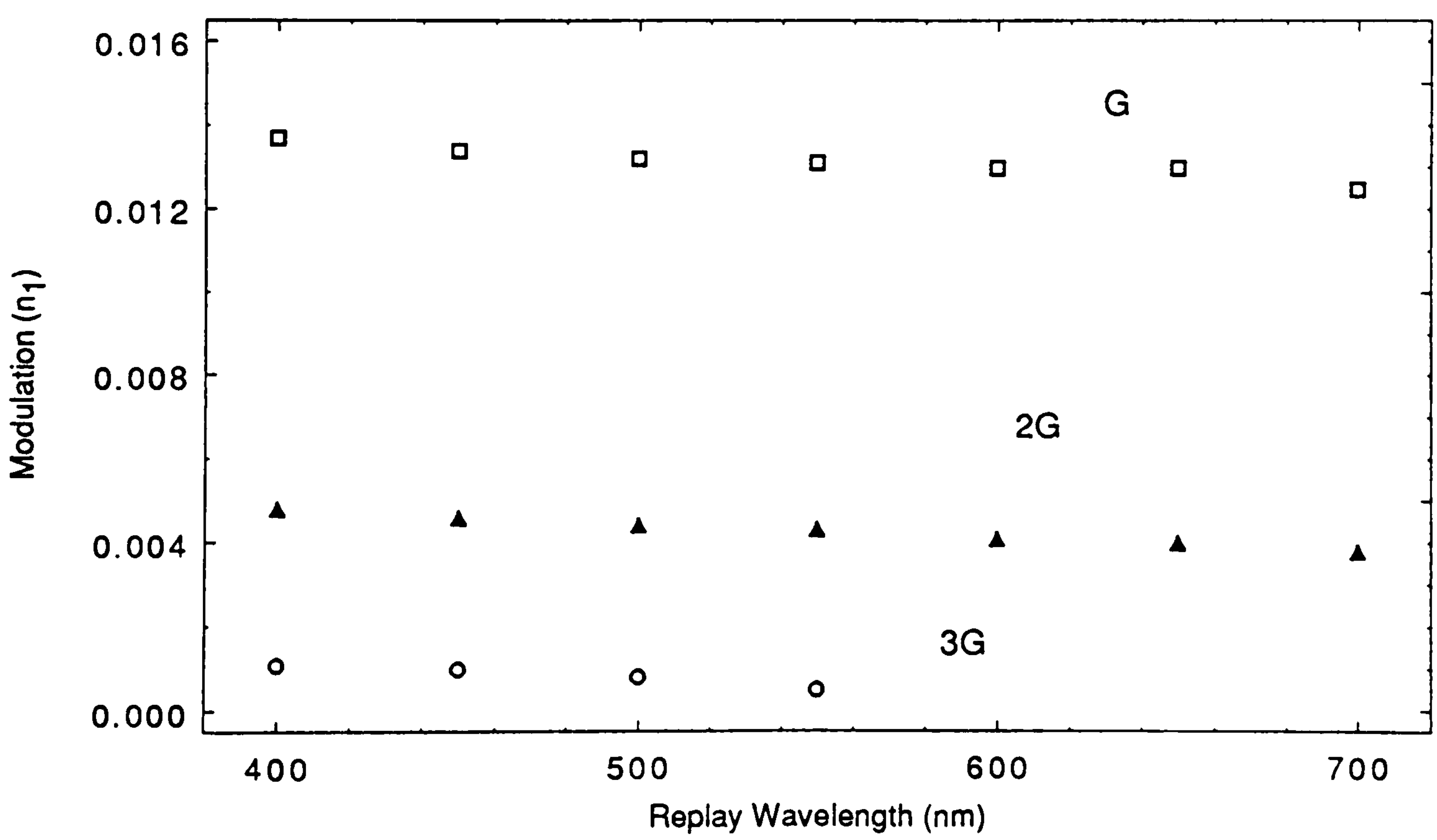


Figure 4.6 Experimental plot of dispersion for a single transmission grating recorded at 2000 mJ / cm$^2$.

It illustrates an almost linear drop in modulation with an increase in wavelength for both the fundamental G and harmonics 2G and 3G. The drop appears to be consistent at 0.001 for all three measurements. This is a very small change in modulation over the visible spectrum and the results are similar to the dispersion found by Newell [New87].

4.2.2 *Double exposure transmission gratings*

Two unslanted transmission gratings were recorded sequentially using the geometry shown in Figure 4.7. Plates were index matched, using Marcol 52 oil (n = 1.459), to a neutral density filter to reduce reflections from the rear glass / air boundary. The beam ratio was kept constant at 1:1. The recording angles in air were $\phi_1 = \pm 35.4°$ and $\phi_2 = \pm 27.6°$. After the first exposure at $\pm\phi_1$ using mirrors M3 and M6, mirrors M4 and M5 were then used to record at $\pm\phi_2$. The plates were exposed over a range of total energies from 100 mJ / cm$^2$ to 2000 mJ /cm$^2$ and the exposure ratio was kept constant at 1:1, i.e. the same energy was used for both recordings. Again the plates were replayed at a wavelength of 400 nm to observe the effect of an increasing exposure energy.

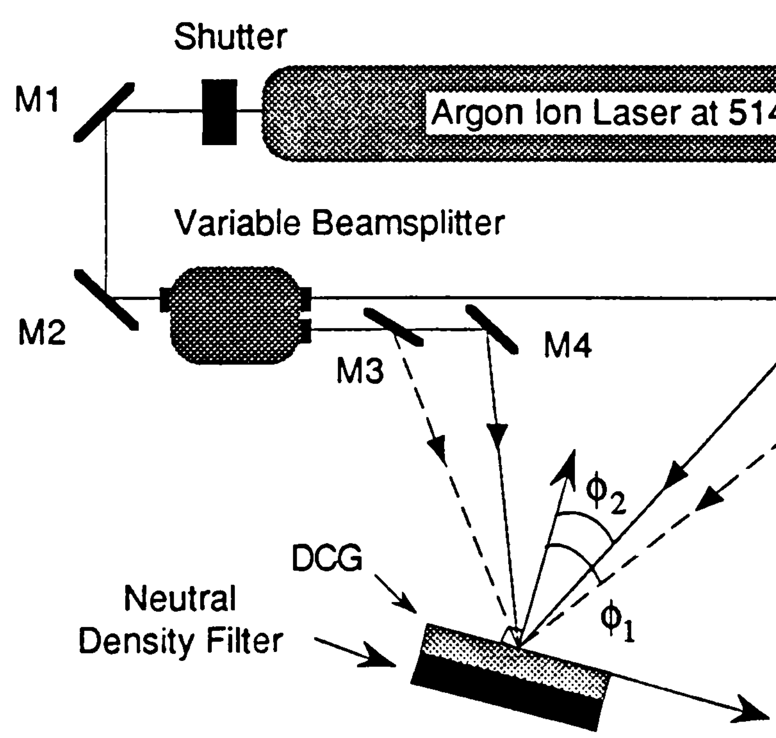


Figure 4.7 Recording geometry for sequential double exposure transmission gratings.

Figure 4.8 shows angular transmittance scans of these plates. Since the gratings are unslanted only positive angles are shown from 0° to 45° incidence.

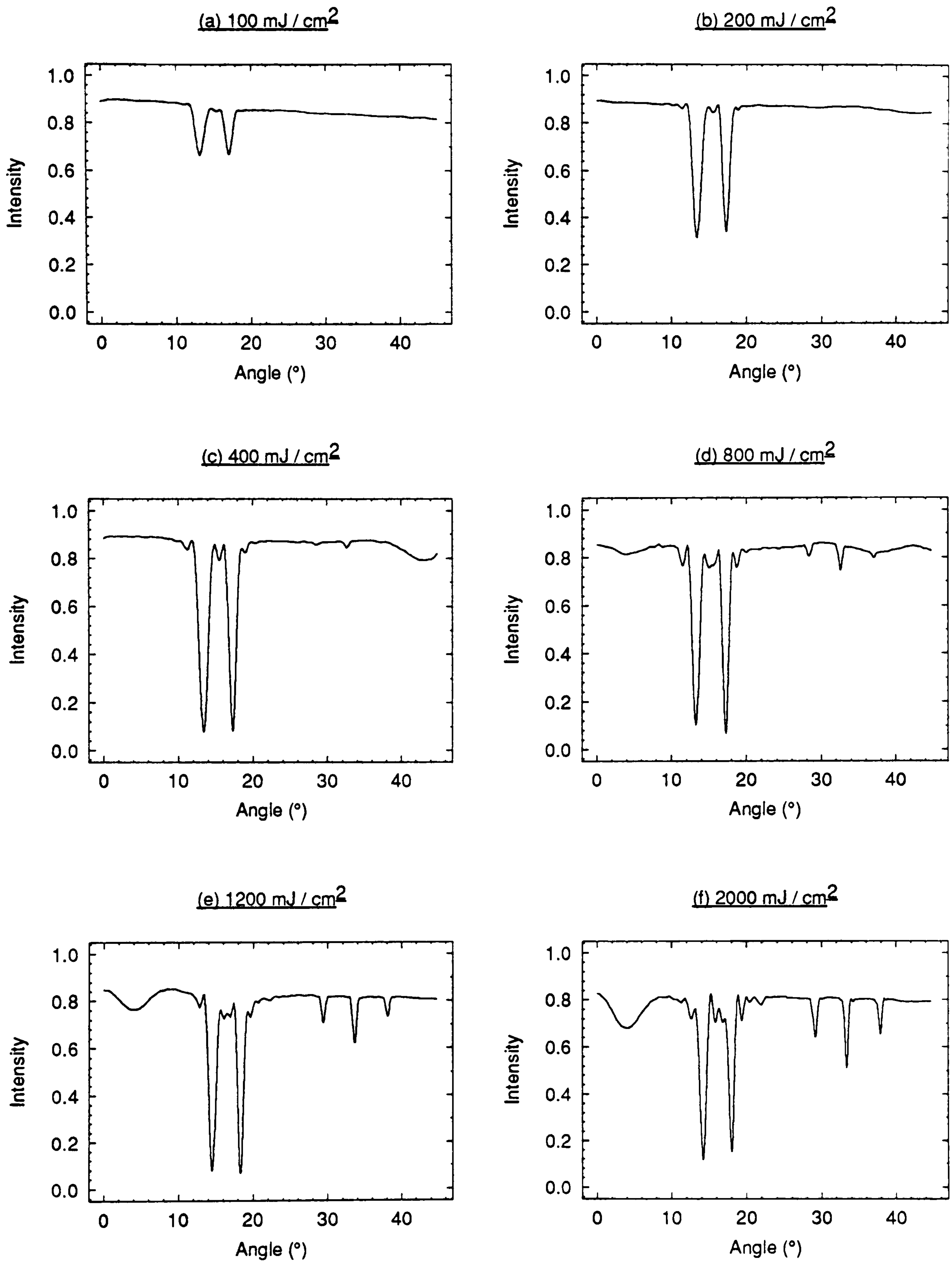


Figure 4.8 Experimental angular transmittance scans of double exposure recordings for varying exposure energies (replayed at 400 nm).

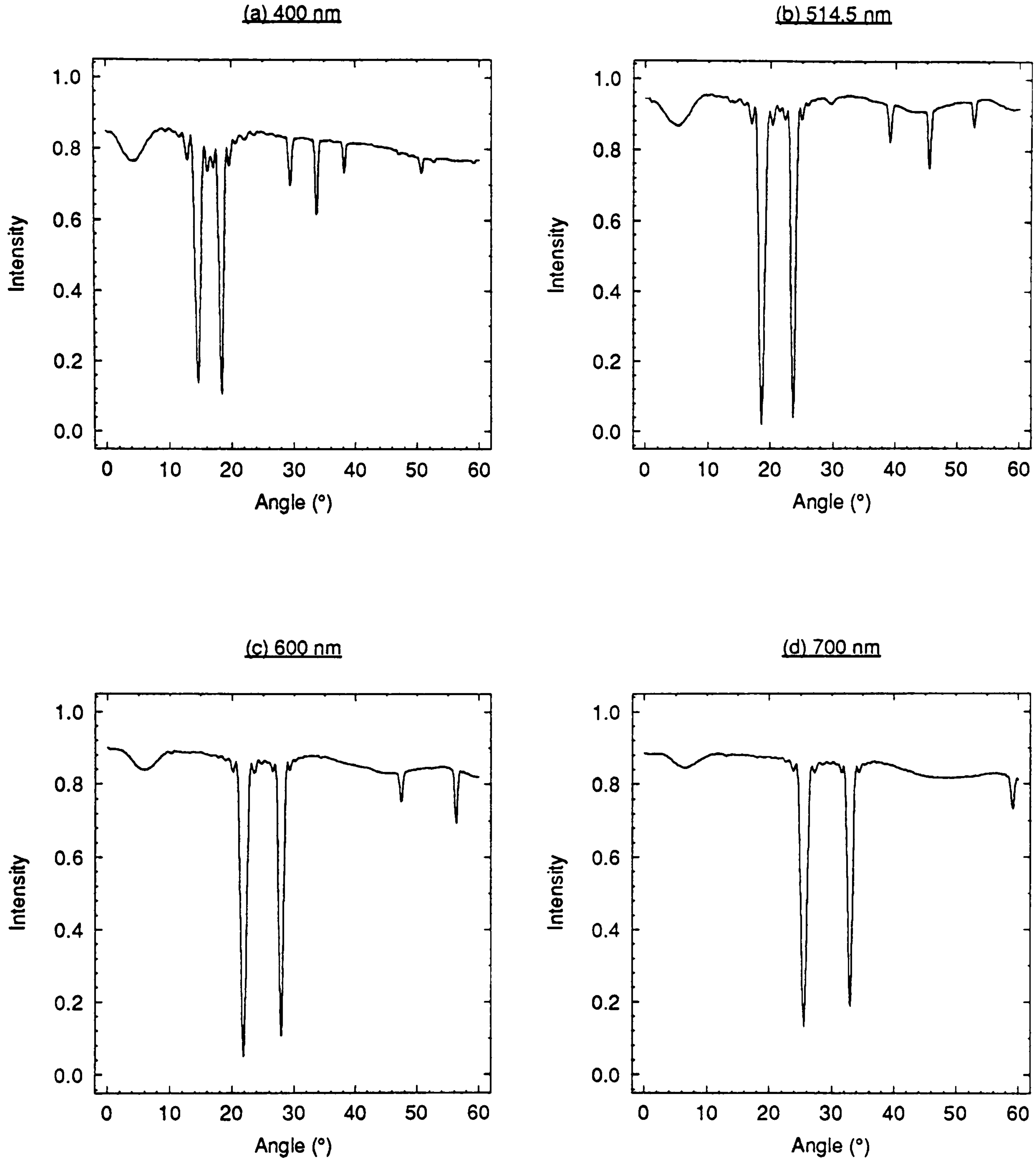


Figure 4.9 Experimental angular transmittance scans for double exposure gratings at varying wavelengths (total exposure = 1200 mJ / cm$^2$).

At low energies we observe only two dips at the recording Bragg conditions, however, as the recording energy is increased we can see the formation of at least six dips. These correspond to the primary gratings with vectors $\overline{K}_1$ and plus spatial harmonics $2\overline{K}_1$ , $2\overline{K}_2$ and the combined terms $\overline{K}_1 - \overline{K}_2$ and $\overline{K}_1 + \overline{K}_2$ . Once more, for simplicity we will name these gratings $G_1$, $G_2$, $2G_1$, $2G_2$, $G_1$ - $G_2$ and $G_1$ + $G_2$ respectively

By replaying one of the above plates with longer wavelengths (Figure 4.9), we are able to observe the Bragg dips increase their angle of replay. This movement in replay angle corresponds to the application of Bragg's law for each of the individual gratings. The fundamental gratings $G_1$ and $G_2$ replay around ±17° and ±13° in the index matching tank, however we can also expect the gratings $2G_1$, $2G_2$, $G_1$ - $G_2$ and $G_1$ + $G_2$ to replay at the angles ±38°, ±29°, ±4° and ±33° respectively. Swelling of the hologram has no real effect on the replay conditions since the transmission gratings are unslanted and therefore have no vector component perpendicular to the hologram surface.

*The effect of dispersion*

The refractive index modulation for each of the above dips was measured at varying wavelengths to observe the effect of dispersion. The same method of calculation was used as in the single grating case (for all gratings it was assumed that the hologram was optically thick and could therefore be assumed volume). Figure 4.10 shows plots of refractive index modulation ($n_1$) versus replay wavelength for a hologram recorded with a total energy of 1200 mJ / cm$^2$. In this case it is interesting to observe a similar drop in modulation values for $G_1$, $G_2$, $2G_1$, $2G_2$ and $G_1$ + $G_2$ of about 0.001. However, the values for replay at $G_1$ - $G_2$ are seen to increase with wavelength. This measurement was repeated for other gratings and found to be consistent.

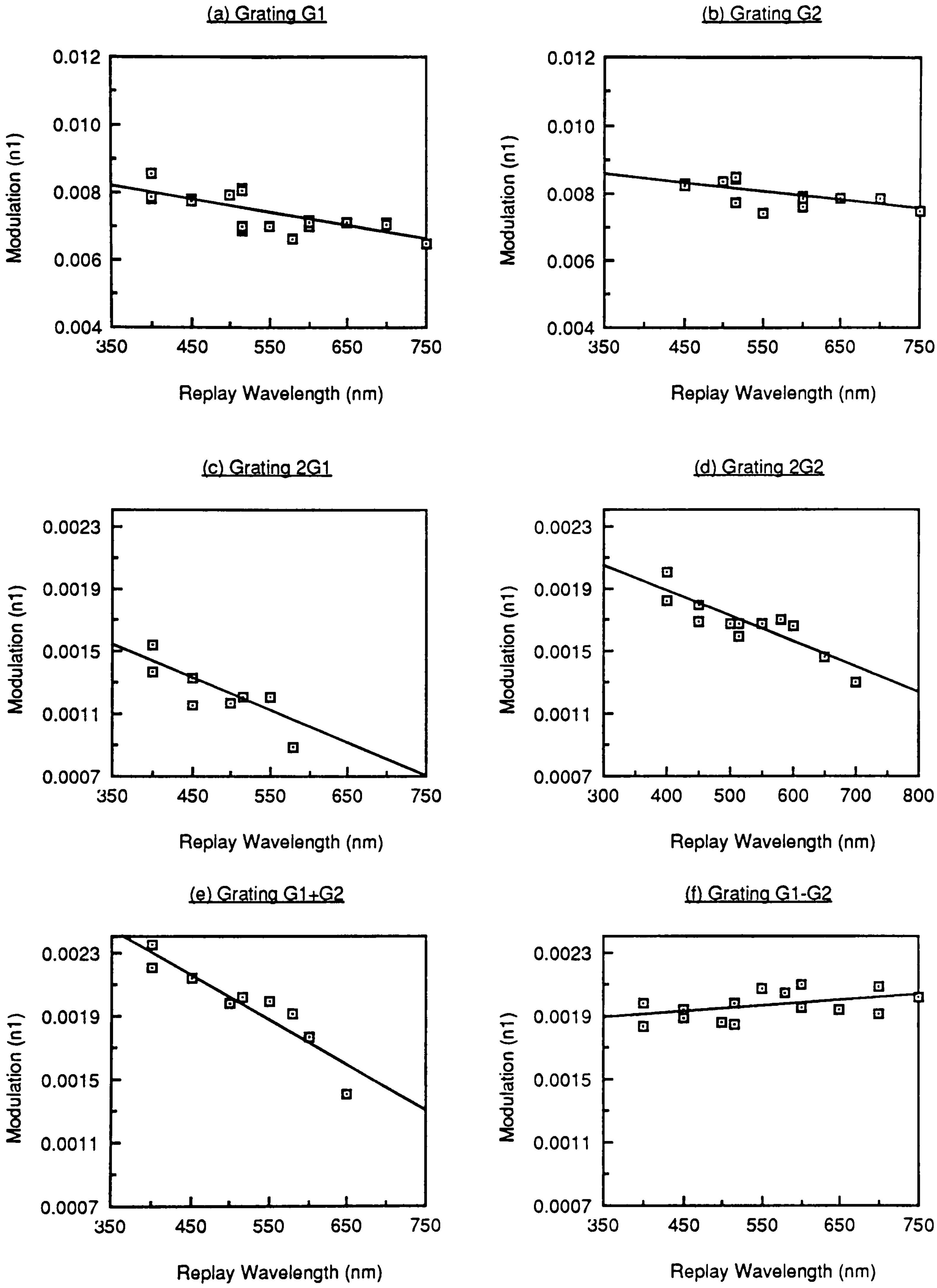


Figure 4.10 Experimental plots of dispersion for double gratings at 1200 mJ / cm$^2$.

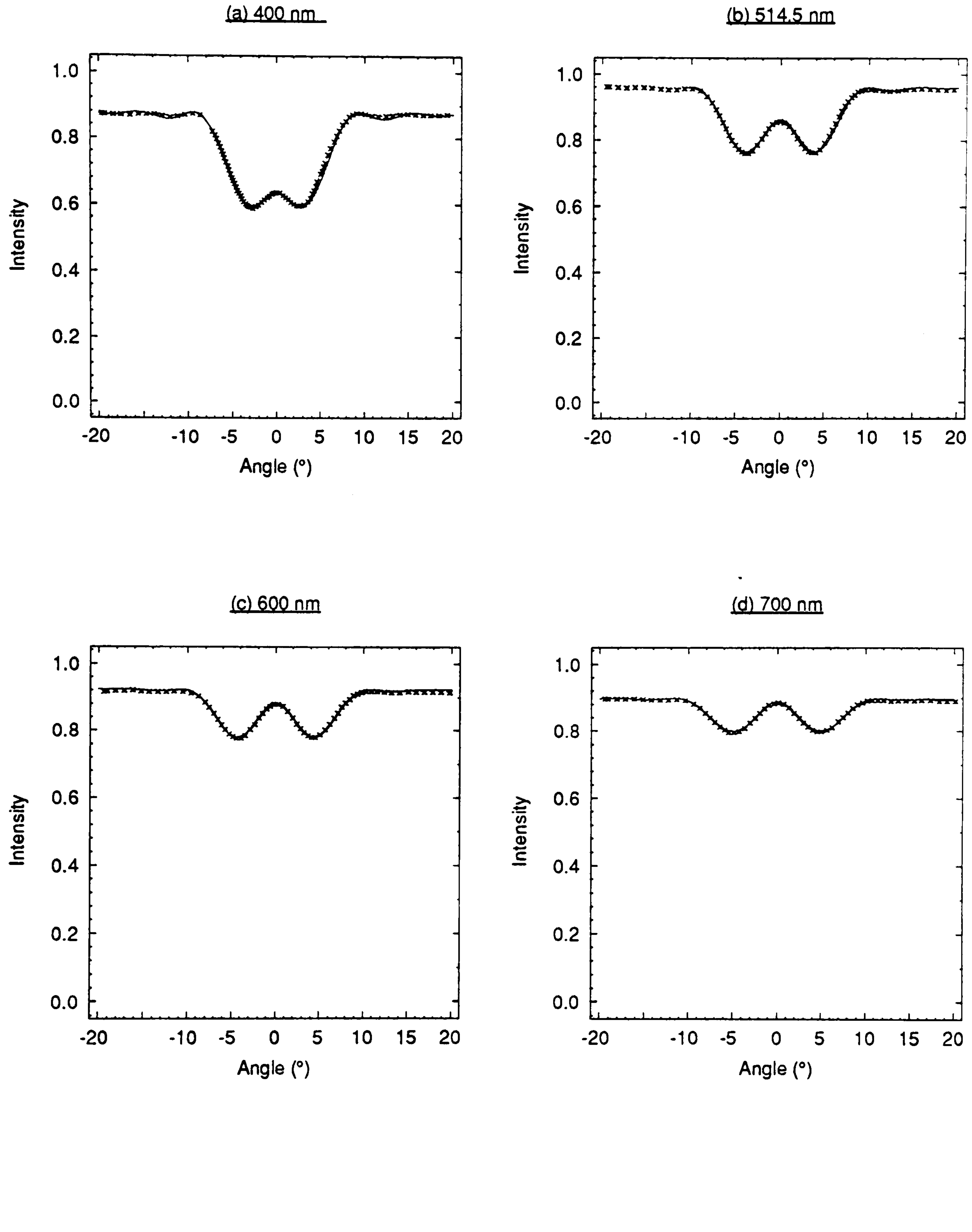


Figure 4.11 Single grating with low spatial frequency: theoretical matching (solid line) of experimental (dashed line) angular transmittance plots at varying replay wavelengths.

To confirm that this is a real effect, we recorded a single, independent transmission grating at low angles of incidence. The simulation angles were ±3.5° (within the emulsion) and the energy level was kept low to avoid saturation and hence the formation of harmonic gratings. The plate was scanned and the angular transmission data modelled using a simple coupled wave model which assumes the existence of only one sinusoidal grating.

Figure 4.11 shows theoretical matching of the experimental results for replay at 400 nm, 514.5 nm, 600 nm and 700 nm (the solid line indicates the theoretical curve). Figure 4.12 shows a plot of modulation ($n_1$) versus replay wavelength for this grating.

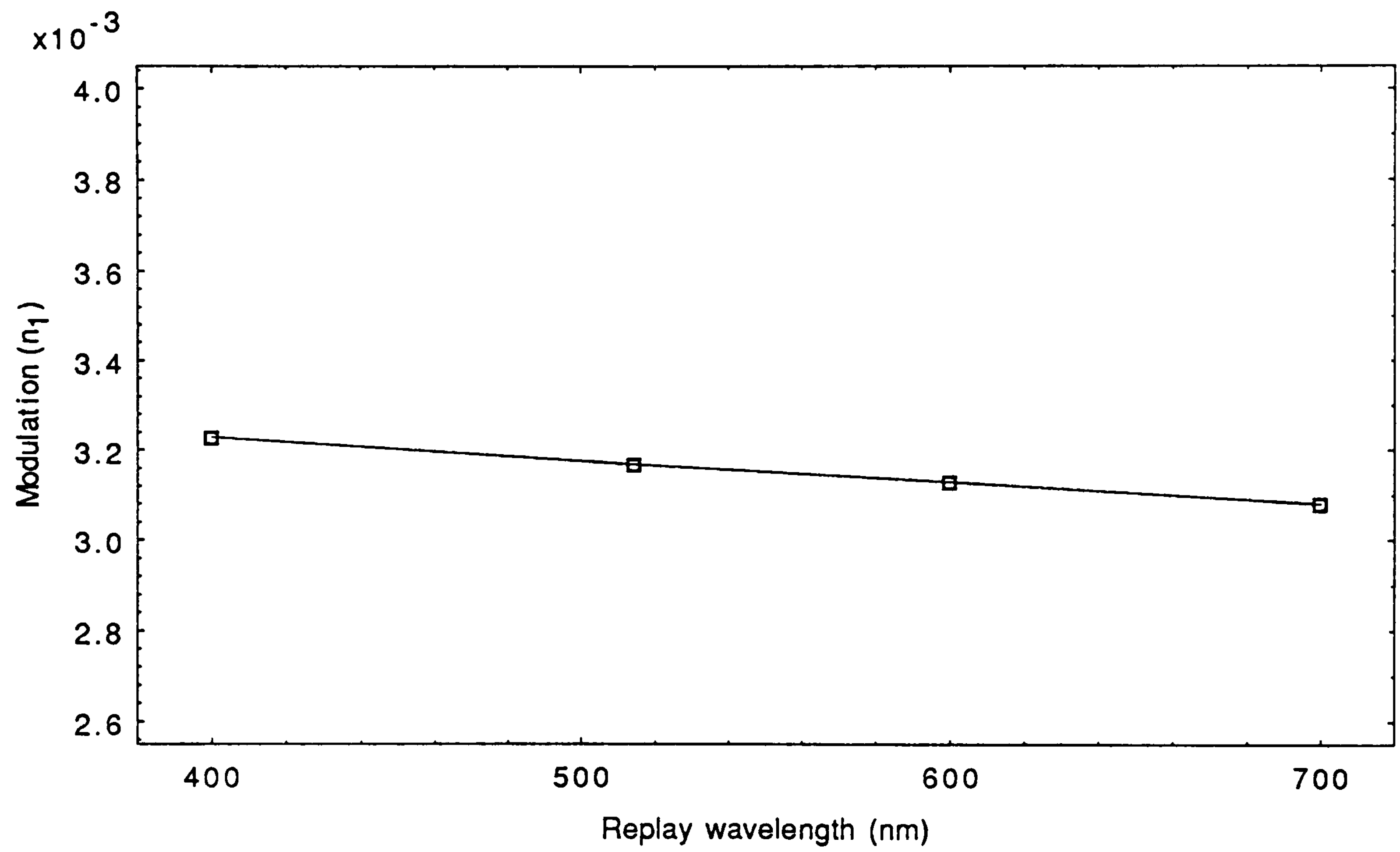


Figure 4.12 Dispersion plot for single grating with low spatial frequency.

We notice that it follows the same trend as in the previous single recordings shown in Figure 4.6 and decreases for longer wavelengths. So it is not the case that the dispersion is different because the grating vector is very small. The increase in modulation against wavelength found in Figure 4.10(f) must be a consequence of inadequate modelling. When the angle between the primary gratings is small then we need to take into account multiple interactions occurring via the $G_1$ and $G_2$ gratings and our assumption that each Bragg dip may be regarded as being independent is no longer valid. We shall return to this problem with the aid of a more complete model in Chapter 6. In the present chapter we shall restrict ourselves to explaining the origins of these spurious gratings by taking into account the nonlinearity of DCG.

## 4.3 Theory

We have previously stated that the refractive index of dichromated gelatin saturates with an increase in exposure. To model this we will use an assumption by Chang and Leonard [Cha79] and Case and Alferness [Cas76] who state that refractive index varies as a saturating exponential function. We can then expand on the work of Newell [New87] and assume a nonlinear refractive index response to exposure as:-

$$n(\bar{r}) = N_o\left[1-\exp\left(-\frac{E(\bar{r})}{E_o}\right)\right] \tag{4.4}$$

where $n(\bar{r})$ is the variation of refractive index over the position vector $\bar{r}$ , $N_o$ and $E_o$ are the constants corresponding to the maximum possible modulation and rate of decay in sensitivity respectively. $E(\bar{r})$ is a measure of the total exposure which, in the case of a double exposure hologram, is given by:-

$$E(\bar{r}) = E_1(\bar{r}) + E_2(\bar{r}) \tag{4.5}$$

$E_1(\bar{r})$ and $E_2(\bar{r})$ are the independent exposures of gratings 1 and 2 respectively and may be represented by:-

$$\sum_{i=1}^{2} E_i(\bar{r}) = \sum_{i=1}^{2}\left\{E_i\left[(1+b_i)+2\sqrt{b_i}\cos(\bar{K}_i.\bar{r})\right]\right\} \tag{4.6}$$

where $E_i$ is the exposure value of one beam, $b_i$ is the beam ratio of exposure i and $\bar{K}_i$ is the grating vector of exposure i.

By substituting equations (4.5) and (4.6) into (4.4) we obtain:-

$$n(\bar{r}) = N_o\left[1 - \exp\{-C\}\exp\left\{-z_1\cos(\overline{K}_1.\bar{r})\right\}\exp\left\{-z_2\cos(\overline{K}_2.\bar{r})\right\}\right] \tag{4.7}$$

where $C = \dfrac{E_1(1+b_1)+E_2(1+b_2)}{E_o}$ (4.8)

$$z_1 = 2\sqrt{b_1}\frac{E_1}{E_o}$$

and $z_2 = 2\sqrt{b_2}\dfrac{E_2}{E_o}$

By expanding the exponential terms with the familiar expansion (see Reference [How72])

$$\exp\{h\cos\theta\} = I_o(h) + 2\sum_{k=1}^{\infty} I_k(h)\cos(k\theta) \tag{4.9}$$

where $I_k(h)$ is a modified Bessel Function of the order $k$, we can expand equation (4.7) as:-

$$\begin{aligned} n(\bar{r}) = N_o\Bigg[1 - \exp\{-C\} \times \Bigg\{ & 2I_o(z_1)\sum_{m=1}^{\infty} I_m(z_2)\cos\left(m[\overline{K}_2.\bar{r}+\pi]\right) \\ & +2I_o(z_2)\sum_{n=1}^{\infty} I_n(z_1)\cos\left(n[\overline{K}_1.\bar{r}+\pi]\right) \\ & +4\sum_{n=1}^{\infty}\sum_{m=1}^{\infty} I_n(z_1)I_m(z_2)\cos\left(n[\overline{K}_1.\bar{r}+\pi]\right)\cos\left(m[\overline{K}_2.\bar{r}+\pi]\right)\Bigg\}\Bigg] \end{aligned} \tag{4.10}$$

The final term of (4.10) can be expanded using the cosine expansion:-

$$\cos A\cos B = \frac{1}{2}\left[\cos(A-B)+\cos(A+B)\right]$$

thus allowing us to obtain the following expression for the refractive index of the material:-

$$n(\bar{\mathrm{r}}) = N_o\left[1 - \exp\{-C\} \times \{\Omega_1 + \Omega_2 + \Omega_3 + \Omega_4 + \Omega_5\}\right]$$

where $\Omega_1 = I_o(z_1)I_o(z_2)$

$$\Omega_2 = 2I_o(z_1)\sum_{m=1}^{\infty} I_m(z_2)\cos(m\overline{\mathrm{K}}_2.\bar{\mathrm{r}} + m\pi)$$

$$\Omega_3 = 2I_o(z_2)\sum_{n=1}^{\infty} I_n(z_1)\cos(n\overline{\mathrm{K}}_1.\bar{\mathrm{r}} + n\pi)$$

$$\Omega_4 = 2\sum_{n=1}^{\infty}\sum_{m=1}^{\infty} I_n(z_1)I_m(z_2)\cos(n\overline{\mathrm{K}}_1.\bar{\mathrm{r}} - m\overline{\mathrm{K}}_2.\bar{\mathrm{r}} + n\pi - m\pi)$$

$$\Omega_5 = 2\sum_{n=1}^{\infty}\sum_{m=1}^{\infty} I_n(z_1)I_m(z_2)\cos(n\overline{\mathrm{K}}_1.\bar{\mathrm{r}} + m\overline{\mathrm{K}}_2.\bar{\mathrm{r}} + n\pi + m\pi) \quad (4.11)$$

This equation allows us to calculate the theoretical amplitudes of refractive index modulation for the fundamental gratings and any harmonics of $G_1$ and $G_2$ when $n$ and $m$ may take any values from 1 to $\infty$. It also describes the strength of the sum and difference intermodulation gratings. It is interesting to note here that there is a $\pi$ phase shift between different gratings depending on the order of the harmonic being considered. For example, if we consider the case where $n = 1$ and $m = 1$ in $\Omega_4$ and where $n = 1$ in $\Omega_3$ we can see that there will exist a $\pi$ phase shift between the gratings $G_1$ and $G_1$ - $G_2$. This observation is not so critical in the present analysis where we are simply modelling the amplitudes of the individual gratings, but it does become more important when we decide to synthesise the modulation profile of the recorded gratings later on in this chapter. The phase terms are also a critical factor when we come to analyse the double contribution to diffraction by $G_1$ - $G_2$ in Chapter 6.

Figure 4.13 shows a spectrum of recorded gratings which may be of importance when replaying a double exposure grating which has been recorded in the region of saturation. The plot is of theoretical modulation ($n_1$) versus the spatial frequency of each grating which has been normalised against one of the primary gratings $G_1$.

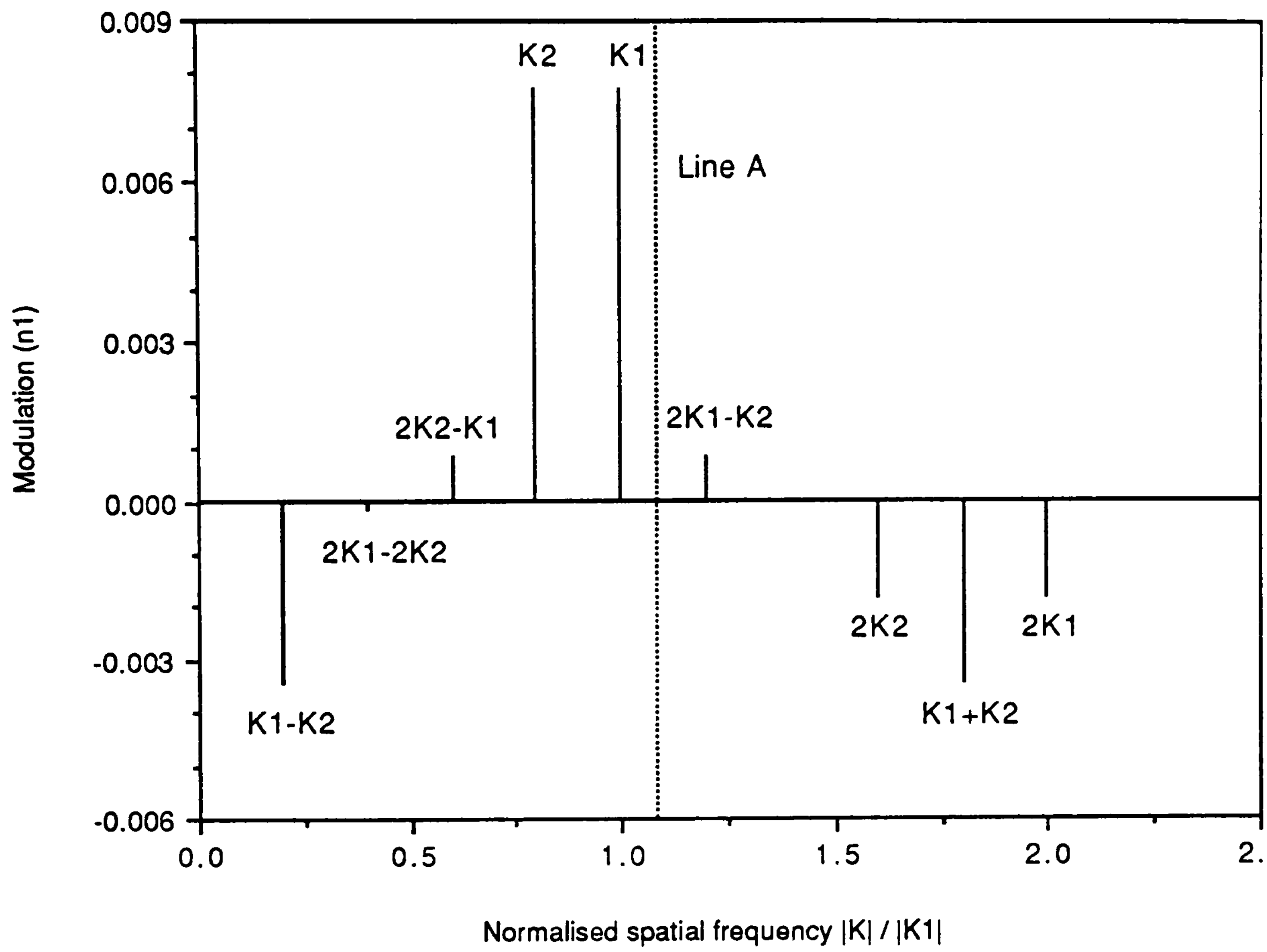


Figure 4.13 Spectrum of recorded gratings due to nonlinearity of DCG, assuming $|\overline{K}_2| = 0.8\,|\overline{K}_1|$ with constants $N_o = 0.04$ and $E_o = 500$.

In this particular case we assume that $|\overline{K}_2| = 0.8\,|\overline{K}_1|$ and the constants $N_o = 0.04$ and $E_o = 500$. We assume exposure values of 1000 mJ / cm$^2$ for each of the primary gratings. Using the above theory, we can easily observe which gratings have an associated $\pi$ phase shift by a negative modulation value. To simplify the number of gratings, we will only assume the cases where the integers $n$ and $m$ equal 1 and 2. Any combination of third harmonics and above result in low modulation values which we will neglect.

The figure shows high modulation values for the primary gratings $G_1$ and $G_2$, however, the sum and difference gratings $G_1 \pm G_2$ show modulation strengths close to half their value. These gratings also display a phase reversal.

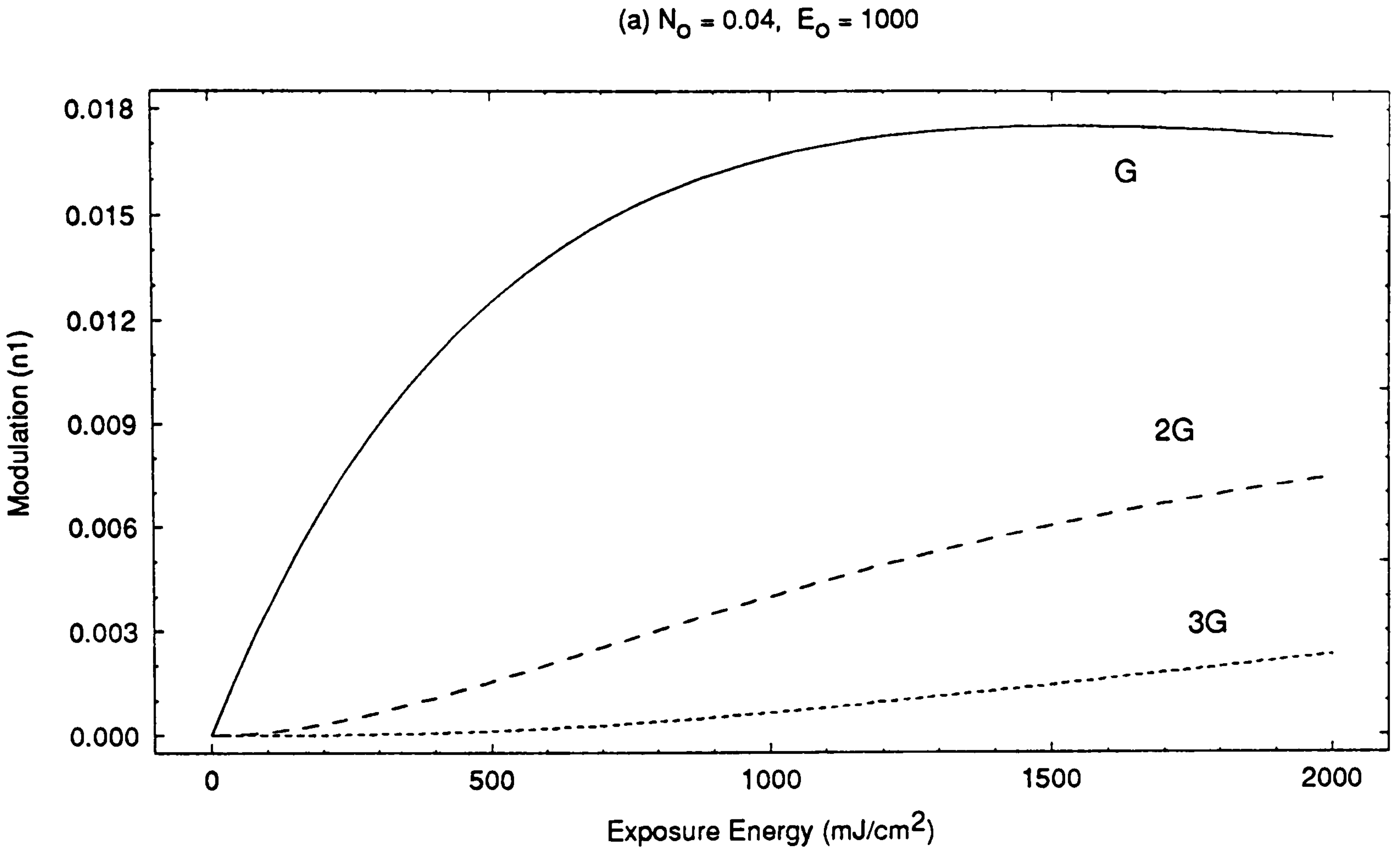


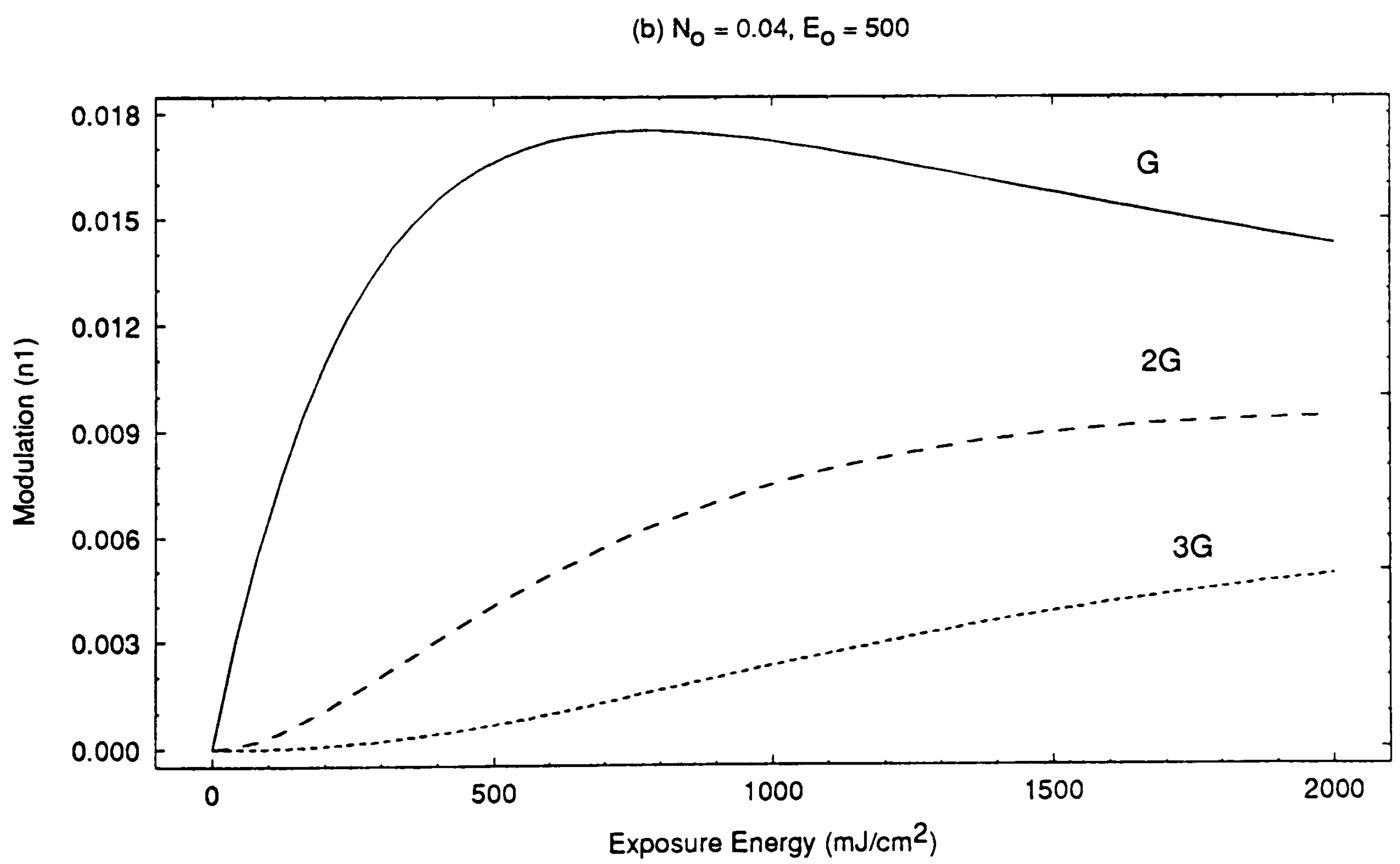


Figure 4.14 Theoretical plots of modulation versus exposure energy for varying $E_o$.

For a single grating we neglect the exposure $E_2(\bar{r})$ in equation (4.5) and obtain an expression for refractive index as:-

$$n(\bar{r}) = N_o\left[1-\exp\left\{-\frac{E_1(1+b_1)}{E_o}\right\}\times\left\{I_o(z_1)+2\sum_{n=1}^{\infty}I_n(z_1)\cos(n\bar{K}_1.\bar{r}+n\pi)\right\}\right] \quad (4.12)$$

This allows us to calculate the refractive index modulation values of the fundamental grating $G_1$ and subsequent harmonics. Again we observe the change in phase between even and odd harmonic gratings.

Calculation of the relevant modulation is dependent upon the total exposure energy, beam ratio, exposure ratio (in the case of two recordings) and the constants $N_o$ and $E_o$.

Figure 4.14 shows how $N_o$ and $E_o$ effect the variation of modulation with exposure. A decrease in $N_o$ reduces the maximum achievable modulation, since it is simply a multiplying factor. By increasing $E_o$ (Figure 4.14 (b)) we can see that the energy value for saturation to occur has increased accordingly. It is interesting to observe a drop in modulation for the fundamental grating at high exposure energies as the harmonic gratings increase in strength.

By keeping $N_o$ and $E_o$ constant (at $N_o$ = 0.04 and $E_o$ = 1000) we can observe the effect of changing the beam ratio. Figure 4.15 shows theoretical predictions for the fundamental grating G and second harmonic 2G over a range of beam ratios from 1 to 10. This illustrates a reduction in saturation modulation for both gratings and perhaps a more rapid decline in fundamental modulation at high exposures for higher beam ratios.

Figure 4.16 shows the effect of varying the exposure ratio for a double recording. The constants used here were $N_o$ = 0.04 and $E_o$ = 500. As the exposure ratio increases we see $G_1$ increase in strength and $G_2$ fall. Similarly for $2G_1$ and $2G_2$. At the same time $G_1$ - $G_2$ and $G_1$ + $G_2$ remain constant. In general, as the exposure ratio increases we see the profiles tending towards the case of a single recording.

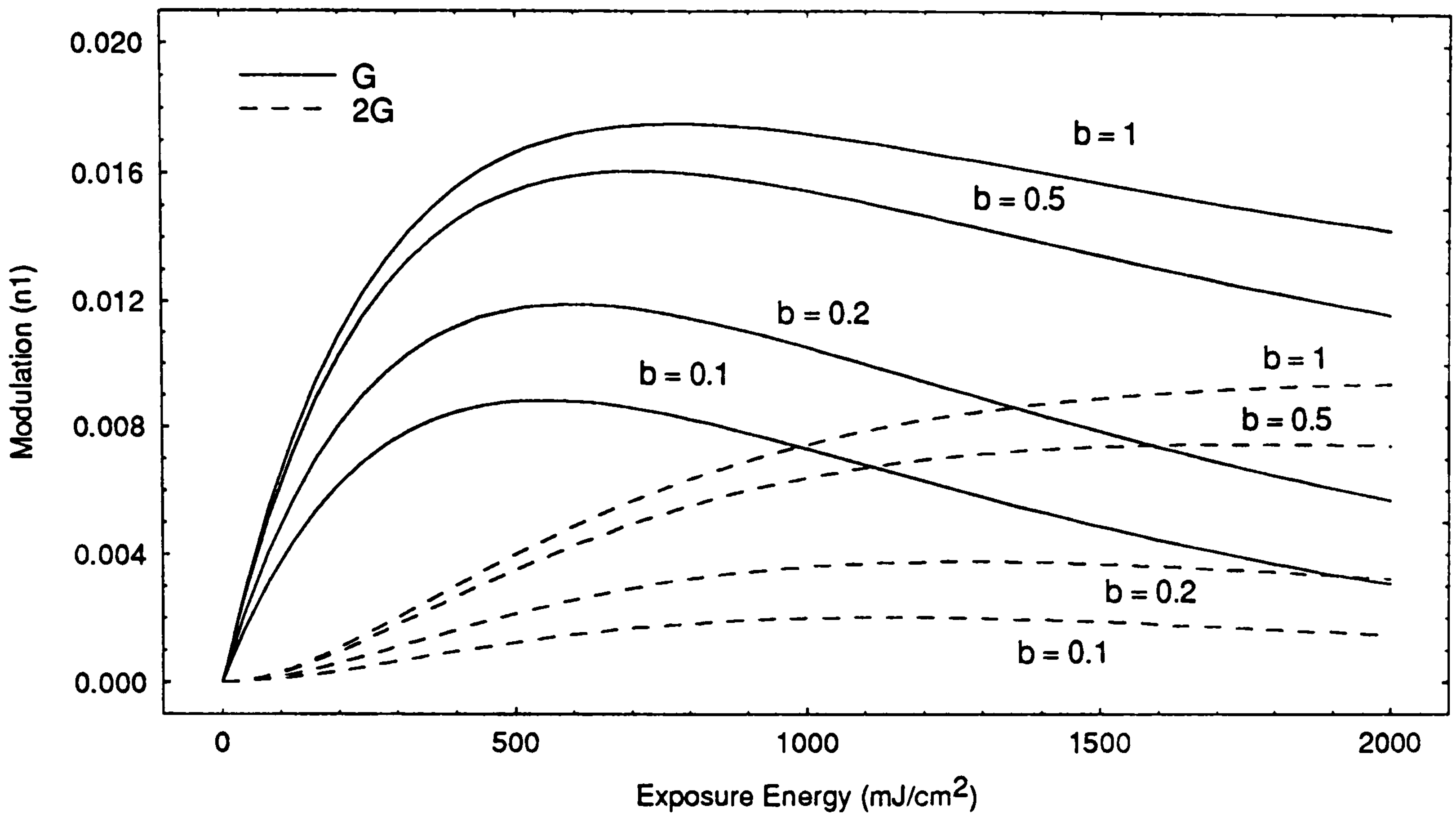


Figure 4.15 Theoretical variation of modulation versus exposure energy for a single grating illustrating the effect of varying the beam ratio $b$ ($N_o = 0.04$, $E_o = 500$).

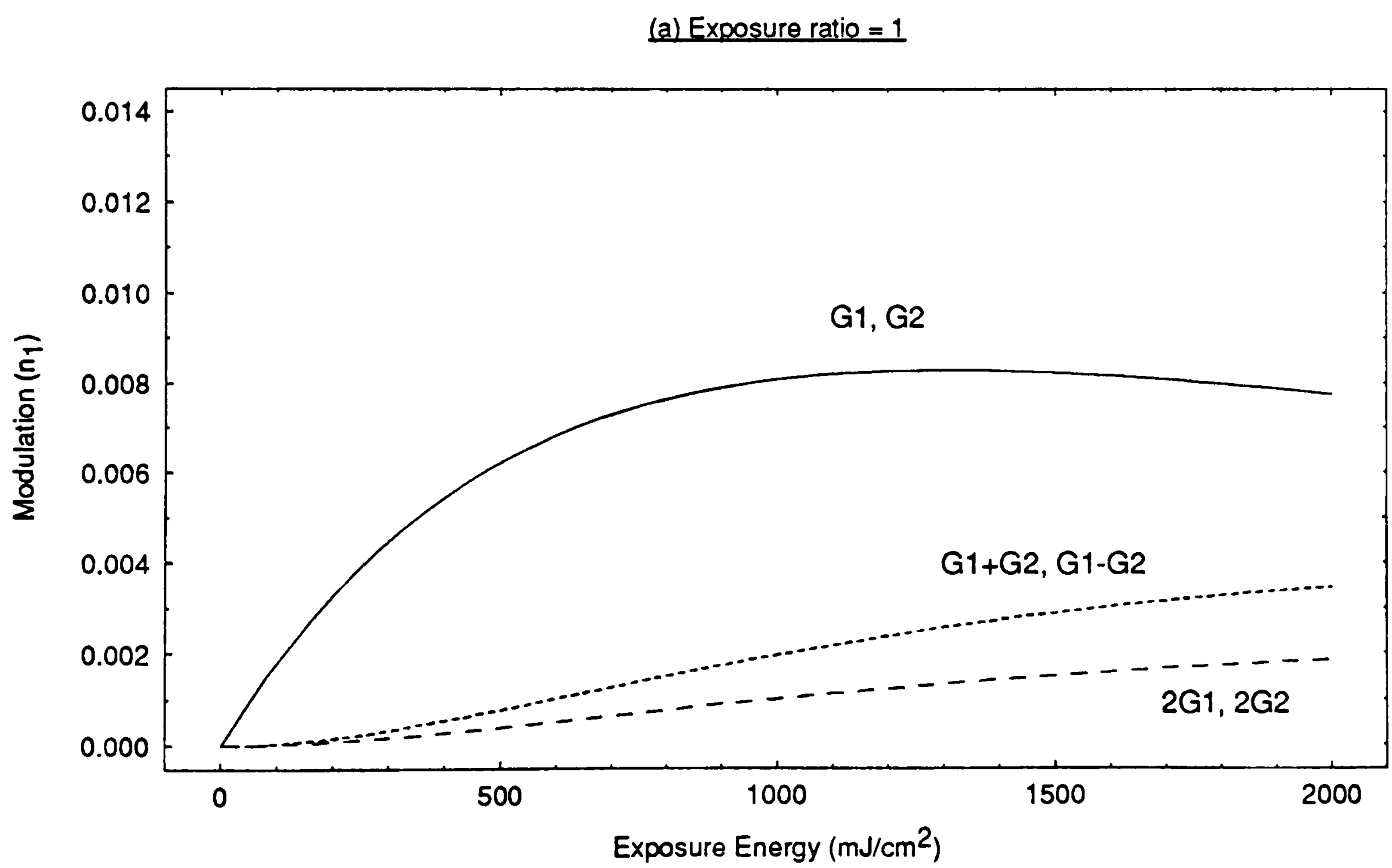


Figure 4.16 Theoretical variation of modulation versus exposure energy for a double grating illustrating the effect of varying the exposure ratio ($N_o = 0.04$, $E_o = 500$).

(b) Exposure ratio = 1.5

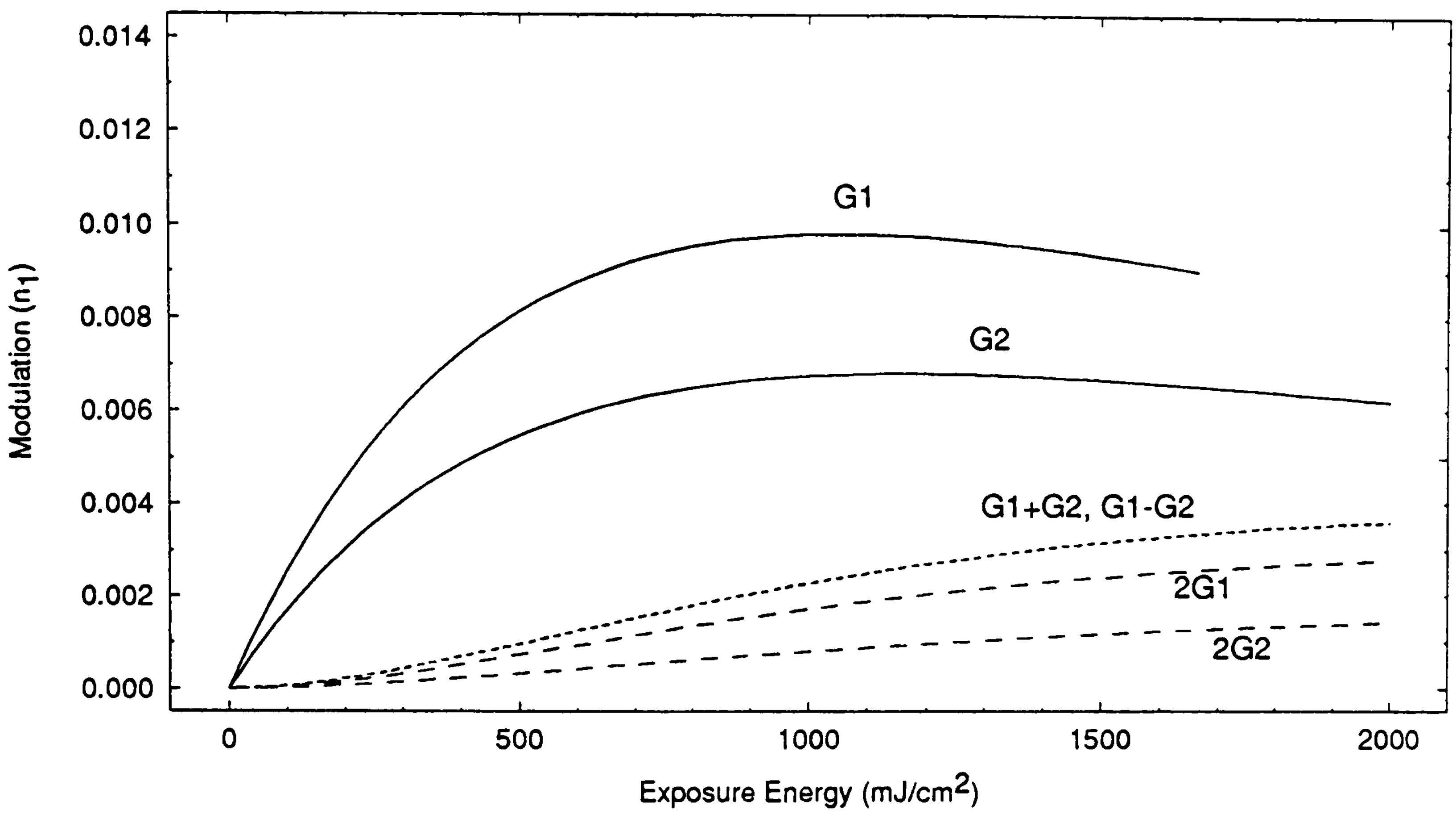


(c) Exposure ratio = 3

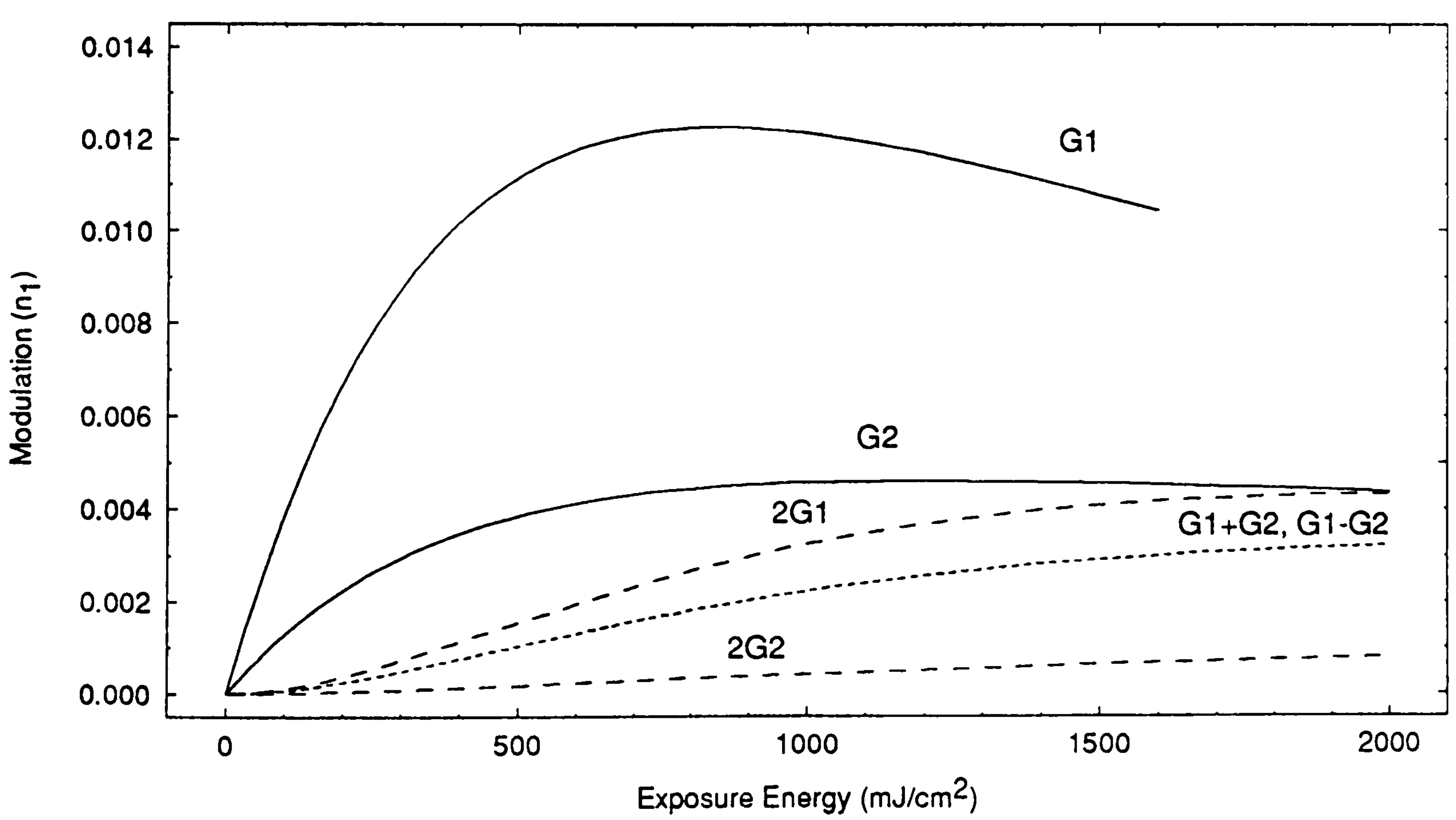


Figure 4.16 (Continued).

## 4.4 Comparison between experiment and theory

### 4.4.1 *Single exposure transmission gratings*

By measuring the experimental modulation values of plates of increasing exposure energy, we are able to fit the recording characteristic of DCG using the above model. Figure 4.17 shows results for both the fundamental and second harmonic of a set of single exposure transmission gratings. Experimental results are given by dots and the theoretical fit is shown by a solid line.

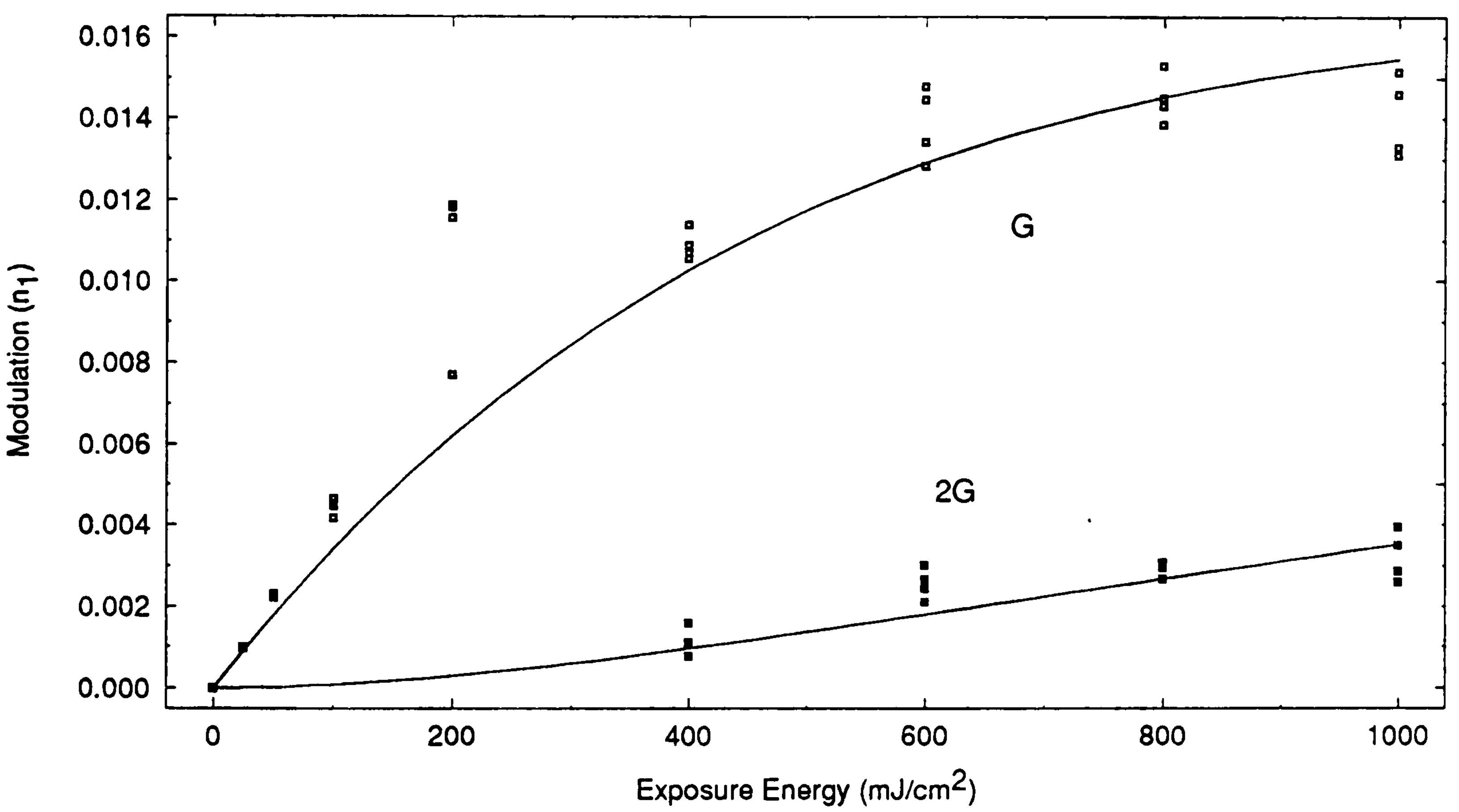


Figure 4.17 Plot of modulation versus exposure energy showing a theoretical match (solid line) of experimental data (dots) for the fundamental and second harmonic of a single grating.

We can see the strength of the fundamental grating initially increases linearly with exposure before starting to saturate at a level of $n_1$ = 0.016 and an exposure energy of 1000 mJ / cm$^2$. As the fundamental grating saturates the second harmonic steadily increases. A good fit was found for both G and 2G using the constants $N_o$ = 0.04 and $E_o$ = 1000.

Although results show good agreement it still has to be shown that we can neglect any contribution from multiple diffraction by the fundamental grating (as discussed by Alferness [Alf76]).

Alferness analysed propagation at the second-order Bragg angle of thick holographic gratings taking into account the replay of spatial harmonic gratings of the primary grating. He has shown that under certain circumstances double diffraction may be neglected. Following his reasoning for replay at the second order Bragg angle we can let:-

$$\gamma_1 = \frac{\pi n_1 d}{\lambda(\cos\theta_1 \cos\theta_o)^{\frac{1}{2}}} \tag{4.13}$$

$$\gamma_2 = \frac{\pi n_2 d}{\lambda \cos\theta_2} \tag{4.14}$$

and

$$\zeta = \frac{4\pi n_o d \sin^2\theta_o}{\lambda(1-\cos\theta_o)} \tag{4.15}$$

where d is the hologram thickness; $n_1$ is the modulation value and $\theta_1$ is the Bragg angle for the fundamental grating; $n_2$ is the modulation value and $\theta_2$ is the Bragg angle for the second harmonic; $\lambda$ is the replay wavelength; $n_o$ is the average refractive index; $\theta_o$ is the angle of incidence. $\gamma_1$ indicates the contribution to efficiency by double diffraction by the fundamental grating, whereas $\gamma_2$ tells us about the strength of the recorded spatial harmonic.

For the experiment, as a specific example, we can let $n_1 = 0.016$, $\theta_1 = 20°$, $n_2 = 0.004$, $\theta_2 = 38°$, $\lambda = 514.5$ nm and $n_o = 1.5$. Here we can see clearly that $\frac{\gamma_1}{\zeta} = 0.0144$ and $\frac{\gamma_2}{\zeta} = 0.004$ are both very much less than 1. This allows us to assume the following expression for diffraction efficiency at the second order Bragg condition. Again following Alferness [Alf76]:-

$$\eta_2 = \sin^2\left(\frac{\gamma_1^2}{2\zeta} - \gamma_2\right) \tag{4.16}$$

We can see that $\frac{\gamma_1^2}{2\zeta}$ is going to be very much less than $\gamma_2$ as $\zeta$ is increased, reducing the relative importance of double diffraction. Calculating the respective values using our parameters above we find that $\frac{\gamma_1^2}{2\zeta} = 0.02$.

By calculating efficiencies with and without neglecting the first term we obtain an error of approximately 4% which is well within experimental error. It is therefore concluded that for the present recording conditions it is relatively safe to assume that diffraction is solely from spatial harmonics.

4.4.2 *Double exposure transmission gratings*

Here we can observe the modelling of modulation versus exposure energy for double exposure transmission gratings. Figure 4.18 shows the results where the dots are experimentally measured values and the solid line is a theoretical fit. Once more we can see the fundamental gratings at both exposures saturate around 1000 mJ / $cm^2$ however, the maximum modulation value at saturation has dropped by half to about 0.008. As saturation occurs we see that the harmonics gain in strength. Gratings corresponding to the vectors $2\overline{K}_1$ and $2\overline{K}_2$ both reach the theoretical prediction of approximately 0.002, however the experimental values for $\overline{K}_1 + \overline{K}_2$ and $\overline{K}_1 - \overline{K}_2$ fall to slightly lower modulations than the theory predicts at higher energies. Again this is believed to be due to an additional contribution by the interaction of the fundamental gratings at the same frequencies and will be discussed in Chapter 6. To fit all six plots, the constants $N_o = 0.04$ and $E_o = 500$ were used.

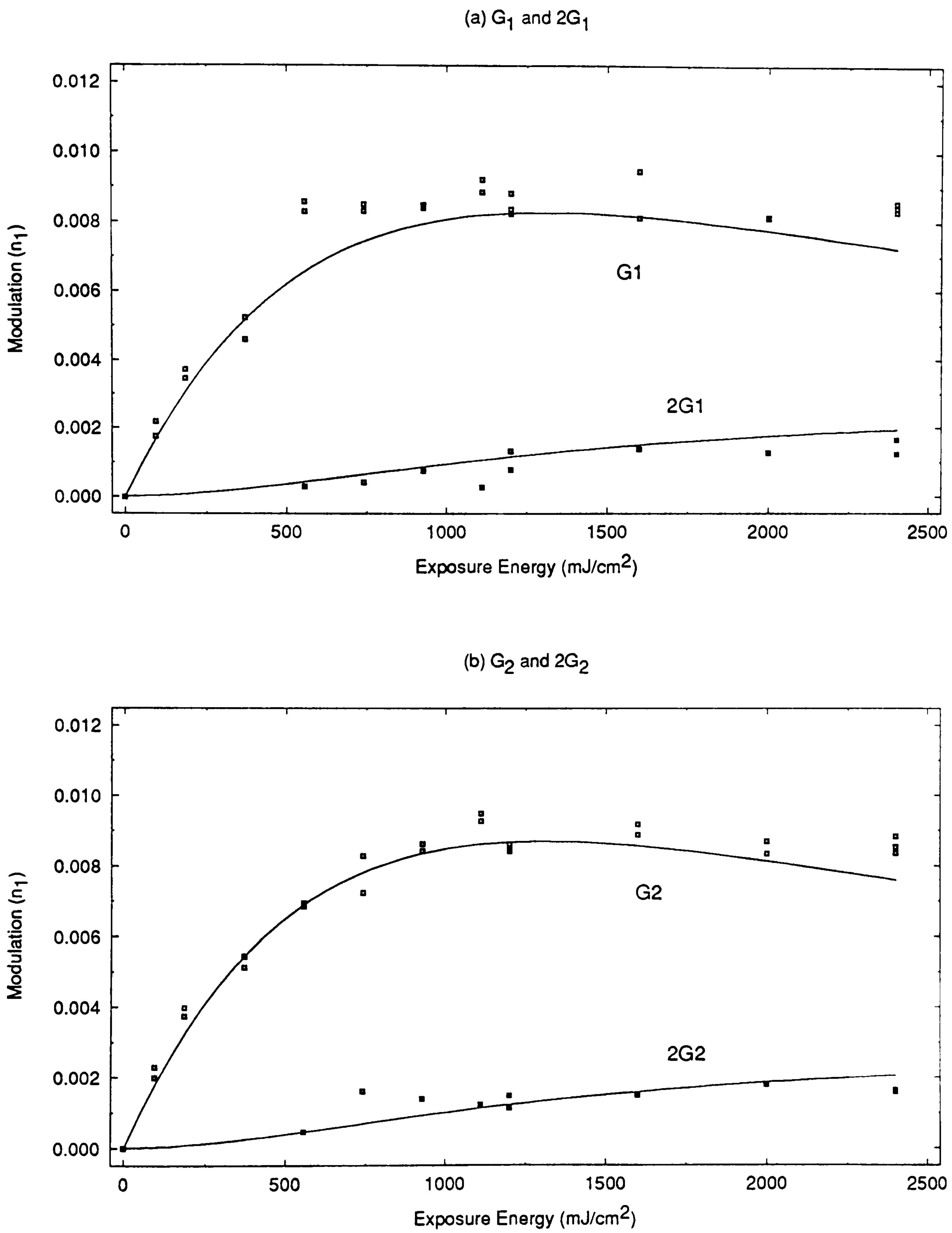


Figure 4.18 Plots of modulation versus exposure energy showing a theoretical match (solid line) of experimental data (dots) for a double exposure recording.

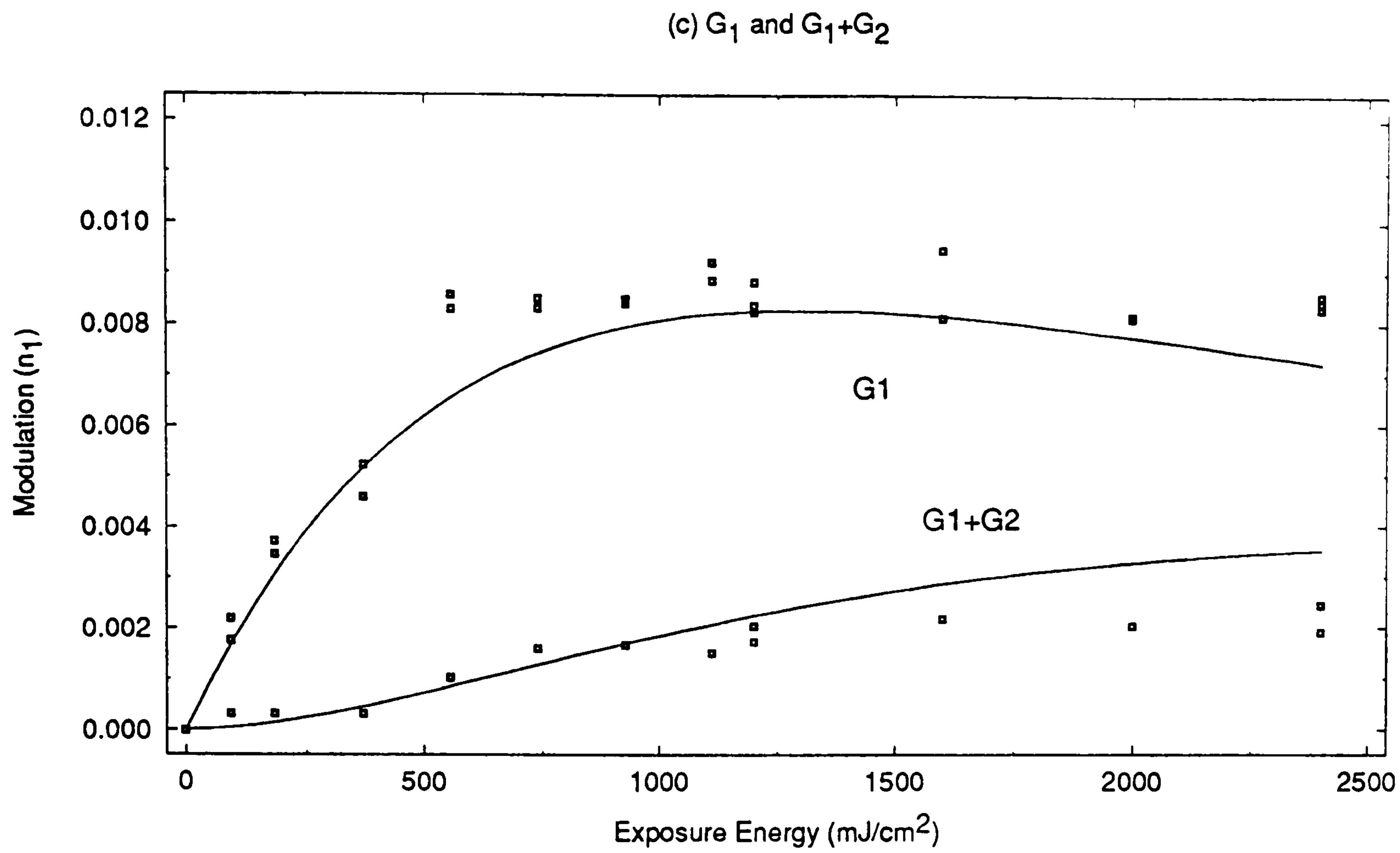


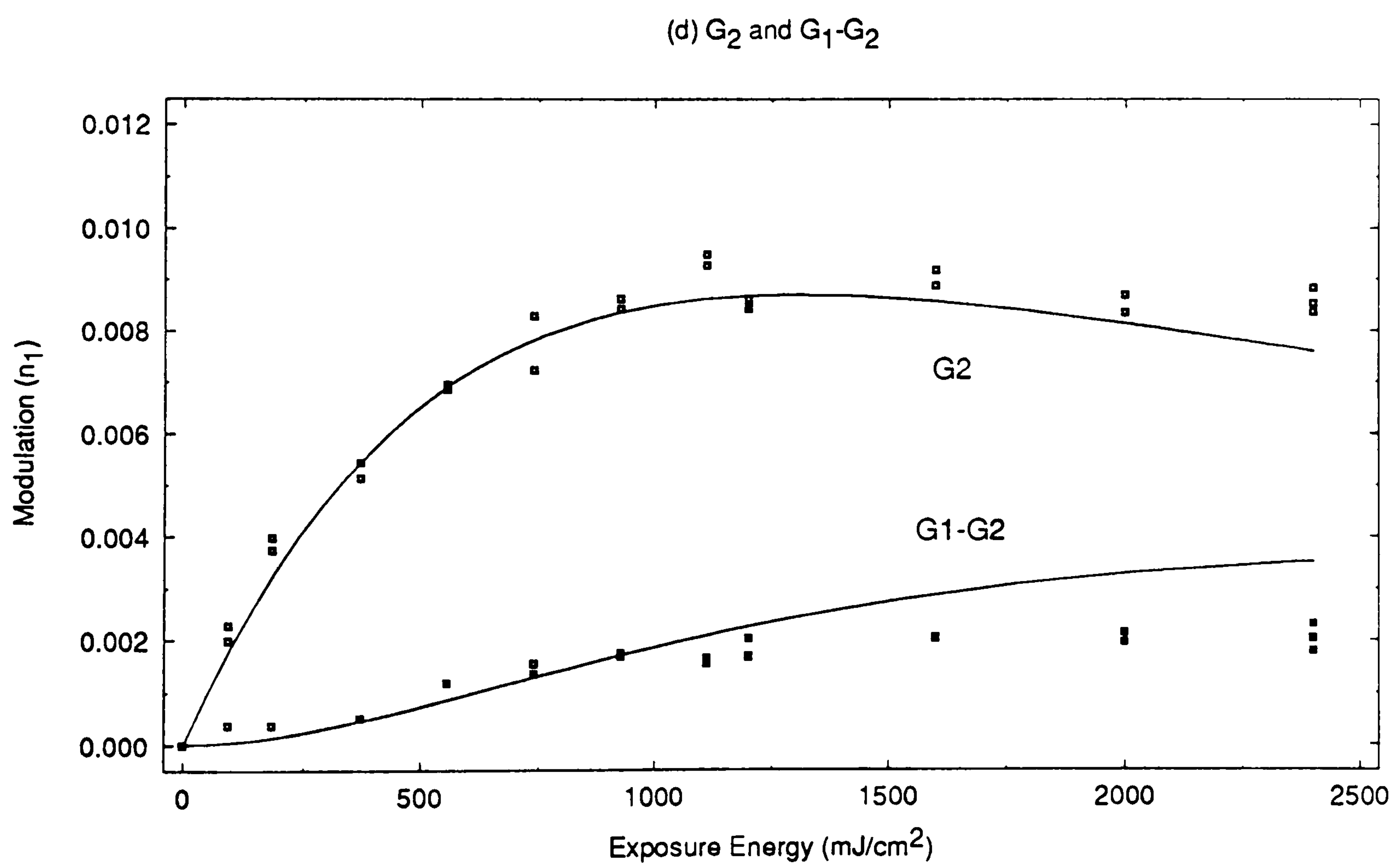


<u>Figure 4.18</u> (Continued).

It is interesting to compare the results from the single recording and the double recording experiments. We see that for both cases our indication of maximum available modulation $N_o$ remains constant at 0.04. However, our measure of sensitivity for double exposures, $E_o$ = 500, is half that for single exposures where $E_o$ = 1000, i.e. in the linear region we need to double the total exposure energy for the double hologram to obtain the same modulation as the single exposure case. But, because the first exposure has sufficiently hardened the material, the modulation value at saturation of $G_1$ and $G_2$ is half that of a single grating G.

## 4.5 Modulation profile of a single grating

The above theory may be used to form a Fourier synthesised modulation profile of a single grating to illustrate the effect of saturation upon the sinusoidal recording. Using the Fourier assumption that any periodic waveform may be described by the summation of orthogonal harmonic functions (i.e. pure sinusoidal waveforms) of varying amplitude and frequency, we are able to let the grating structure $n(\bar{r})$ take the form:-

$$n(\bar{r}) = n_o + n_1\cos(\bar{K}.\bar{r}) - n_2\cos(2\bar{K}.\bar{r}) + n_3\cos(3\bar{K}.\bar{r}) - n_4\cos(4\bar{K}.\bar{r}) \qquad (4.18)$$

Here we will only assume contributions from the first four spatial harmonics and let further terms be negligible in this calculation. The phase terms have been chosen to agree with the prediction from the previous model, ie. odd harmonics being positive and even harmonics negative. This agrees with Slinger's [Sli85b] assumption that at high exposures the expected profile would be that of a 'partially rectified sine wave'. He was then able to determine that the second and fourth harmonic terms would have a negative phase term in order to maintain the correct shape.

By using Equation (4.12) to calculate the relevant amplitudes we can sum the theoretical contributions from each spatial harmonic and form a profile of the recorded grating structure.

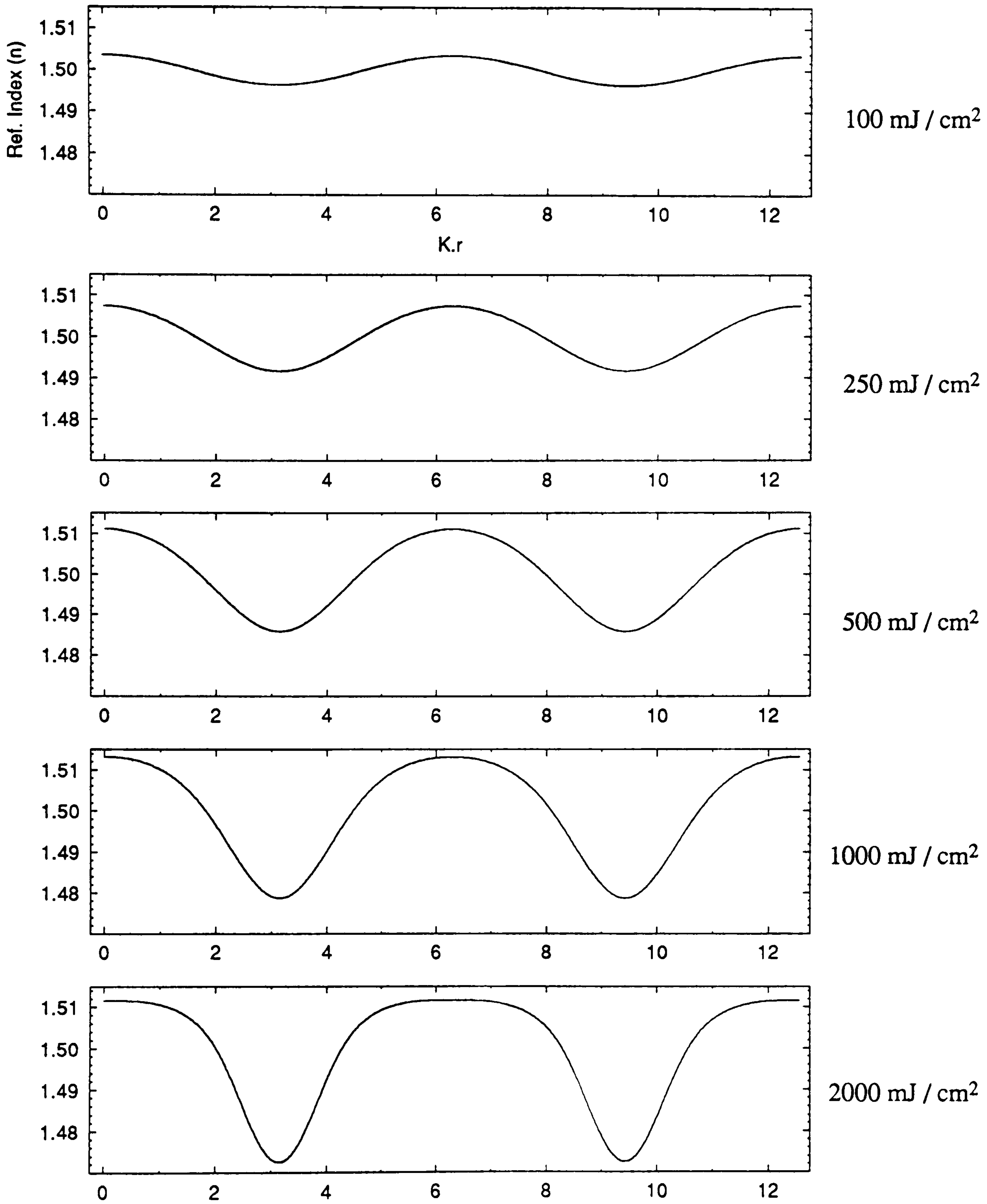


Figure 4.19 Modulation profiles (taking account of up to 4th harmonics) for increasing exposure energy where $N_o = 0.04$ and $E_o = 1000$.

Figure 4.19 shows some theoretical waveforms of refractive index variation for an increase in exposure energy assuming nonlinear recording. For these calculations the same conditions were used as for Figure 4.14(a); $N_o = 0.04$, $E_o = 1000$, the beam ratio is 1:1 and the average refractive index is assumed constant at 1.5 for simplicity. We can see a sinusoidal variation at low exposures but as energy is increased we observe the effect of saturation. The waveform starts to flatten out on top where the material has been unable to respond linearly to the high exposure levels. This allows us to explain why, in Figure 4.17 for example, the modulation value for G starts to fall at high exposures. The grating profile is becoming less sinusoidal in profile illustrating an increase in dependence on high frequency components of the Fourier spectrum.

The theory is also capable of showing the effect of an increase in beam ratio for a constant exposure level. Figure 4.20 shows theoretical plots for energies of 500 mJ / cm$^2$ and 2000 mJ / cm$^2$ respectively. Since the constants were again fixed at $N_o = 0.04$ and $E_o = 1000$ these represent recordings in the linear and nonlinear regions of the recording characteristic. At 500 mJ / cm$^2$ we can see that the shape of the recorded waveform remains sinusoidal throughout a range of beam ratios, however the amplitude falls as the beam ratio is increased. At the higher exposure we can see the shape of the grating tend towards a sinusoid as the beam ratio increases away from 1:1 illustrating that by increasing the beam ratio we can reduce spatial harmonic gratings at a cost of reducing modulation of the fundamental.

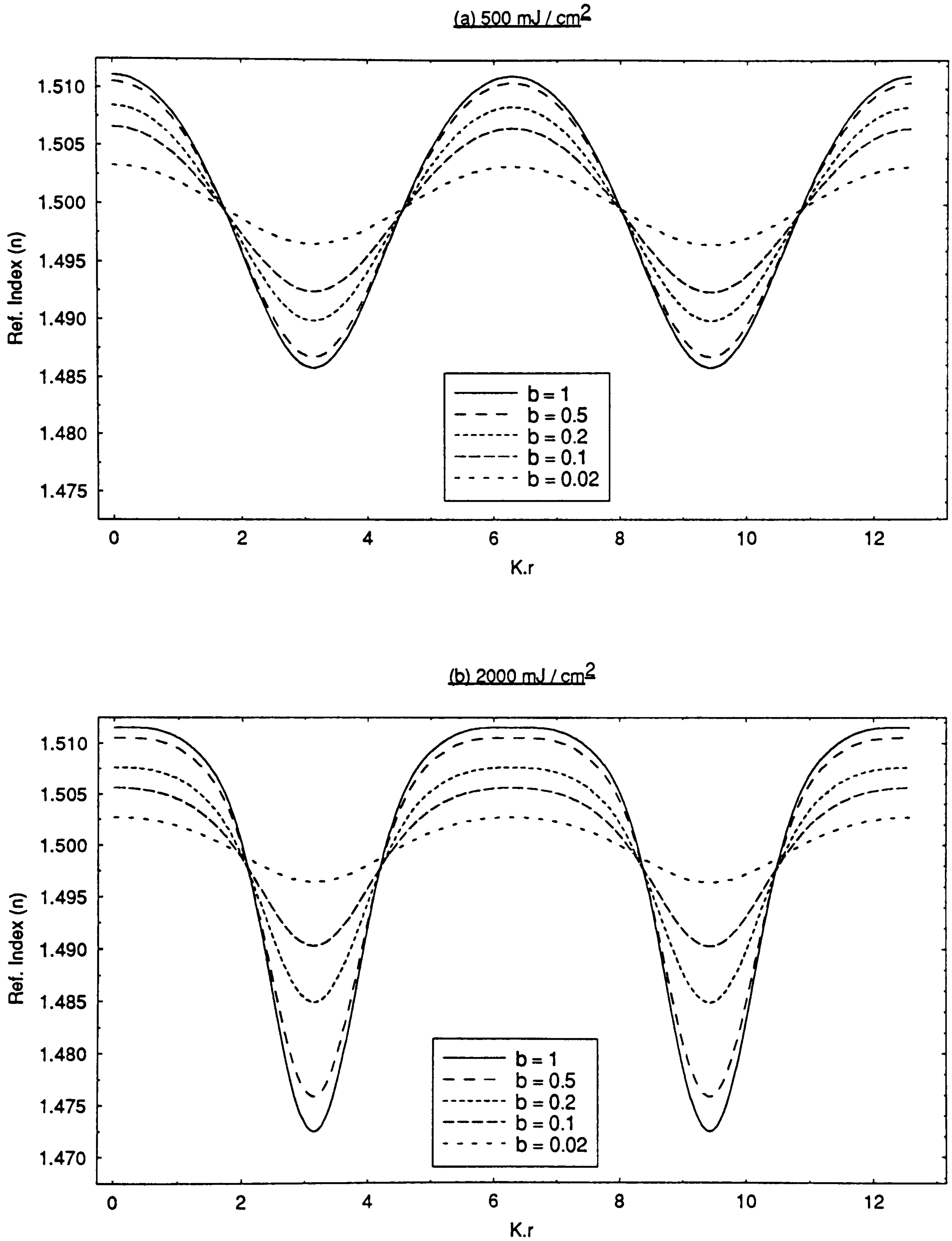


Figure 4.20 Theoretical plots showing the effect of the beam ratio on the modulation profile of (a) low and (b) high exposure energies where $N_o = 0.04$ and $E_o = 1000$.

## 4.6 Summary

In this chapter the effect of the nonlinear recording in dichromated gelatin has been considered for both single and double exposure transmission gratings. At low energy levels we obtained linear replay of the recorded interference pattern, however as the exposure level increased we observed the formation of additional Bragg dips corresponding to the diffraction of higher order grating structures due to saturation of the recording material. Refractive index measurements over a wide range of exposure energies were compared with a simple nonlinear model and good approximation was found for both cases. The model was used to predict the effect of varying recording parameters such as beam ratio and exposure ratio (for the double exposure case). It was also used to give us an indication of the modulation profile of a single recorded grating at low and high exposure levels.

# Chapter 5

# *The effect of beam ratio*

## 5.1 Introduction

The ratio of intensities of the recording waves plays an important role in holographic recording. It has been shown that brighter images with improved contrast may be reconstructed in silver halide emulsions by making the reference beam intensity larger than that of the object beam [Kas68] [Wya69]. However, Upatnieks and Leonard [Upa70] illustrated experimentally that there is a trade off between improved signal to noise ratio and diffraction efficiency as the beam ratio is increased. Syms [Sym89] thinks this may be due to the recording of noise gratings in silver halide emulsions. In 1973 Colburn *et al* [Col73] presented results of varying beam ratio in dichromated gelatin. They found that the maximum diffraction efficiency of planar gratings recorded over a range of exposure energies reduced as the beam ratio increased, however, for holograms formed with a diffuse object wave, they measured an increase in signal to noise ratio. Recently Chen [Che88] has studied theoretically the role of the beam ratio in both the simultaneous and sequential recording of multiple gratings. Ward and Solymar [War89] have used recordings of varying beam ratio to study the limitations on diffraction efficiency in silver halide emulsions.

In Chapter 3 we studied the formation of spurious gratings when recording simply a transmission grating in air. These were due to reflections at the plate / air boundaries. However, according to Fresnel's laws of reflection we know that, at the boundary, the reflected intensity will vary with the angle of incidence. Thus, any grating formed between the incident and reflected waves will have a beam ratio which is dependent on angle. Figure 5.1 shows how the beam ratio will vary with angle of incidence for the case of polarisation perpendicular to the plane of incidence. For this case we will assume that the refractive index of the glass substrate is equal to 1.515.

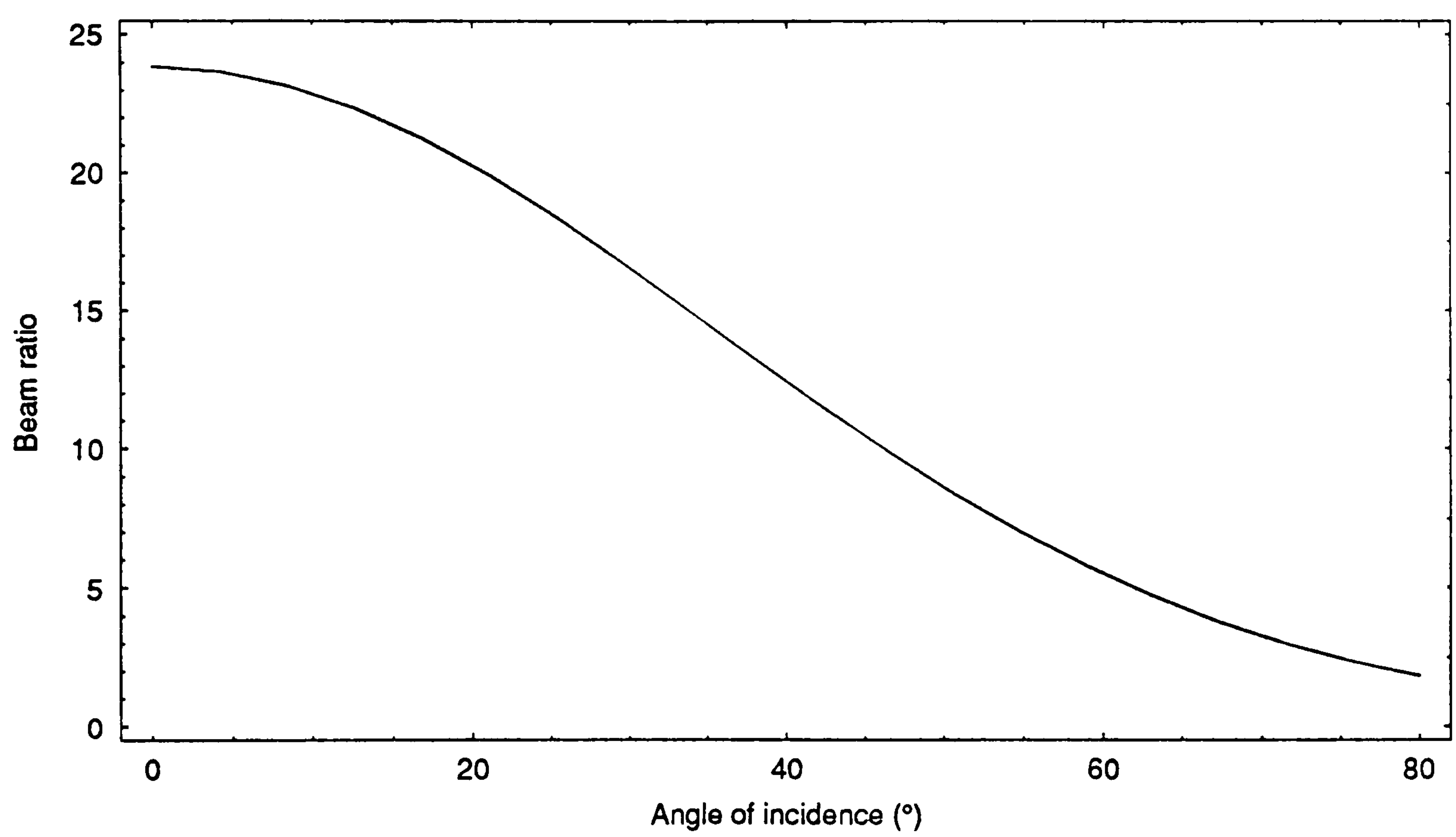


Figure 5.1 Variation of beam ratio as a function of the angle of incidence of a single beam reflected from an air / glass boundary.

When a sinusoidal grating is formed in an ideal photosensitive medium we can see from equation (1.8) that the intensity distribution will take the form :-

$$E(\bar{r}) = A_r^2 + A_s^2 + 2A_rA_s\cos(\bar{K}.\bar{r}) \tag{5.1}$$

where $E(\bar{r})$ is intensity, $A_r$ and $A_s$ are the amplitude of reference and signal waves respectively, $\overline{K}$ is the grating vector, and $\bar{r}$ is the position vector. We can define the beam ratio as $b = (A_r / A_s)^2$.

As $b$ increases, the value of $A_r A_s$ will drop with respect to the the bias term $A_r^2 + A_s^2$, reducing the modulation strength. If we assume a linear exposure characteristic (as in Chapter 3) we need only increase the exposure energy to obtain a preferred modulation. In Chapter 4, however, we saw that DCG has a saturating exposure characteristic. This means that we have a limited exposure range over which the material response is linear, thus limiting the maximum modulation value available.

In this short chapter, I will present some experimental observations for single reflection gratings recorded in dichromated gelatin (DCG) by reflecting a single incident beam from the back surface at different angles of incidence. From these results we will be able to observe how the 'spurious' gratings seen in Chapter 3 vary with recording angle. These experiments are carried out for different levels of sensitisation concentration.

In addition, I will present experimental results of refractive index modulation versus exposure energy for both transmission and reflection gratings recorded in an index matching tank for different beam ratios. These will be compared to the nonlinear theory outlined in Chapter 4, which we found capable of predicting the variation of modulation with energy.

## 5.2 Experiments

### 5.2.1 *Varying the angle of incidence*

3 sets of DCG plates were sensitised with 2%, 5% and 10% concentrations of ammonium dichromate and exposed using an energy of 700 mJ / cm$^2$. Recordings of unslanted reflection gratings were made with a single beam in air using the setup shown in Figure 5.2.

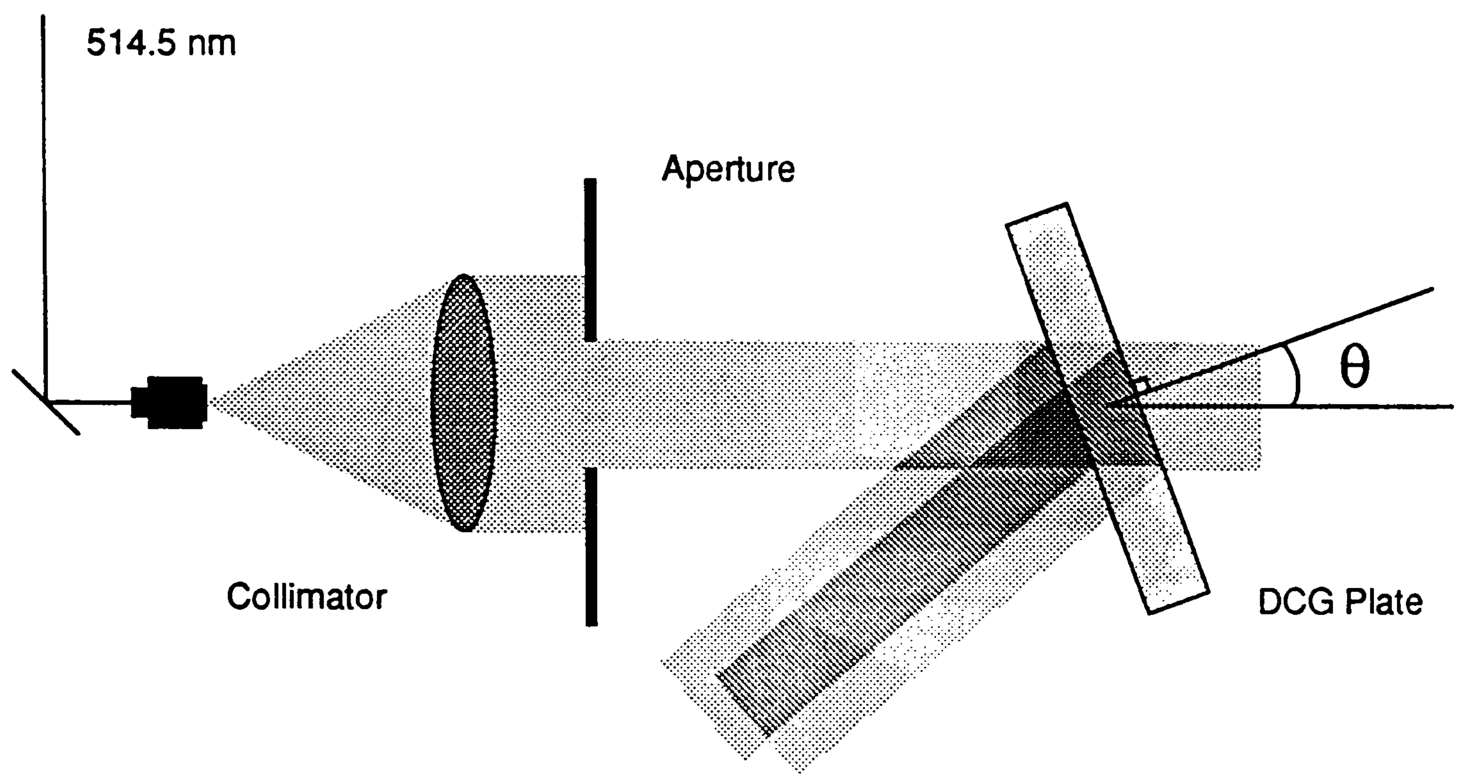


Figure 5.2 Recording geometry for single beam, variable beam ratio experiments.

The incident beam was collimated and polarised perpendicular to the plane of incidence. The DCG plates were exposed at angles of 0°, 20°, 40° and 60° in air corresponding to 0°, 12.5°, 24° and 33.5° within the gelatin. These values are approximate since the refractive index of sensitised gelatin has been found to vary with sensitiser concentration [New87]. Referring to Figure 5.1 we can see that the chosen angles correspond to recording gratings with beam ratios of approximately 25:1, 20:1, 12:1 and 5:1 respectively within the gelatin. The exposure level was maintained at 700 mJ / $cm^2$ at the different recording angles by varying the incident energy to comply with Fresnel's laws. The plates were all processed using the standard procedure outlined in Chapter 1 and coverplated using 2 mm thick glass. The gratings were analysed using the spectrometer apparatus shown in Chapter 1.

Figure 5.3 shows spectral scans of transmittance versus replay wavelength for each set of gratings. Each scan was performed at the recording angle for each specific grating, taking account of replay within an index matching tank. The results were the normalised against the system with the plate removed.

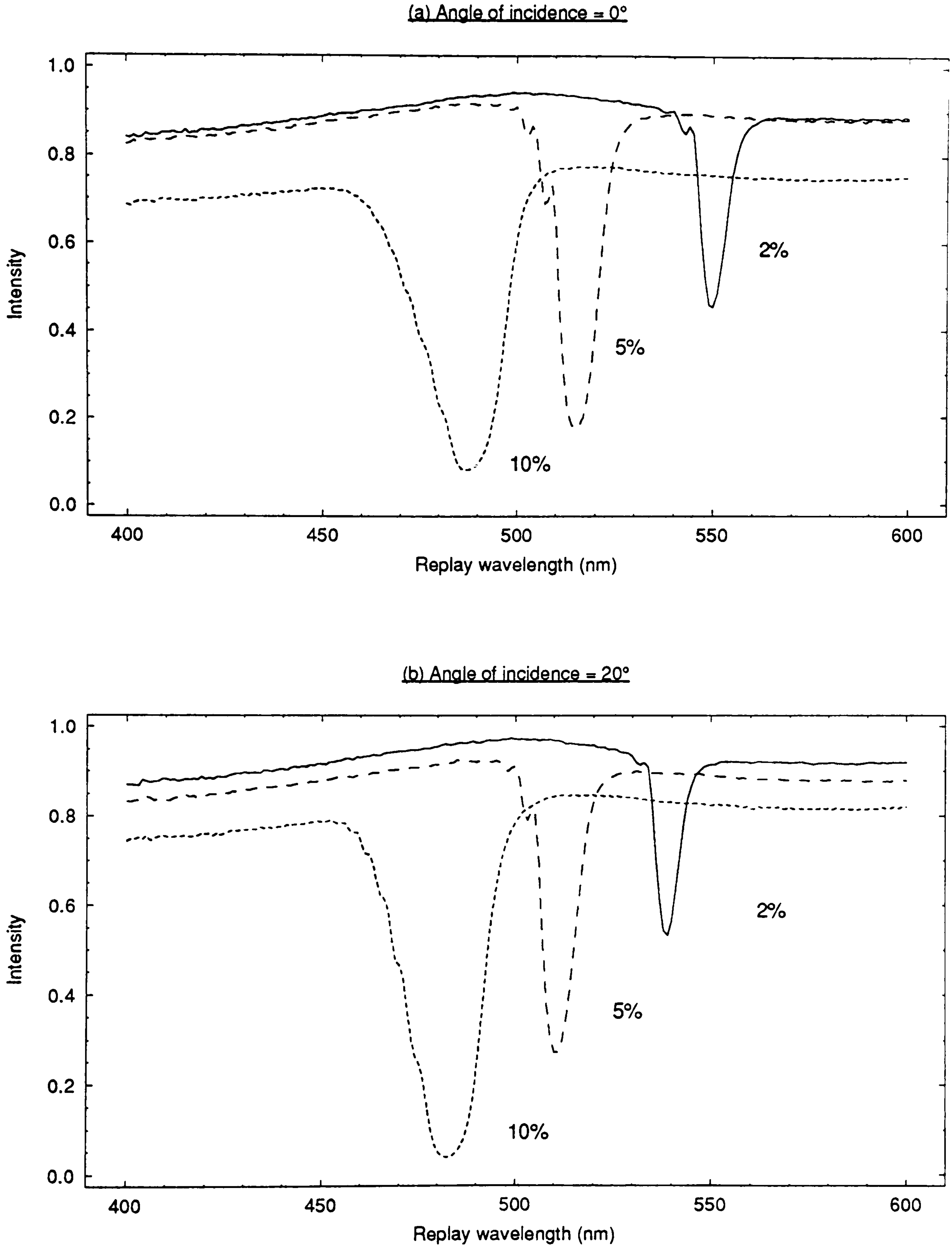


Figure 5.3 Spectral transmittance scans for gratings recorded at (a) 0° and (b) 20° using sensitisations of 2%, 5% and 10% ammonium dichromate. Each grating was replayed at its own recording angle.

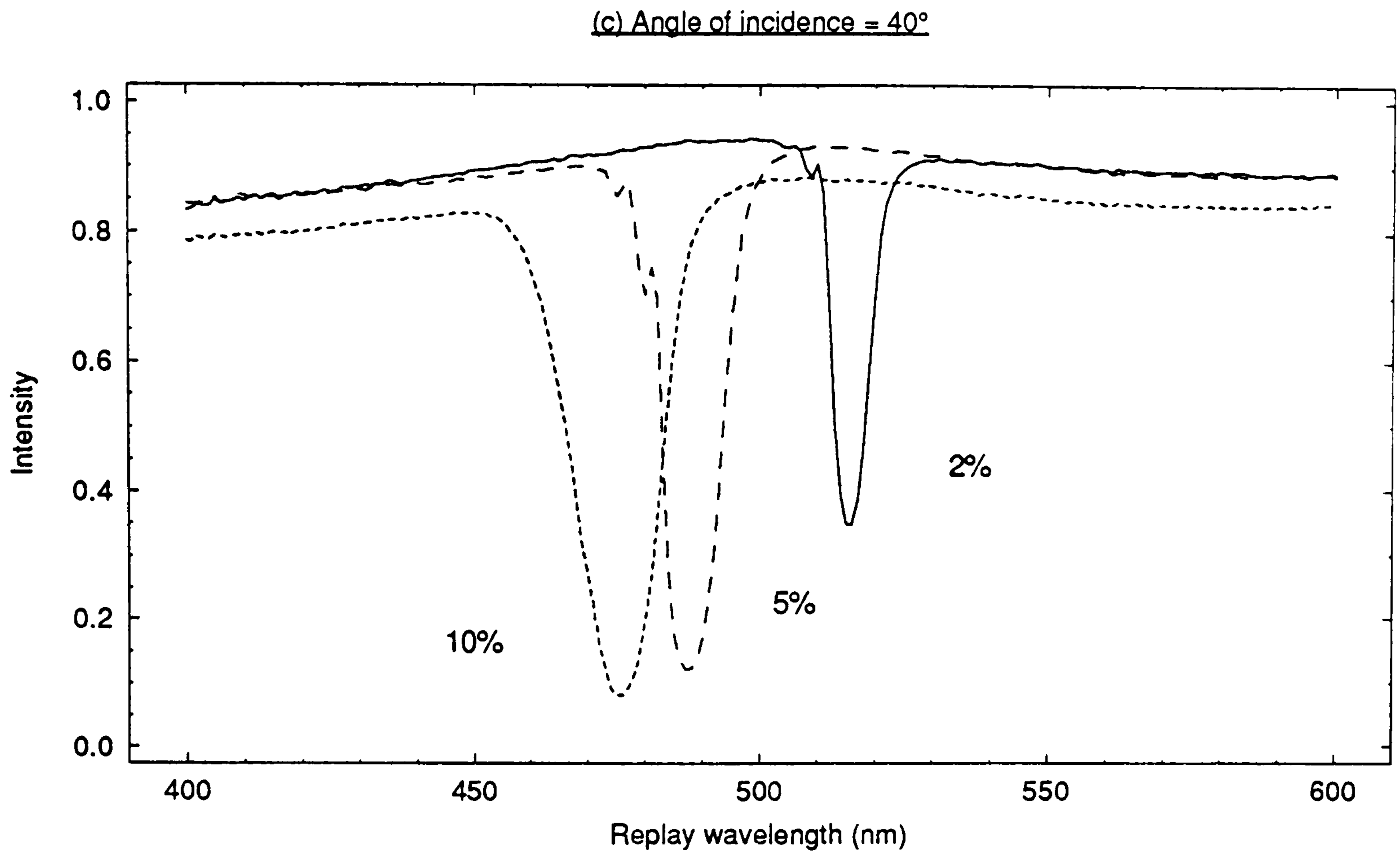


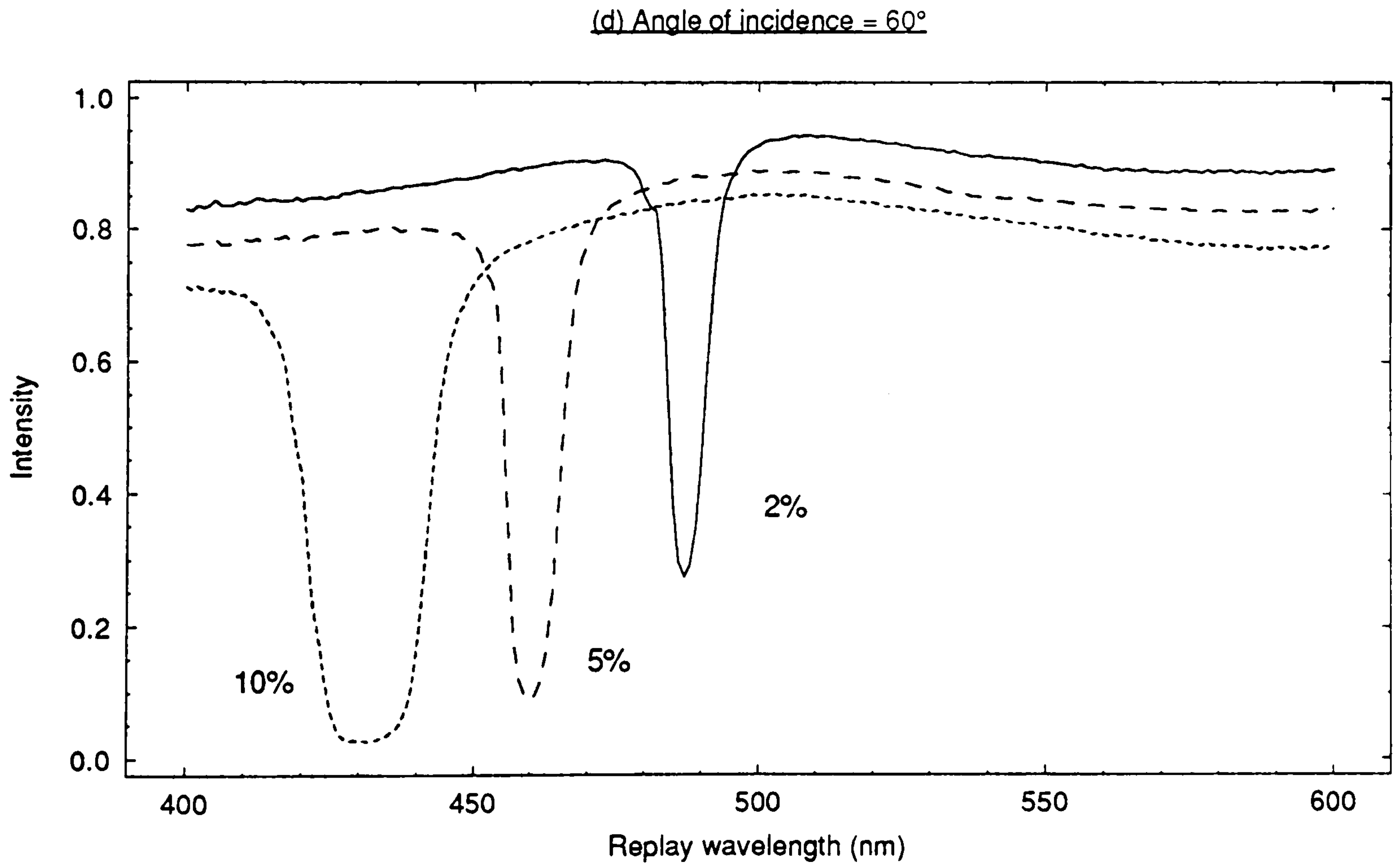


Figure 5.3 Spectral transmittance scans for gratings recorded at (c) 40° and (d) 60° using sensitisations of 2%, 5% and 10% ammonium dichromate. Each grating was replayed at its own recording angle.

For each recording we are therefore able to extract information regarding the efficiency and change in dimension of the recorded reflection gratings.

For all recording angles we can observe several similar trends. We notice that as the sensitiser concentration is increased for each recording angle, the Bragg dip is seen to increase in strength. This is partly due to the fact that at high sensitisations we are replaying at lower wavelengths therefore coupling is greater. However, it is also due to the fact that plates of higher sensitivity are capable of recording higher modulation values before saturation occurs. Therefore, even at 0° where the beam ratio is 25:1, we are able to observe a large efficiency value around 75%. We notice that as the recording angle increases to 60° the 2% dips saturate with a peak efficiency around 55%, however the 10% case approaches 90% illustrating an ability to record high modulation strengths.

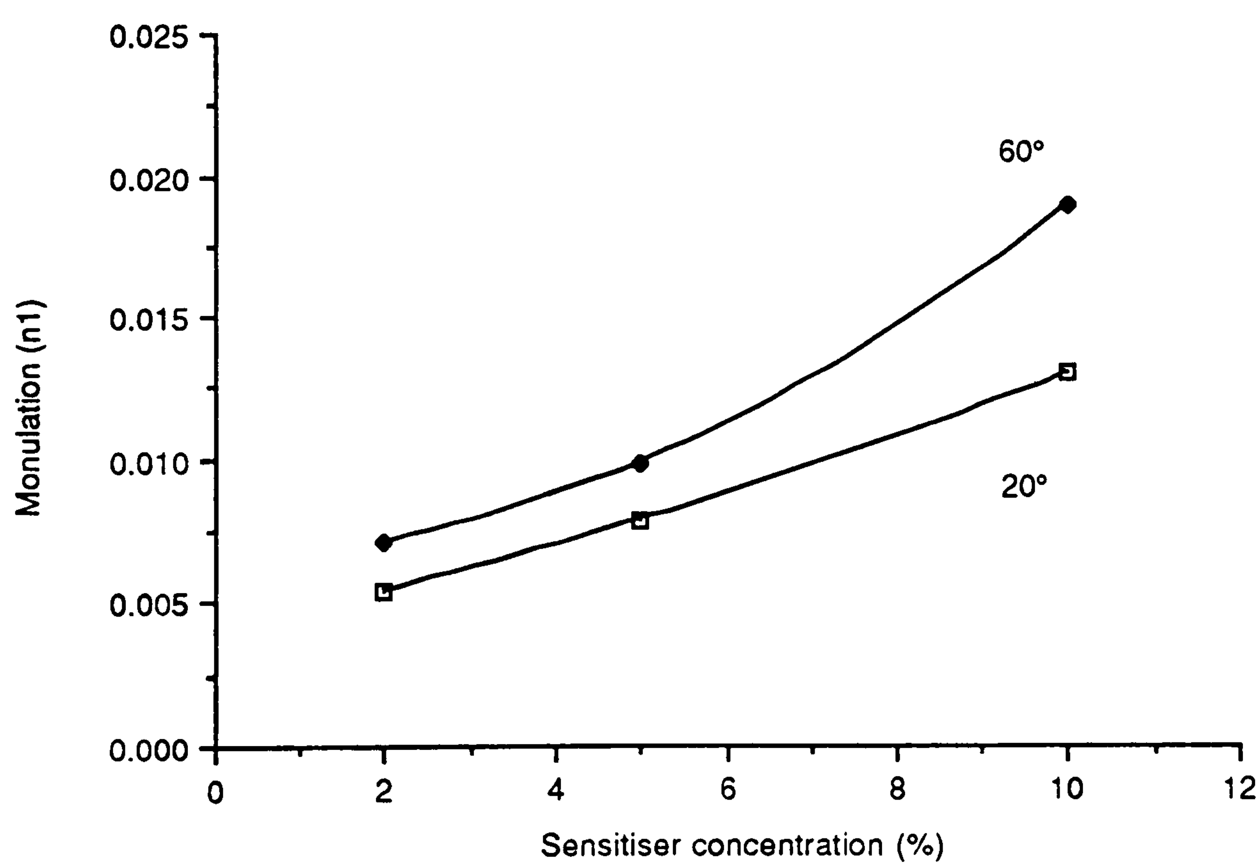


Figure 5.4 Plot of modulation ($n_1$) versus sensitiser concentration (%) for different recording angles at a constant exposure energy of 700 mJ / cm$^2$.

The modulation values for each Bragg dip were calculated by curve fitting with a simple coupled wave model similar to that described in Appendix I. Figure 5.4 shows how the modulation[1] varies with sensitiser concentration for the two recording angles 20° and 60° (which correspond to beam ratios of 20:1 and 5:1 respectively). The trend is for the modulation to increase with sensitiser concentration. However, for any specific sensitisation, we see the modulation fall with increasing beam ratio.

### 5.2.2 *Varying the total exposure energy*

The following section describes a second set of experiments designed to observe the effect of the beam ratio upon modulation for an increasing exposure energy. Both reflection and transmission gratings were recorded in an index matching tank at beam ratios of 1:1, 10:1 and 50:1. The recording geometries for each case are shown in Figures 5.5 (a) and (b).

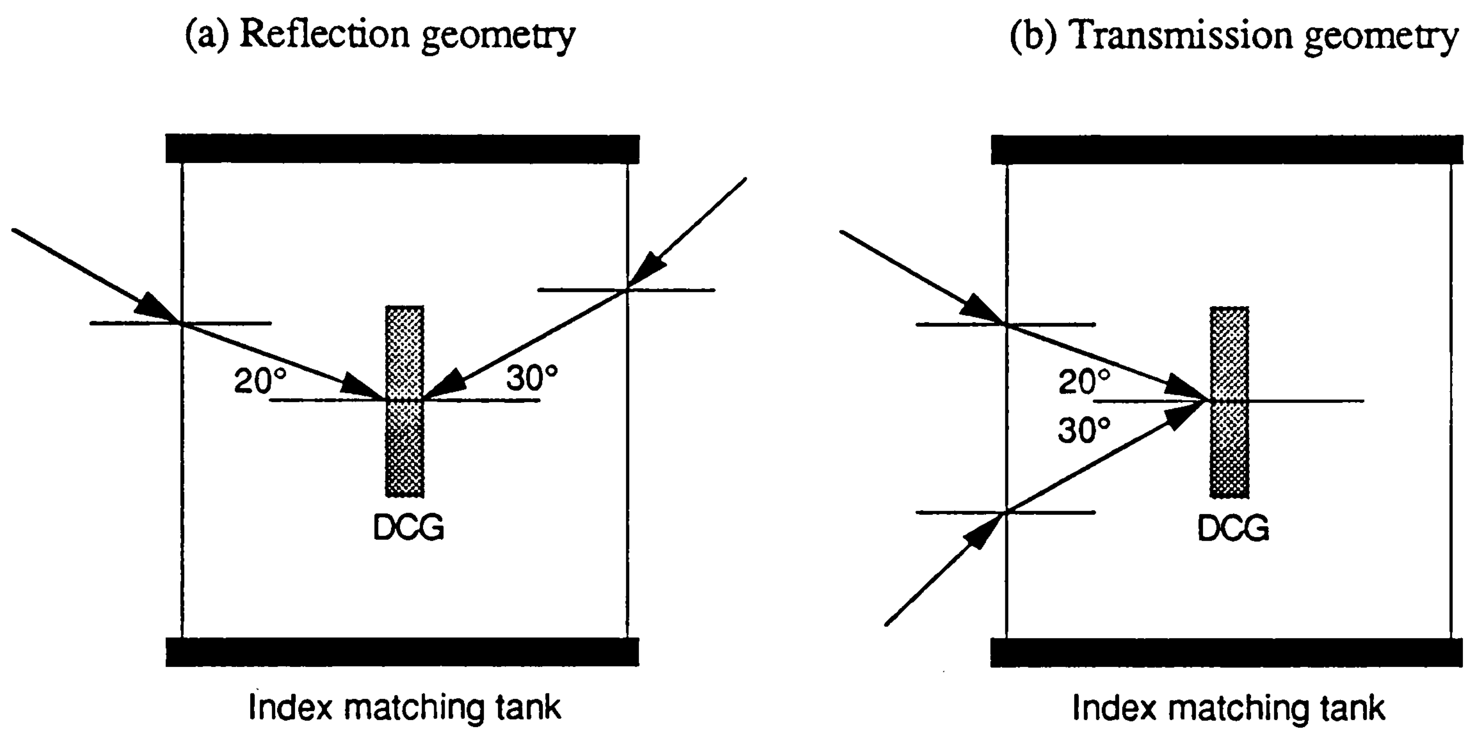


Figure 5.5 Recording geometries for beam ratio experiments in an index matching tank for (a) reflection and (b) transmission geometries.

The index matching liquid used was Xylene with a refractive index of approximately 1.497. The recording angles were +30°, -20° for the transmission geometry and +30°, +160° for the reflection case. For each beam ratio a series of exposure energies were used, taking account

[1] It must be noted that these modulation values have been derived using a uniform coupled wave model. However, a great deal of nonuniformities exist which make accurate modelling difficult, particularly at high exposure levels. Therefore, these results are presented only to show the general trend.

of specular reflections from the tank / air boundary using Fresnel reflection coefficients. For each beam ratio the total exposure energy was kept constant. Altogether, eighty four holograms were recorded and tested.

Figure 5.6 shows experimental plots (dots) of modulation versus total exposure energy for (a) reflection and (b) transmission geometries for the different beam ratios. Good theoretical (solid line) agreement is found for both geometries using the constants $N_o$ = 0.023, $E_o$ = 1000 for the reflection and $N_o$ = 0.04, $E_o$ = 1000 for transmission gratings. In the reflection case a maximum modulation value of 0.009 is found compared with 0.015 for the transmission geometry. It was expected that the $N_o$ value for the reflection holograms would be the same as that for the transmission case. This was not the case. Perhaps this is due to instabilities when recording the high frequency reflection gratings, particularly at high energies where long exposure times were necessary. This would cause additional blurring of the fringes and an effective drop in modulation.

Nevertheless, in each case we see that, as the beam ratio is increased, the modulation value at saturation drops. This is because increasing the beam ratio also causes a reduction in fringe contrast and therefore an increase in the bias exposure level. As this bias level increases, the DCG will increase in bias hardness which reduces the final refractive index modulation. An increase in modulation may be achieved, at higher beam ratios, by reducing the initial hardness of the gelatin and thus compensating for the expected increase.

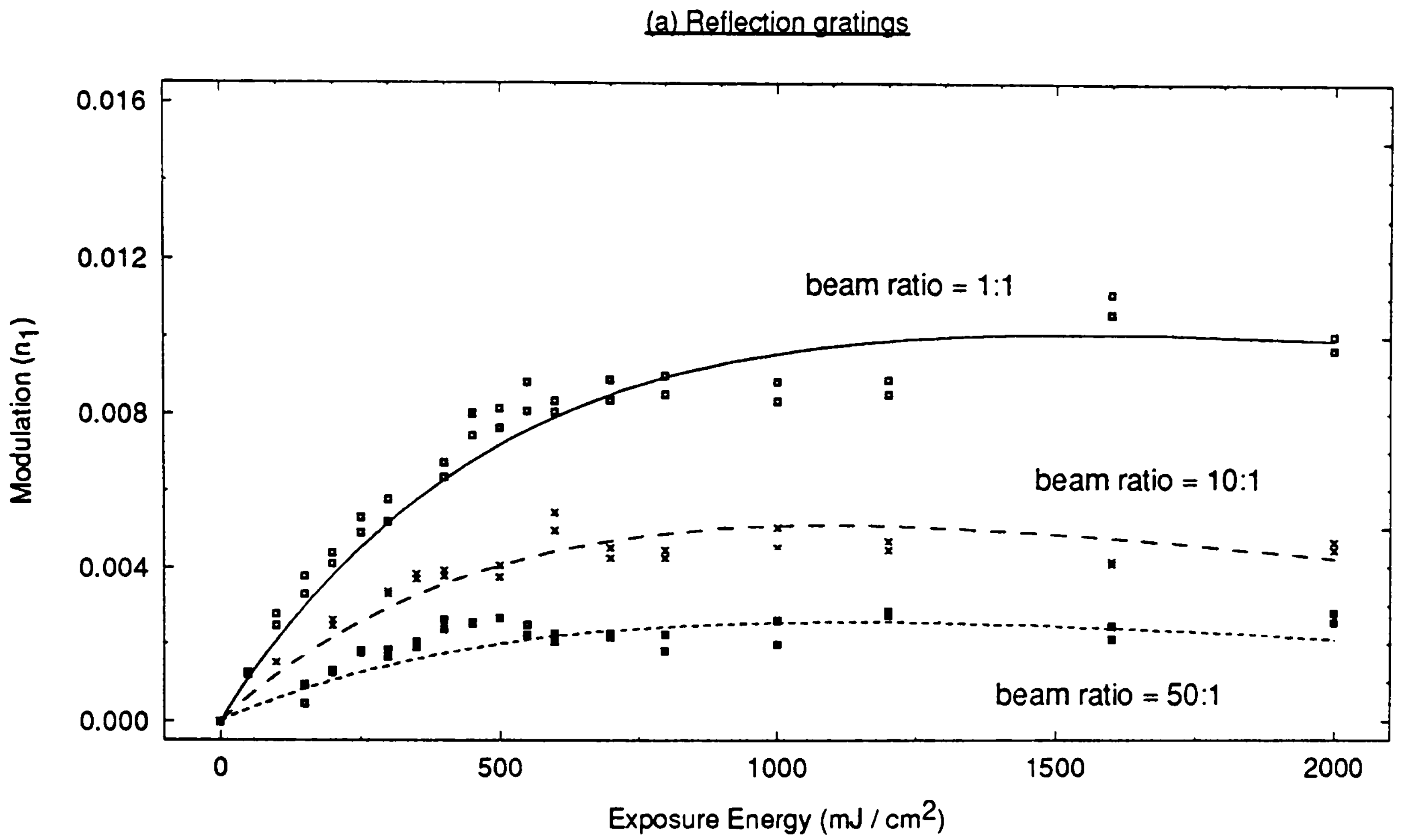


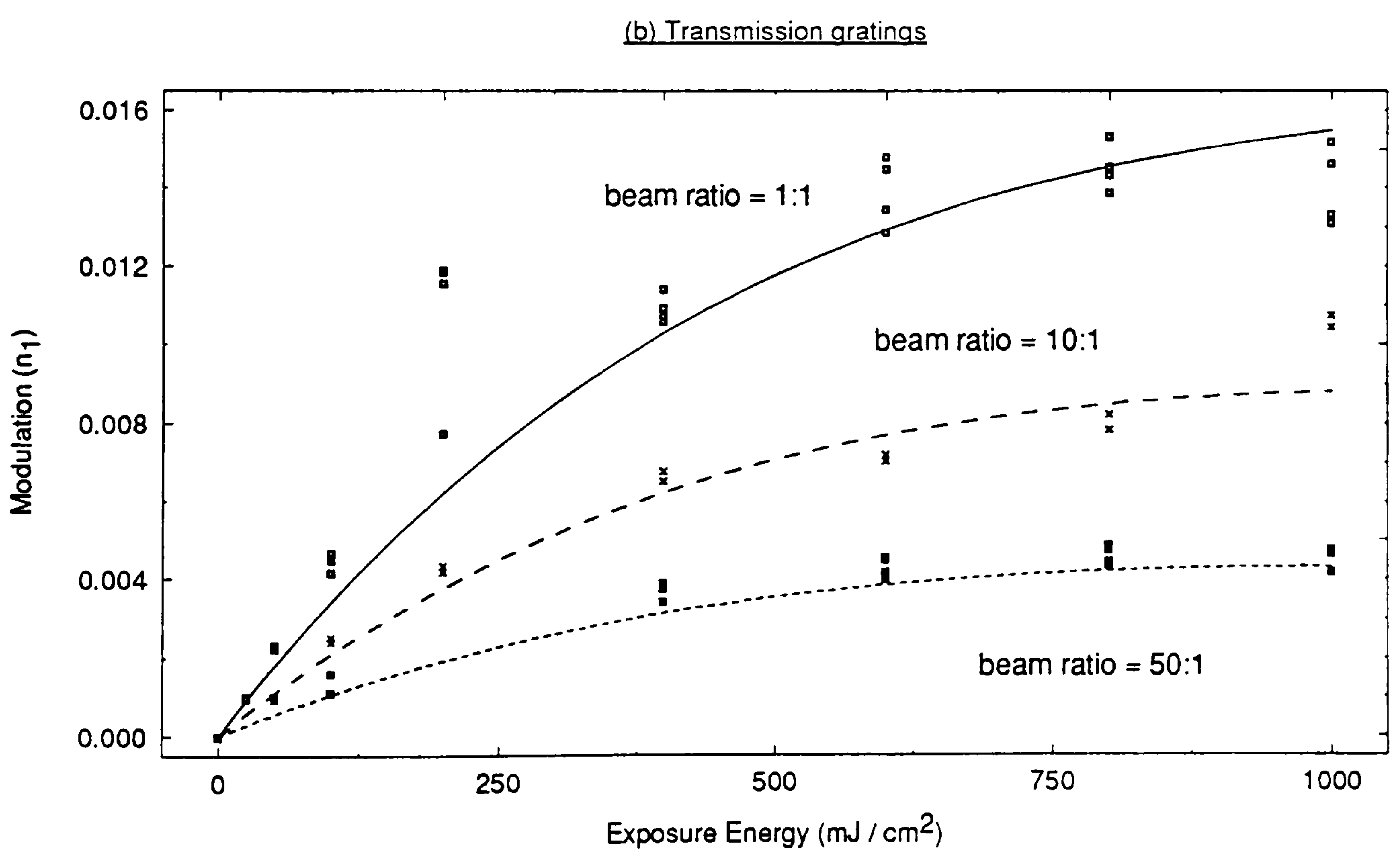


Figure 5.6 Experimental (dots) and theoretical (solid line) plots of refractive index modulation versus total exposure energy for (a) reflection ($N_o$ = 0.023, $E_o$ = 1000) and (b) transmission ($N_o$ = 0.04, $E_o$ = 1000) geometries.

## 5.3 Summary

In this chapter I have presented results of transmission and reflection gratings recorded with varying beam ratios. In the first case we observed that gratings formed by reflecting a single incident beam from the plate / air boundary are capable of high modulation strengths, particularly when working with high sensitiser concentrations. We found that, for a specific sensitiser concentration, the modulation strength of the recorded gratings would drop as the angle of incidence decreased and the beam ratio increased. In the second case, we found that experimental results of modulation versus exposure energy verified the results of the non linear theory presented in Chapter 4. The modulation values for both transmission and reflection gratings were seen to saturate with increasing exposure energy. As the beam ratio was increased, the maximum modulation achieved at saturation reduced.

# Chapter 6

# Double exposure recording in nonlinear dichromated gelatin

## 6.1 Introduction

In Chapter 4 we saw how it is possible to form spatial harmonic gratings in dichromated gelatin (DCG) due to a nonlinear recording characteristic. In particular, for the case of double exposure transmission gratings, we saw the formation of gratings corresponding to the vectors $\overline{K}_1 - \overline{K}_2$ , $\overline{K}_1 + \overline{K}_2$ , $2\overline{K}_1$ and $2\overline{K}_2$ . In that study we made the assumption that diffraction was due solely to the independent replay of nonlinear gratings. This simple assumption led mostly to accurate modelling of the experimental data. However, in the case of $\overline{K}_1 - \overline{K}_2$ some discrepancies were found. At high exposure levels the measured modulation ($n_1$) was found to be lower than theoretically predicted. Also, the variation of $n_1$ with wavelength did not follow the same trend as all the other gratings. We therefore require a more complex model to be able to deal with this situation.

As discussed previously in Chapter 3, many authors have studied the recording of multiple gratings. In addition to these publications relevant work has been carried out by Lewis *et al* [Lew83] and Slinger *et al* [Sli86] who looked at the formation of spurious waves due to multiple grating interactions. Alferness [Alf76] has studied the replay conditions at the second order Bragg angle of a single, volume transmission grating. In his study he takes account of both the recorded spatial harmonic grating and second order diffraction of the primary grating at replay. Tsukada *et al* [Tsu79] have studied theoretically the effect of relative phase upon the output power where both two and three gratings have been recorded. Recently, much attention has been paid to the area of multiple optical interconnects [Goo84]. These depend on the ability of a material to store a number of sequentially or simultaneously recorded transmission or reflection components. For transmission devices it is therefore important to take account of both material nonlinearities and grating interactions when studying their replay.

In this chapter I will describe a coupled wave theory which is capable of modelling the angular transmittance scans shown in Chapter 4 for double exposure transmission gratings. It will take account of the nonlinear recording characteristic of dichromated gelatin by assuming the existence of gratings $G_1$ and $G_2$, and a third recorded grating $G_3$, equal to the difference of the fundamentals. Also, as in the study by Alferness, it will take account of multiple diffraction grating interactions as well.

It will be shown that under certain conditions both effects must be considered. The effect of relative phase shift as predicted by the model in Chapter 4 is investigated. Results are presented for varying exposure energies where recording angles can be considered sufficiently separated in order to reduce grating interactions. Later, angles are recorded closer together to encourage double diffraction. Finally, an attempt is made to explain the apparent rise in modulation value against wavelength for the replay of $G_3$.

## 6.2 Theory

### 6.2.1 *Introduction*

Let us assume the sequential recording of two unslanted transmission gratings in dichromated gelatin, as shown in Figure 6.1. In this diagram A and B represent plane, collimated beams. A1 and A2 record grating number 1 at the angles $\pm\theta_1$ and B1 and B2 record grating number 2 at the angles $\pm\theta_2$.

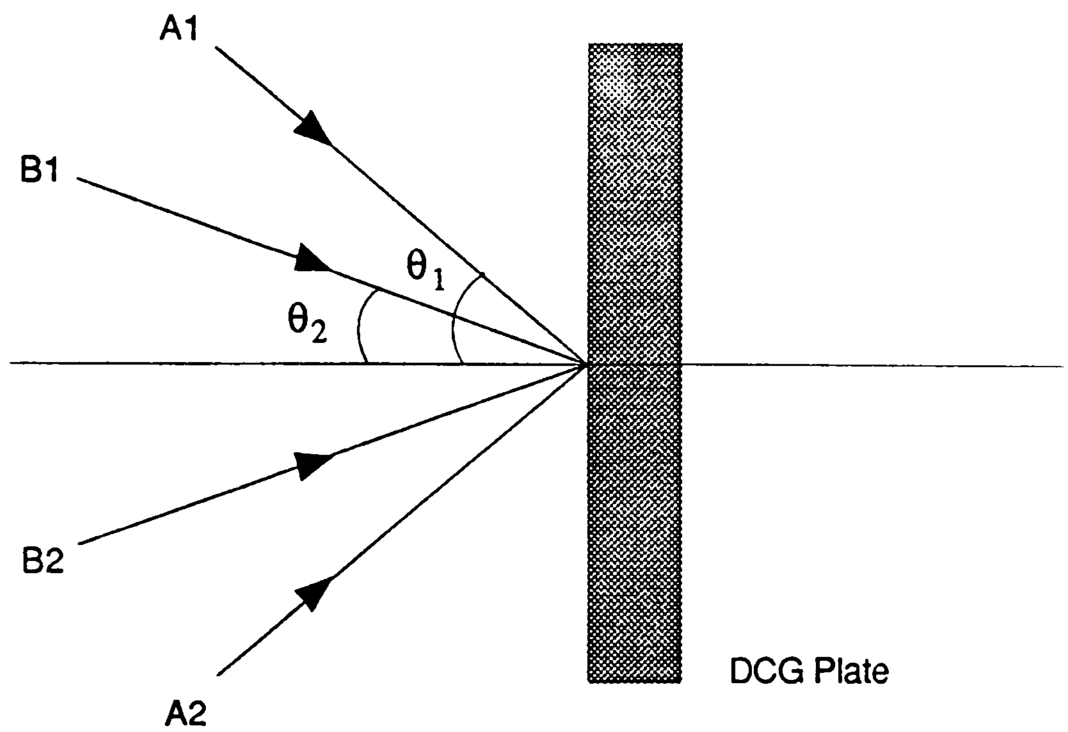


Figure 6.1 Recording geometry for double exposure transmission gratings

We will also assume that the material is nonlinear (i.e. saturates with increasing exposure energy) and therefore we must allow for the possible existence of spatial harmonic gratings. To simplify this however, we will only allow the additional recording of the difference grating $G_3$ corresponding to the vector relation $\overline{K}_1 - \overline{K}_2$ and restrict ourselves to replay within the angular range which allows on - Bragg replay for all three gratings. This is the same as assuming only $n, m < 2$ in equation (4.11) and replaying the gratings with spatial frequencies to the left of line A in Figure 4.13. We must note that other gratings with values of n, m > 1 also replay within this angular range. In order to simplify an already complex situation, these were neglected on the assumption that their modulation strengths are negligible compared with the fundamental values. However, the condition $2\overline{K}_2 - \overline{K}_1$ may be significant at low wavelengths. Therefore this assumption will undoubtedly lead to a small error in the final solution.

The recording angles for the grating corresponding to the vector $\overline{K}_1 - \overline{K}_2$ may be calculated using simple geometry as:-

$$\sin\theta_3 = \sin\theta_1 - \sin\theta_2 \tag{6.1}$$

For simplicity, we will assume that the recording material is thick enough to neglect effects from higher diffraction orders. However, the model will be complicated because it includes multiple interactions between the different gratings. Figure 6.2 shows these interactions and the waves that are considered.

In Figure 6.2, $\bar{\sigma}_o$ represents the wave vector of the $0^{th}$ order replay wave at an angle $\theta_o = 0°$. Figures (a), (b), and (c) illustrate the effect of simple $\pm 1^{st}$ order diffraction by gratings $G_1$, $G_2$ and $G_3$ respectively. Grating $G_1$ scatters light from $\bar{\sigma}_o$ to waves $\bar{\sigma}_1$ and $\bar{\sigma}_2$ with amplitudes A1 and A2, grating $G_2$ scatters light from $\bar{\sigma}_o$ to waves $\bar{\sigma}_3$ and $\bar{\sigma}_4$ with amplitudes A3 and A4, and similarly $G_3$ scatters light from $\bar{\sigma}_o$ to waves $\bar{\sigma}_5$ and $\bar{\sigma}_6$ with amplitudes A5 and A6. Figures (d), (e), (g) and (h) show the replay of interactions between gratings $G_1$ and $G_2$. In (d) the wave $\bar{\sigma}_5$ is coupled to $\bar{\sigma}_1$ through $G_2$ which in turn is coupled to $\bar{\sigma}_o$ through $G_1$. This represents the interaction via the grating vectors $\bar{K}_1$ up then $\bar{K}_2$ down. Diagram (e) shows the opposite of this where the grating vector $\bar{K}_1$ is replayed first downwards then $\bar{K}_2$ is replayed up the way, i.e. $\bar{\sigma}_6$ is coupled to $\bar{\sigma}_2$ through $G_2$ which in turn is coupled to $\bar{\sigma}_o$ through $G_1$. Similarly, $\bar{\sigma}_6$ and $\bar{\sigma}_5$ also have contributions from the interactions where the vector $\bar{K}_2$ is replayed first followed by $\bar{K}_1$ , as shown in diagrams (g) and (h). Interactions between the fundamental gratings $G_1$ and $G_2$ and the nonlinear grating $G_3$ are shown in diagrams (f) and (i). In (h) waves $\bar{\sigma}_7$ and $\bar{\sigma}_3$ are replayed by the interactions of grating vectors $+(\bar{K}_1 \pm \bar{K}_3)$ respectively and waves $\bar{\sigma}_4$ and $\bar{\sigma}_8$ are replayed by the interactions of grating vectors $-(\bar{K}_1 \pm \bar{K}_3)$ . The situation is similar for $G_2$ shown in diagram (i). Waves $\bar{\sigma}_1$ and $\bar{\sigma}_9$ are replayed by the interactions of the gratings with the vector relations $+(\bar{K}_2 \pm \bar{K}_3)$ , and waves $\bar{\sigma}_{10}$ and $\bar{\sigma}_2$ are replayed by the interactions $-(\bar{K}_2 \pm \bar{K}_3)$ . All these diagrams are shown using '$\beta$-valued' geometry. For this condition the modulus of each wave is equal to the propagation constant $\beta$ and the off - Bragg parameters $\psi_i$ are perpendicular to the surface of the hologram, thus conserving the wave component parallel to the hologram surface. The magnitude of this vector controls the strength of replay away from the Bragg condition.

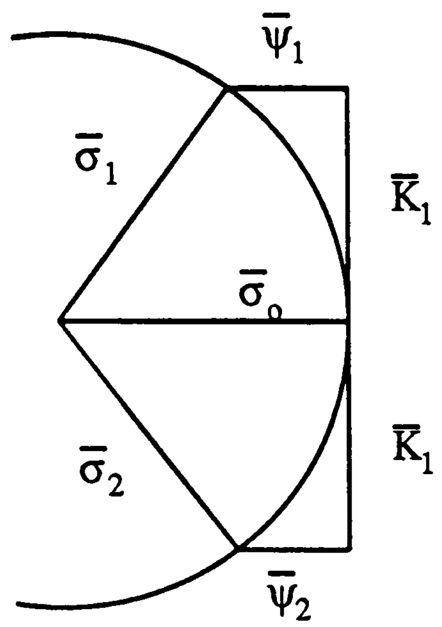


(a) $\overline{\sigma}_0 + \overline{K}_1 = \overline{\sigma}_1 + \overline{\psi}_1$

$\overline{\sigma}_0 - \overline{K}_1 = \overline{\sigma}_2 + \overline{\psi}_2$

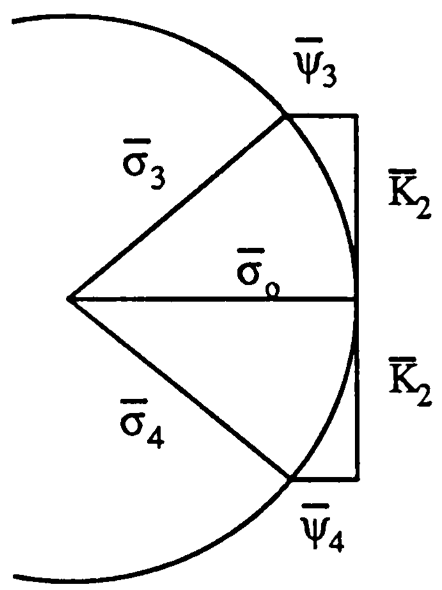


(b) $\overline{\sigma}_0 + \overline{K}_2 = \overline{\sigma}_3 + \overline{\psi}_3$

$\overline{\sigma}_0 - \overline{K}_2 = \overline{\sigma}_4 + \overline{\psi}_4$

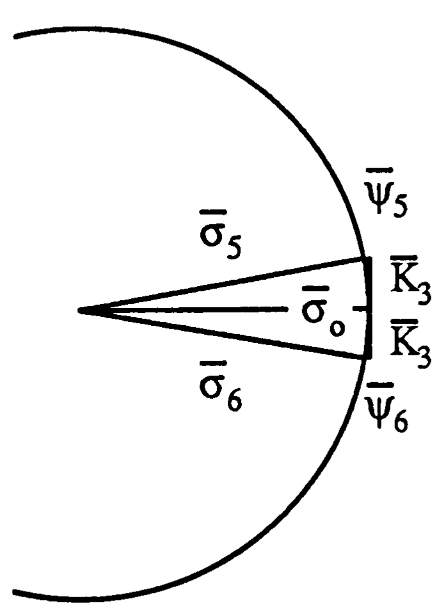


(c) $\overline{\sigma}_0 + \overline{K}_3 = \overline{\sigma}_5 + \overline{\psi}_5$

$\overline{\sigma}_0 - \overline{K}_3 = \overline{\sigma}_6 + \overline{\psi}_6$

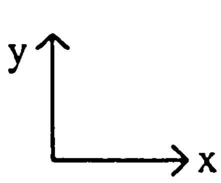


Figure 6.2 Replay waves assumed in theoretical model.

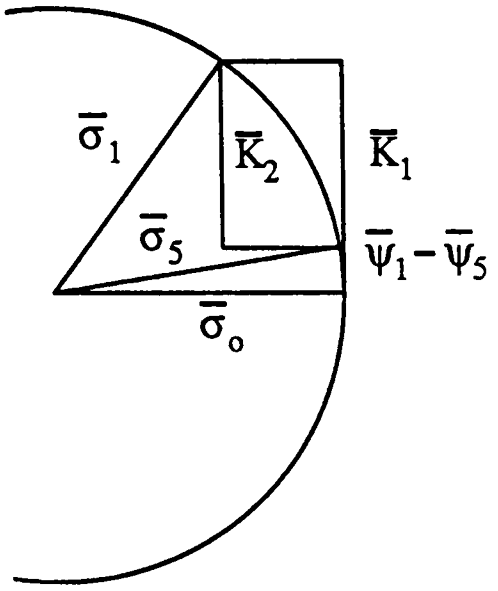


(d) $\bar{\sigma}_1 - \bar{K}_2 = \bar{\sigma}_5 - (\bar{\psi}_1 - \bar{\psi}_5)$

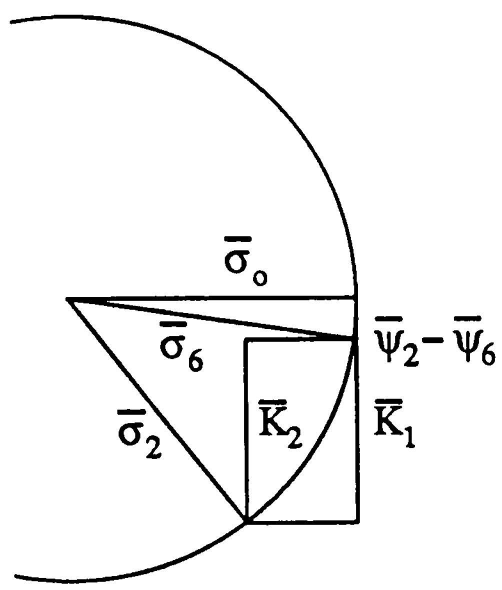


(e) $\bar{\sigma}_2 + \bar{K}_2 = \bar{\sigma}_6 - (\bar{\psi}_2 - \bar{\psi}_6)$

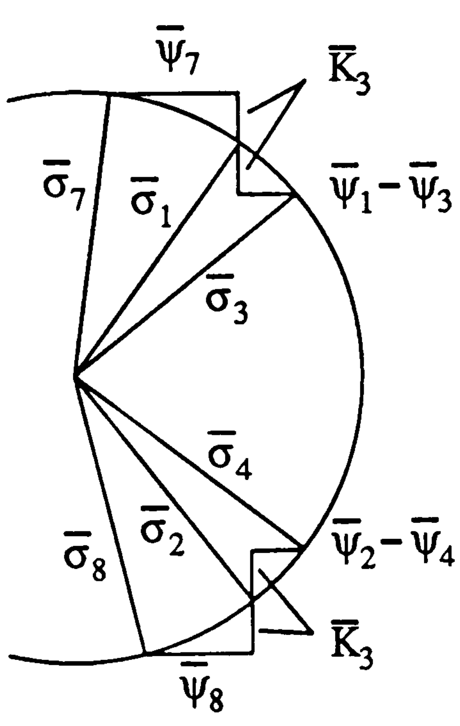


(f) $\bar{\sigma}_1 + \bar{K}_3 = \bar{\sigma}_7 + \bar{\psi}_7$

$$\bar{\sigma}_1 - \bar{K}_3 = \bar{\sigma}_3 - (\bar{\psi}_1 - \bar{\psi}_3)$$

$$\bar{\sigma}_2 + \bar{K}_3 = \bar{\sigma}_4 - (\bar{\psi}_2 - \bar{\psi}_4)$$

$$\bar{\sigma}_2 - \bar{K}_3 = \bar{\sigma}_8 + \bar{\psi}_8$$

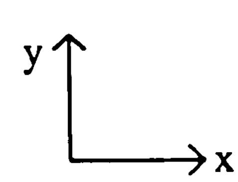


Figure 6.2 (continued).

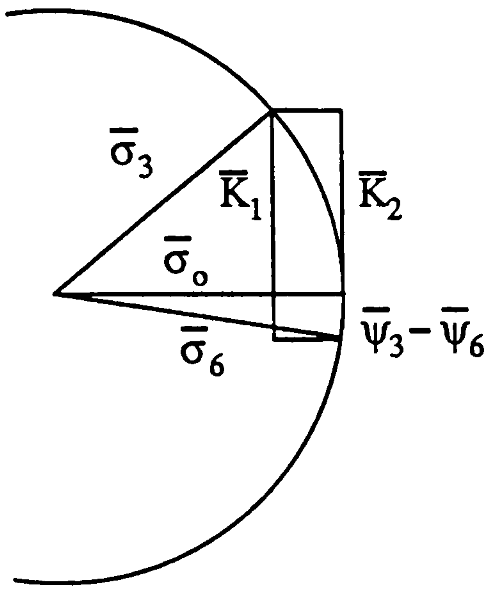


(g) $\bar\sigma_3 - \bar K_1 = \bar\sigma_6 - (\bar\psi_3 - \bar\psi_6)$

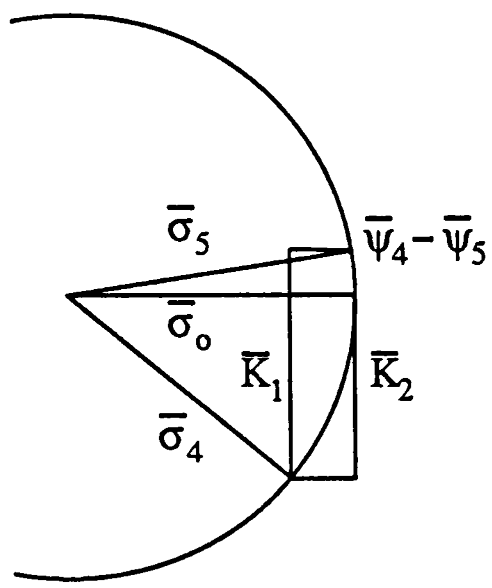


(h) $\bar\sigma_4 + \bar K_1 = \bar\sigma_5 - (\bar\psi_4 - \bar\psi_5)$

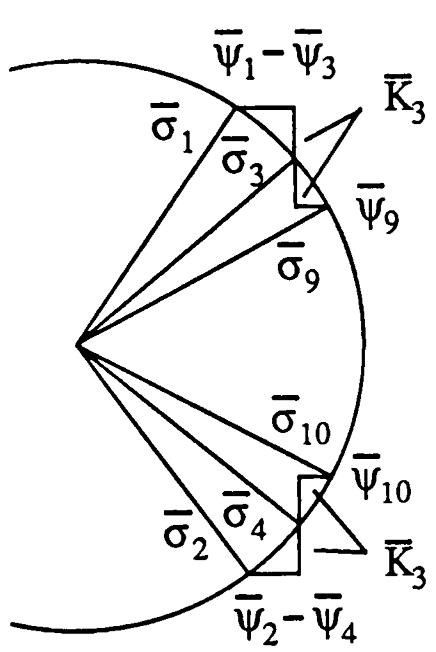


(i) $\bar\sigma_3 + \bar K_3 = \bar\sigma_1 + (\bar\psi_1 - \bar\psi_3)$

$\bar\sigma_3 - \bar K_3 = \bar\sigma_3 - \bar\psi_9$

$\bar\sigma_4 + \bar K_3 = \bar\sigma_{10} - \bar\psi_{10}$

$\bar\sigma_4 - \bar K_3 = \bar\sigma_2 + (\bar\psi_2 - \bar\psi_4)$

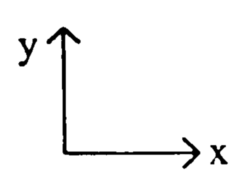


Figure 6.2 (continued).

### 6.2.2 *Coupled wave theory*

We have assumed the recording of three gratings, therefore the permitivity ($\varepsilon_r$) variation within the hologram may be expressed as:-

$$\varepsilon_r = \varepsilon_{ro} + \varepsilon_{r1}\cos(\overline{K}_1.\bar{r}+\delta_1) + \varepsilon_{r2}\cos(\overline{K}_2.\bar{r}+\delta_2) + \varepsilon_{r3}\cos(\overline{K}_3.\bar{r}+\delta_3) \tag{6.2}$$

where $\overline{K}_3 = \overline{K}_1 - \overline{K}_2$ .

$\varepsilon_{ro}$ is the average dielectric constant; $\varepsilon_{r1}$ , $\varepsilon_{r2}$ and $\varepsilon_{r3}$ are the modulations; $\overline{K}_1$ , $\overline{K}_2$ and $\overline{K}_3$ are the grating vectors; and $\delta_1$ , $\delta_2$ and $\delta_3$ are relative phase terms of gratings 1, 2 and 3 respectively.

In Chapter 4, in our derivation of refractive index modulation for spatial harmonic gratings, we discovered the existence of a $\pi$ phase shift between different grating components depending on the harmonics considered. By examining the cases for $\overline{K}_1$ , $\overline{K}_2$ and $\overline{K}_1 - \overline{K}_2$ we find that a $\pi$ phase term exists between the fundamentals and the harmonic, allowing us to set $\delta_1$ , $\delta_2$ and $\delta_3$ to the values 0, 0 and $\pi$ respectively. Equation (6.2) may now be rewritten as:-

$$\varepsilon_r = \varepsilon_{ro} + \varepsilon_{r1}\cos(\overline{K}_1.\bar{r}) + \varepsilon_{r2}\cos(\overline{K}_2.\bar{r}) - \varepsilon_{r3}\cos(\overline{K}_3.\bar{r}) \tag{6.3}$$

where we can see that the difference grating is out of phase with the two fundamentals.

We can control the relative modulation of $G_3$ to those of $G_1$ and $G_2$ by again using the model presented in Chapter 4. Figure 6.3 shows a plot of modulation versus total exposure energy. Thus, by finding $\varepsilon_{r1}$ and $\varepsilon_{r2}$ and knowing the total exposure, we can predict $\varepsilon_{r3}$ .

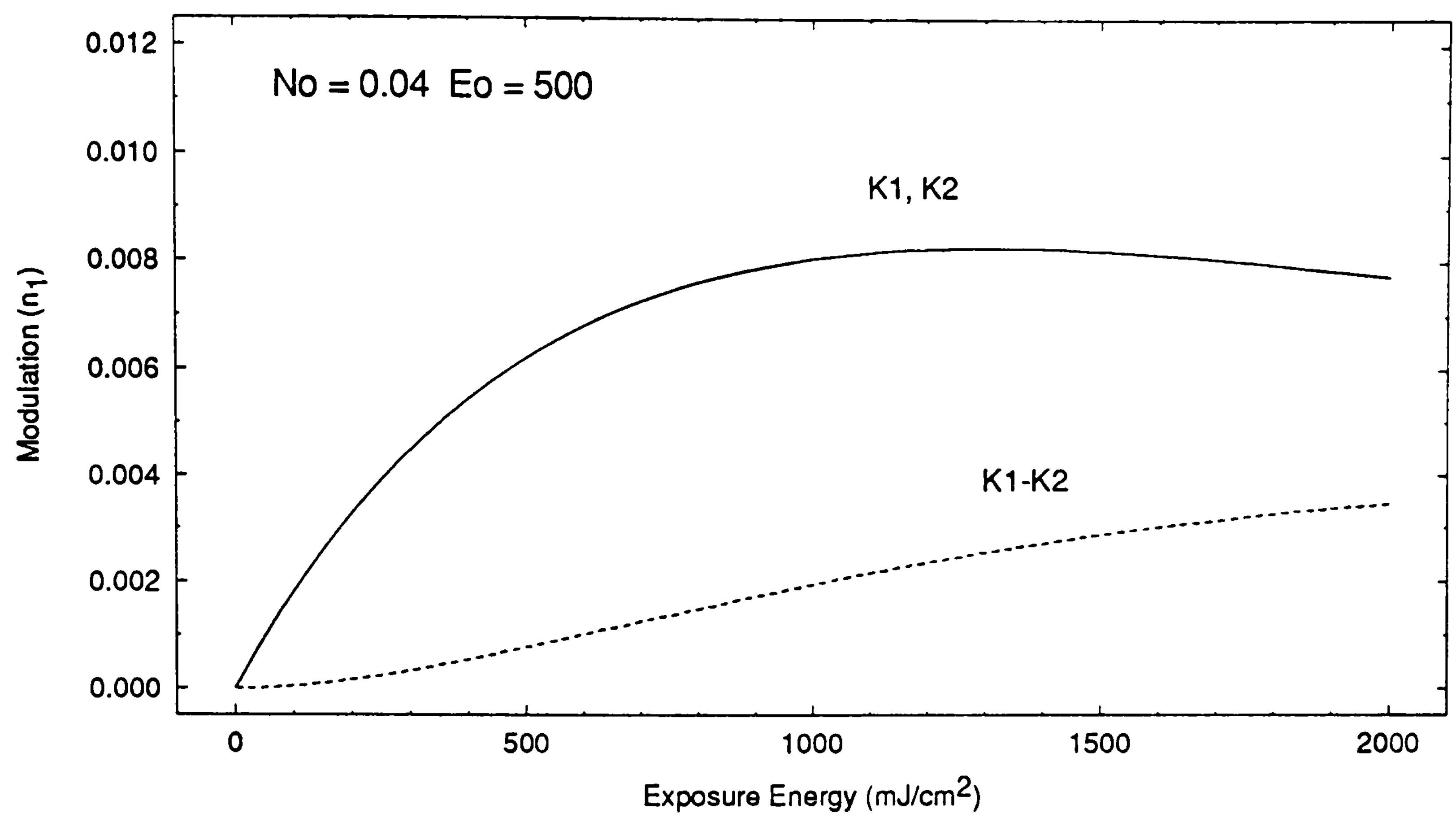


Figure 6.3 Theoretical plot of refractive index modulation versus total exposure energy for a double exposure transmission grating illustrating the dependence of $\varepsilon_{r3}$ upon $\varepsilon_{r1}$ and $\varepsilon_{r2}$ .

Following the coupled wave derivation outlined in Appendix II we are able to solve the scalar wave equation and derive the following set of coupled differential equations.

$$\frac{dA_o}{dx} = -\frac{j}{\cos\theta_o}\left\{-j\alpha A_o + \kappa_1\left[A_1 e^{+j\psi_1 . x} + A_2 e^{+j\psi_2 . x}\right] + \kappa_2\left[A_3 e^{+j\psi_3 . x} + A_4 e^{+j\psi_4 . x}\right]\right.$$
$$\left. -\kappa_3\left[A_5 e^{+j\psi_5 . x} + A_6 e^{+j\psi_6 . x}\right]\right\}$$

$$\frac{dA_1}{dx} = -\frac{j}{\cos\theta_1}\left\{-j\alpha A_1 + \kappa_1 A_o e^{-j\psi_1 . x} + \kappa_2 A_5 e^{-j(\psi_1 - \psi_5) . x} - \kappa_3\left[A_3 e^{-j(\psi_1 - \psi_3) . x} + A_7 e^{+j\psi_7 . x}\right]\right\}$$

$$\frac{dA_2}{dx} = -\frac{j}{\cos\theta_2}\left\{-j\alpha A_2 + \kappa_1 A_o e^{-j\psi_2 . x} + \kappa_2 A_6 e^{-j(\psi_2 - \psi_6) . x} - \kappa_3\left[A_4 e^{-j(\psi_2 - \psi_4) . x} + A_8 e^{+j\psi_8 . x}\right]\right\}$$

$$\frac{dA_3}{dx} = -\frac{j}{\cos\theta_3}\left\{-j\alpha A_3 + \kappa_1 A_6 e^{-j(\psi_3 - \psi_6) . x} + \kappa_2 A_o e^{-j\psi_3 . x} - \kappa_3\left[A_1 e^{+j(\psi_1 - \psi_3) . x} + A_9 e^{-j\psi_9 . x}\right]\right\}$$

$$\frac{dA_4}{dx} = -\frac{j}{\cos\theta_4}\left\{-j\alpha A_4 + \kappa_1 A_5 e^{-j(\psi_4 - \psi_5) . x} + \kappa_2 A_o e^{-j\psi_4 . x} - \kappa_3\left[A_2 e^{+j(\psi_2 - \psi_4) . x} + A_{10} e^{-j\psi_{10} . x}\right]\right\}$$

$$\frac{dA_5}{dx} = -\frac{j}{\cos\theta_5}\left\{-j\alpha A_5 + \kappa_1 A_4 e^{+j(\psi_4-\psi_5).x} + \kappa_2 A_1 e^{+j(\psi_1-\psi_5).x} - \kappa_3 A_o e^{-j\psi_5.x}\right\}$$

$$\frac{dA_6}{dx} = -\frac{j}{\cos\theta_6}\left\{-j\alpha A_6 + \kappa_1 A_3 e^{+j(\psi_3-\psi_6).x} + \kappa_2 A_2 e^{+j(\psi_2-\psi_6).x} - \kappa_3 A_o e^{-j\psi_6.x}\right\}$$

$$\frac{dA_7}{dx} = -\frac{j}{\cos\theta_7}\left\{-j\alpha A_7 - \kappa_3 A_1 e^{-j\psi_7.x}\right\}$$

$$\frac{dA_8}{dx} = -\frac{j}{\cos\theta_8}\left\{-j\alpha A_8 - \kappa_3 A_2 e^{-j\psi_8.x}\right\}$$

$$\frac{dA_9}{dx} = -\frac{j}{\cos\theta_9}\left\{-j\alpha A_9 - \kappa_3 A_3 e^{+j\psi_9.x}\right\}$$

$$\frac{dA_{10}}{dx} = -\frac{j}{\cos\theta_{10}}\left\{-j\alpha A_{10} - \kappa_3 A_4 e^{+j\psi_{10}.x}\right\} \qquad (6.4)$$

From these equations it is possible to calculate the relative output intensities of each wave at varying angles of incidence in order to give a full description of angular selectivity. It must be noted that at certain angles of incidence the off - Bragg parameter $\psi$ will not touch the Ewald circle at all. Thus some waves may not replay at all. For example, if we replay at a large positive angle, $A_1$ and possibly $A_2$ will not replay at the desired wavelength. For such cases the relevant equations are neglected and the amplitudes of these waves are set to zero.

### 6.2.3 *Effect of arbitrary phase shift at recording*

It is still necessary to prove the validity of our assumption which was to neglect the influence of arbitrary phase terms between $G_1$ and $G_2$ at recording.

We can can include this arbitrary phase ($\gamma$) in Equation (6.3) as:-

$$\varepsilon_r = \varepsilon_{ro} + \varepsilon_{r1}\cos(\overline{K}_1.\bar{r}+\gamma_1) + \varepsilon_{r2}\cos(\overline{K}_2.\bar{r}+\gamma_2) - \varepsilon_{r3}\cos(\overline{K}_3.\bar{r}+\gamma_3) \qquad (6.5)$$

However, from Equation (4.11) in Chapter 4, it is possible to show that $\gamma_3 = \gamma_1 - \gamma_2$ for the harmonic grating equivalent to $\overline{K}_1 - \overline{K}_2$ . This yields :-

$$\varepsilon_r = \varepsilon_{ro} + \varepsilon_{r1}\cos(\overline{K}_1.\bar{r} + \gamma_1) + \varepsilon_{r2}\cos(\overline{K}_2.\bar{r} + \gamma_2) - \varepsilon_{r3}\cos(\overline{K}_3.\bar{r} + \gamma_1 - \gamma_2) \qquad (6.6)$$

Now, by following the working above we can rewrite the amplitudes in the following form:-

$$\begin{array}{ll} B_1 = A_1 e^{+j\gamma_1} & B_6 = A_6 e^{-j(\gamma_1 - \gamma_2)} \\ B_2 = A_2 e^{-j\gamma_1} & B_7 = A_7 e^{+j(2\gamma_1 - \gamma_2)} \\ B_3 = A_3 e^{+j\gamma_2} & B_8 = A_8 e^{-j(2\gamma_1 - \gamma_2)} \\ B_4 = A_4 e^{-j\gamma_2} & B_9 = A_9 e^{-j(\gamma_1 - 2\gamma_2)} \\ B_5 = A_5 e^{+j(\gamma_1 - \gamma_2)} & B_{10} = A_{10} e^{+j(\gamma_1 - 2\gamma_2)} \end{array} \qquad (6.7)$$

By substituting these amplitudes into the mathematics we obtain a set of differential equations which show no change in character from (6.4), illustrating that the introduction of phase terms $\gamma_1$ and $\gamma_2$ have no effect on the amplitudes of the diffracted waves.

## 6.3 Properties of the model

The following section will give an indication of the capabilities of the above model to deal with the existence of nonlinear recordings. For clarity, theoretical plots will demonstrate relevant points. In order to standardise these plots the effect of absorption at replay will be neglected (i.e. $\alpha = 0$) and the thickness and average refractive index values both at recording and replay will be set typically to 25 μm and 1.57 respectively. The modulation ($n_1$) values of $G_1$ and $G_2$ will each be set to 0.008 in order to obtain high efficiency diffraction. The recording and replay wavelengths will be kept constant at 514.5 nm and angles inside the holographic medium will be assumed in the calculations.

Figure 6.4 shows the effect of reducing the angle of separation between the two recordings when neglecting the existence of nonlinearities at recording, i.e. we assume that *the difference grating $G_3$ is not present.*

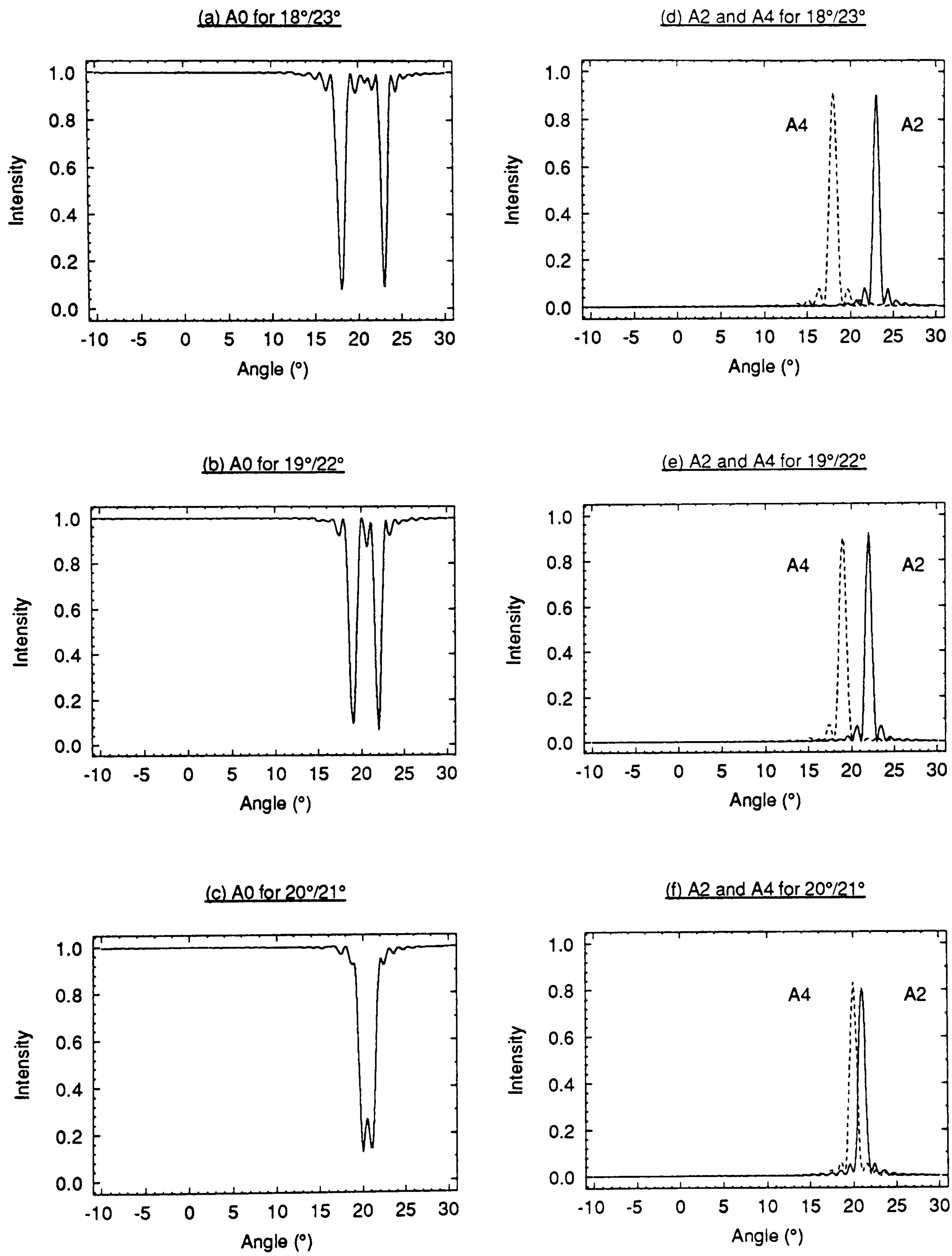


Figure 6.4 Theoretical plots of a double exposure transmission hologram neglecting the existence of a difference grating $G_3$.

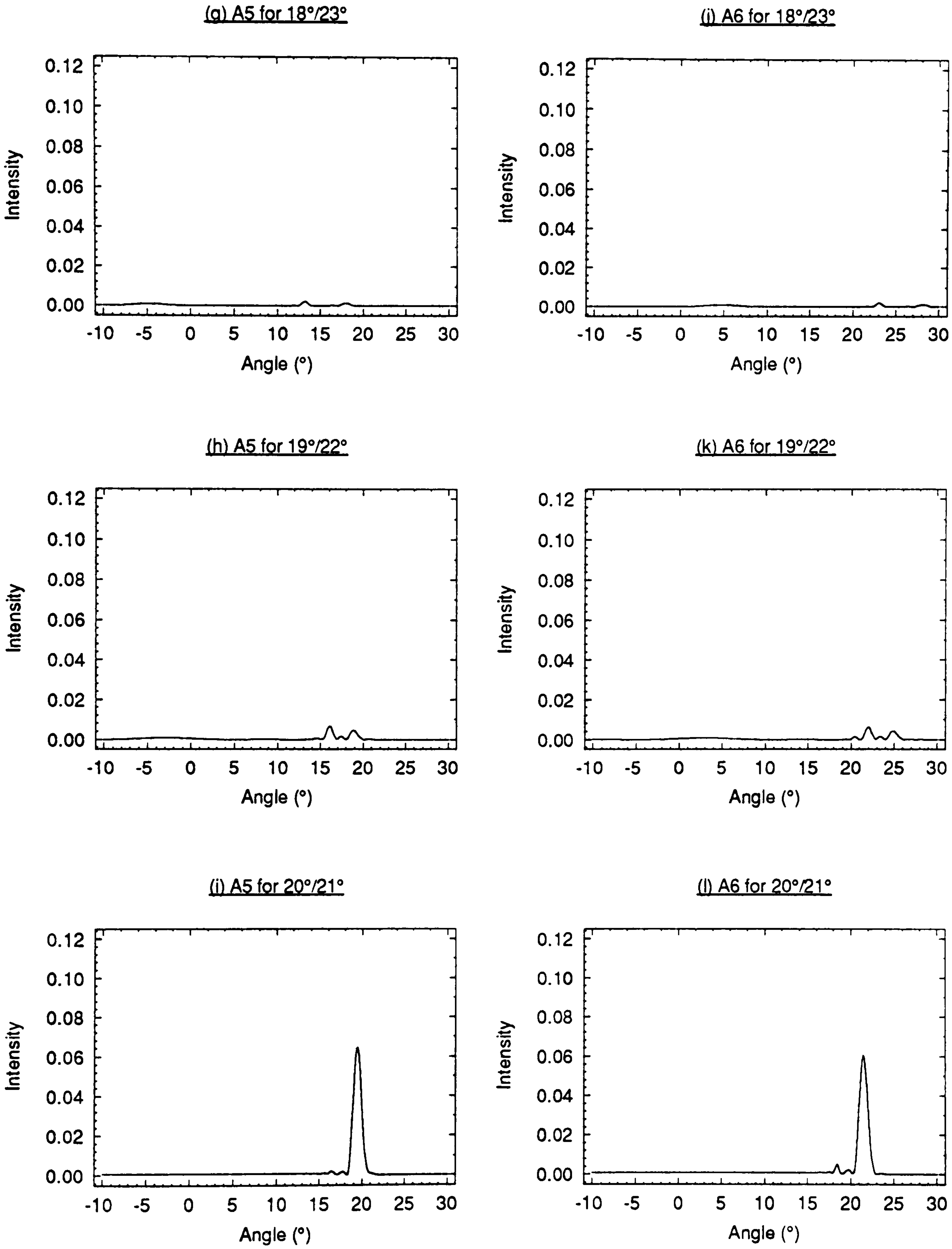


Figure 6.4 (Continued).

In each figure we will view the theoretical angular replay of each wave A0, A2, A4, A5, A6, A8 and A10. The other waves need not be shown since the the recording conditions are symmetrical and the wave amplitudes identical. Diagrams (a), (b) and (c) show the zeroth order transmitted wave A0 as the recording angles are moved closer together from ±18° and ±23° to ±20° and ±21°. Similarly (d), (e) and (f) show the first order diffracted waves A2 and A4. Both the amplitudes show similar diffraction efficiencies around 95%. Plots (g) to (l) show how reducing the recording angles affects the amount of energy coupled into waves A5 and A6 due to double diffraction by the interaction of $G_1$ and $G_2$. With a large separation (Plots (g) and (j)) we do not notice much energy transfer , however, with recording angles of ±20° and ±21° we see A5 and A6 reach significant efficiencies of about 6% for this specific case. For this model, we will ignore the replay of waves A8 and A10. We do not expect any coupling into these waves since they are dependent solely on the existence of $G_3$.

Let us now look at theoretical replay of the hologram where the spatial difference grating has been included. We will assume a realistic value for modulation of this grating as 0.002 which corresponds approximately to a total exposure energy of 1000 mJ / cm$^2$ in Figure 6.3.

Figure 6.5 shows what happens if no account is taken of a phase shift between $G_1$, $G_2$ and $G_3$. Again diagrams (a), (b) and (c) show the zeroth order transmitted wave A0 at replay as the recording angles are moved closer together. This time we observe additional dips at low replay angles corresponding to to the inclusion of the difference grating $G_3$. As the recording angles get closer together we observe that the nonlinear dips merge into one at low replay angles and the corresponding dip for A2 reduces in strength. The plots for A2 and A4 (i.e. (d), (e) and (f)) confirm this change in efficiency. By looking at the replay waves A5 and A6 (Figures (g) to (l)), we see that there are two sources of replay. We observe the same multiple interaction occurring as before around the recording angles, however there appears to be a slight change in efficiencies and the waves are now superimposed upon the diffracted energy from the nonlinear grating. We see that as the recording angles get closer together, the angular selectivity of A5 and A6 reduces as the grating period increases.

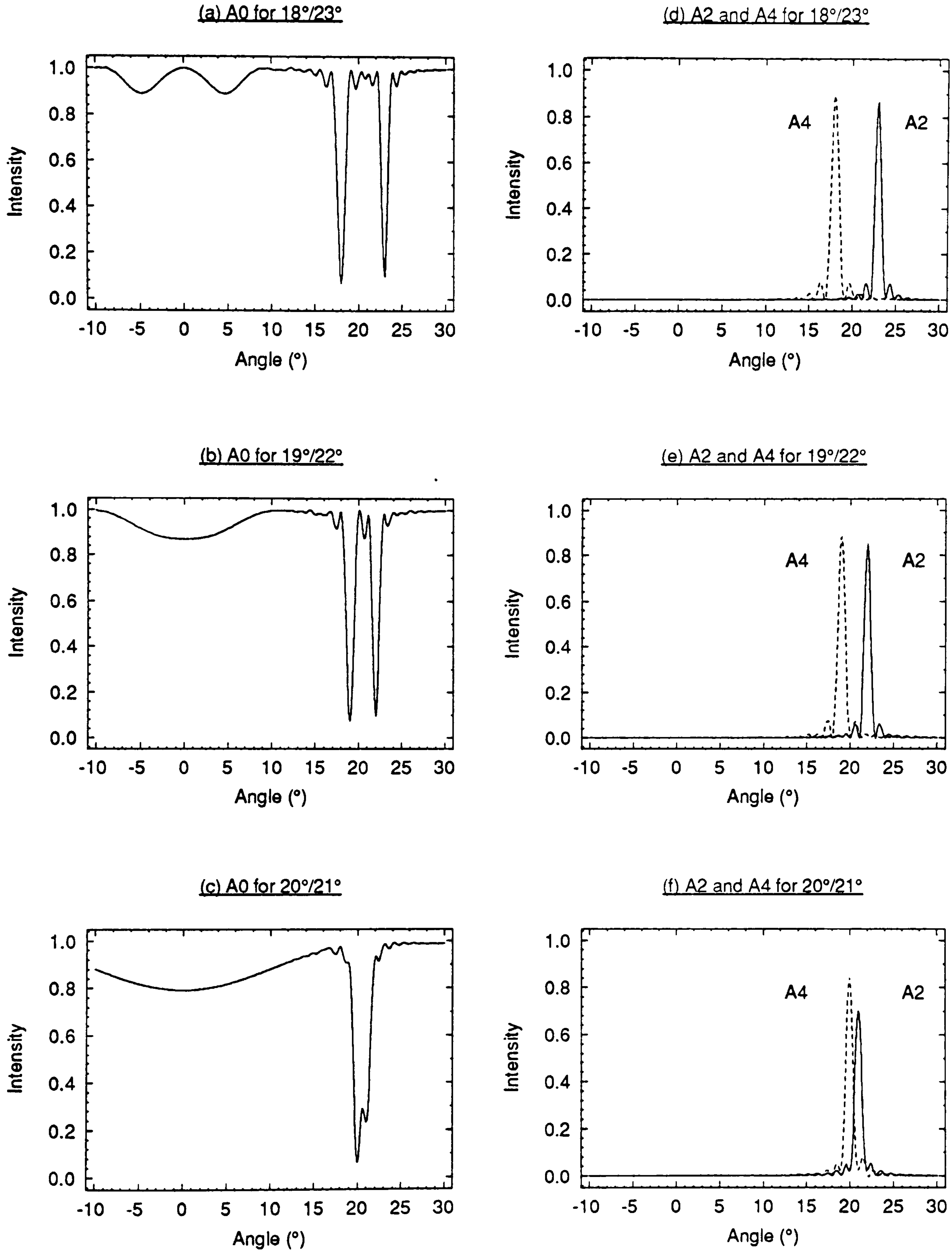


Figure 6.5 Theoretical plots of a double exposure transmission hologram including the existence of a difference grating $G_3$ with 0 radians phase shift.

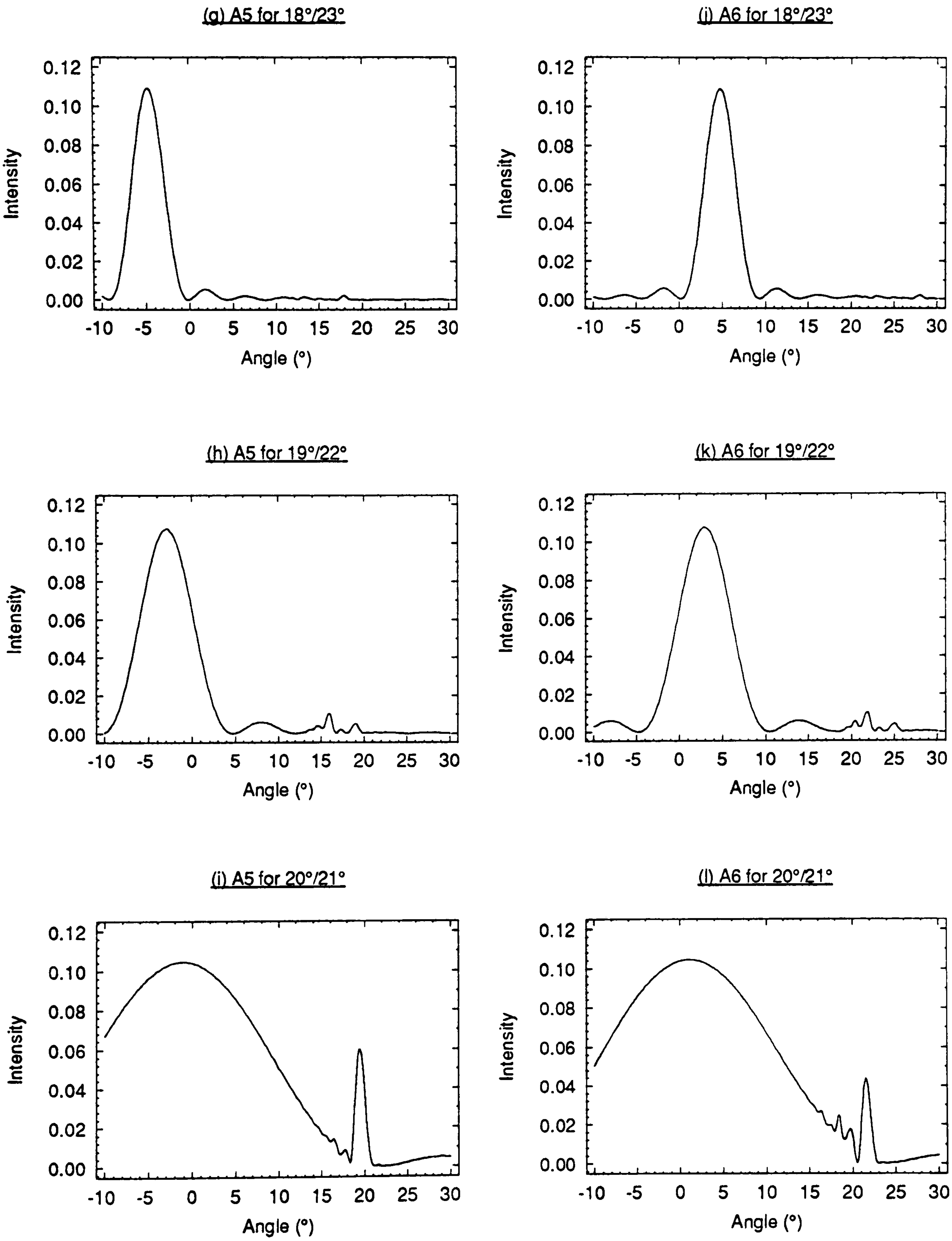


Figure 6.5 (Continued).

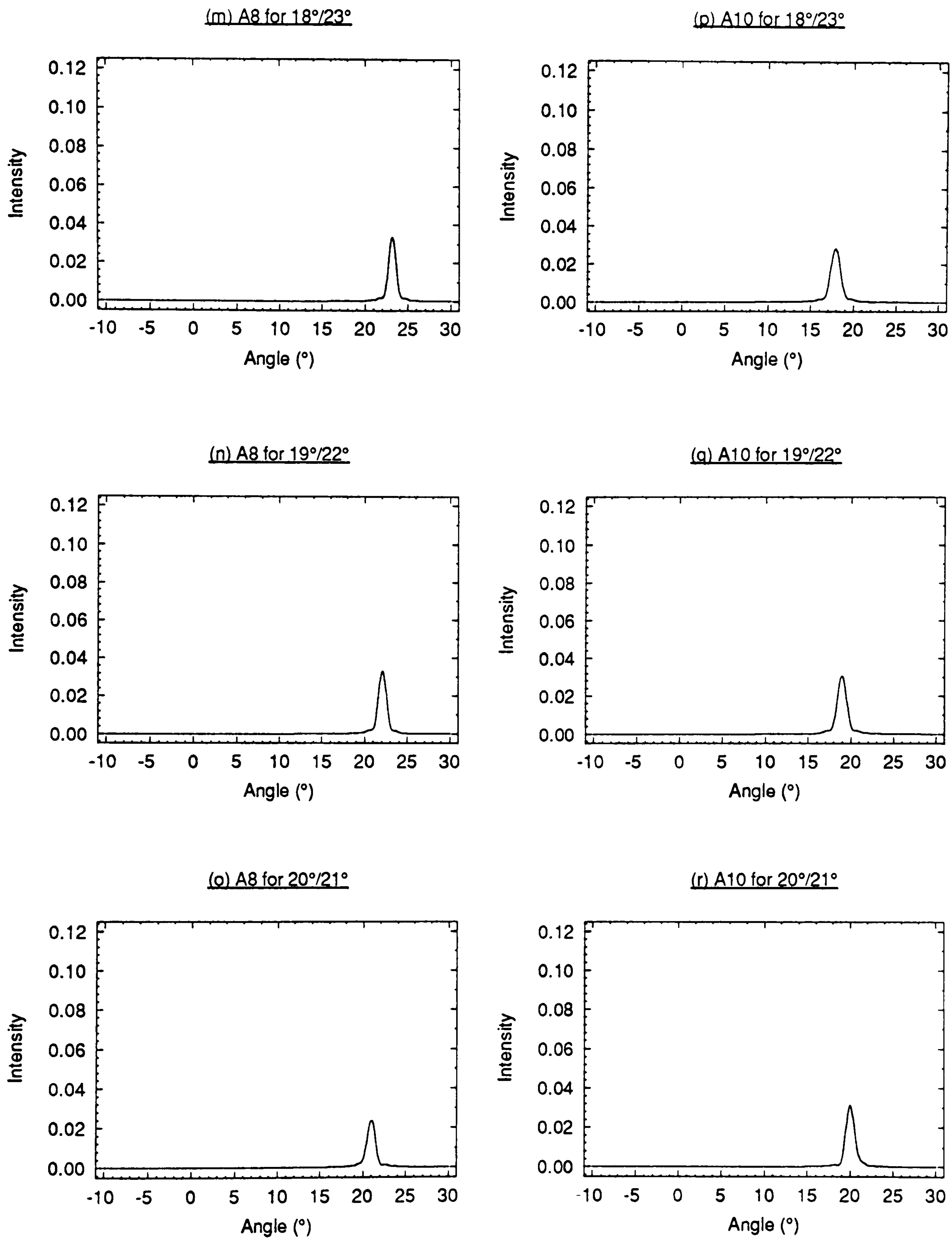


Figure 6.5 (Continued).

Plots (m) to (r) show the effect of grating interactions between $G_1 \pm G_3$ (i.e. (m), (n) and (o)) and $G_2 \pm G_3$ (i.e. (p), (q) and (r)). These show significant intensities of about 3% for this particular case and are seen to replay at the angles corresponding to the Bragg peaks of waves A2 and A4. At close recording angles we see that A10 has a larger amplitude than A8, indicating that these waves are partly responsible for the difference in efficiency of the fundamental gratings.

If a $\pi$ phase shift is now introduced between the fundamental gratings and the difference grating, as discussed in the above theory, we obtain the theoretical plots seen in Figure 6.6. Looking at the transmitted zeroth order beam, we once more obtain extra dips at low replay angles due to replay of the difference grating. However, as we move to closer recording angles, we see that the wave corresponding to A4 reduces in efficiency with respect to wave A2. This is opposite to the previous case. Figures (d) to (f) confirm this for the amplitudes A2 and A4. Looking at A5 and A6 we again see the effect of grating interactions superimposed on the output from the nonlinear grating, however the diffraction efficiency of A6 at 21° is now about 7% and is larger than A5. It is also interesting to note that, due to the $\pi$ phase shift, the efficiency of the nonlinear difference grating has dropped from its previous value of >10% to about 7%. Thus, the effect of the $\pi$ phase shift is to reduce the efficiency of the difference grating and cause an apparent 'reduction' in modulation. Figures (m) to (r) show the diffraction efficiencies for A8 and A10. This time we observe A8 displaying a larger efficiency than A10 which helps to explain the reduction in efficiency of A4 with respect to A2.

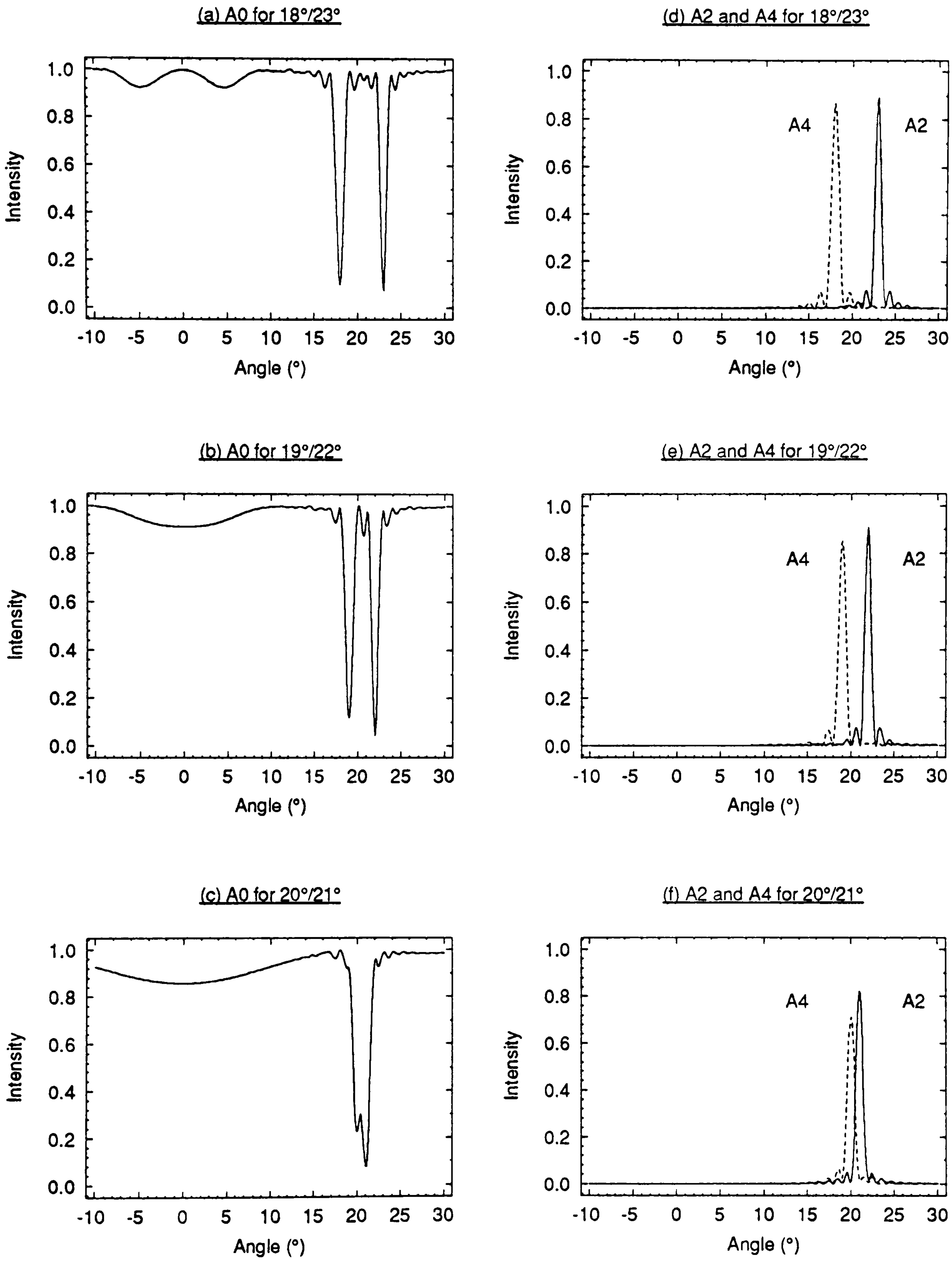


Figure 6.6 Theoretical plots of a double exposure transmission hologram including the existence of a difference grating $G_3$ with $\pi$ radians phase shift.

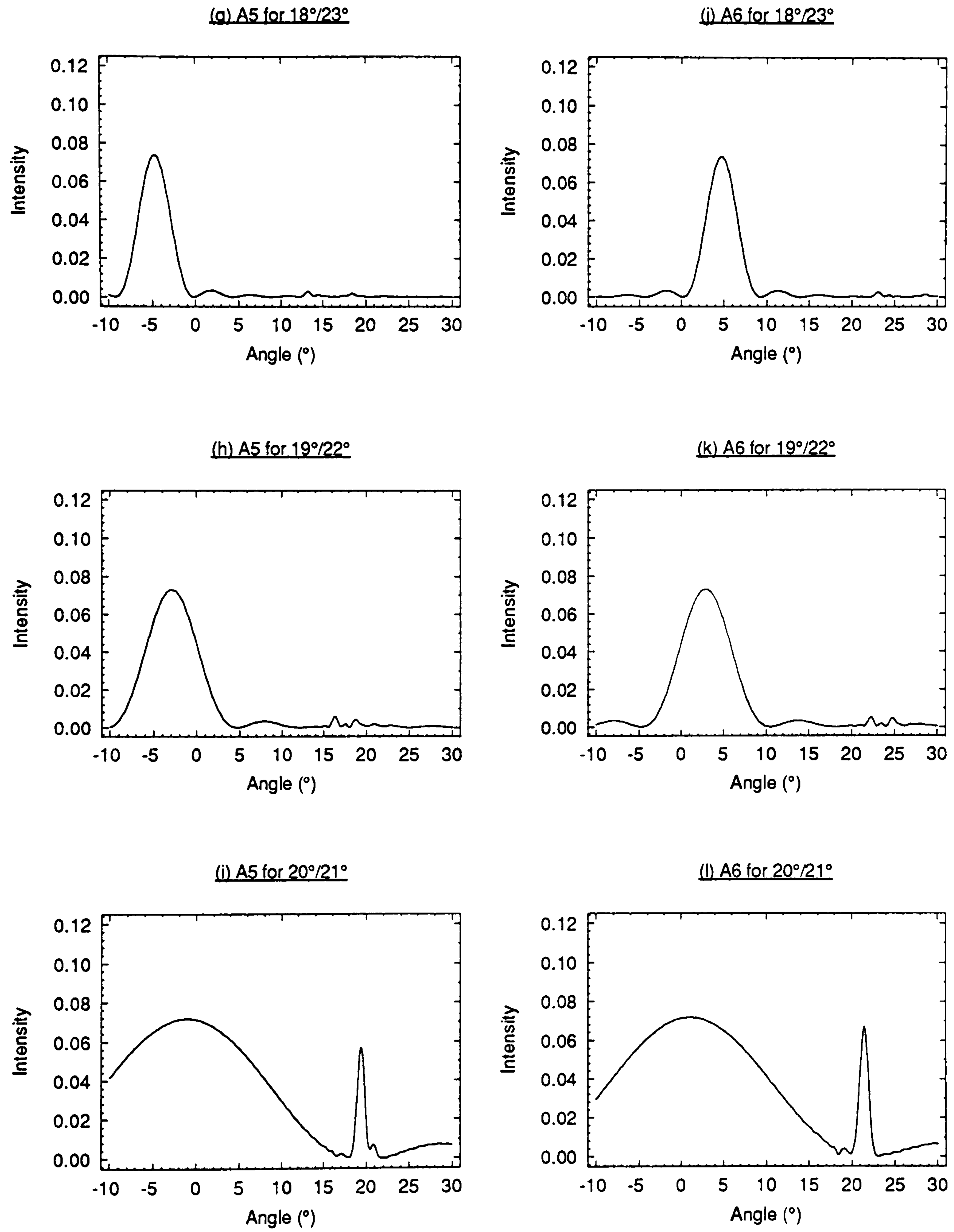


Figure 6.6 (Continued).

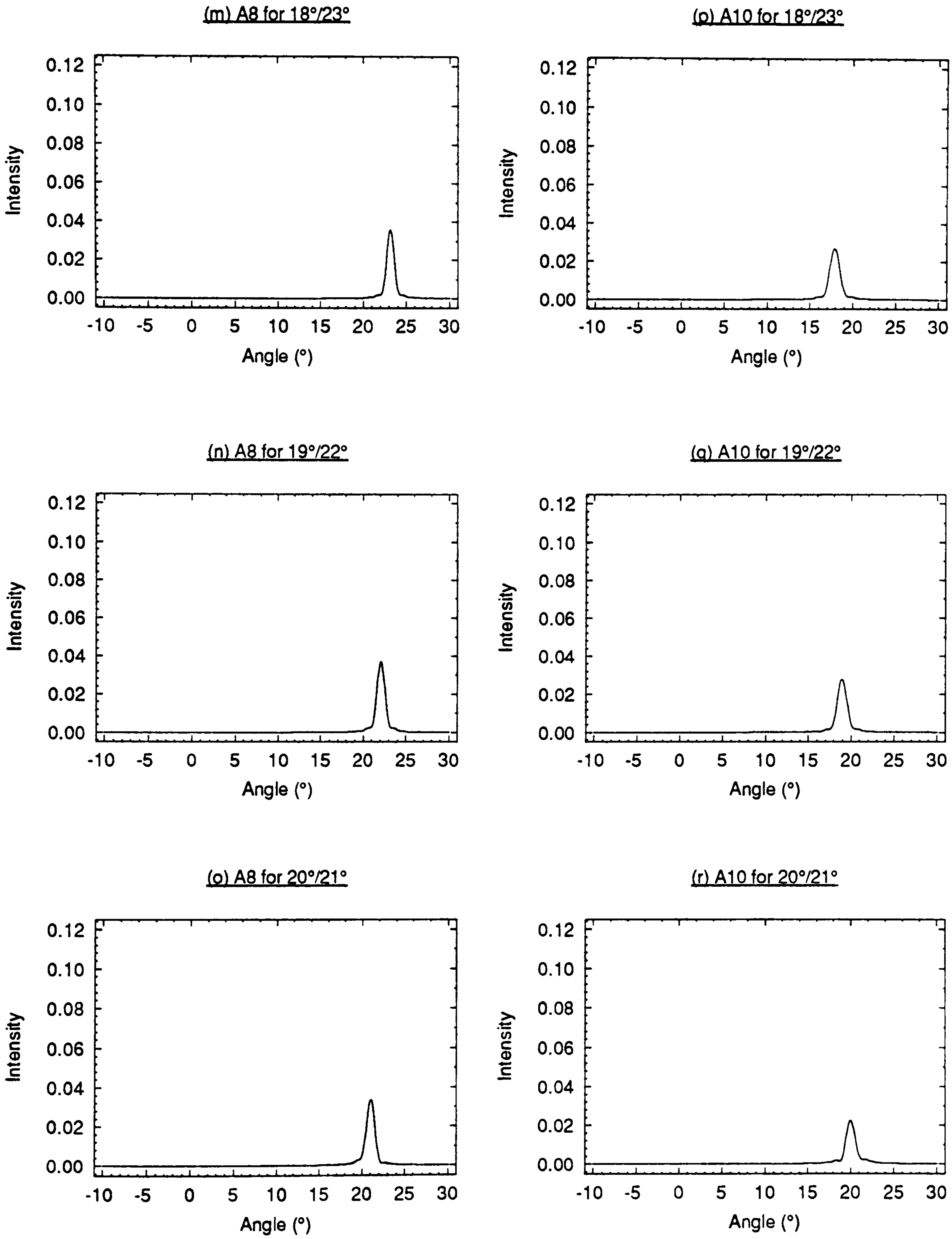


Figure 6.6 (Continued).

Figure 6.7 shows plots of A5 and A6 where the case in which no grating interactions occur (i.e. $G_3$ is the only grating to exist) is compared with waves A5 and A6 for the case of grating interactions and a $\pi$ phase shift. In each case the modulation for $G_3$ is kept constant at 0.002. Here we can see that the efficiency of A5 and A6 drop by around 2% due to the inclusion of grating interactions and illustrate that it is not possible to treat the difference recording as an independent recording.

We can therefore see from these plots that, by recording two sequential gratings in the saturating region of the recording characteristic, we will record a third grating with spatial frequency equal to the difference of the two fundamentals. This grating therefore replays at the Bragg angle for such a spatial frequency. However, due to a $\pi$ phase difference between this 'nonlinear' grating and the fundamentals, and multiple interactions of the recorded gratings, it is not possible to assume three independent recordings, particularly when the recording angles for the two fundamental gratings are close together. In fact the interaction of all three gratings is is going to influence the efficiency of each grating.

The above plots also show that the efficiency of each wave is dependent upon the difference in angle ($\Delta\theta$) between the two primary recordings. We will now show how the waves A2, A4, A5, A6, A8 and A10 vary with $\Delta\theta$. For simplicity we choose the specific case where:-

(i) the recording wavelength equals the replay wavelength of 514.5 nm

(ii) the recording average refractive index equals the replay refractive index of 1.57

(iii) absorption is neglected ie $\alpha = 0$

(iv) the recording thickness equals the replay thickness of 25 μm

(v) the refractive index modulation for $G_1$ and $G_2$ were chosen to give high efficiency replay at 0.008

and (vi) the difference in recording angles for G1 and G2 was varied from 0.1° to 5° about a central angle of 20.5°

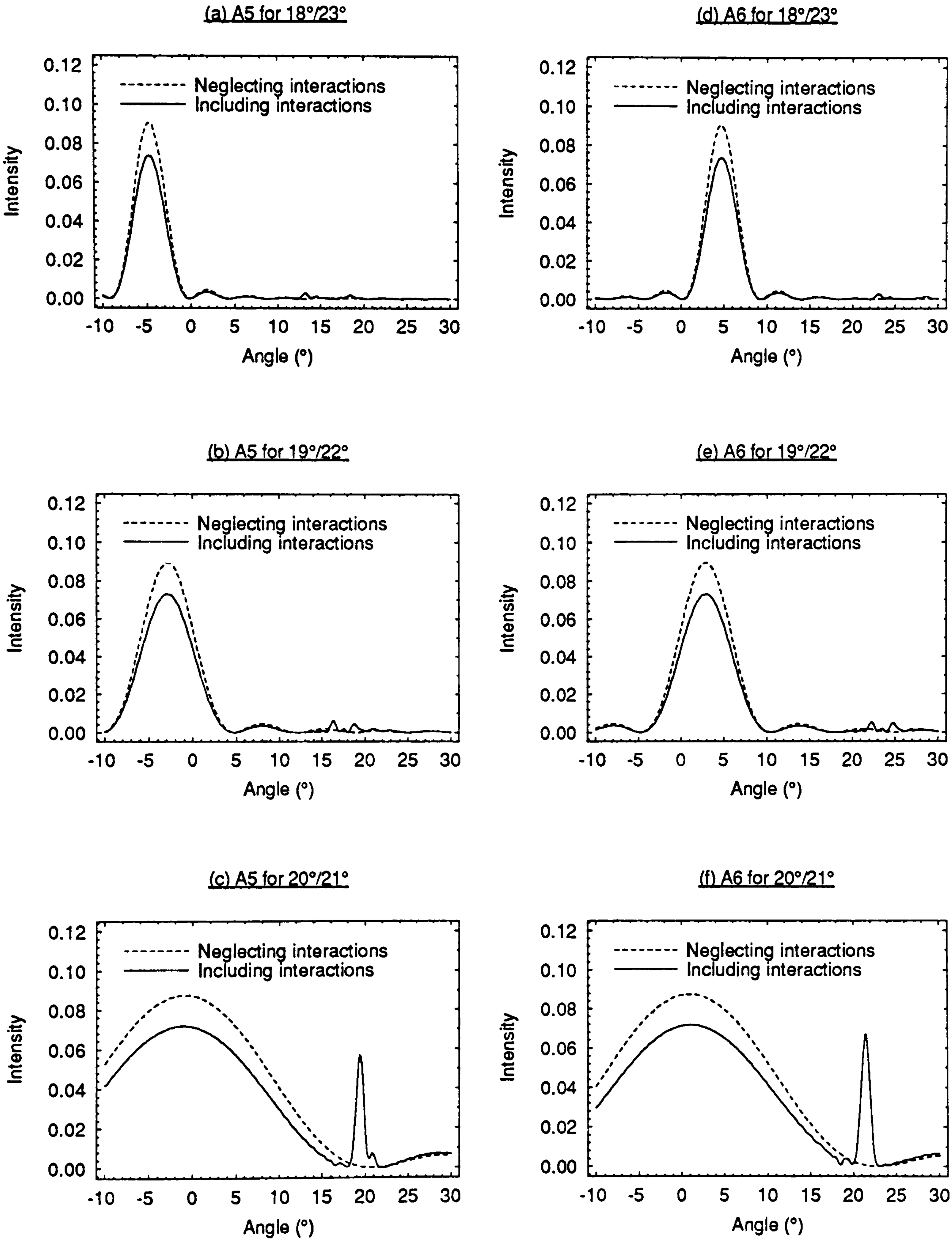


Figure 6.7 Theoretical comparison for A5 and A6 where grating interactions have been (i) neglected and (ii) included.

Figure 6.8 (a) to (c) show how the amplitudes are affected by introducing the nonlinear grating with different modulation strengths of 0, 0.0015 and 0.003 respectively.

In diagram (a) we see that the trend is for A2 and A4 to replay at the same efficiency. As $\Delta\theta$ decreases, however, the efficiency of these waves falls towards a value of approximately 20%. At the same time the spurious waves A5 and A6 increase in strength due to the grating interactions $G_1 \pm G_2$.

If we now introduce the nonlinear grating $G_3$ we can see from diagrams (b) and (c) that waves A2 and A4 start to replay with different efficiencies. A2 is consistently stronger than A4, and A6 displays greater efficiency than A5. We also start to notice the introduction of the waves A8 and A10 replaying due to the interactions of $G_1 \pm G_3$ and $G_2 \pm G_3$. In particular, when the modulation of $G_3$ reaches 0.003 the differences in efficiencies become quite substantial.

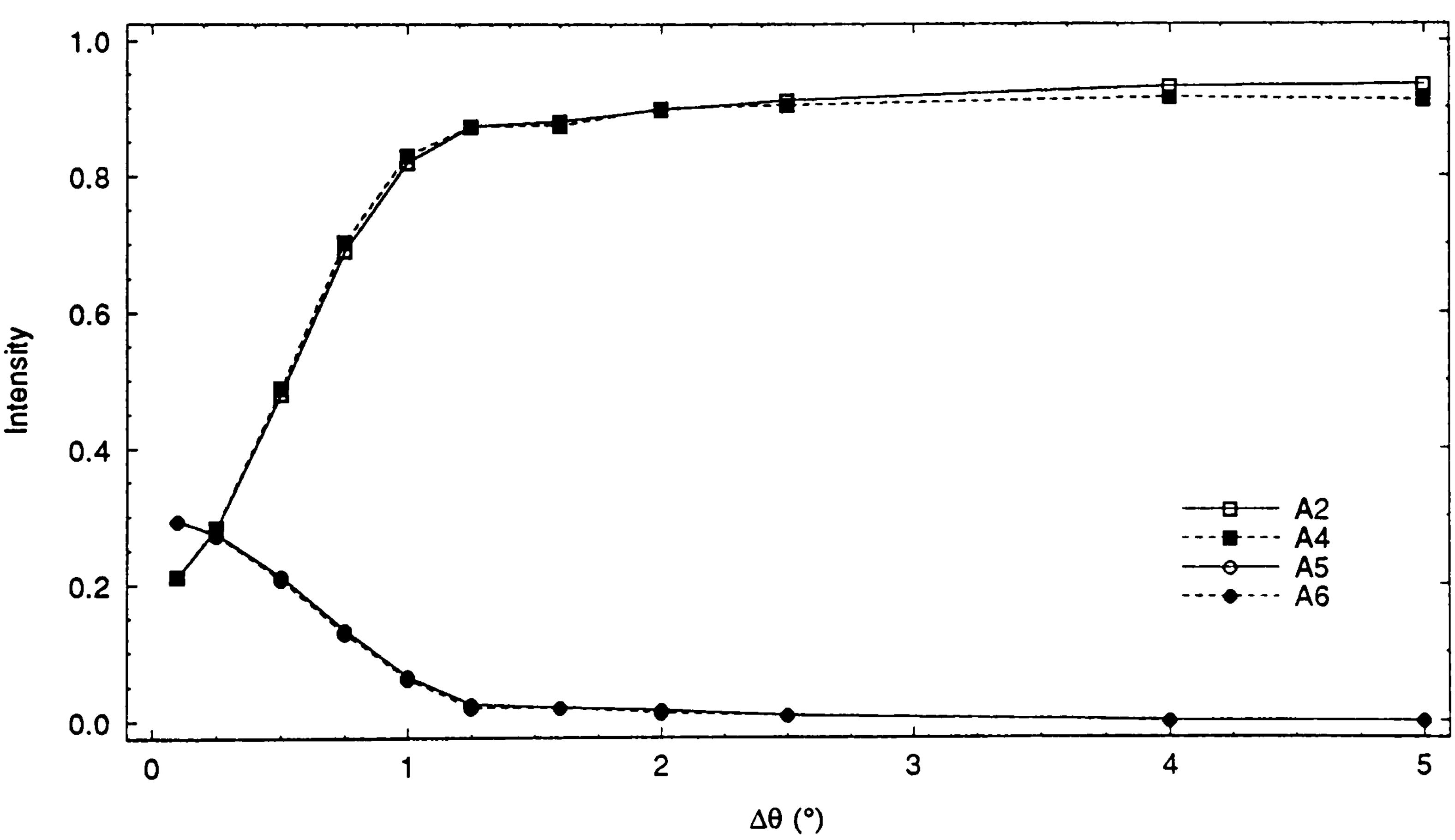


Figure 6.8 (a) Theoretical plot of output intensity versus angular difference between the two sets of recording beams ($\Delta\theta$) where $n_{11} = n_{12} = 0.008$, $n_{13} = 0$.

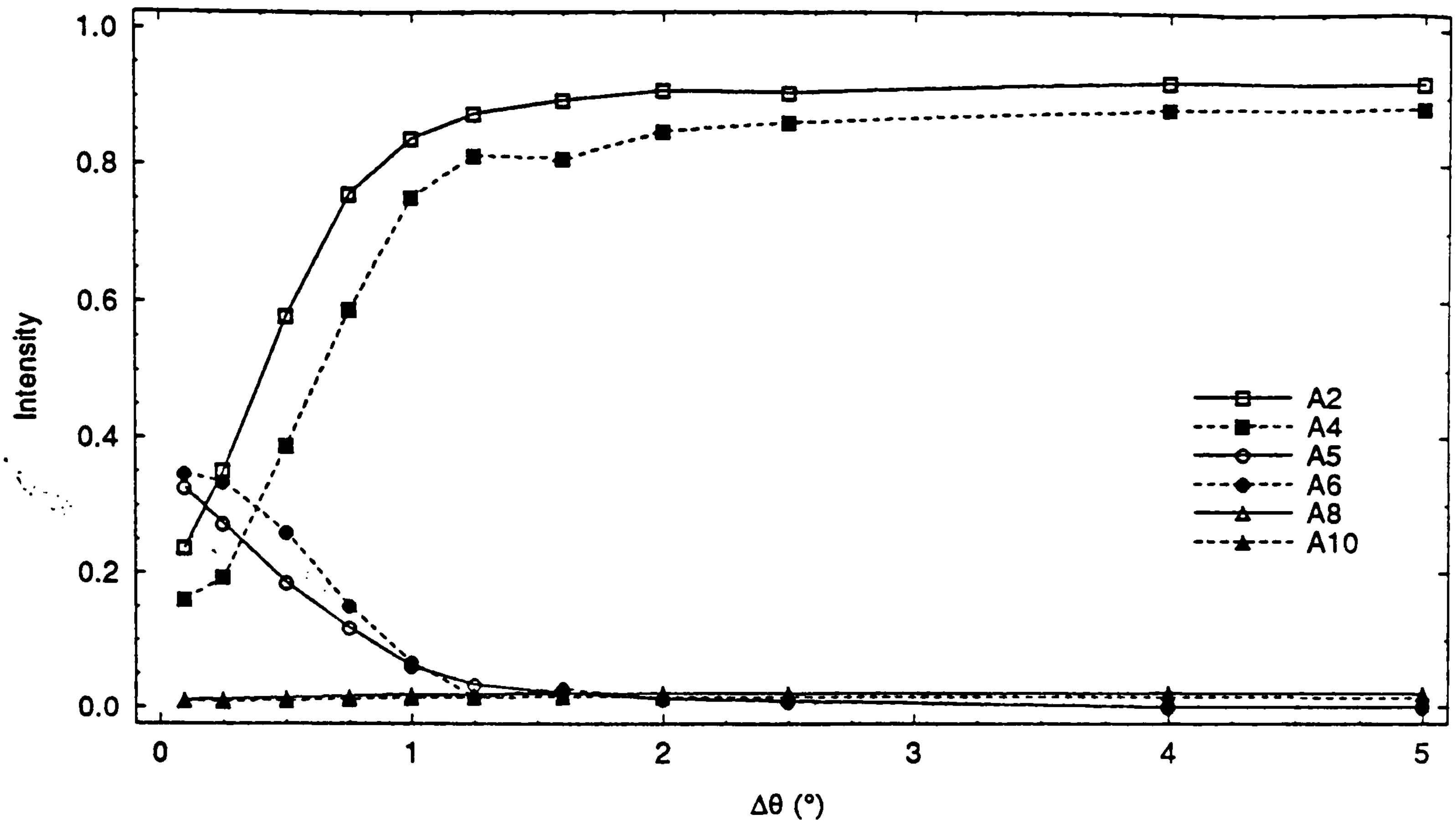


Figure 6.8 (b) Theoretical plot of output intensity versus angular difference between the two sets of recording beams (Δθ) where $n_{11} = n_{12} = 0.008$, $n_{13} = 0.0015$.

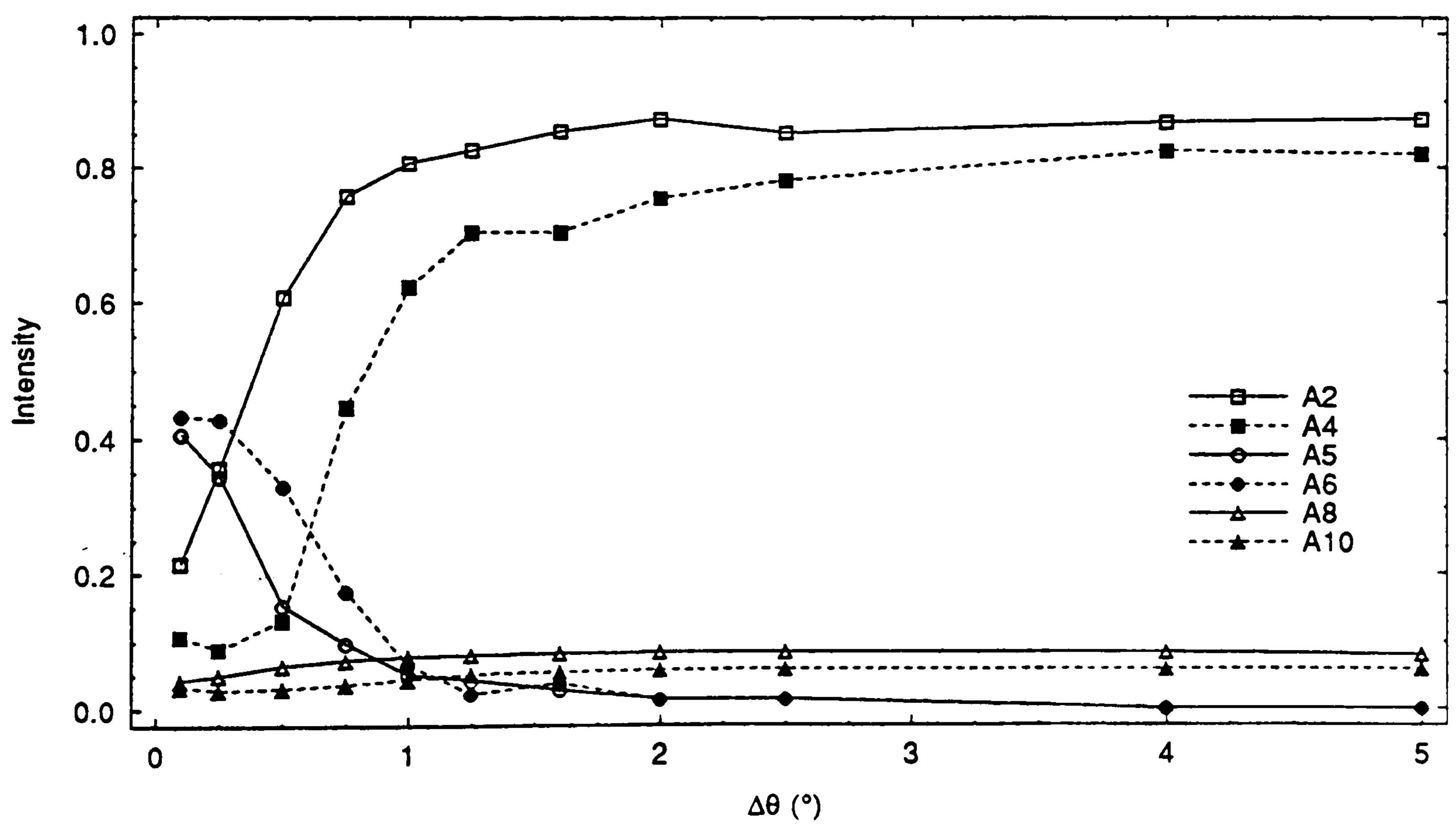


Figure 6.8 (c) Theoretical plot of output intensity versus angular difference between the two sets of recording beams (Δθ) where $n_{11} = n_{12} = 0.008$, $n_{13} = 0.003$.

Of course, we have chosen a highly selective condition for these results. If the thickness or recording angles are reduced, however, we would expect lower angular selectivity and hence an increase in the range where $\Delta\theta$ is important.

## 6.4 Experiments

### 6.4.1 *Recording*

Double exposure transmission gratings were recorded sequentially using a geometry similar to that described in Chapter 4. Figure 6.9 shows the recording setup. Once again the 25 μm thick DCG plates were sensitised with 2% ammonium dichromate and exposed at a wavelength of 514.5 nm to varying levels of energy. The exposure and beam ratios were each kept constant at 1:1.

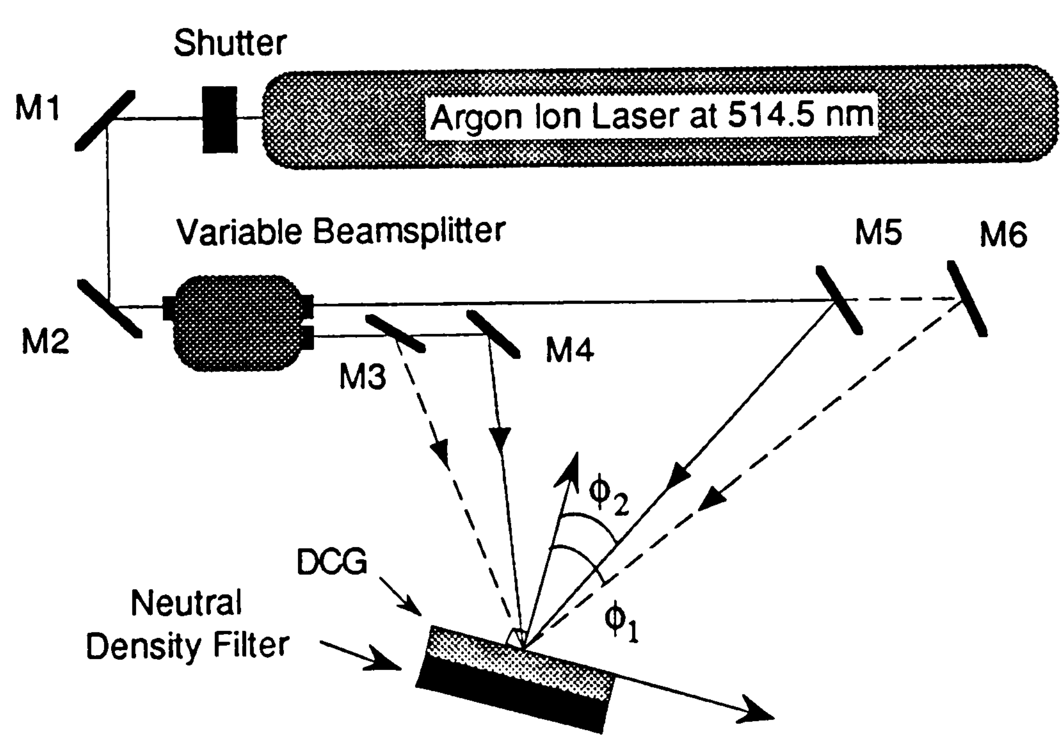


Figure 6.9 Recording geometry for double exposure transmission gratings.

In this experiment two sets of recording angles were chosen:-

(a) In this first set the recording angles were sufficiently separated so as to reduce interactions between the fundamental gratings i.e. at $\phi_1 = \pm 23°$ and $\phi_2 = \pm 18°$. Six plates were exposed using total energy values of 100, 200, 400, 800, 1200 and 2000 mJ / cm$^2$. The grating at ±18° was recorded first.

(b) In the second set the recording angles were made closer together so as to encourage grating interactions, i.e. at $\phi_1 = \pm 21°$ and $\phi_2 = \pm 20°$. Again, six plates were exposed at energy levels of 200, 400, 1000, 1500, 2000 and 2500 mJ / cm$^2$. In this case the grating at ±21° was recorded first.

Note that these angles are as measured within an index matching tank.

The plates were processed and analysed using the methods described in Chapter 2.

## 6.5 Comparison of theory with experiments

By feeding the relevant recording and replay conditions (such as wavelength, average refractive index, thickness, recording angles and refractive index modulation) into the above model, we are able to simulate the transmitted 0th order intensity of the above experimental holograms. Thus we are able to take into account the effect of grating interactions between the two fundamental recordings and the replay of a third difference grating. The following section describes how the theory compares with experimental results.

### 6.5.1 *Set (a):* $\phi_1 = \pm 23°$, $\phi_2 = \pm 18°$

Figure 6.10 shows angular transmittance scans of holograms recorded at ±23° and ±18° for increasing exposure energies. The experimental data is shown as data points connected by a dashed line. A theoretical curve is given by a solid line.

At low exposures we observe only the existence of two Bragg dips corresponding to the two fundamental gratings. In each case we can see that the dip at the lower angle is slightly deeper than the other. This is believed to be due to the effects of absorption at recording. After the first exposure was taken, no compensation was made for any darkening of the gelatin. Thus, we can expect the second exposure to be of a lower modulation than the first and hence of lower efficiency. The theoretical modulation values used to model the experimental data confirm this. As the exposure energy increases we notice the formation of dips at around ±5° due to the replay of the spatial harmonic grating $G_3$.

(a) 100 mJ / cm$^2$ ($n_{11}$=0.00225, $n_{12}$=0.0025, $n_{13}$=0)

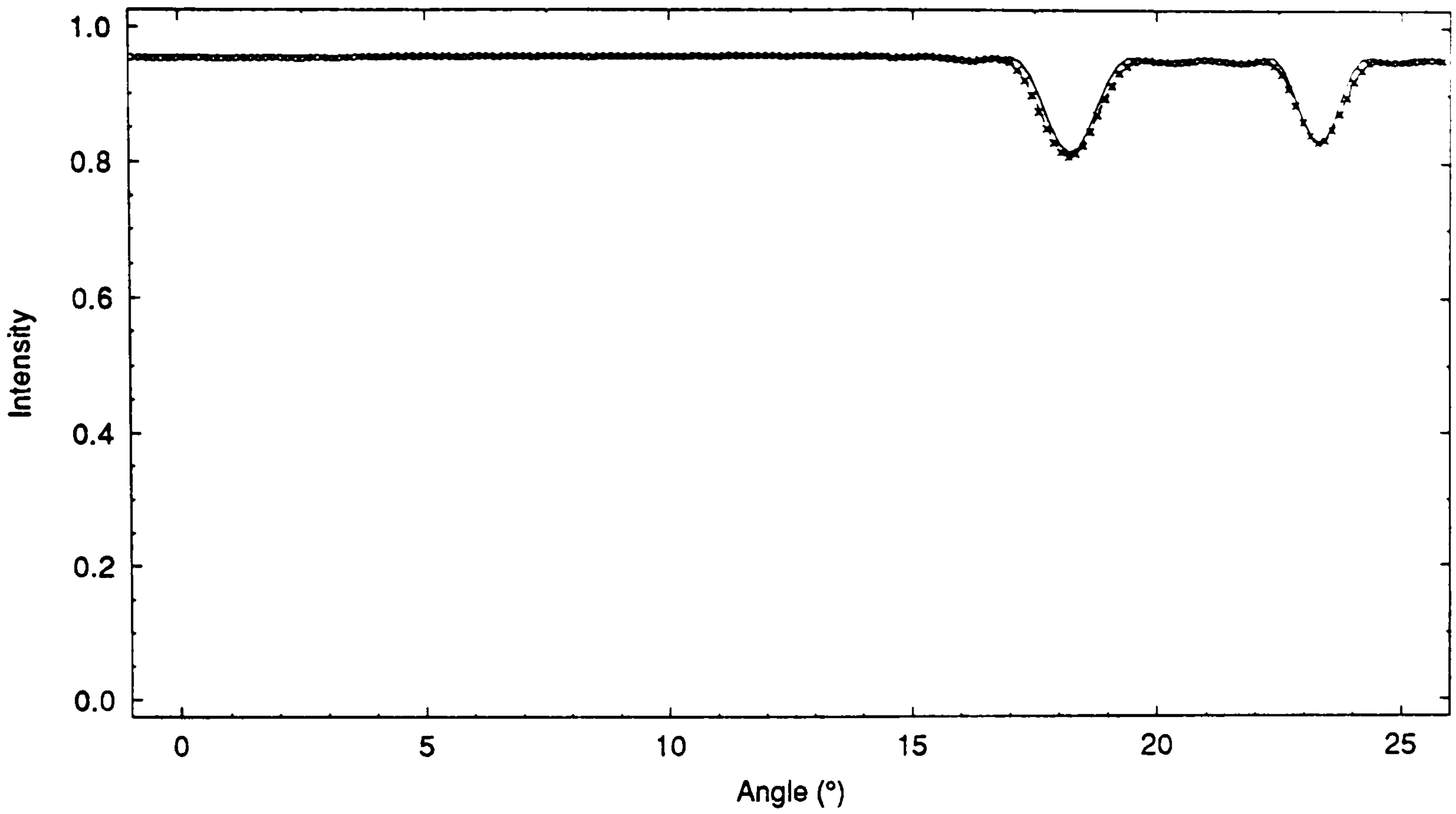


(b) 200 mJ / cm$^2$ ($n_{11}$=0.00435, $n_{12}$=0.0047, $n_{13}$=0)

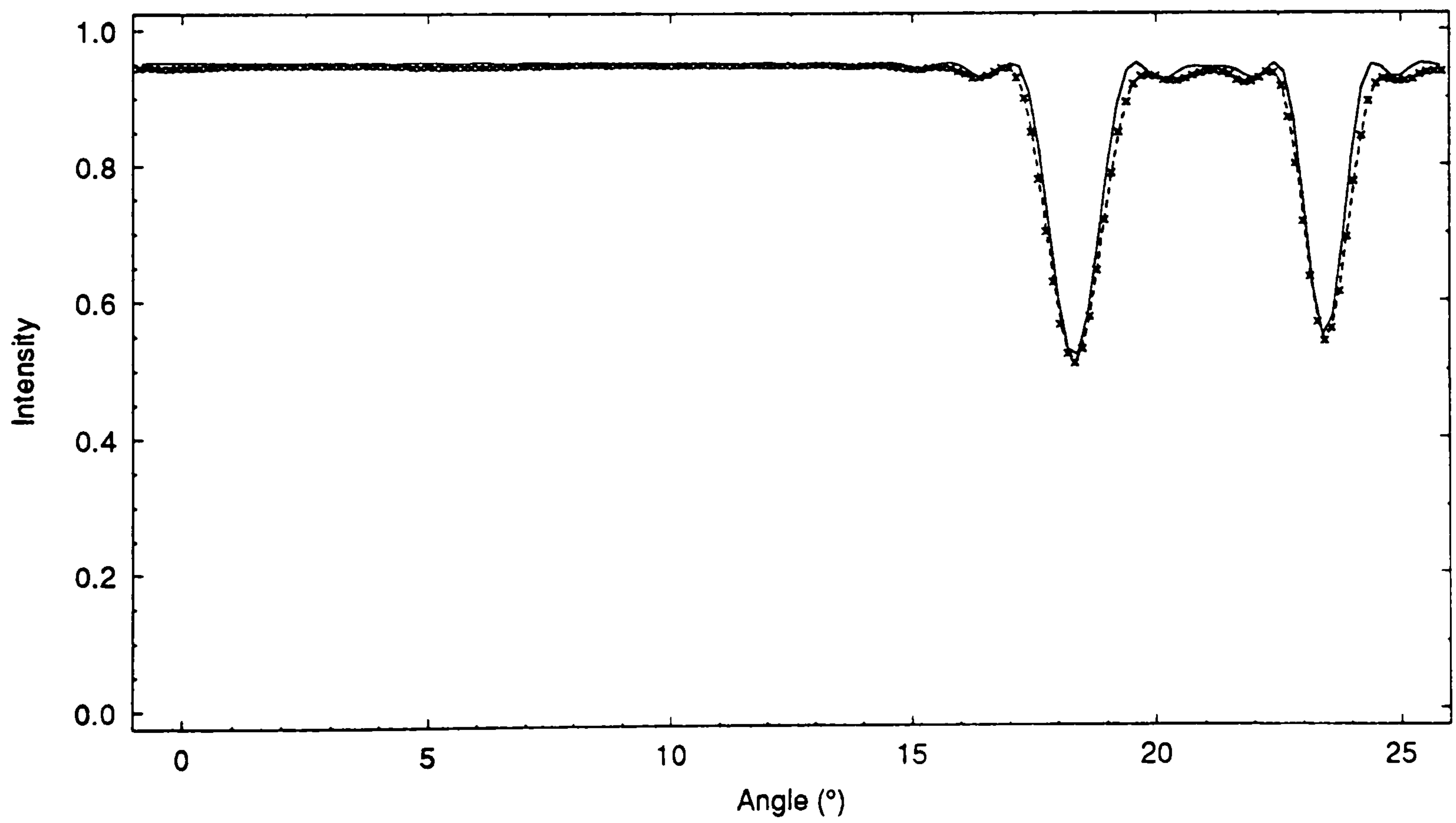


Figure 6.10 Theoretical matching (solid line) of experimental (dashed line) angular transmittance scans as a function of exposure energy for recording angles 17° and 22°.

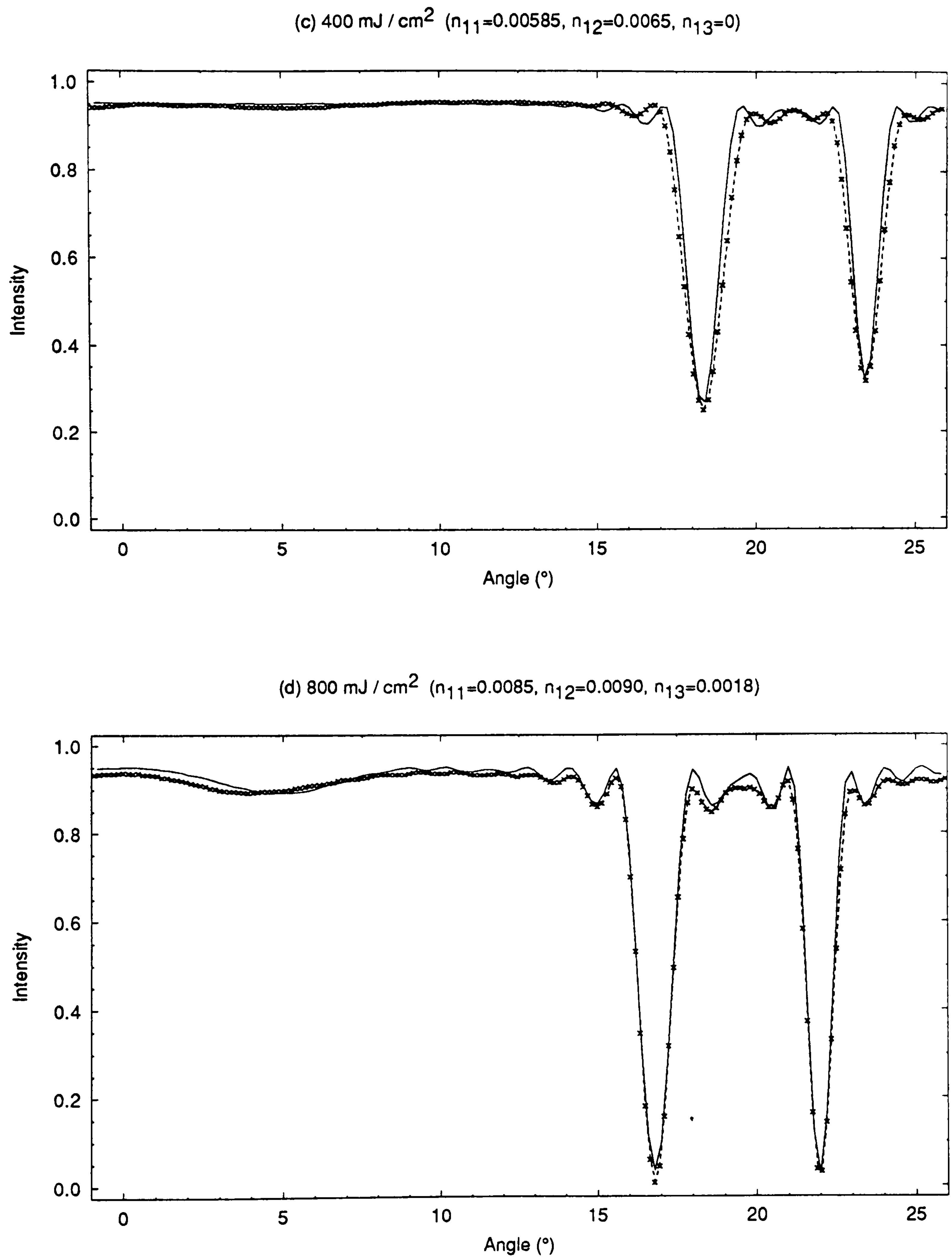


Figure 6.10 (Continued).

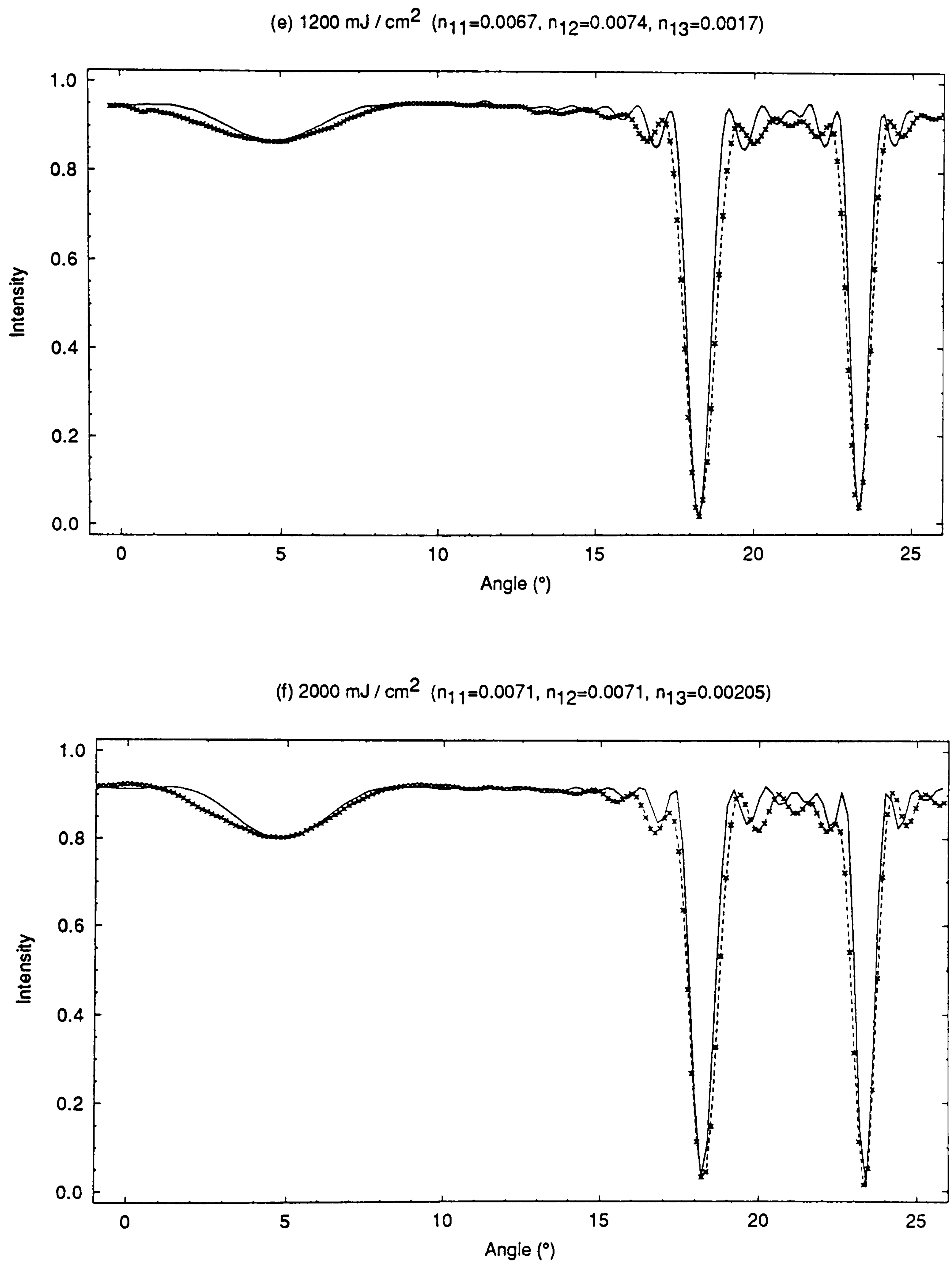


Figure 6.10 (Continued).

However, here is no noticeable dramatic change in the efficiency of $G_1$ or $G_2$ due to the formation of this grating.

Good theoretical fits are found for all the scans using the above theory. The details of each fit may be found above each curve. It is interesting, however, to note that although the modulation of $G_2$ is consistently greater than that of $G_1$ (due to absorption at recording), we see that, at higher exposures, the efficiency difference is not as large as would be expected, i.e. the efficiency of $G_2$ is being suppressed by the detrimental contribution from $G_3$.

### 6.5.2 *Set (b):* $\phi_1 = \pm 21°$, $\phi_2 = \pm 20°$

Figure 6.11 shows the experimental results and theoretical curve fits for holograms recorded at ±21° and ±20°. Once again, at low exposures we see one dip slightly deeper than the other, due to absorption at recording. The theoretical modulation values consistently show the grating $G_2$ to be slightly stronger than $G_1$ . However, as the exposure energy is increased we can see the formation of a wide dip centred on 0°. This is due to the formation of the grating $G_3$ which is so small that it is effectively replaying around 0° and thus displays very low angular selectivity. We notice that as the exposure energy increases, the efficiency value of $G_2$ tends to decrease. This, again, is believed to be due to the $\pi$ phase difference between $G_3$ and the fundamentals (as described above). If this effect was due solely to absorption at recording, we would expect the dips to be reversed and $G_1$ to be smaller (as shown in the previous section for $\phi_3 = 0$).

## 6.6 Variation with wavelength

In Chapter 4 we measured the variation of gratings $G_1$, $G_2$ and $G_3$ with a change in wavelength. Using a simple first order theory taken from Kogelnik [Kog69] we calculated the modulation value for each grating at different wavelengths as if they were single independent recordings. The results, shown in Figure 4.11, showed the modulation values of $G_1$ and $G_2$ to decrease with an increase in replay wavelength, as expected.

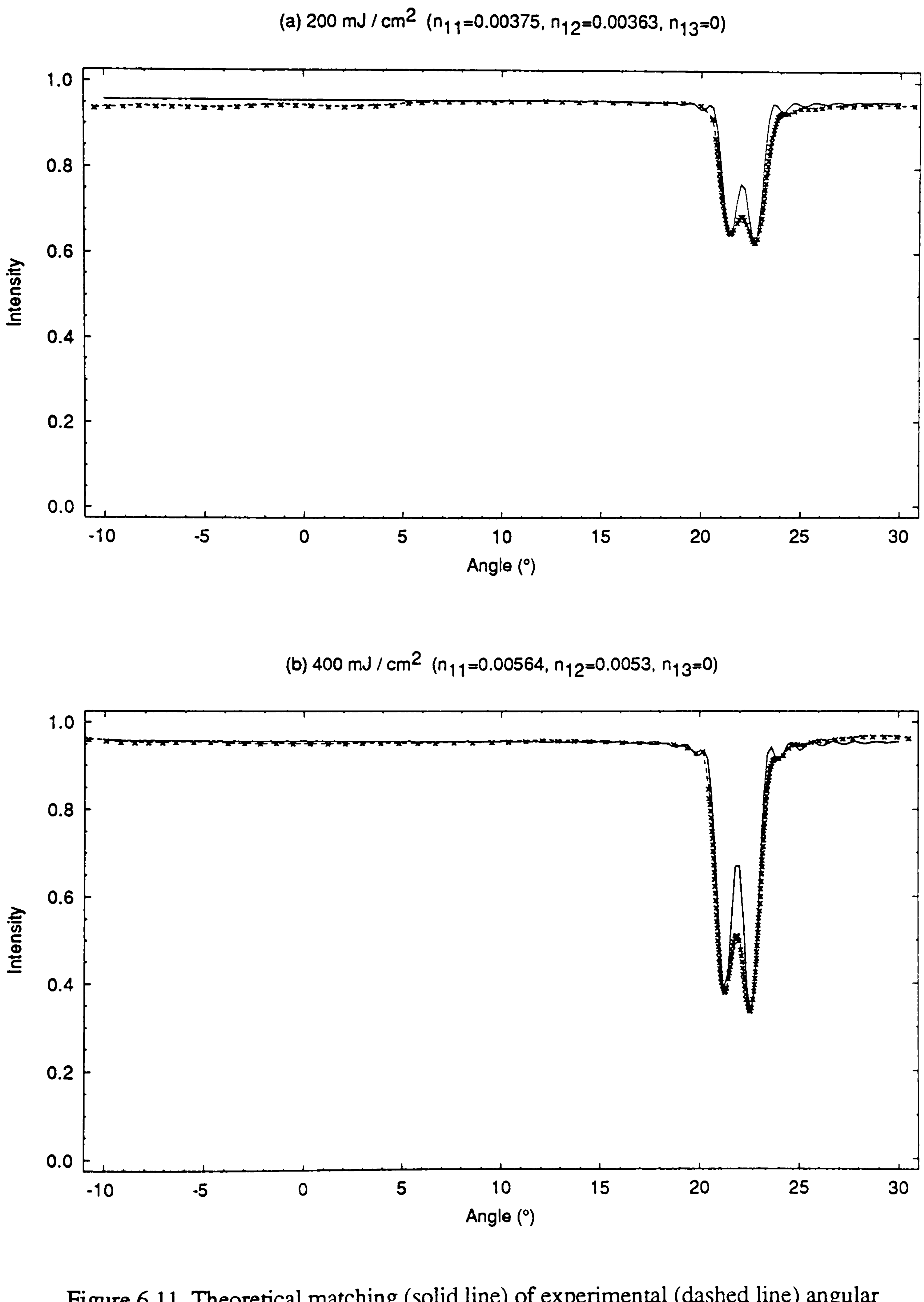


Figure 6.11 Theoretical matching (solid line) of experimental (dashed line) angular transmittance scans as a function of exposure energy for recording angles 20° and 21°.

(c) 1000 mJ / cm$^2$ ($n_{11}$=0.0071, $n_{12}$=0.00738, $n_{13}$=0.0011)

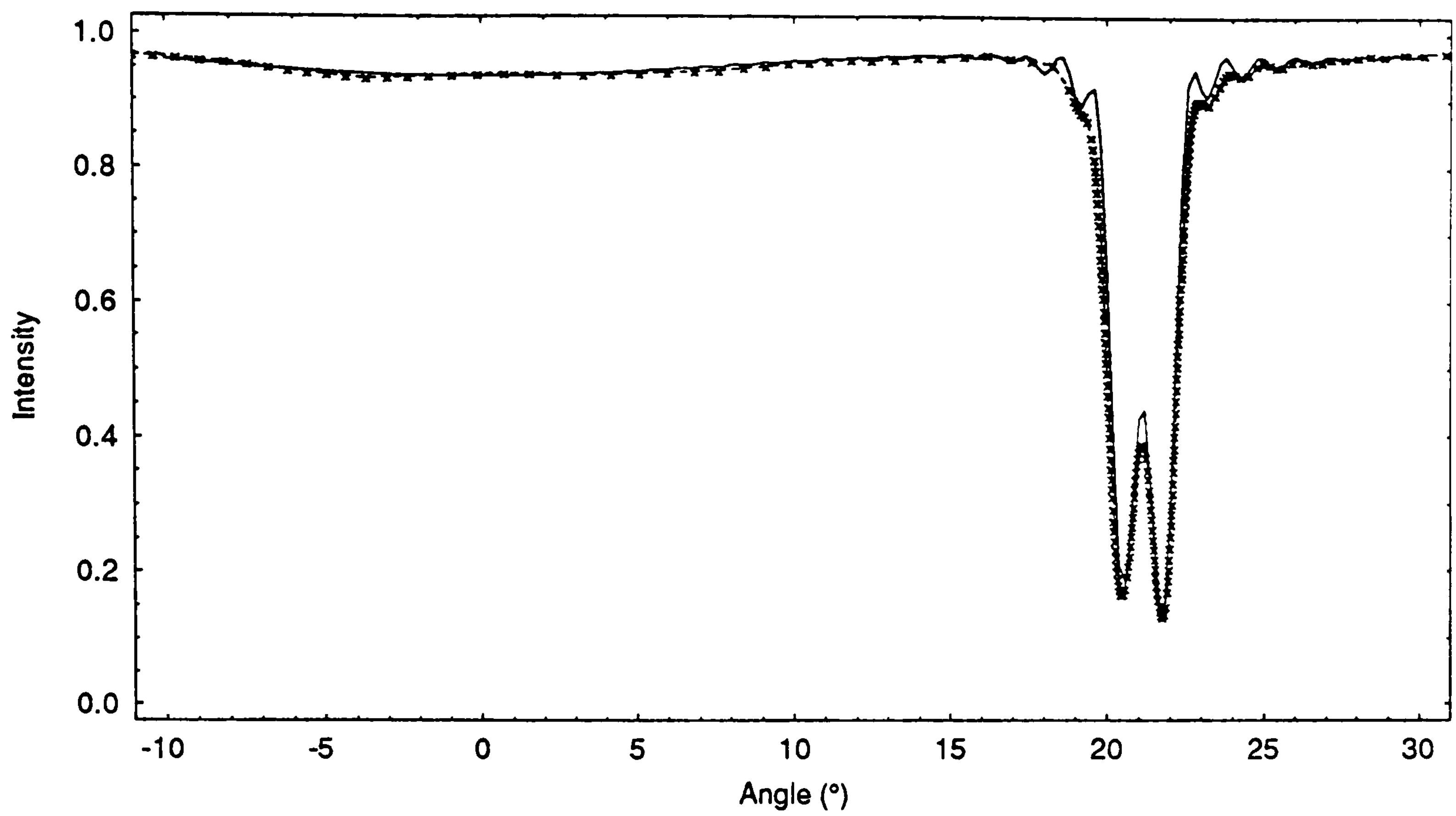


(d) 1500 mJ/cm$^2$ ($n_{11}$=0.00756, $n_{12}$=0.0076, $n_{13}$=0.00168)

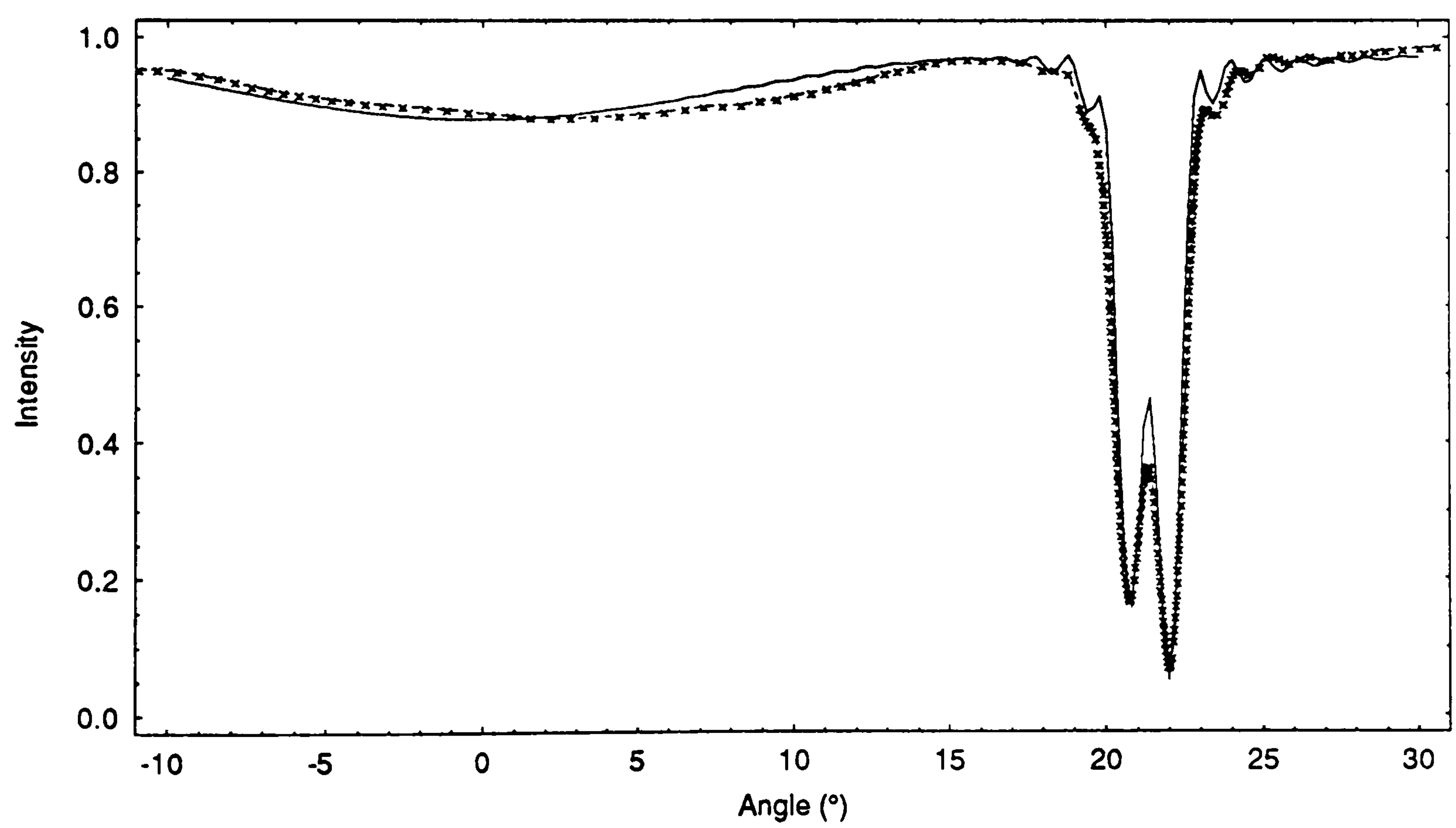


Figure 6.11 (Continued).

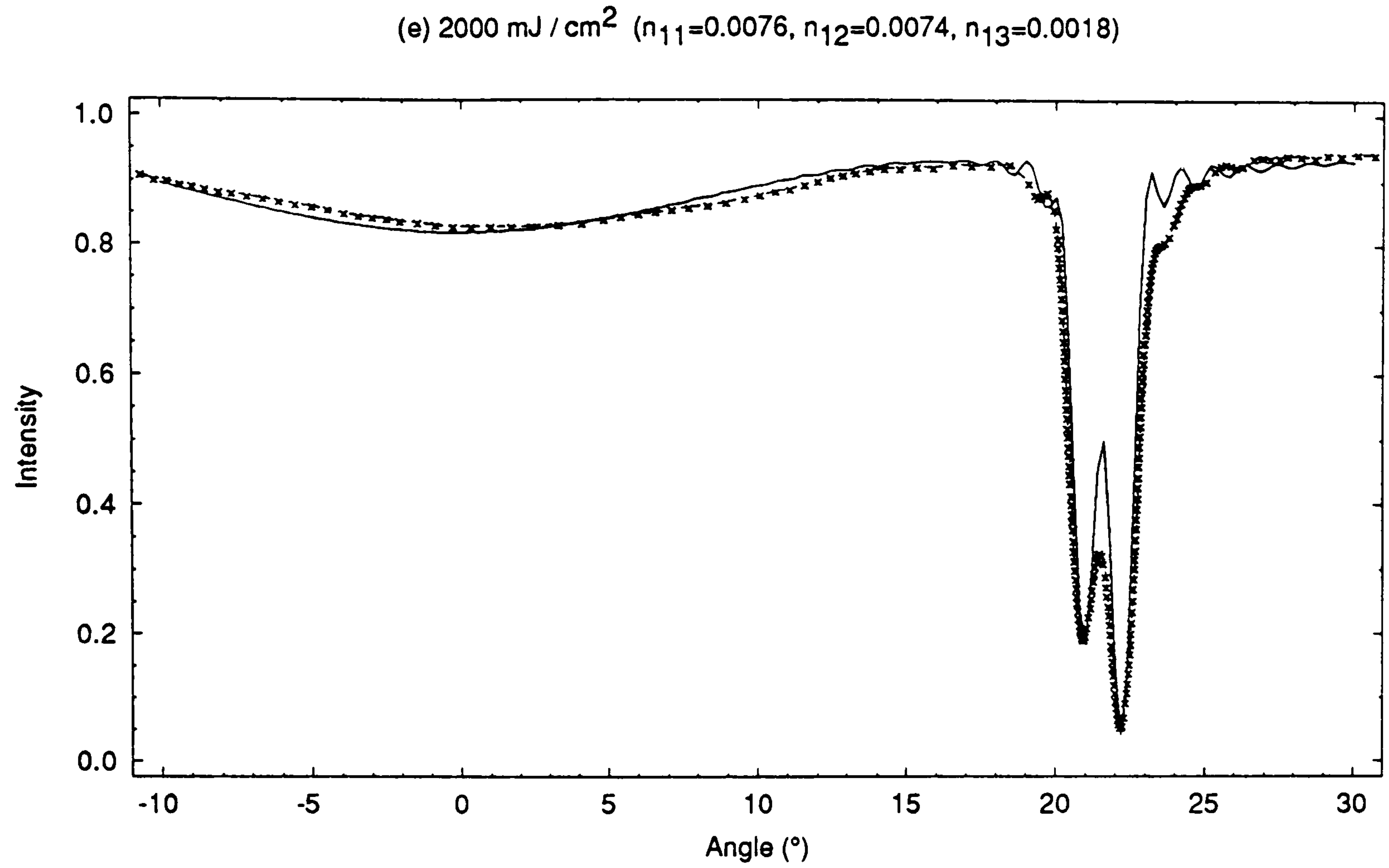


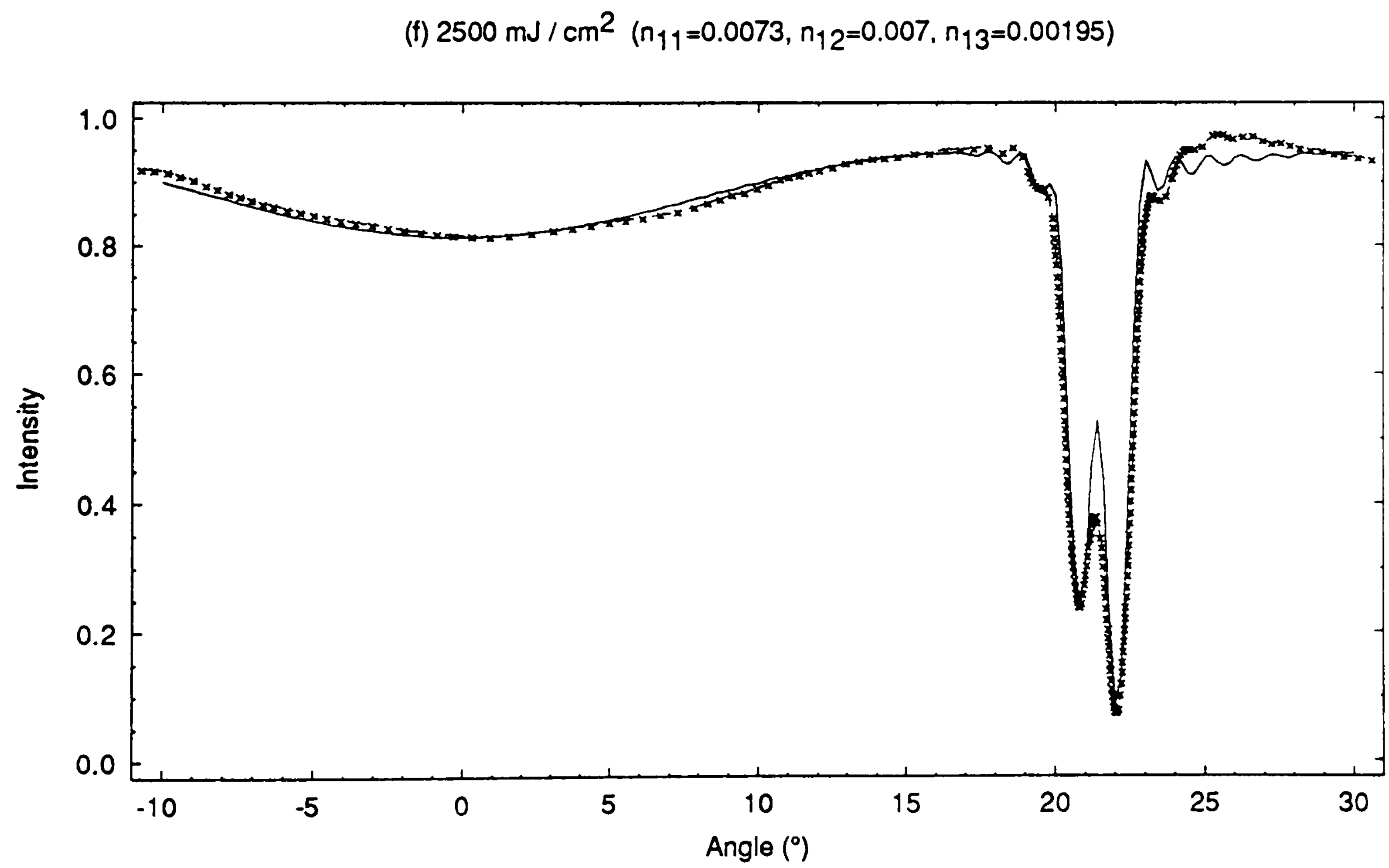


Figure 6.11 (Continued).

However, the result for the difference grating $G_3$ showed an apparent rise in modulation with increasing wavelength. When we compared this result to that of a single recording at low angles of incidence, we found that this rise was not due to the spatial frequency of the grating, since the modulation values of the independent recording were seen to drop.

In the present chapter, we have developed a theory which shows that the efficiency of the difference grating is dependent on both the modulation of the nonlinear grating and grating interactions between the two fundamental recordings. Thus, the dispersion results from Chapter 4 were not accurate and this more complex model is required to measure the variation of modulation with wavelength.

For an explanation of the replay of the fundamental gratings $G_1$ and $G_2$, let us look once more at Figure 6.2. At the Bragg angle for $G_1$ we will also obtain a contribution from the other gratings $G_2$ and $G_3$. However, if the gratings are sufficiently separated (as is this case), the effect from $G_2$ and $G_3$ will be relatively small allowing the general trend of $G_3$ to follow that of a single grating, i.e. a reduction in modulation as replay wavelength is increased. Similarly $G_2$ will show normal dispersion results and drop with an increase in wavelength.

When replaying at the Bragg angle for $G_3$ the situation is different, especially if $G_1$ and $G_2$ have high modulations. In this case the effect of the grating vector relations $\pm(\overline{K}_1 \pm \overline{K}_2)$ due to grating interactions at the Bragg angle for $G_3$ will have a more significant contribution to the efficiency. At a high wavelength we expect a small Ewald circle (see Figure 6.12 (a)). This allows the fundamental gratings to interact and replay through the off Bragg vectors $2\psi_x$, which detracts from the diffractive power of $G_3$ (due to the difference in phase). However, as the replay wavelength is decreased, the grating vector interactions $\pm(\overline{K}_1 \pm \overline{K}_2)$ will replay through the off Bragg vectors $2\psi_y$, (see Figure 6.12 (b)) where $\psi_y < \psi_x$, thus increasing their detrimental effect on $G_3$.

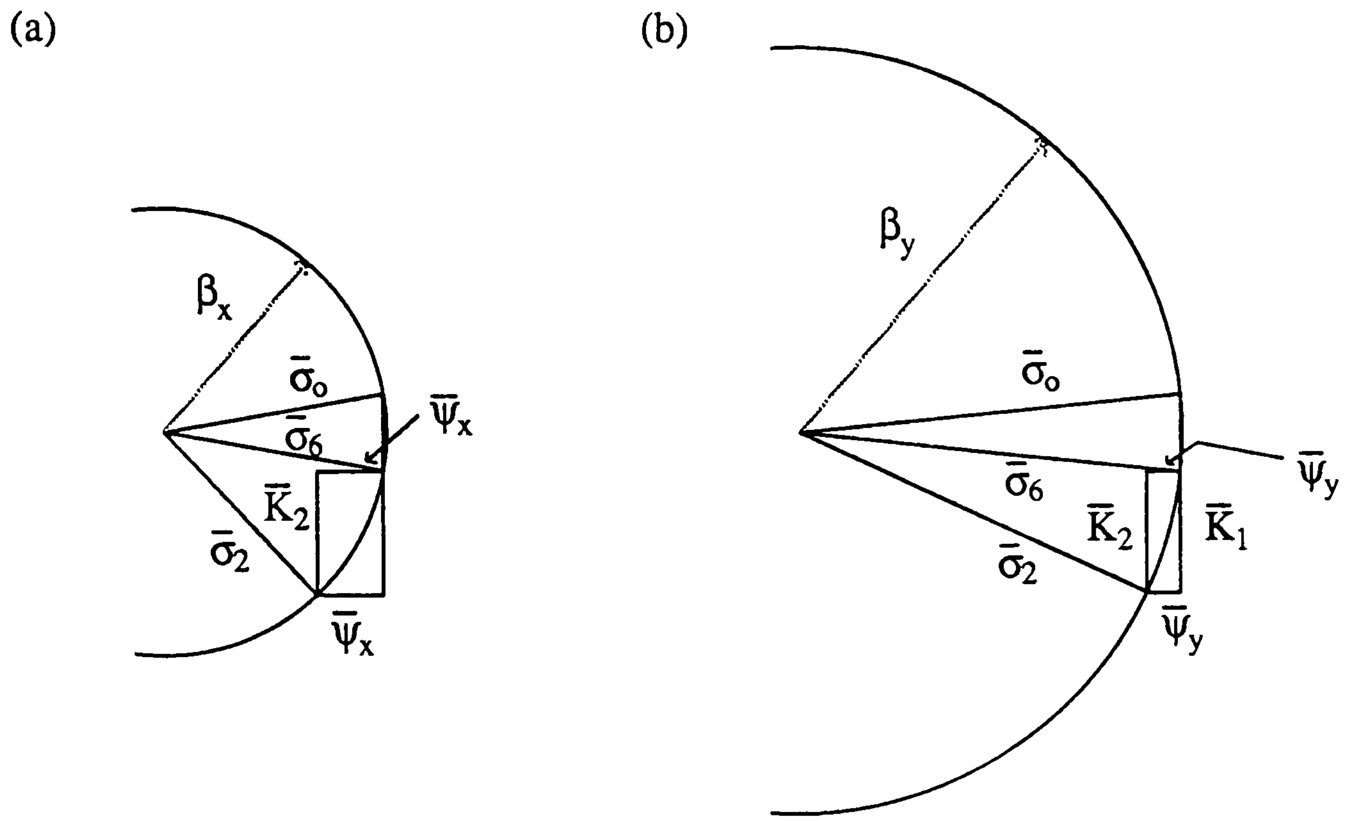


Figure 6.12 Ewald circle representing the replay of grating interactions at (a) long and (b) short wavelengths.

In order to demonstrate the above explanation, results of transmittance versus replay angle (see Figure 4.10) were matched at different replay wavelengths using the above coupled wave model. Figures 6.13 (a), (b), (c) and (d) show experimental (dashed line) and theoretical (solid line) plots for replay at 400 nm, 514.5 nm, 600 nm and 700 nm respectively. The modulation values used to match theory and experiment are plotted in Figure 6.14. These show a tendency to drop slightly with an increase in replay wavelength. For comparison, modulation values are also plotted as a result of using a simple theory which describes each dip as a single, independent recording. These show an apparent rise in value with wavelength. It appears that the inclusion of multiple grating interactions is therefore quite important for accurate measurement of grating dispersion characteristics.

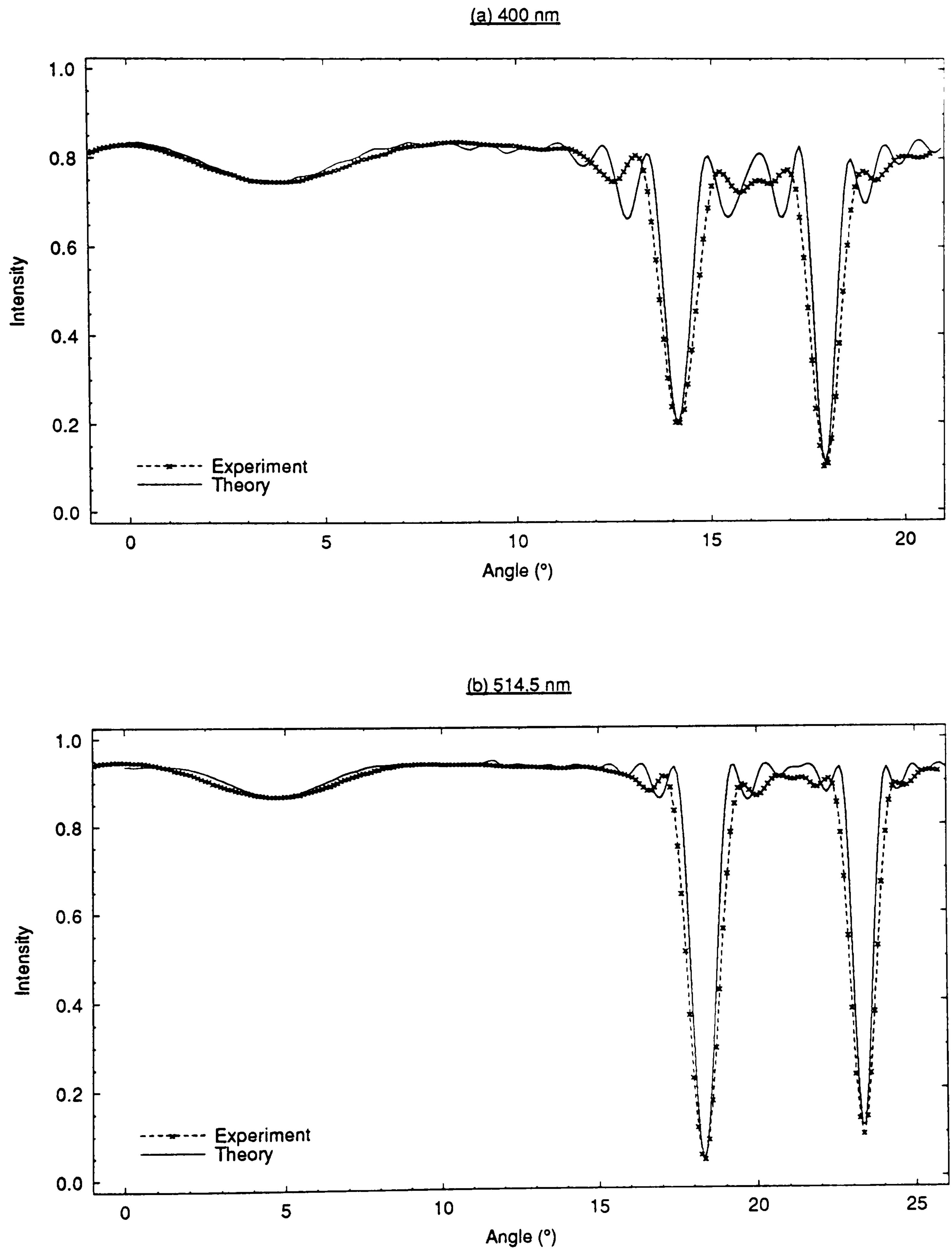


Figure 6.13 Theoretical matching (solid line) of experimental (dashed line) angular transmittance scans as a function of replay wavelength for recording angles 17° and 22° and total exposure energy = 1200 mJ / $cm^2$.

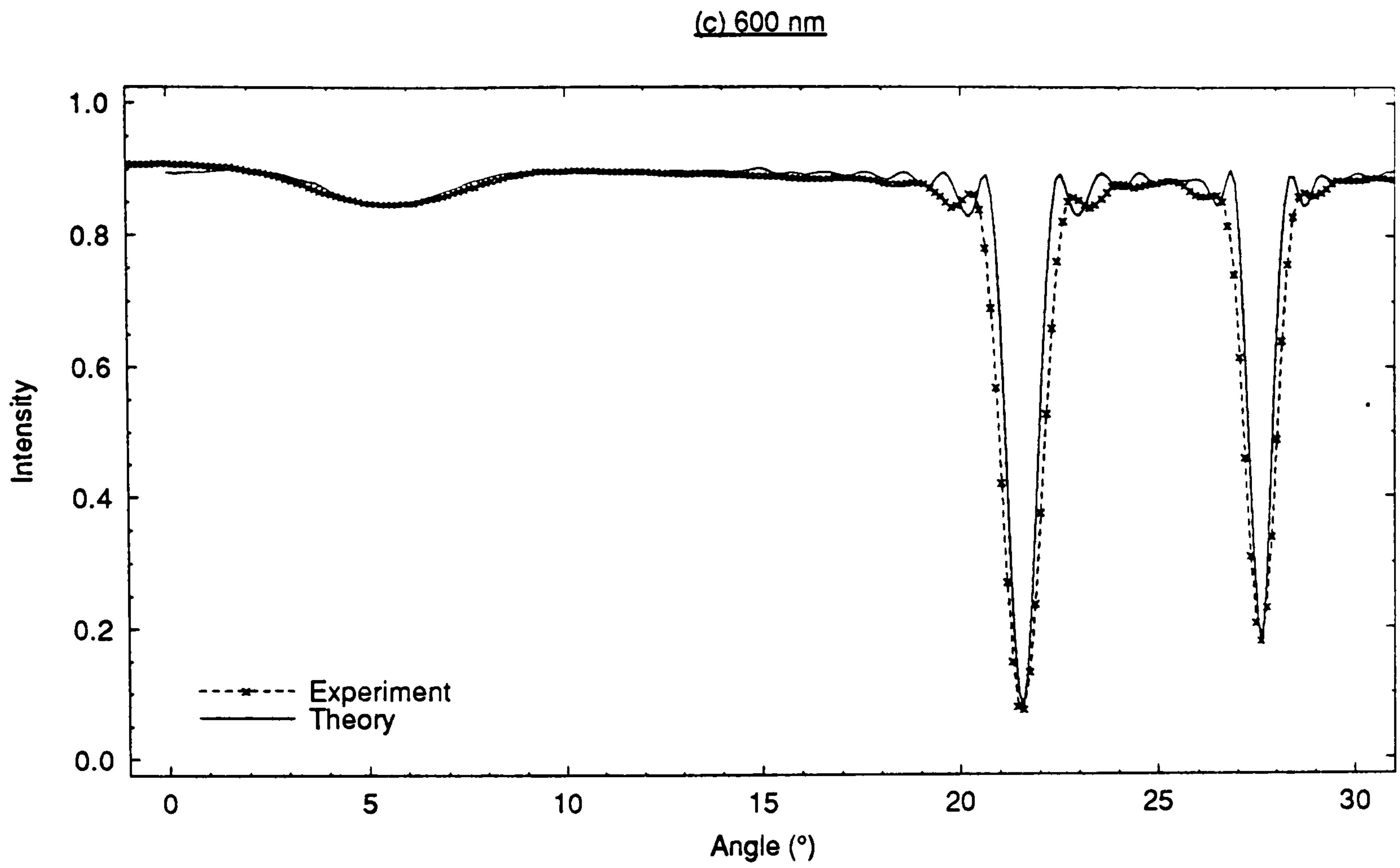


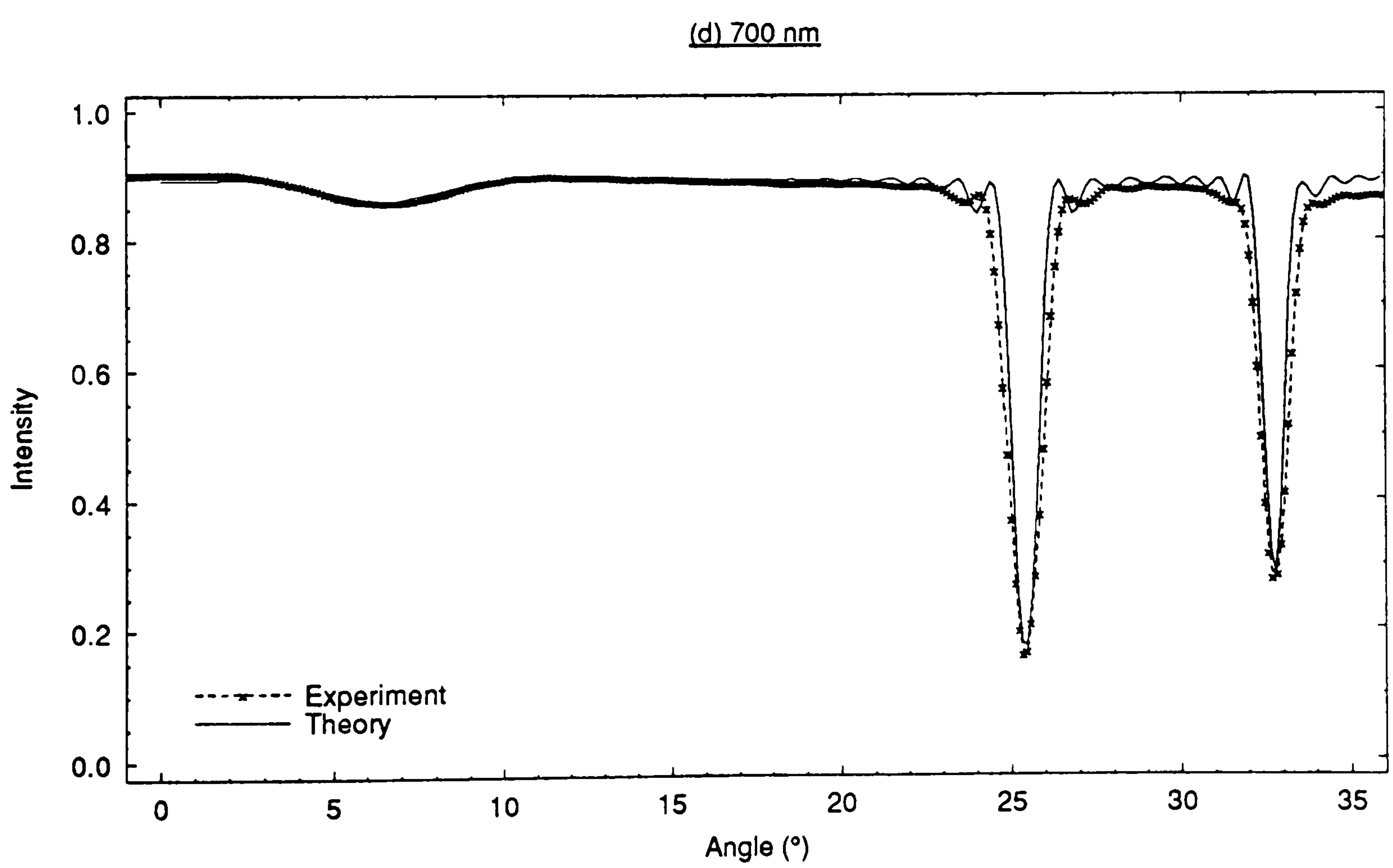


Figure 6.13 (Continued).

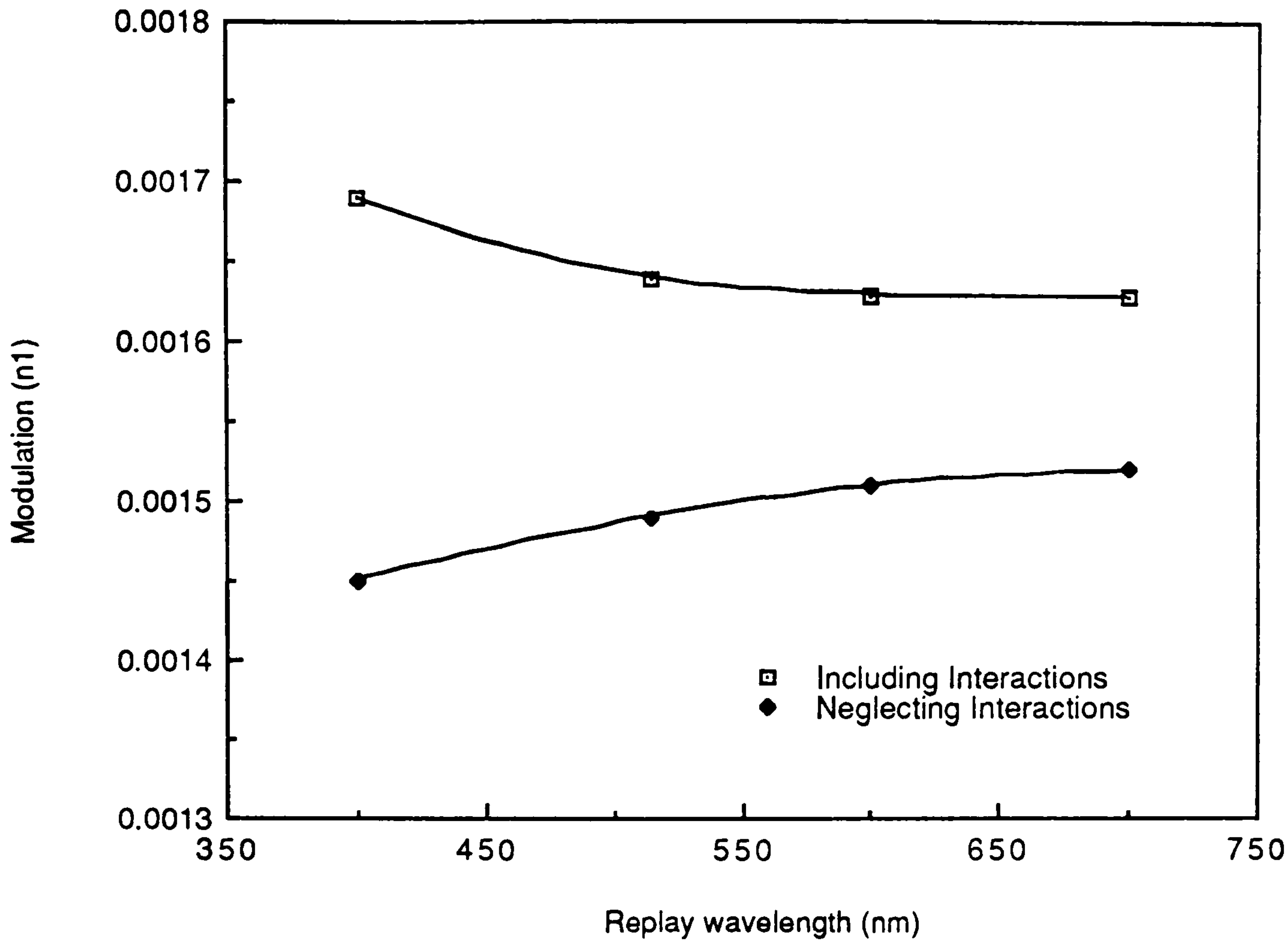


Figure 6.14 Dispersion plot of modulation versus replay wavelength for difference grating $G_3$, (a) neglecting and (b) including the effect of grating interactions.

## 6.7 Summary

In this chapter I have introduced a complex coupled wave model which is capable of describing the replay of two sequentially recorded transmission gratings ($G_1$ and $G_2$) in dichromated gelatin. The model allows for the formation of a third difference grating ($G_3$) at high exposure energies, due to the nonlinear recording characteristic of DCG. Multiple grating interactions between each grating were considered. The model was used to match experimental results of increasing exposure energy and decreasing angular separation between recording angles. Good agreement was found. The model was also used to explain the apparent 'rise' in modulation with increasing wavelength for the difference grating $G_3$ found in Chapter 4. In conclusion, it has been observed that, when operating at high modulation levels, the combined effect of nonlinear gratings and multiple interactions cannot be ignored.

# *Chapter 7*

# *Silver halide noise gratings recorded in dichromated gelatin*

## 7.1 Introduction

The majority of holographic recording materials exhibit some degree of inhomogeneity, a consequence of which is the scatter of incident light. In particular, if a hologram is recorded using coherent illumination, this scattered light can interfere with the incident beam forming what are known as *noise gratings*. These spurious gratings can severely limit the quality of practical holographic optical elements by reconstructing the recorded scatter at replay.

The existence of holographic noise gratings has been recognised for several years and has been observed in a variety of recording materials. In 1970, Biederman [Bie70] first recognised the existence of recorded scatter in silver halide emulsions. In his experiment he noticed an increase in scatter at replay when using a coherent light source. Noise gratings have since been reported by several authors in the form of *scattering rings* [Jam77] in photopolymers [Mor73] [For73] [For75] and photorefractive crystals [Mag74] [Ava78] [Vor80] [Ewb86]. Forshaw [For73] [For74] was the first to explain this far field replay of recorded scatter in terms of Ewald spheres and the concept was later modified by Ragnarsson [Rag78].

The majority of work in this field has been carried out by investigating the recorded noise in silver halide emulsions. These emulsions contain small grains of silver halide and additional dyes which are randomly distributed throughout a gelatin support [Jam77]. The dimensions of these range from about 10 nm in the case of Soviet emulsions to approximately 90 nm [Phi80]. A typical value may be approximately 30 to 40 nm. Although Biedermann [Bie70] [Bie75] was first to recognise this recorded scatter in silver halide Syms and Solymar [Sym82b] [Sym83b] were first to describe the replay of noise gratings in terms of angular transmittance information. Later Ward *et al* [War84] altered the processing procedure [Coo84] for reflection holograms and discovered that they could deplete the transmitted beam to almost 0%. Riddy and Solymar [Rid86] [Rid88] have made a comprehensive study of spurious scatter within silver halide emulsions culminating in a model capable of simulating the recording of up to 8000 planar noise gratings. More recently, Kostuk and Sincerbox [Kos88] have described the replay of noise gratings with different polarisations and Wang and Kostuk [Wan89] have studied the efficiency of noise gratings formed in silver halide at infrared wavelengths. Also, Ward and Solymar [War89] and Solymar and Riddy [Sol89b] have observed the effect of noise gratings when recording at high beam ratios.

Dichromated gelatin is essentially a homogeneous material which exhibits very little scatter. However, the recording of noise has been described by Meyerhofer [Mey73] when recording the hologram of a diffusing screen. Newell [New87] and Blair and Hubel [Bla89c] have also recorded noise gratings in DCG by copying from silver halide master gratings to DCG.

## 7.2 Noise gratings

When a single, coherent wave is incident on silver halide emulsion, light will be scattered in both forward and backward directions by the silver halide grains. These weak beams will then interfere simultaneously with the incident wave forming many gratings of varying angle and spatial frequency. This may be represented in the form of planar gratings by the Ewald sphere model. Although this scattering occurs in all three dimensions, it is not easy to visualise. Therefore, for simplicity, we will describe a cross-section of the recorded noise gratings in terms of the two dimensional circle shown in Figure 7.1.

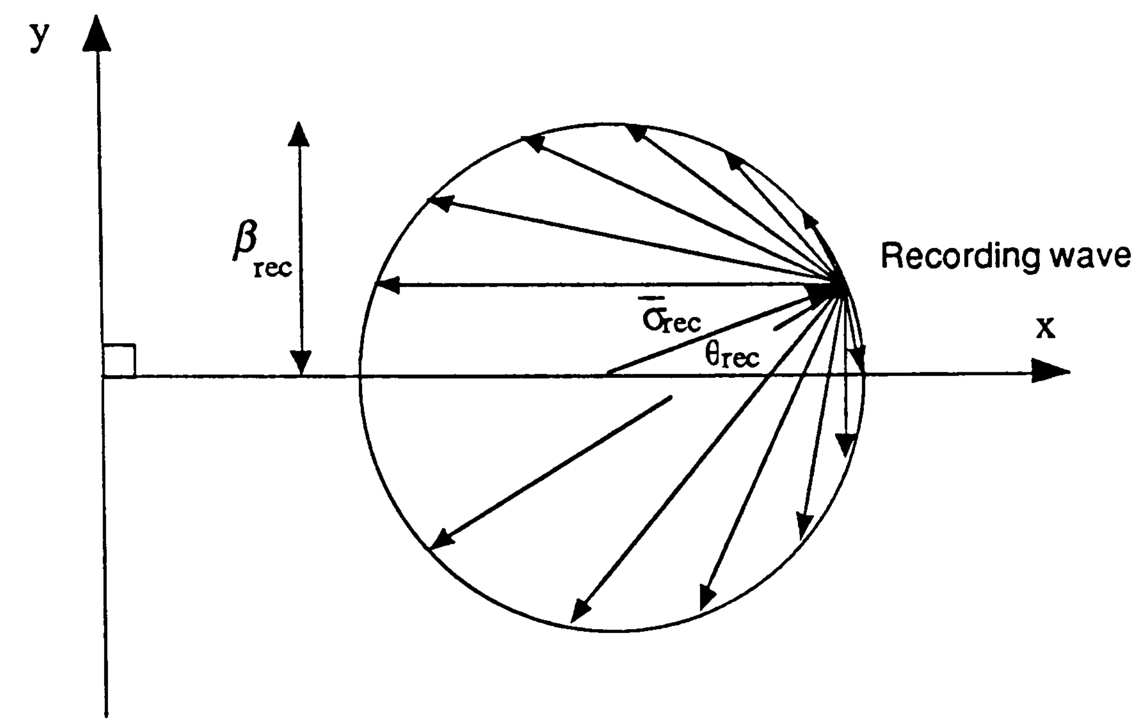


Figure 7.1 Recording geometry for noise gratings using two dimensional Ewald sphere.

Here, we see the wave with vector $\overline{\sigma}_{rec}$ incident at $\theta_{rec}$ propagating with constant $\beta_{rec}$. The surface of the sphere then forms the locus of all the end points of the recorded grating vectors. Riddy [Rid88] has proposed that this scattered noise is due to a large amount of scatter by a small number of silver halide particles.

To replay the noise grating, it is necessary only to replay each grating simultaneously. Thus, we expect the optimum on - Bragg condition to occur if the replay angle $\theta_{rep}$ is the same as at recording and the propagation constant $\beta_{rep}$ equals $\beta_{rec}$ (i.e. the off Bragg parameters for all gratings at replay are zero)

If, however, the replay conditions are not identical to recording then it is not possible for all the recorded gratings to be replayed on - Bragg at any one time. This may happen if (i) the replay wavelength is not the same as the recording wavelength, (ii) the average refractive index changes, (iii) there is a change in thickness or (iv) the replay angle is different from that at recording. Optimum replay will then occur when we minimise the local off - Bragg condition (see Reference [Rid86]). Figure 7.2 shows such a case for optimum replay with a larger Ewald sphere.

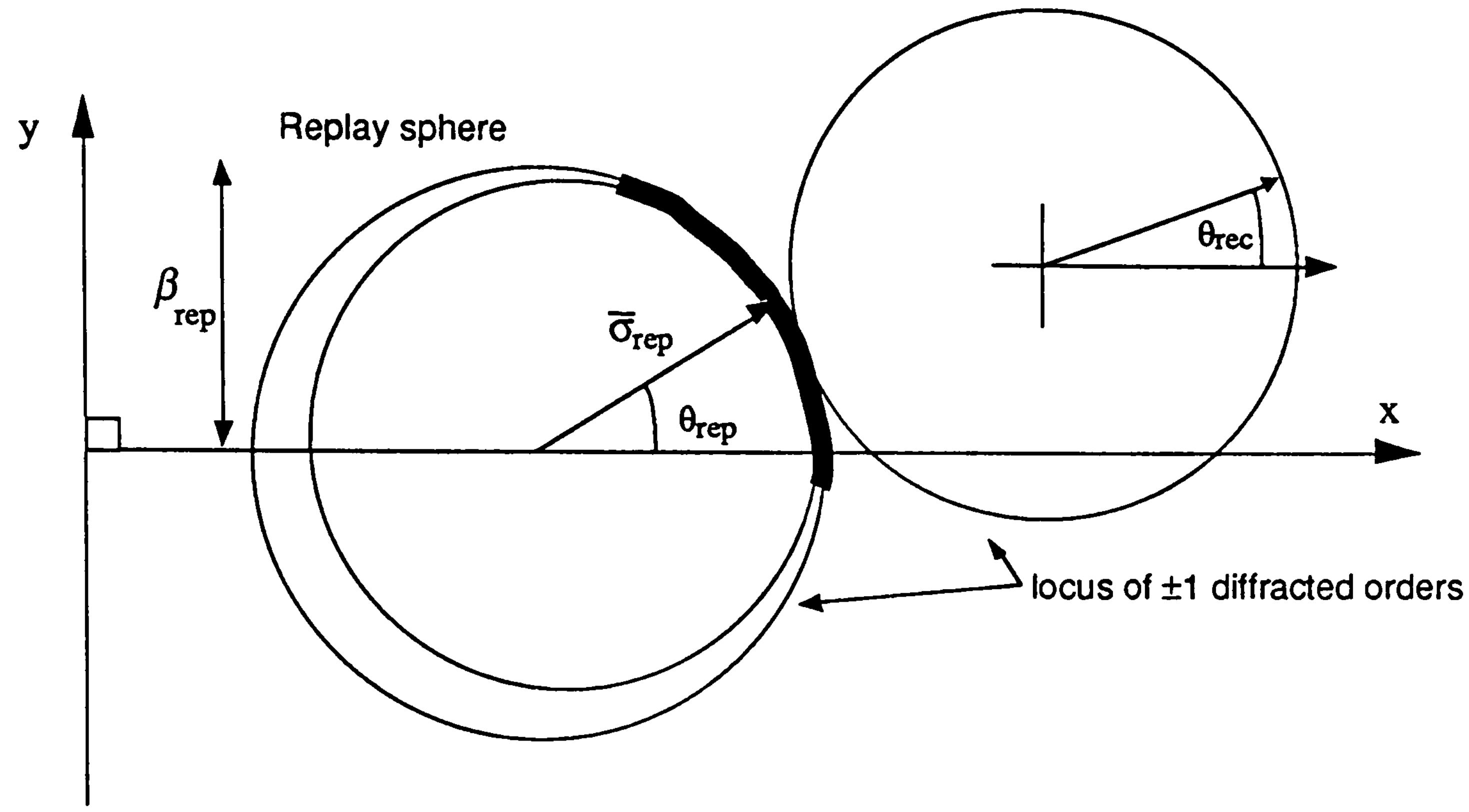


Figure 7.2 (a) Optimum replay of noise gratings when $\beta_{rep} > \beta_{rec}$. Replay at a *higher* angle than recording.

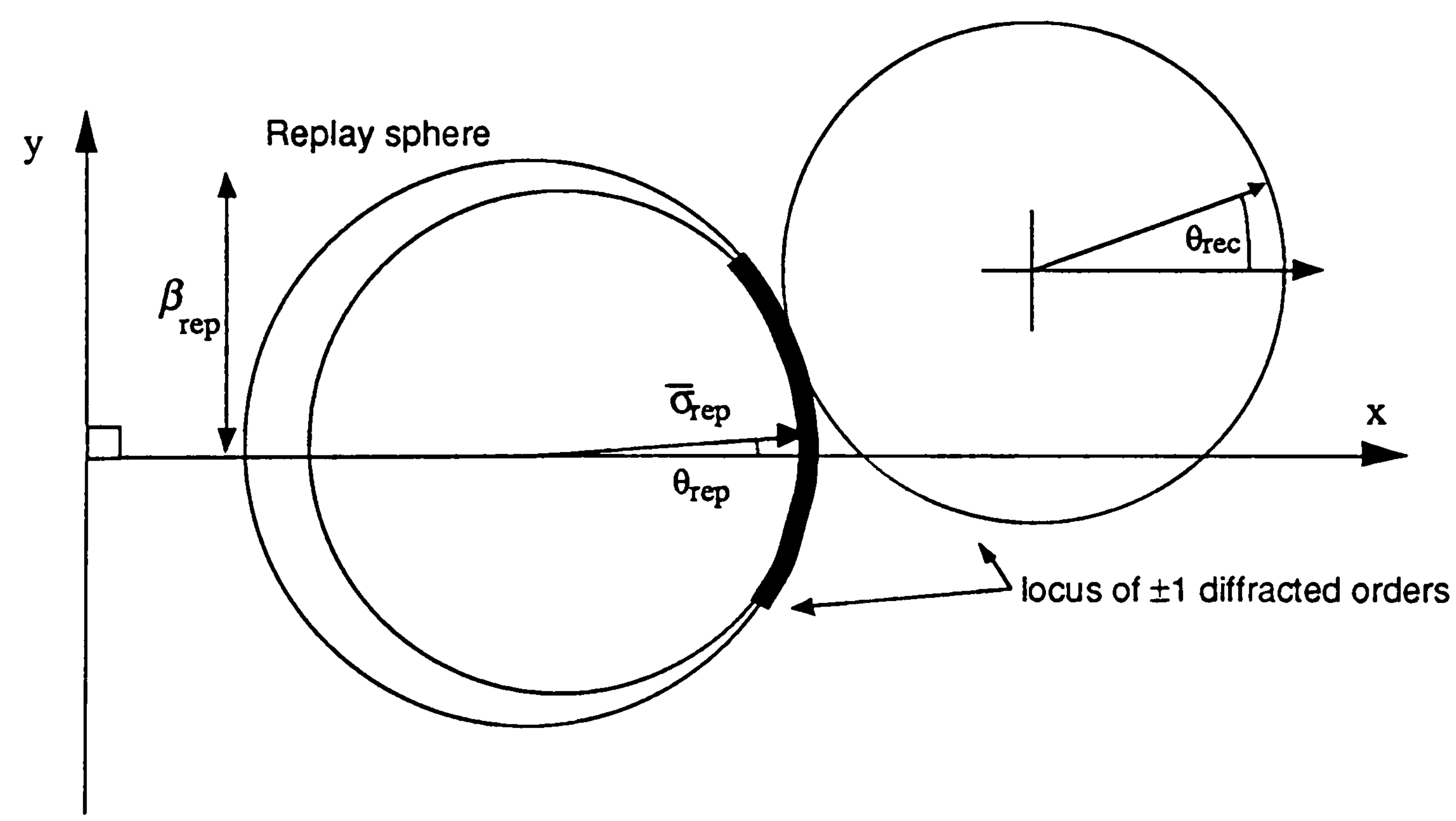


Figure 7.2 (b) Optimum replay of noise gratings when $\beta_{rep} > \beta_{rec}$. Replay at a *lower* angle than recording.

This is equivalent to a shorter replay wavelength or an increase in the average refractive index. The replay wave is represented by the vector $\overline{\sigma}_{rep}$ and the replay angle is represented by $\theta_{rep}$.

We find that local maxima occur with reduced efficiency at angles where the radius of curvature of the replay sphere is similar to that of the locus of grating vectors. These angles of increased scatter are denoted by thick lines. Notice also that two spheres are drawn, representing the locus of both ±1 diffraction orders of all grating vectors. In this example, we may neglect the conjugate order, however, if we replay away from the Bragg condition, we cannot.

If swelling or shrinkage occurs, each $\overline{K}$ - vector will be affected in the direction perpendicular to the surface of the hologram leading to a locus of grating vectors in the shape of an ellipsoid. Figure 7.3 shows replay of a set of noise gratings which have suffered swelling. Similarly shrinkage would cause the ellipse to become 'fatter' in the x direction.

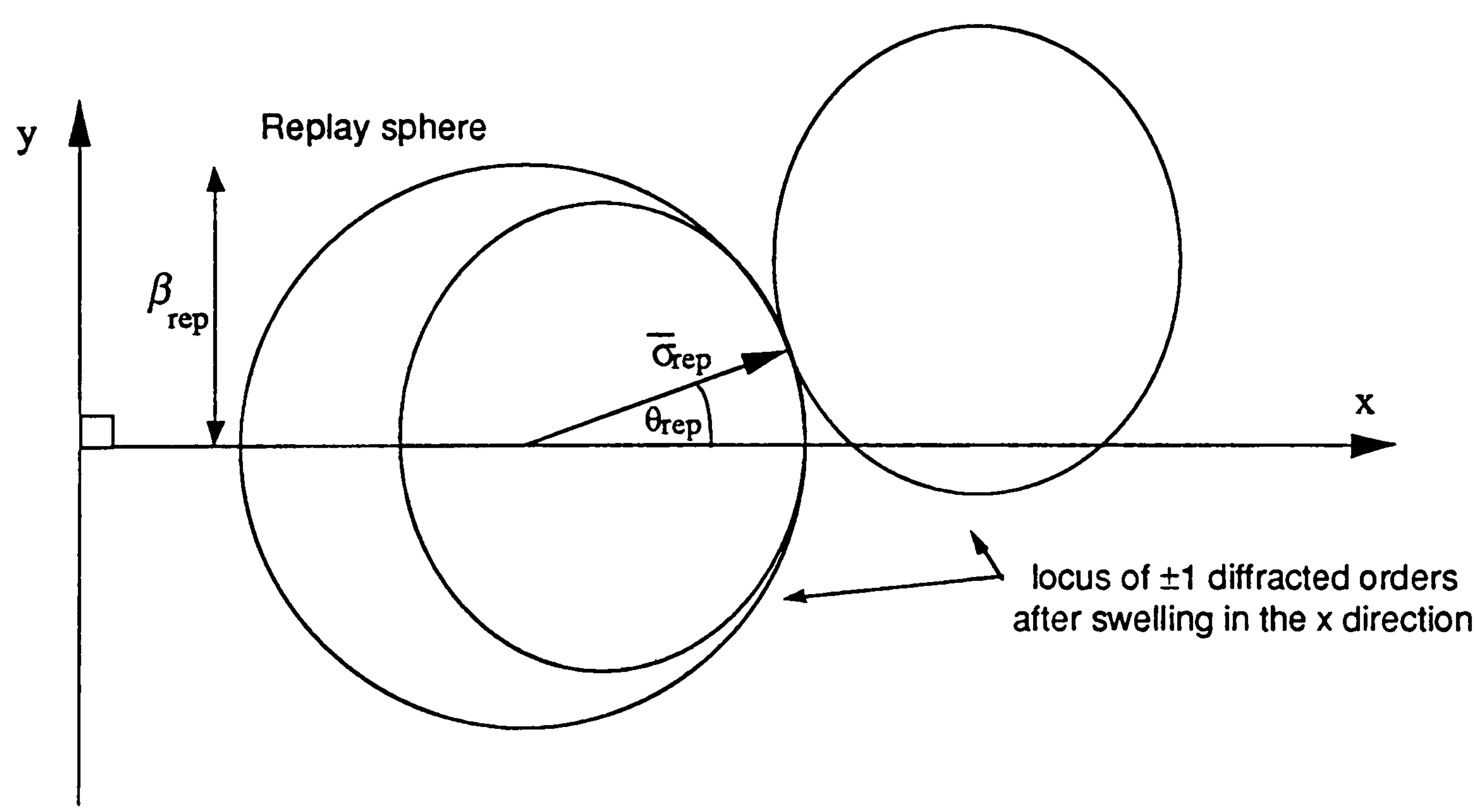


Figure 7.3 Optimum replay of noise gratings after swelling.

Figure 7.4 shows the replay of scattered noise at an angle away from the optimum. Here we see that the replay Ewald sphere intersects both the +1 and -1 order spheres along the lines A and B. In three dimensions, A and B represent circles and thus form two cones of scattered light. These may be displayed on a screen and are known as *scattering rings*. Scattering rings were first described in the field of X-ray crystallography [Jam48], but were first applied to holography by Moran and Kaminow [Mor73] in 1973.

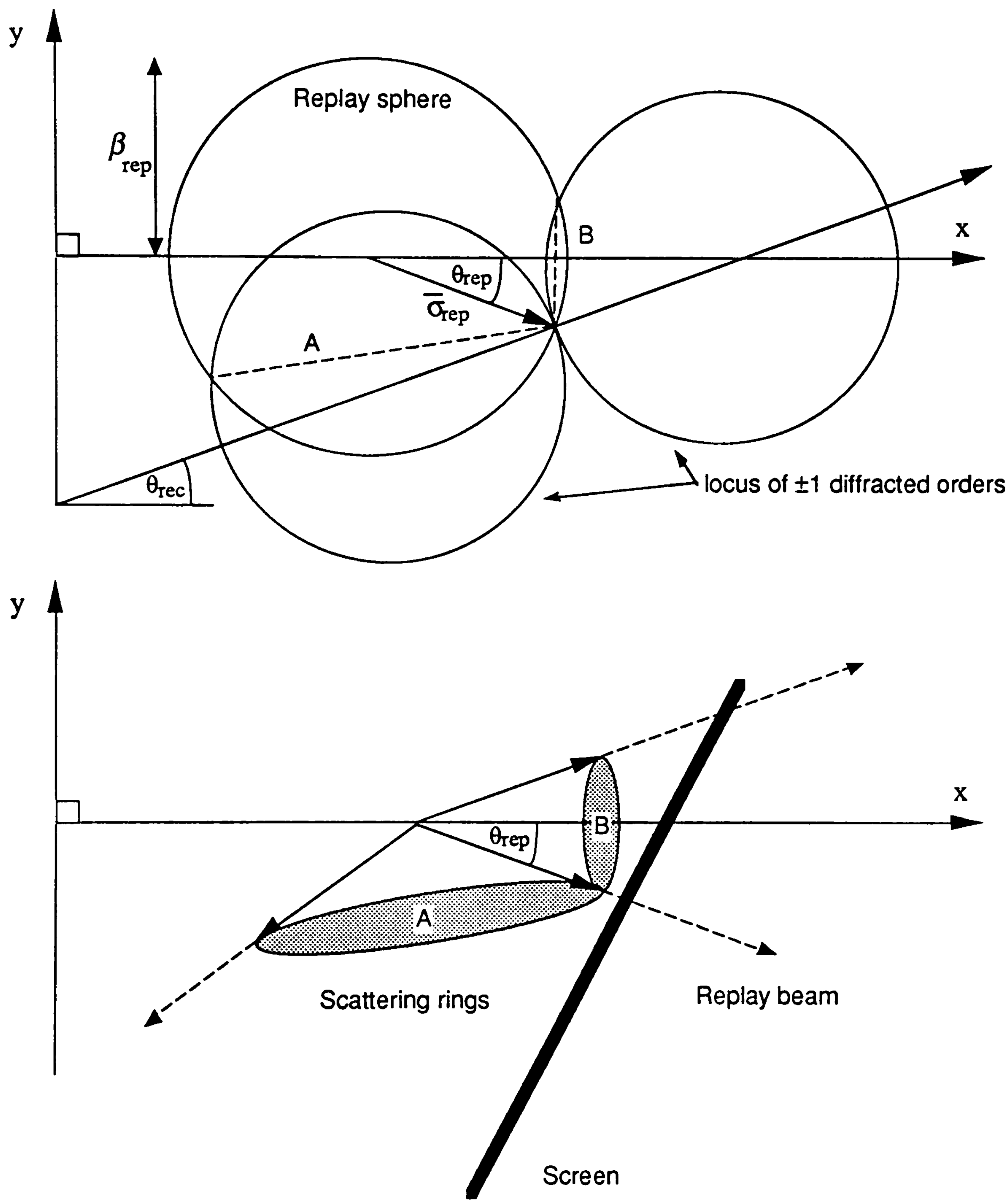


Figure 7.4 Replay of scattered noise away from the optimum on - Bragg condition and the formation of scattering rings.

When we replay a silver halide hologram, we find that there are two sources of noise. The first is known as primary scatter and is due to the recorded noise gratings as described above. However, we also obtain random noise due to the granular nature of the processed film. It then becomes difficult to distinguish between the two types.

If we wish to study solely the recorded noise, a good method is to record the scattered radiation holographically in a noise free medium. Newell [New87] has shown that it is extremely difficult to record noise gratings in DCG due to its high homogeneity. This makes DCG an ideal tool for studying the noise field of silver halide emulsions at recording. In his D. Phil. thesis, Newell recorded transmitted scatter by placing a DCG plate behind silver halide emulsion and concluded that these transmitted noise gratings are dominant at replay.

In this chapter, we will investigate further the recording of silver halide scatter in dichromated gelatin. First of all, we will discuss briefly the response of noise gratings to varying exposure energy and replay wavelengths. We will then compare the relative scatter of three common blue / green sensitive holographic emulsions in terms of recorded noise gratings over a series of exposure energies. The effect of high modulation recording is observed. As part of a continuing investigation into noise gratings here at Oxford University, an experiment was carried out to study the significance of reducing the high angular components of noise gratings by separating the distance between the scattering ($AgH^+$) source and the recording medium (DCG). Results are presented in terms of both angular transmittance and scattering rings for transmitted and reflected scatter.

## 7.3 Experimental procedure

The geometry, shown in Figure 7.5, was used to record transmission noise gratings in dichromated gelatin. It shows a single, planar beam incident on a silver halide plate at $\theta°$ inside an index matching tank filled with Marcol oil. This is necessary to record only scattered noise and avoid the formation of gratings due to specular reflections at the plate / air boundaries. The beam passes through the plate scattering light in both the forward and backward directions. The noise grating is then recorded on a thick, 22 μm DCG plate by interfering the incident beam with transmitted scatter. The plates were held on a clamp which allowed a variation of separations *d*. Also shown is an Ewald sphere representing the recording of copied noise gratings in the DCG. This shows only transmitted noise, thus we need only consider a hemisphere.

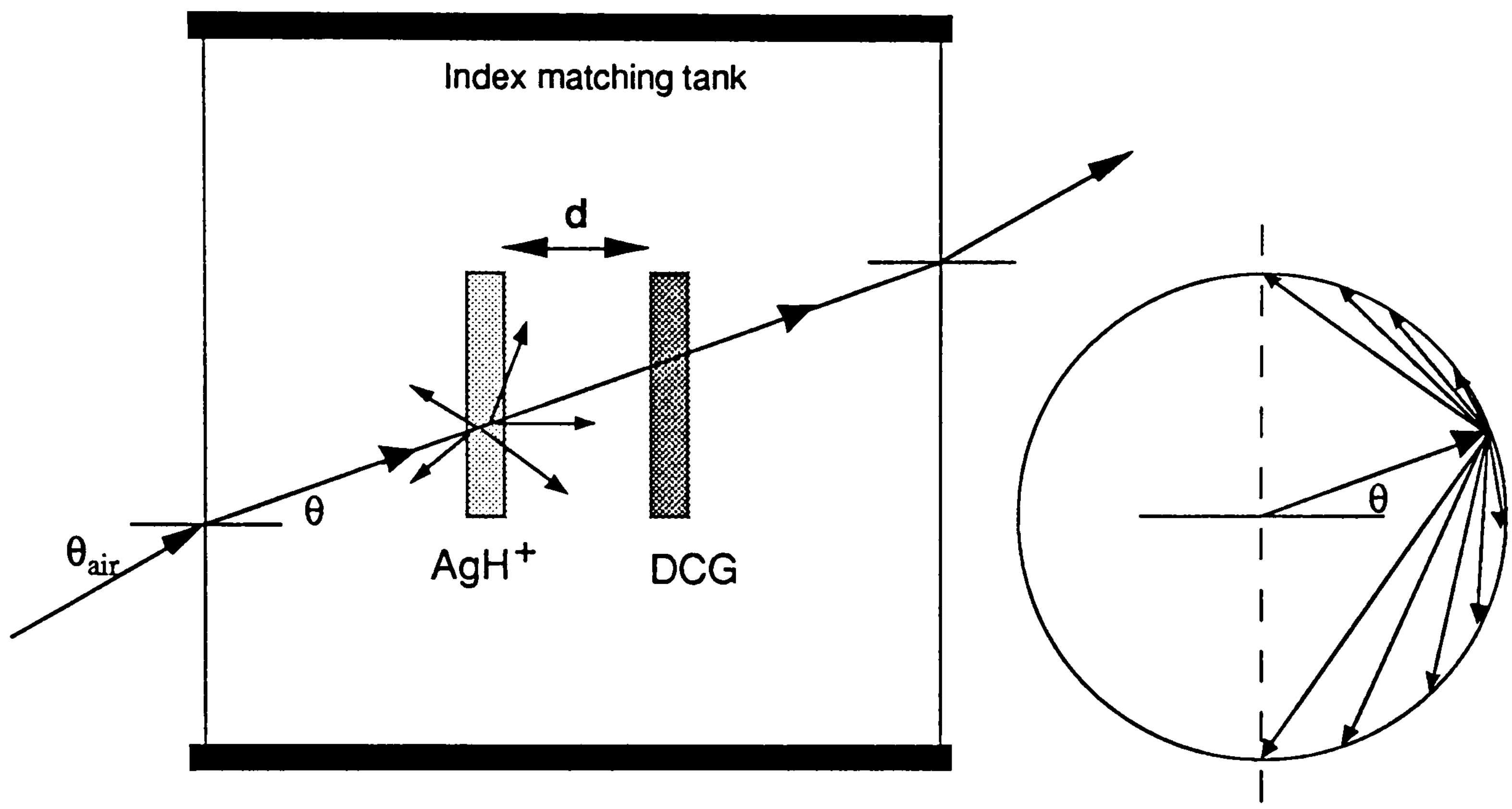


Figure 7.5 Recording geometry for transmission noise gratings in dichromated gelatin.

For all recordings, the wavelength used was 514.5 nm[1] and light was polarised perpendicular to the plane of incidence. The DCG plates were then processed and coverplated using the standard procedure described in Chapter 1.

To analyse the results, angular transmittance scans were made at varying wavelengths using the setup shown also in Chapter 1. Using this method, we observe a drop in transmission as the scattered noise field is reconstructed and power is depleted from the incident beam. However, because noise gratings are extremely sensitive to changes in replay angle in all three dimensions, an adjustable plate holder was added to allow freedom in the vertical axis, thus enabling orientation in three planes.

1 The choice of recording wavelength will affect the amount of recorded noise, since various types of dyes within the silver halide emulsions will scatter at different wavelengths depending on their application.

## 7.4 Variation of diffraction efficiency with exposure energy

Figure 7.6 shows the effect of recording forward scatter using DCG sensitised with a 6% concentration of ammonium dichromate and increasing the exposure energy from 250 mJ / cm$^2$ to 1000 mJ / cm$^2$. The silver halide scattering source was blue / green sensitive emulsion type Agfa 8E56AH and was index matched directly to the DCG plate (i.e. $d = 0$ mm). The angular scans were performed at a replay wavelength of 460 nm and the results are similar to those found by Newell [New87]. The noise dips show an increase in depth as the exposure energy is increased coupled with a decrease in half power angular selectivity. At an exposure energy of 1000 mJ / cm$^2$ we observe almost total depletion of the incident light indicating that most of the replay beam is being coupled efficiently into the reconstruction of recorded scatter.

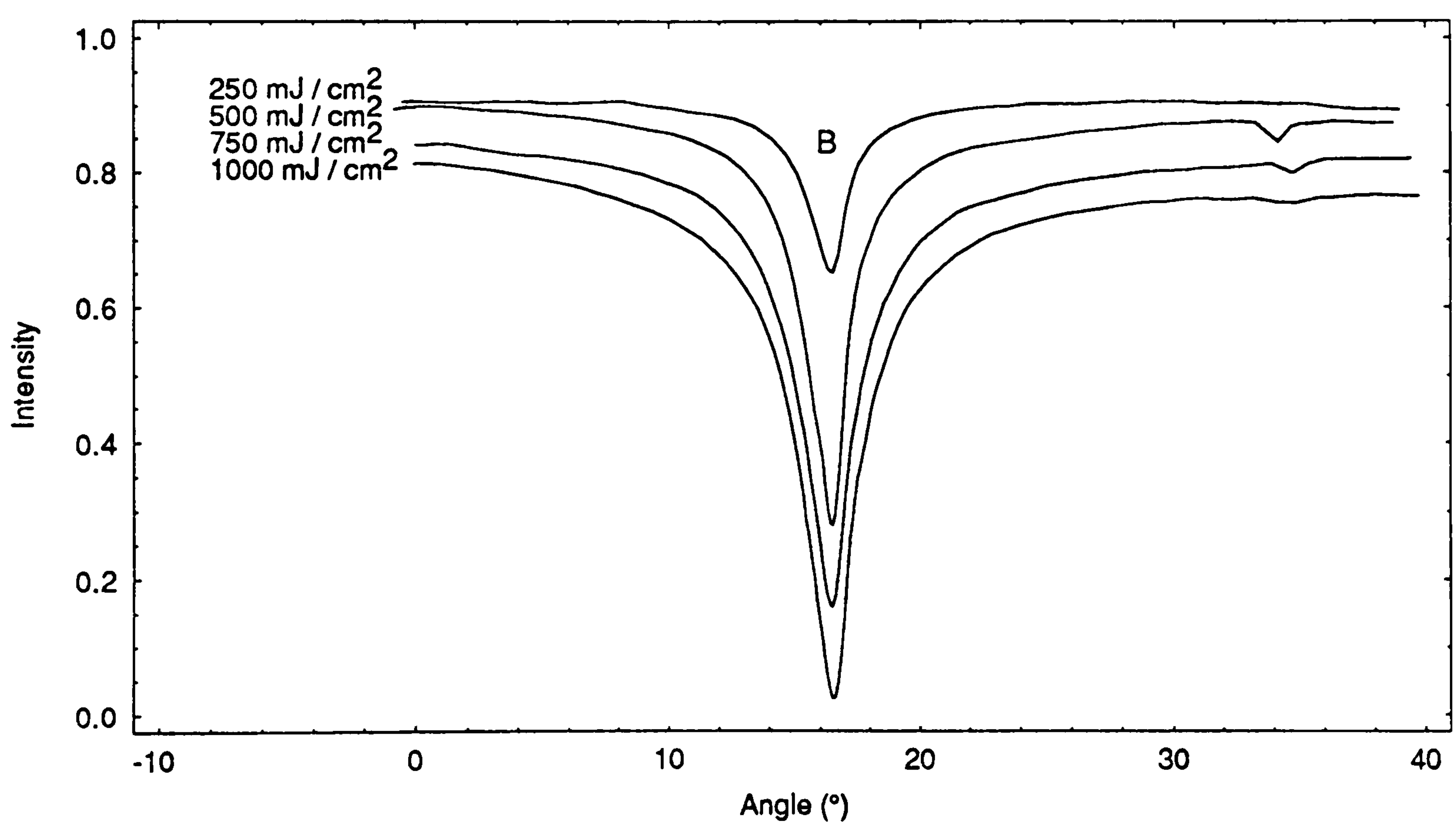


Figure 7.6 Plot of transmittance versus replay angle showing the replay of noise gratings recorded at different exposure energies. The recording angle was 20°, the recording wavelength was 514.5 nm and the replay wavelength was 460 nm.

## 7.5 Variation of diffraction efficiency with replay wavelength

We discussed earlier the effect of changing the replay wavelength upon the diffraction efficiency of noise gratings. Figure 7.7 shows the replay of noise gratings recorded at an exposure energy of 1000 mJ / cm$^2$ at varying replay wavelengths. We see that the gratings replay with a single dip of high efficiency at the wavelength of 460 nm. However, at all other wavelengths above and below this optimum value, two local maxima occur at positions away from the recording angle with lower efficiency. The diffraction efficiencies of these dips are seen to decrease as the replay wavelength varies further from the optimum. It is interesting to note that the optimum replay wavelength for such gratings copied into DCG appears to exist around 460 nm. This is despite the fact that the gratings were recorded at 514.5 nm.

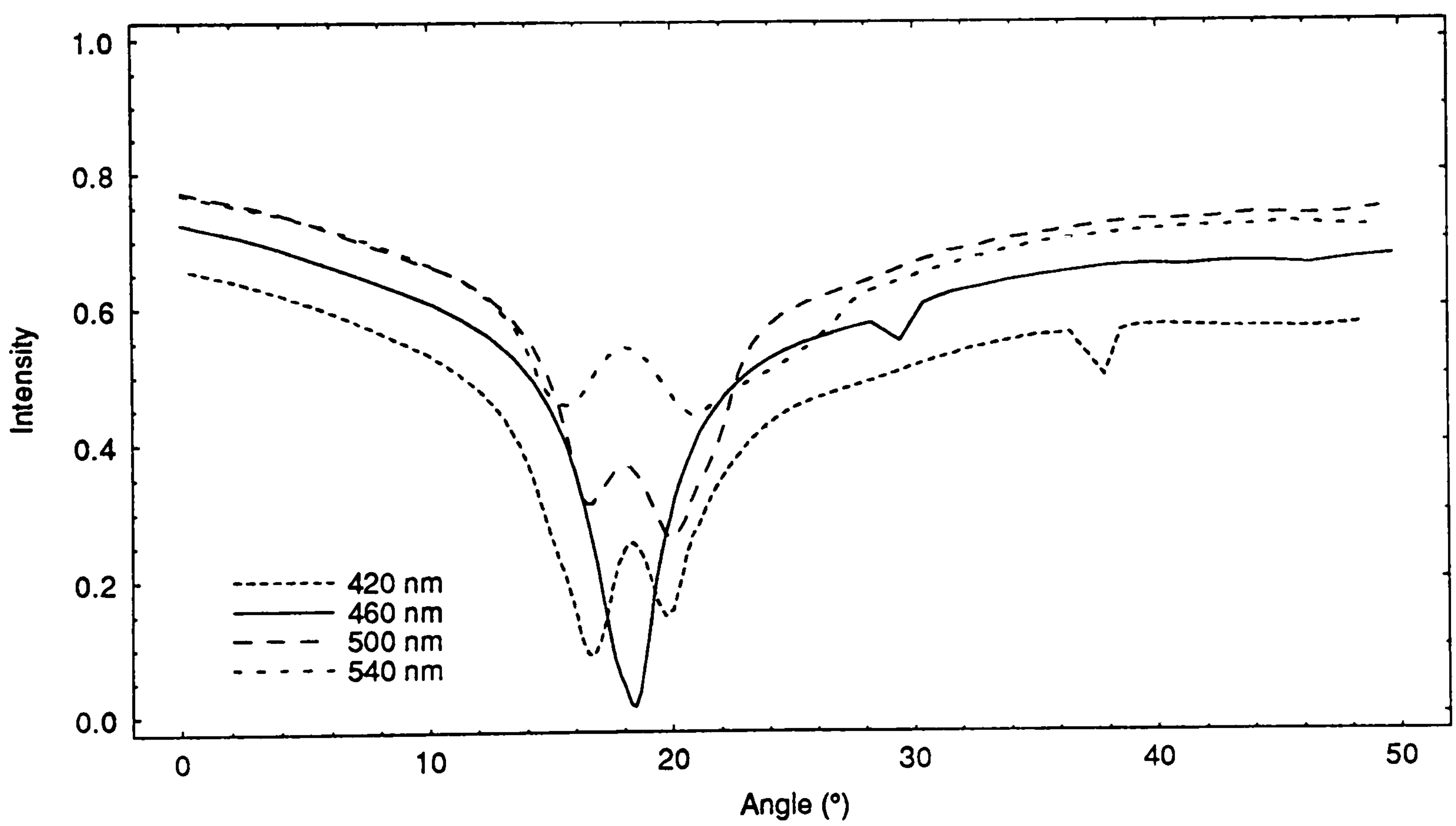


Figure 7.7 Plot of transmittance versus replay angle showing the replay of noise gratings at different replay wavelengths. The recording angle was 20°, the recording wavelength was 514.5 nm, the exposure energy used was 1000 mJ / cm$^2$.

Recently Solymar and Newell [Sol89] have published a theory to explain why silver halide noise gratings recorded in DCG replay with a highly efficient single dip at a replay wavelength around 460 nm. They postulate that this is due to the change in thickness and average refractive index of the DCG between recording and replay due to processing. As we have already seen, if swelling occurs, then the locus of the end points of all recorded gratings will take the form of an ellipsoid. In order to replay with maximum efficiency, the radius of curvature of the replay Ewald sphere should be the same as the local radius of curvature of the ellipsoid at the replay angle. If this condition exists then the values of the off Bragg parameters will be reduced and optimum scatter will occur. They conclude that the replay wavelength is governed by the equation:-

$$\frac{2\pi n_{rep}}{\lambda_{rep}} = \frac{2\pi n_{rec}}{\lambda_{rec}} t \left[ \frac{\sin^2\theta_{rec}}{t^2} + \cos^2\theta_{rec} \right]^{\frac{3}{2}} \tag{7.1}$$

where $n_{\text{rec}}$ and $n_{\text{rep}}$ are the average refractive index values and $\lambda_{\text{rec}}$ and $\lambda_{\text{rep}}$ are the wavelengths at recording and replay respectively. $\theta_{\text{rec}}$ is the angle of incidence at recording and $t$ is a ratio of thickness before and after processing.

Using this equation and an incident angle of 20°, Figure 7.8 shows a theoretical plot of replay wavelength versus the ratio of refractive index before and after processing for different levels of thickness change. Here we see that if the refractive index stays constant and the thickness increases, we should obtain maximum diffraction at a longer wavelength than recording. Similarly, if shrinkage occurs, we expect optimum replay at a lower wavelength. This plot also states that, if we keep the thickness constant, a reduction in average refractive index due to processing will cause replay at a shorter wavelength. In the case of transmitted noise, it appears that the replay wavelength is dominated by the change in refractive index. We know that the average refractive index of DCG is lower after processing than at recording. However, this is dependent upon the concentration of sensitisation and the degree of hardening. Newell [New87] has shown that the refractive index ratio is less for low sensitisations that higher sensitisations, however, the values are in the region of 0.9 to 0.95. If we assume a constant thickness for all sensitisations and look once more at Figure 7.8 we see that we now expect replay around 460 nm.

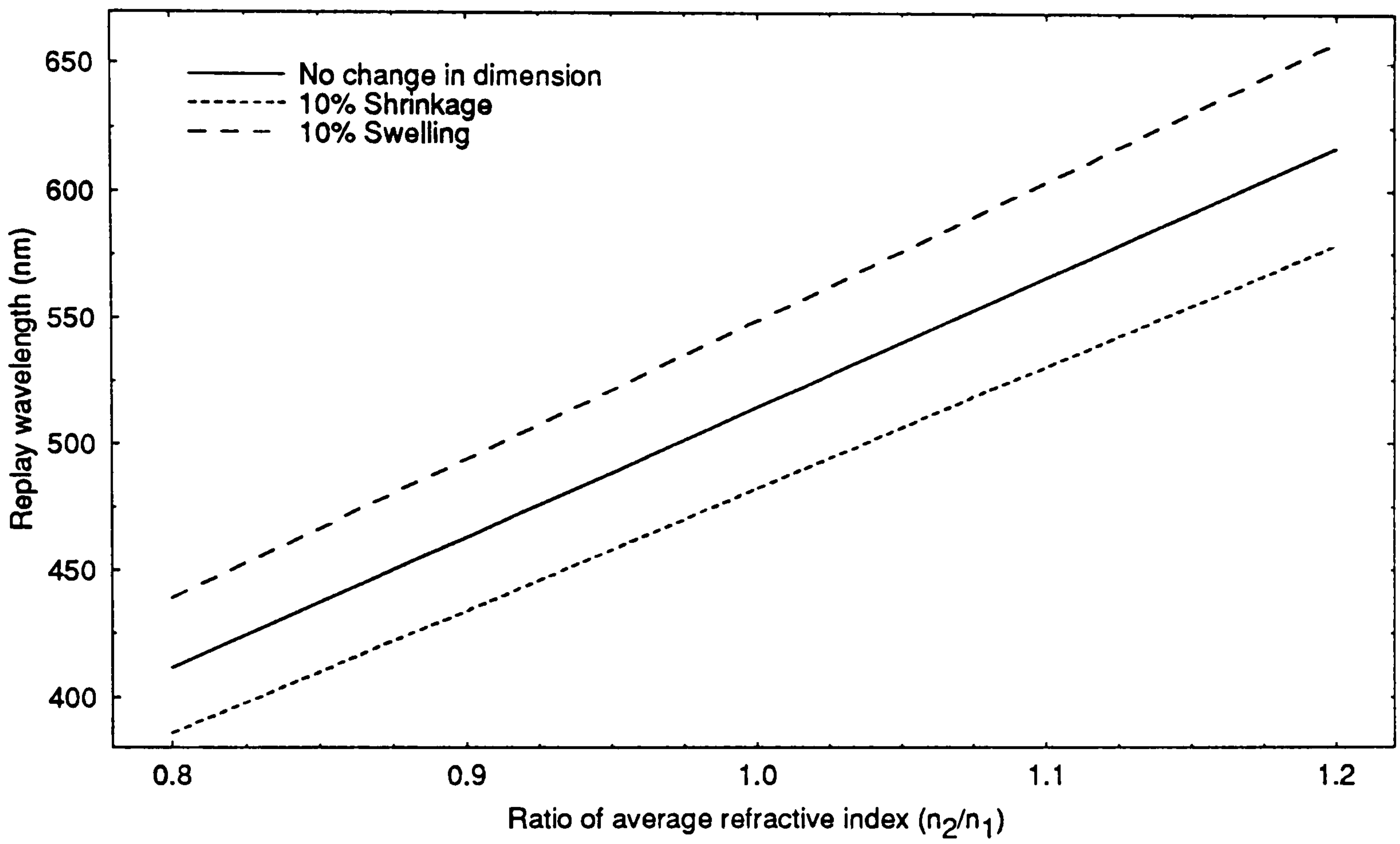


Figure 7.8 Theoretical plot [from Equation (7.1)] of replay wavelength versus ratio of average refractive index assuming a recording wavelength of 514.5 nm.

## 7.6 Comparison of three silver halide emulsions

A comparison was made of the relative scatter of three different silver halide emulsions which are used regularly as recording materials for holography. The emulsions chosen were:-

(i) Agfa 8E56AH (Millimask HD)

(ii) Agfa 8E56NAH

(iii) Ilford SP695T

These emulsions are all commercially available and are sensitive to the blue / green region of the visible spectrum. At recording they contain two main sources of scatter: (i) the photosensitive silver halide grains and (ii) additional dyes. Silver halide grains are primarily sensitive to wavelengths below 490 nm. It is therefore necessary to add a *sensitising dye* to make the emulsion sensitive to operating wavelengths. Also, in some emulsions (e.g. Agfa 8E56AH), an *anti-halation dye* is added for the purpose of absorbing scattered light. This causes scattered light to travel a shorter distance within the emulsion and hence improves the contrast of fringe recording. Hubel and Ward [Hub89a] give a detailed description of the relative scatter in different commercially available holographic emulsions.

Each plate was exposed at energies of 250, 500, 1000 and 2000 mJ / cm$^2$ over different areas of the emulsion surface and noise gratings were recorded on DCG which had been sensitised with a 10% concentration of ammonium dichromate. The high sensitisation concentration was used to allow high modulation recording at all angles. For this experiment, the plates were index matched together ($d$ = 0 mm). The results are presented in Figures 7.9 to 7.11.

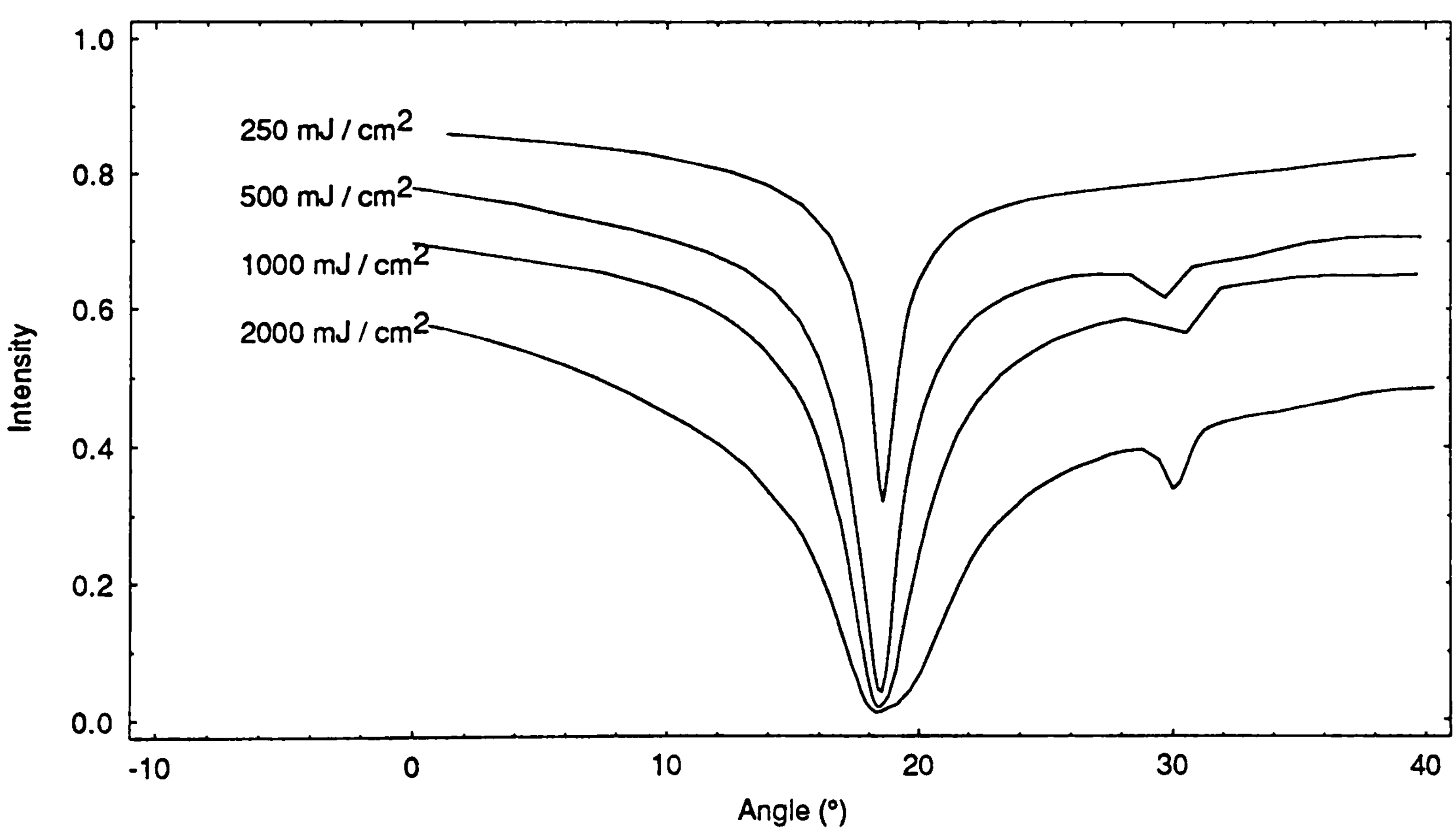


Figure 7.9 Plot of transmittance versus replay angle at 460 nm for Agfa 8E56AH emulsion exposed at varying energies

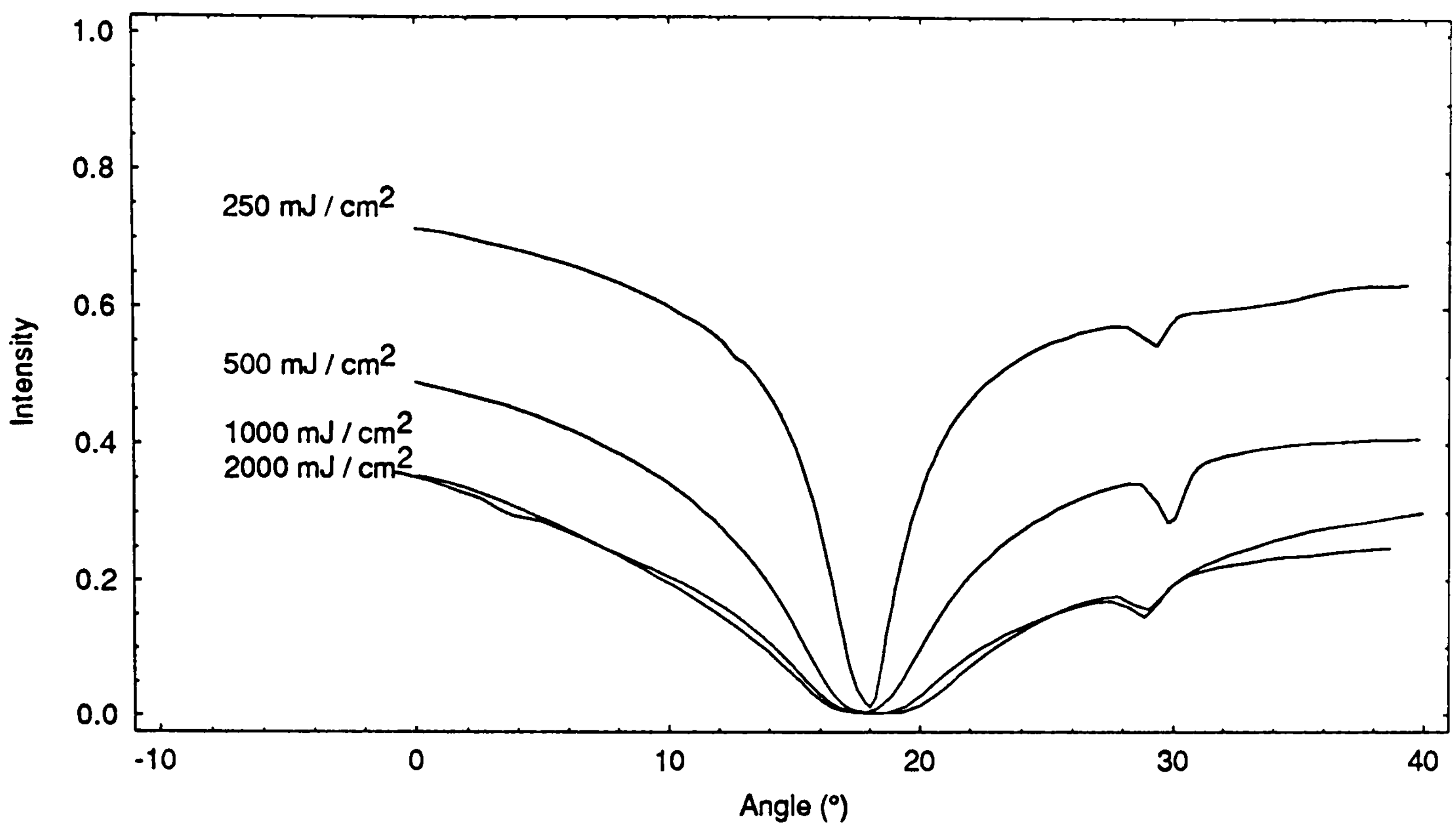


Figure 7.10 Plot of transmittance versus replay angle at 460 nm for Agfa 8E56NAH emulsion exposed at varying energies

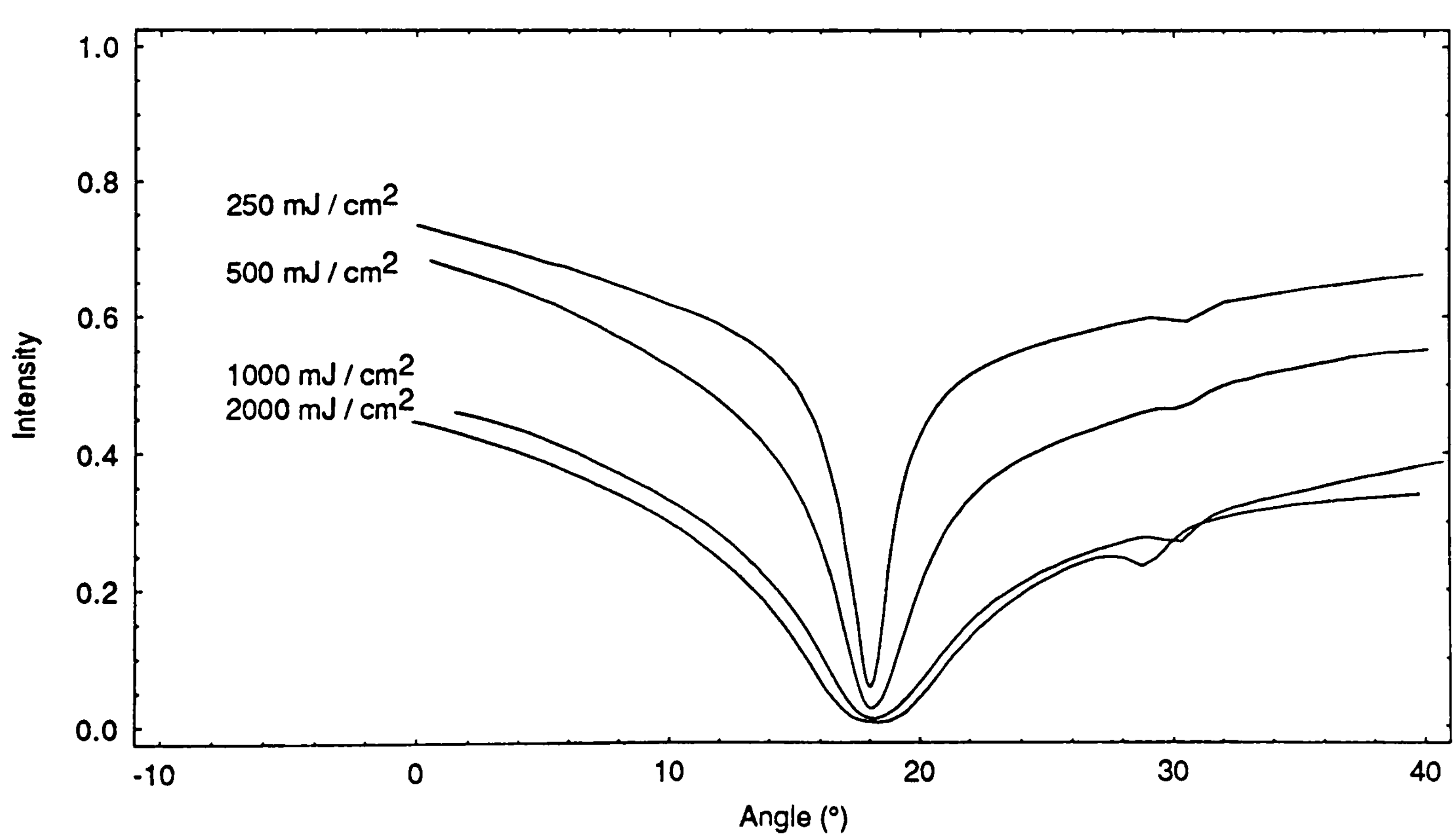


Figure 7.11 Plot of transmittance versus replay angle at 460 nm for Ilford SP695T emulsion exposed at varying energies

Comparing the two Agfa plates (Figures 7.9 and 7.10), we can immediately see differences in angular selectivity, efficiency and absorption. The emulsion which contains the antihalation dye has higher selectivity and lower diffraction efficiency against exposure energy. This is because the anti-halation dye has reduced the distance travelled by scattered light within the the emulsion.

The plate recorded without the anti-halation dye shows a larger angular spread and higher diffraction efficiency against exposure energy. More noise gratings have been recorded with higher modulation, however, the scatter has not been suppressed leading to a reduction in angular selectivity. If we look at the result for the Ilford material (Figure 7.11), we see that it exhibits similar efficiencies to the Agfa 8E56NAH emulsion, illustrating significant scatter. However, it shows a marked increase in angular selectivity.

It is interesting to observe the effect of recording noise gratings at very high exposure energies. Once the dip reaches close to zero transmittance, it broadens out over a wider range of replay angles. This is particularly noticeable with the Agfa 8E56NAH emulsion, however, the transmitted beam is not totally depleted. This is because, at all times, some light will be scattered in the direction of the spectrometer input slit. Thus, we will never achieve total depletion.

Figure 7.12 shows a comparison between the three films in terms of half power angular selectivity. From this we can conclude that Agfa 8E56AH shows least scatter and Agfa 8E56NAH shows the highest. Ilford SP695T is in the middle, which is quite an improvement on Agfa 8E56NAH considering that the Ilford material contains no dyes and the difference in scatter is dependent solely on grain size distribution [Rid88].

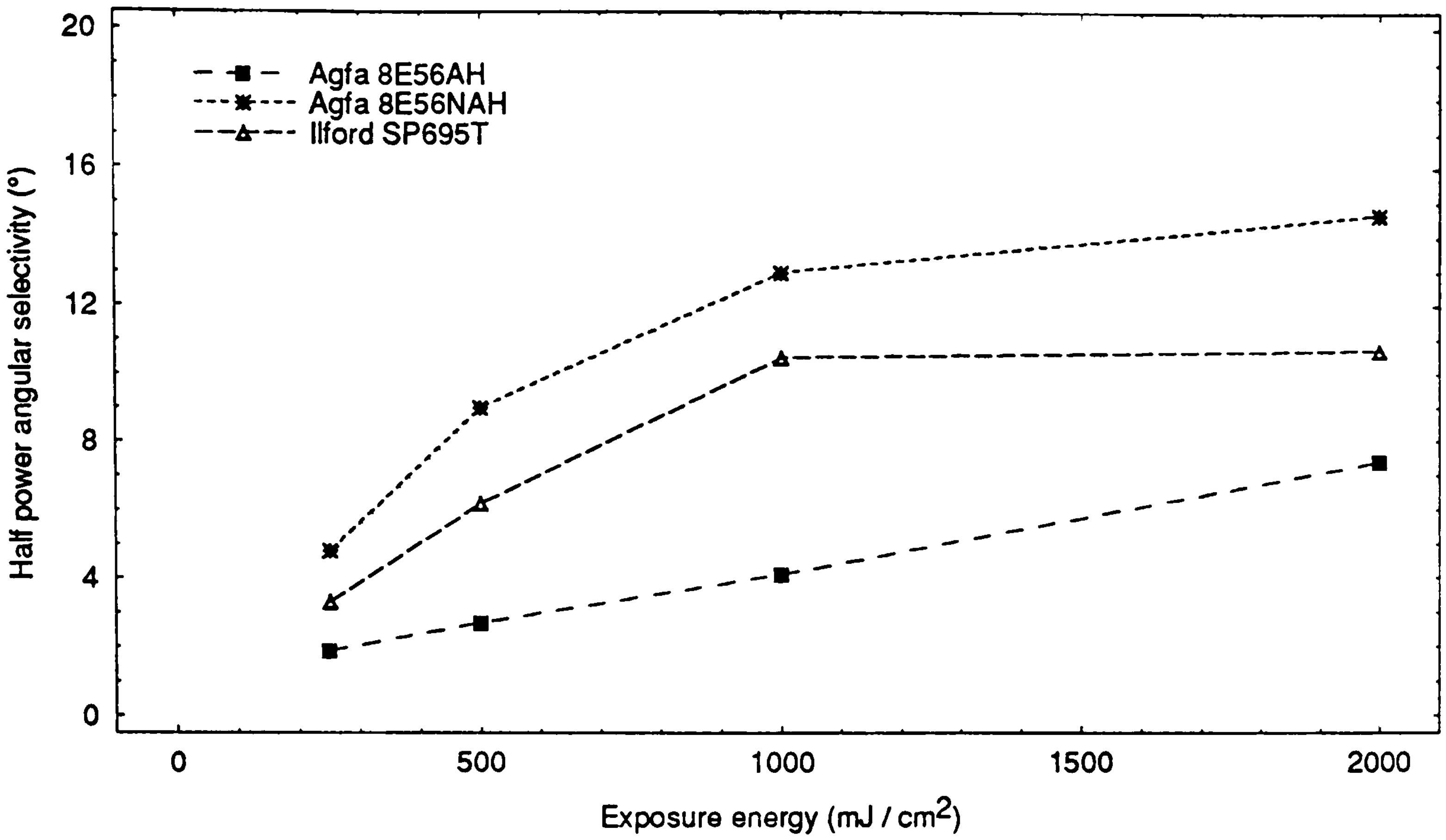


Figure 7.12 Plot of half power angular selectivity versus exposure energy for the three silver halide emulsions Agfa 8E56AH, Agfa 8E56NAH and Ilford SP695T.

## 7.7 The effect of varying the separation d

Riddy [Rid88] has proposed theoretically that the angular selectivity of recorded noise is dependent upon the modulation strength of noise gratings recorded with high angular components. Figure 7.13 (see Reference [Rid88]) shows a theoretical plot of transmittance versus replay angle for two sets of noise gratings recorded at -10°. The solid line illustrates the case where high angle gratings were assumed to have increased modulation strengths. This shows that by increasing the importance of the high angular components, we should obtain greater angular selectivity.

The following experiment was designed to verify the theory. By varying the distance between the scattering $AgH^+$ source and the DCG plate we are able to change the angular spread of the recorded scatter. When the plates are close together, we will record gratings with higher angular components than when the plates are far apart.

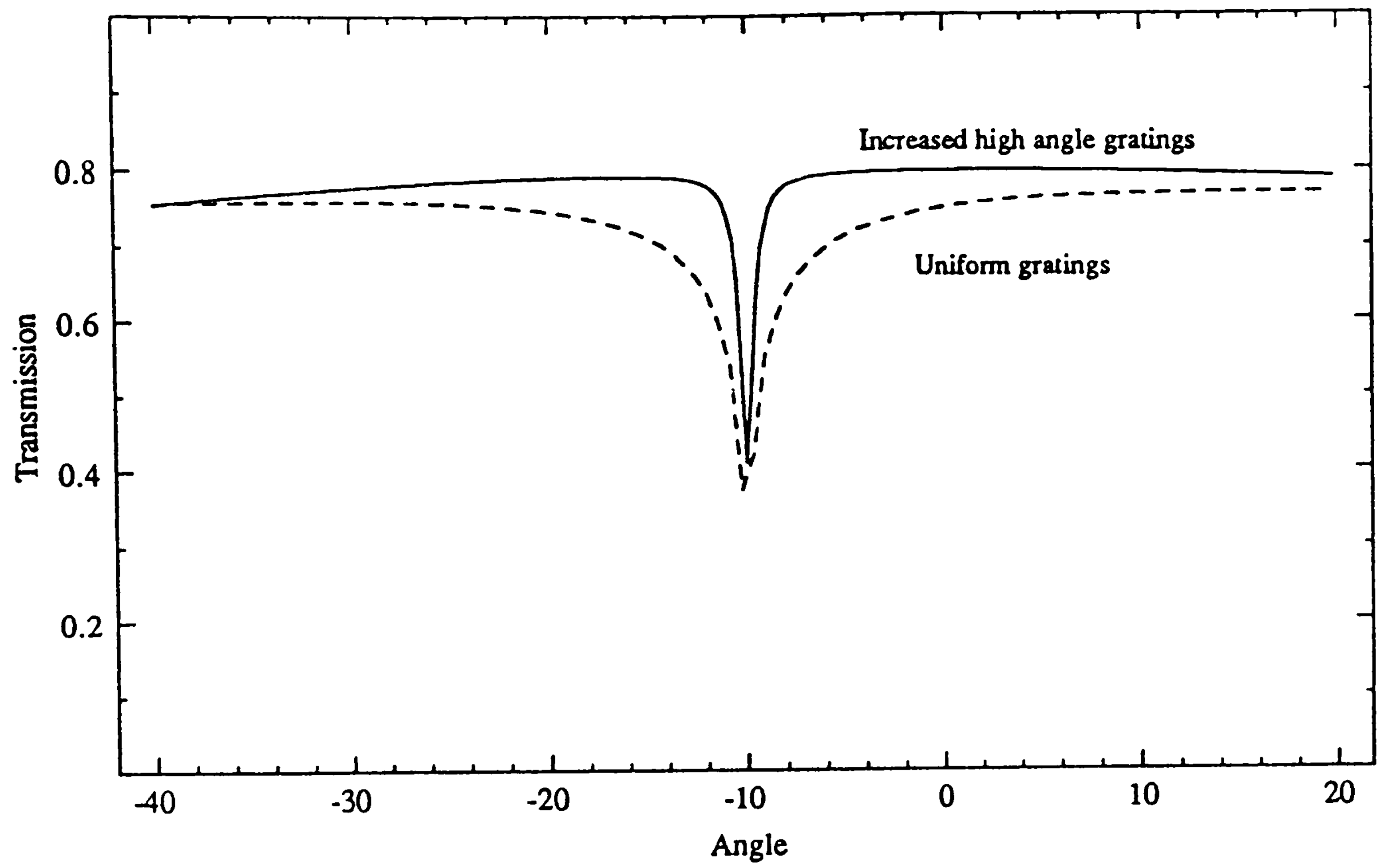


Figure 7.13 Theoretical plot of transmittance versus replay angle for two sets of noise gratings recorded at -10°. The solid line represents noise with increased high angular modulation (see Reference [Rid88]).

Thus, if the recording of gratings with high angular components is important, we will observe a reduction in selectivity as the plates are separated.

In the experiment Agfa 8E56AH plates were used as the scattering source and the DCG plates were sensitised with a 10% concentration of ammonium dichromate. Recordings were made with a single collimated beam with a surface area of 10 mm$^2$. The exposure energies used were 250 and 500 mJ / cm$^2$, and the separation $d$ was varied from 0 mm to 40 mm in steps of 10 mm.

Figures 7.14 (a) and (b) show the angular transmittance scans for each exposure energy at a replay wavelength of 460 nm. In both cases we see the strength of the dips decrease as the separation increases. Also, we note that the angular selectivity decreases with the distance in separation.

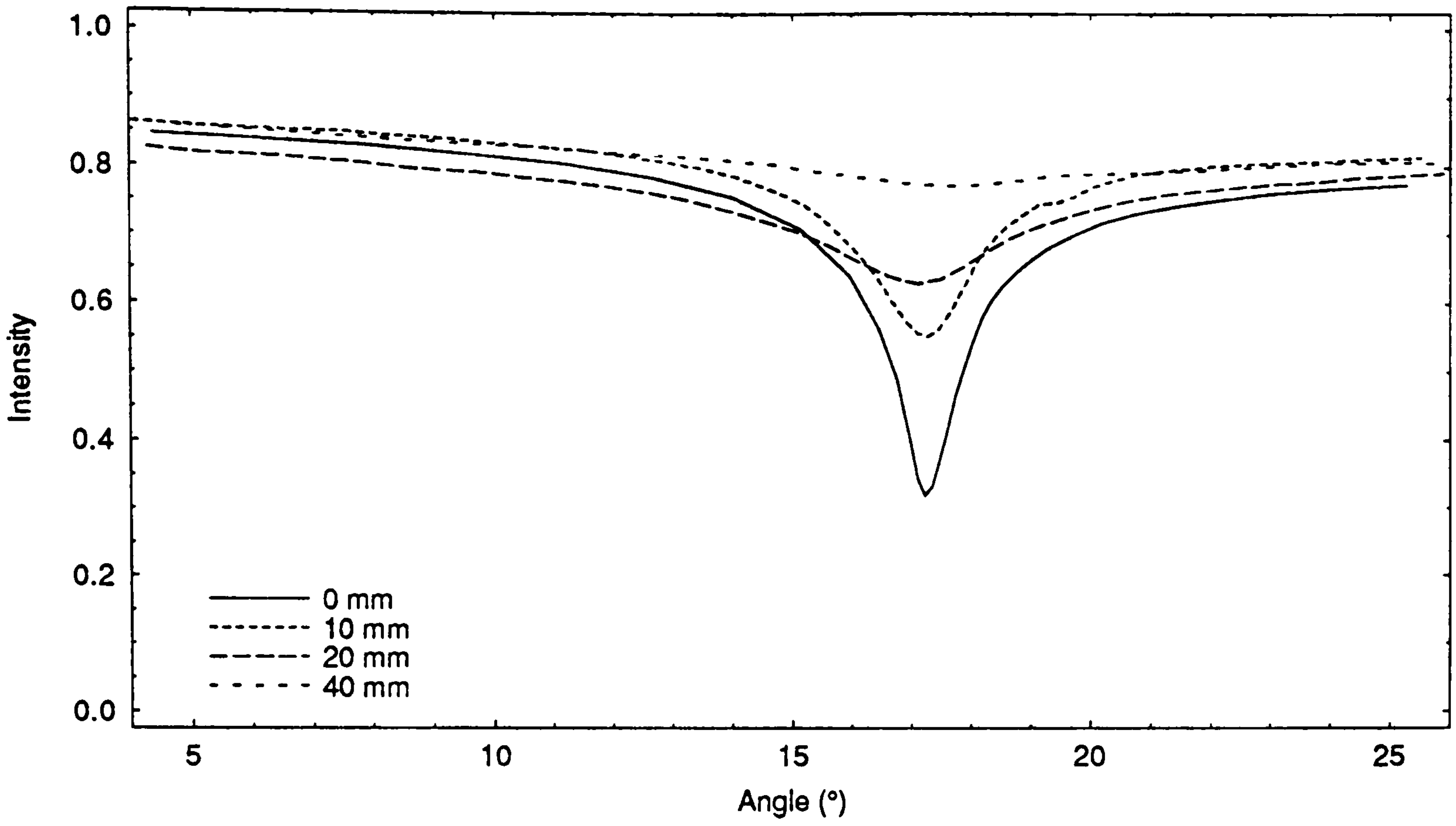


Figure 7.14 (a) Angular transmittance scans for varying separation *d* recorded at 250 mJ / cm$^2$ and replayed at 460 nm.

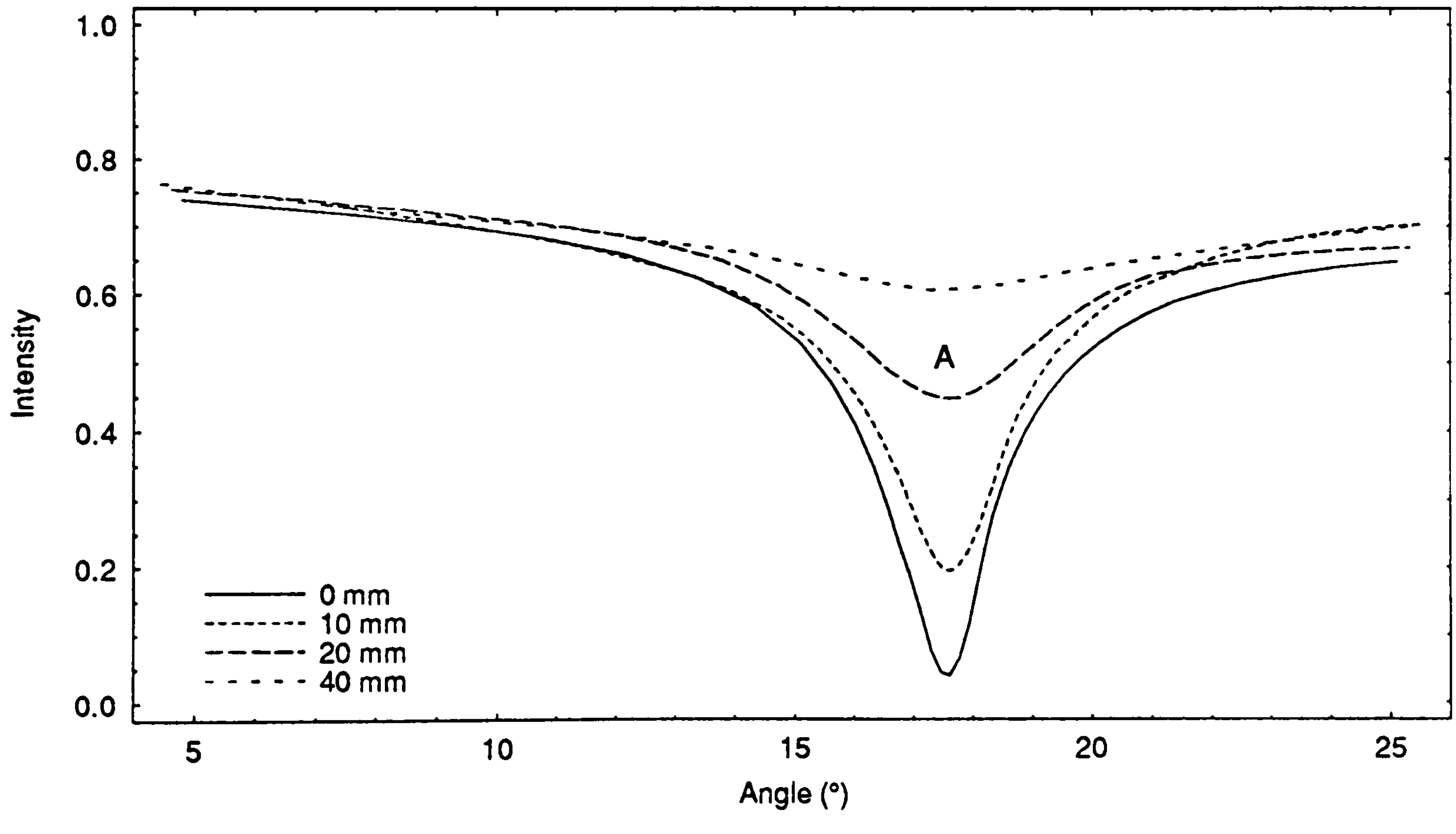


Figure 7.14 (b) Angular transmittance scans for varying separation *d* recorded at 500 mJ / cm$^2$ and replayed at 460 nm.

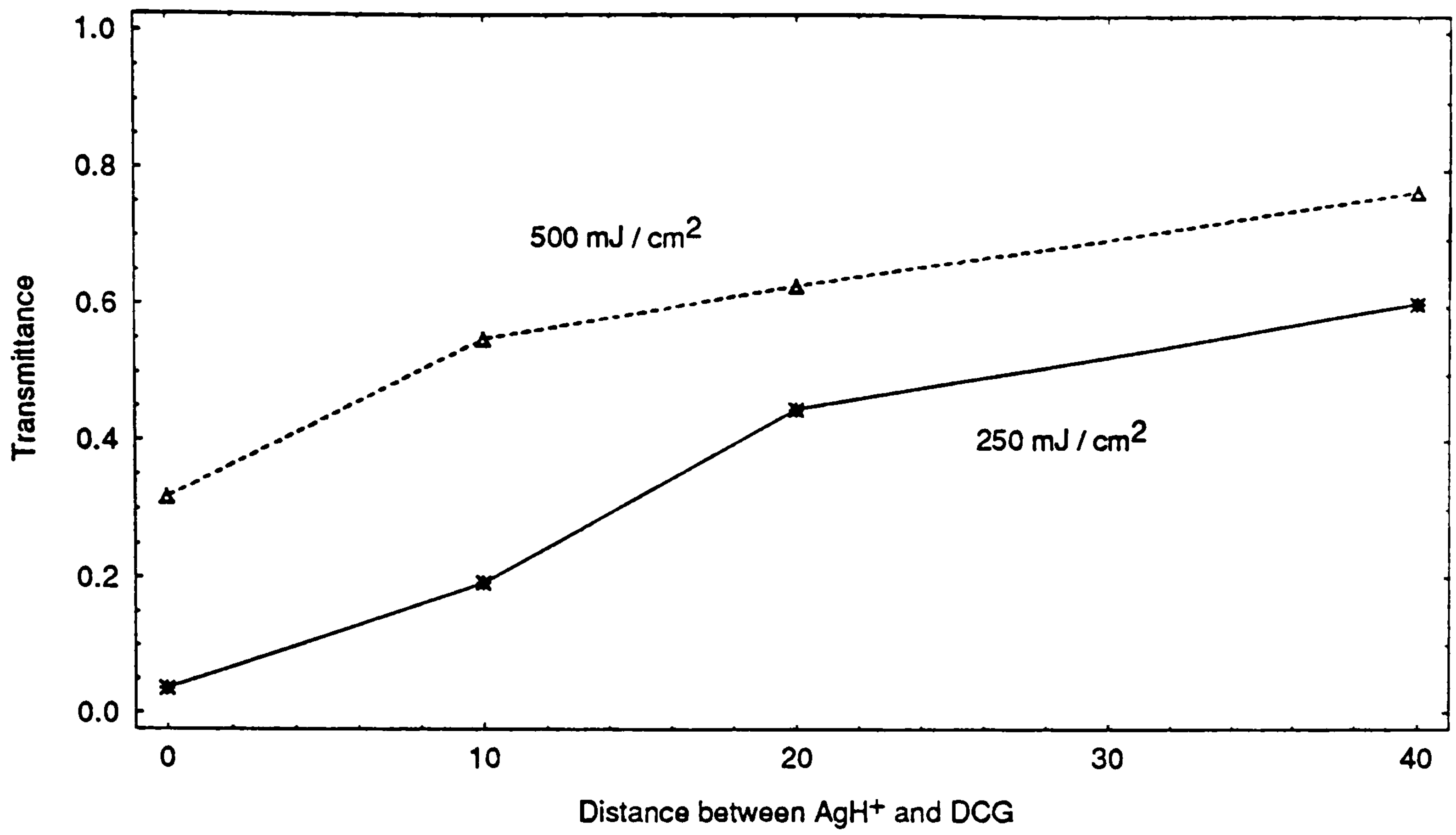


Figure 7.15 Plot of transmittance versus separation $d$ for two exposure levels.

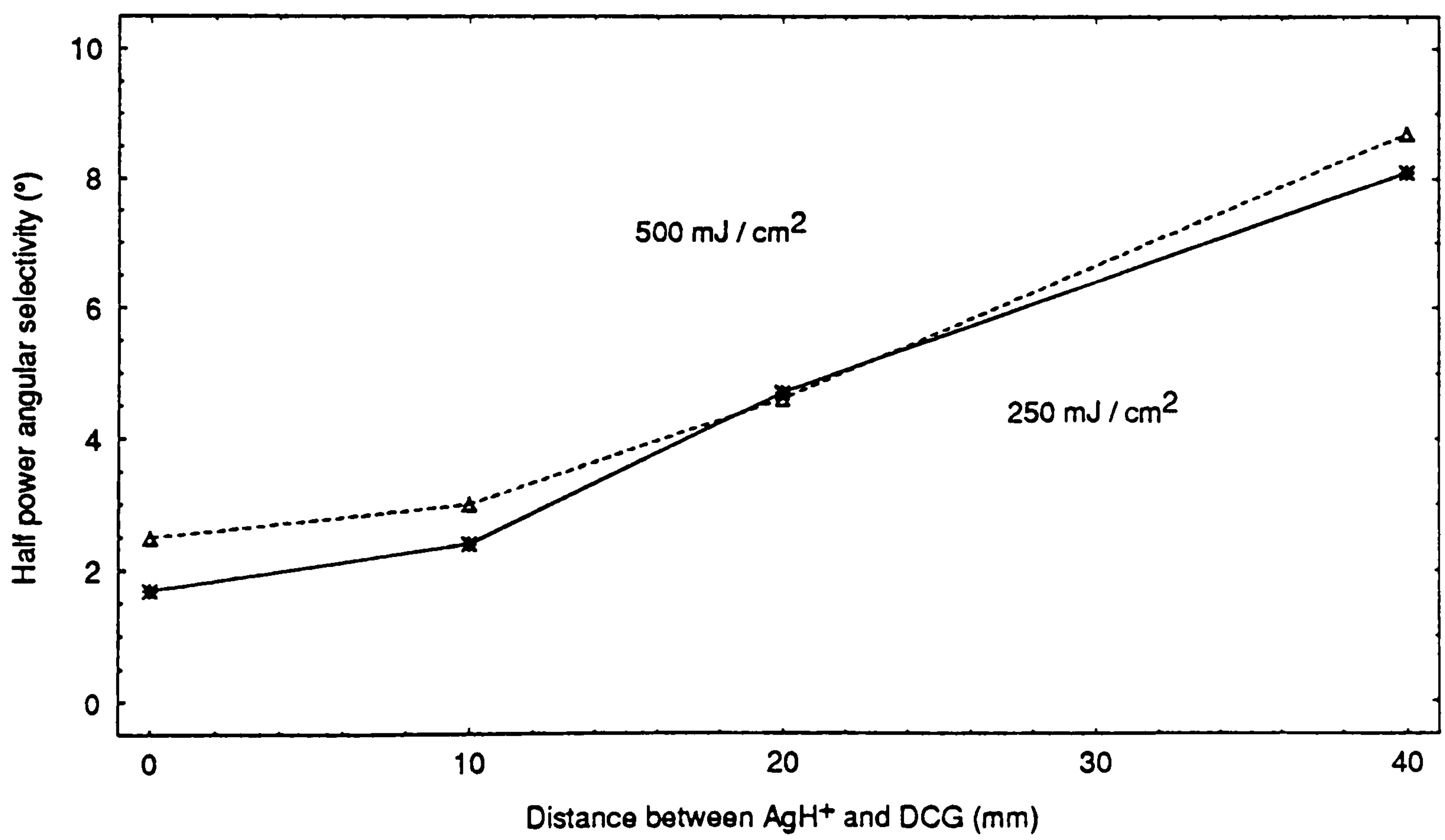


Figure 7.16 Plot of half power angular selectivity versus separation $d$ for two exposure levels.

These transmittance and half power angular selectivity values are plotted against separation in Figures 7.15 and 7.16. This confirms the theory and shows that the high angular components are important in the formation of highly selective noise gratings.

It may be argued that by separating the plates in an index matching tank is going to cause a reduction in exposure of the DCG plate due to the added absorption of the index matching oil. Indeed, this will be the case and we do observe a drop in diffraction efficiency. However, the reduction in angular selectivity suggests a lack of high angular gratings, since if we record with a separation distance of 0 mm and reduce the exposure energy, we still obtain high selectivity (see Figure 7.6).

### 7.7.1 *Scattering rings*

The reduction in selectivity with increasing separation $d$ may be demonstrated by observing scattering rings for an off - Bragg condition. The plates recorded at 500 mJ / cm$^2$, whose transmittance scans are shown in Figure 7.14 (b), were replayed using an unexpanded laser beam at a wavelength of 514.5 nm. The replay angle was chosen at -30° in air. Figure 7.17 shows the replay geometry.

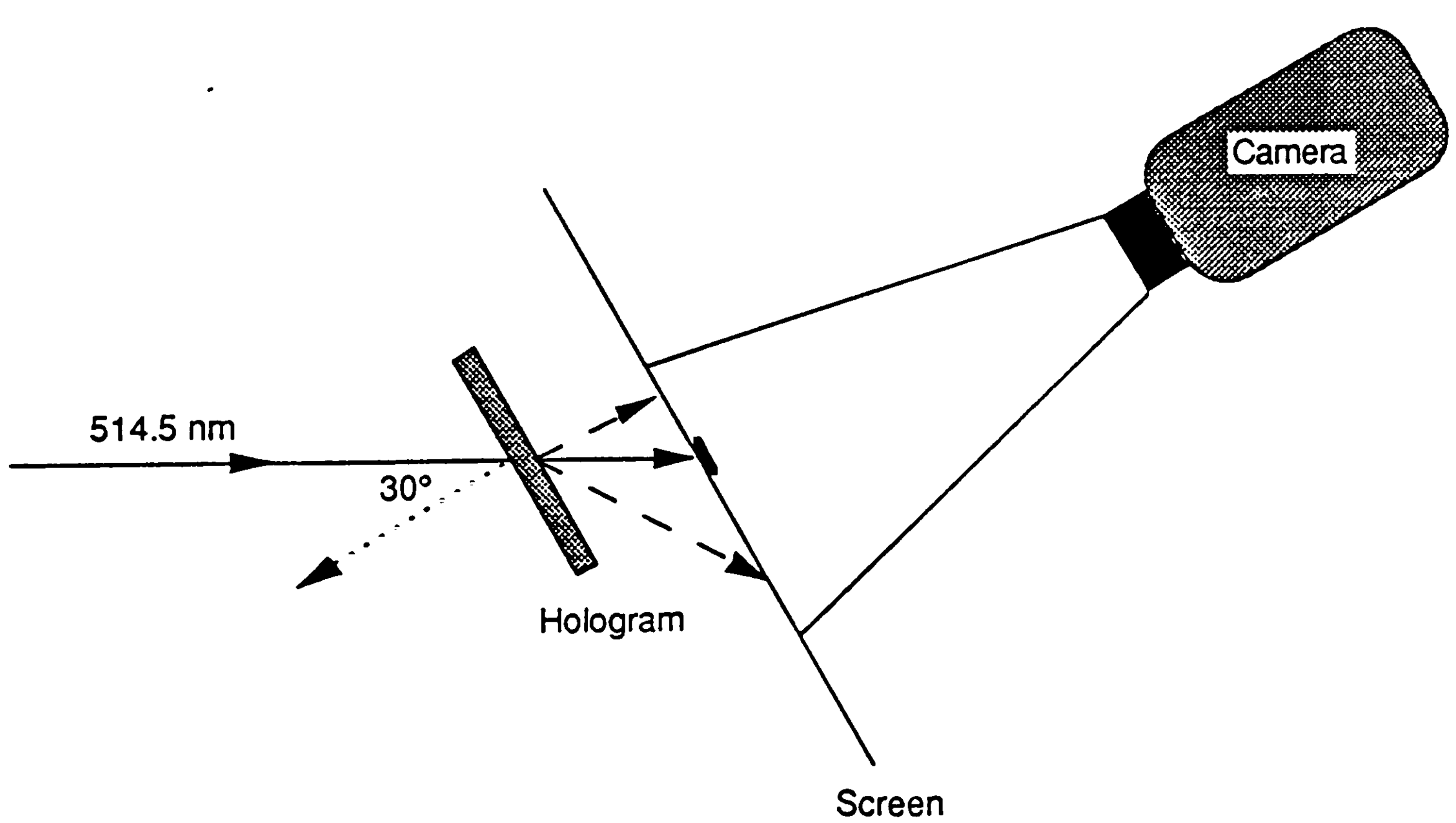


Figure 7.17 Geometry for the replay of scattering rings.

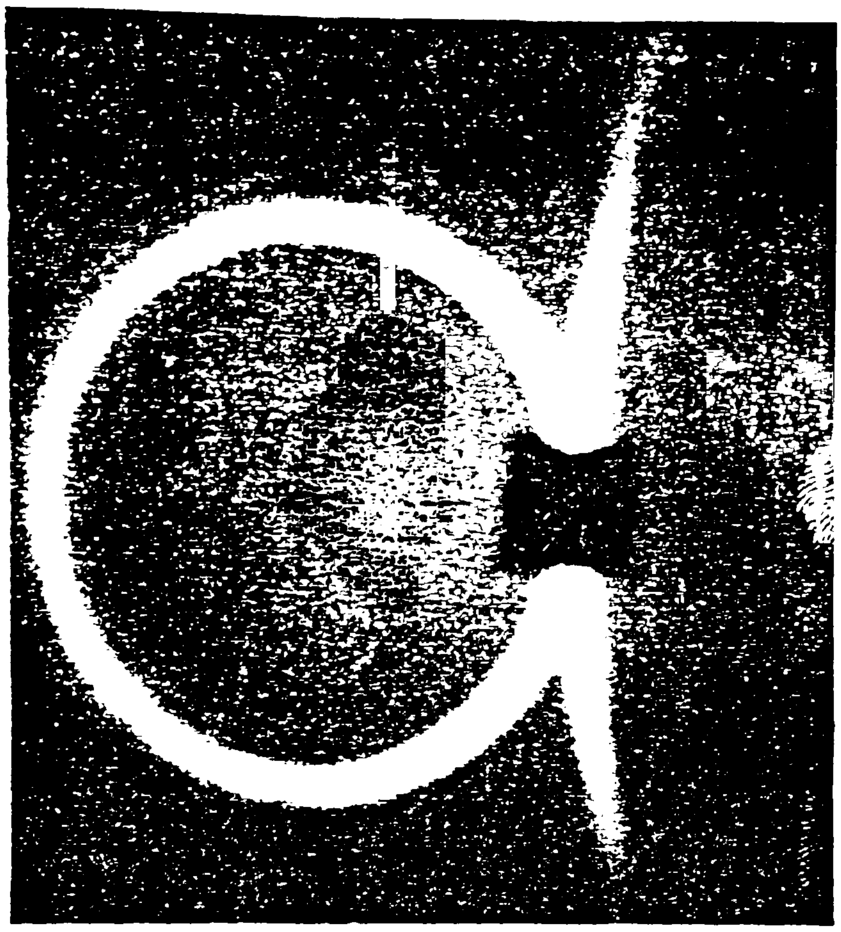

(a) $d = 0$ mm

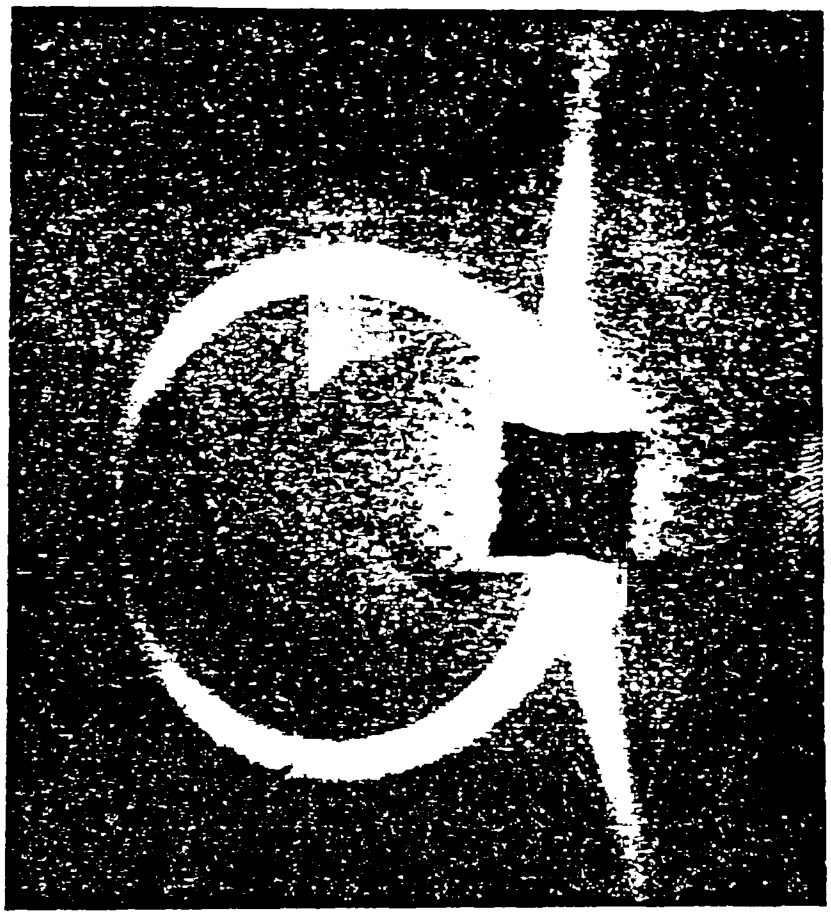

(b) $d = 10$ mm

(c) $d = 20$ mm

(d) $d = 40$ mm

Figure 7.18 Scattering rings of noise recorded from Agfa 8E56AH emulsion at separations of (a) 0 mm, (b) 10 mm, (c) 20 mm and (d) 40 mm.

Figure 7.18 (a), (b), (c) and (d) show the results of scatter from separations of 0, 10, 20 and 40 mm respectively. In each photograph the opaque square in the centre is piece of black tape which was used to block the transmitted zeroth order beam. We observe that at a separation $d = 0$ mm the scatter is described by a complete circle with a radius of about 30 mm and a second circle with a far larger radius. These represent the interaction of the replay Ewald sphere with the locus of +1 and -1 order diffraction by the recorded noise gratings, as described earlier. However, as we increase the separation $d$, we see that the smaller circle becomes less complete until, at $d = 40$ mm, it is barely recognisable. This is due to a reduction of noise gratings recorded at high angles as $d$ is increased.

Figure 7.19 shows why the scattering rings become incomplete. In Figure 7.19 (a) we see the recording of a transmission noise grating with a separation $d = 0$ mm. Thus, we will record a locus of gratings which describes a hemisphere. At replay, away from the recording angle, we see that the $\pm 1$ orders cut the replay sphere totally causing the output of complete cones of light. In Figure 7.19 (b) we see the recording of transmission noise gratings where the separation $d$ is large compared with the recording surface area. Now, the locus of recorded noise gratings will follow the surface of a sphere, but with an area less than a hemisphere. At replay, we see that the $\pm 1$ orders do not fully cross the the surface of the replay sphere, causing the replay of an incomplete cone of scattered light. Thus, the scattering rings will be depleted at the outside angles.

We still have to show that the deterioration of the scattering rings is not solely a consequence of reduced diffraction efficiency. If we compare the recording in Figure 7.14(b) at a separation of $d = 20$ mm (Plot A) with the 250 mJ / cm$^2$ recording in Figure 7.6 (Plot B), we see that they are of similar diffraction efficiency. Figure 7.20 shows the scattering rings from B at the same replay angle of -30°. Here, in comparison to Figure 7.18(c), we see that the circle is complete, illustrating that the high angular components have been recorded and play an important role in the selectivity of recorded noise.

(a) Transmitted noise when $d = 0$ mm

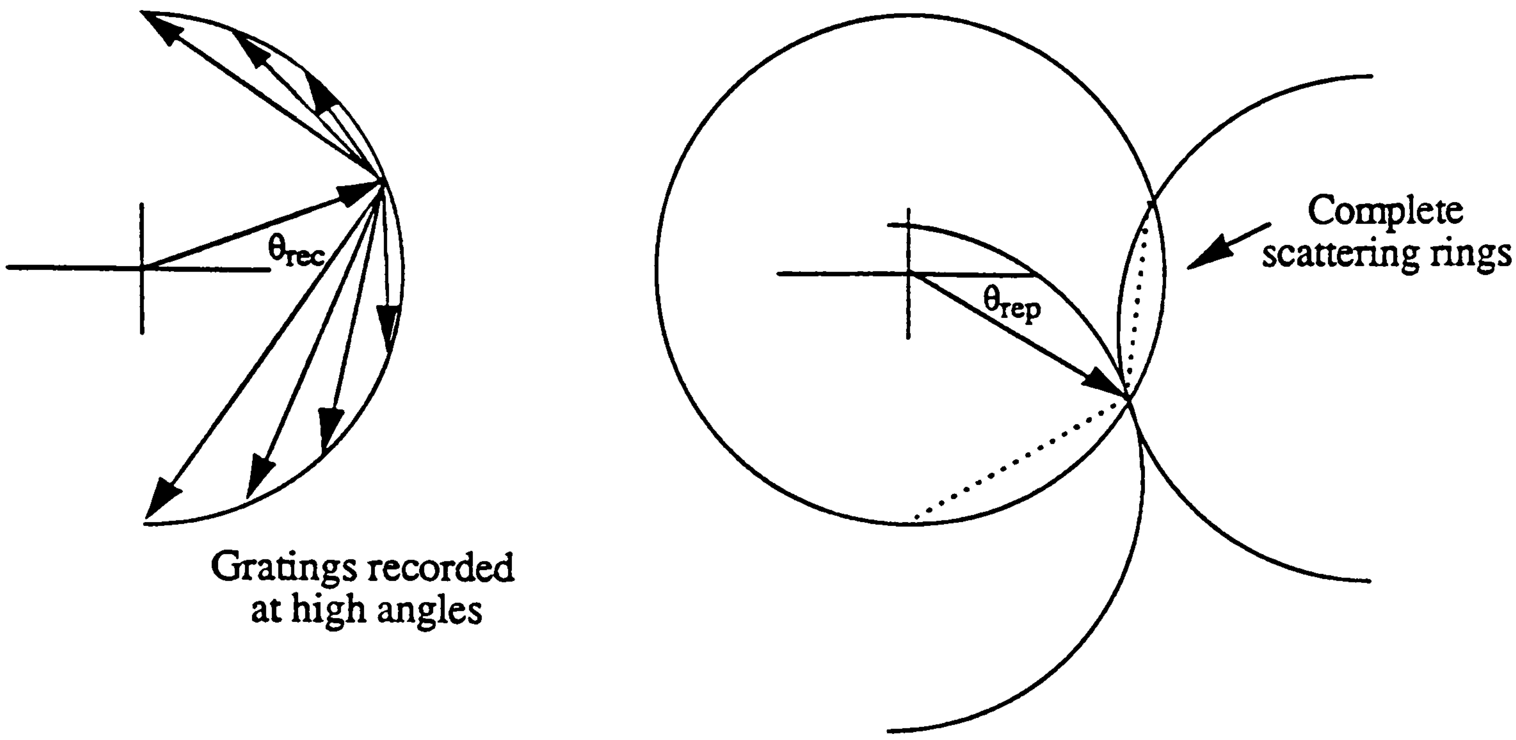


(b) Transmitted noise when $d$ is large

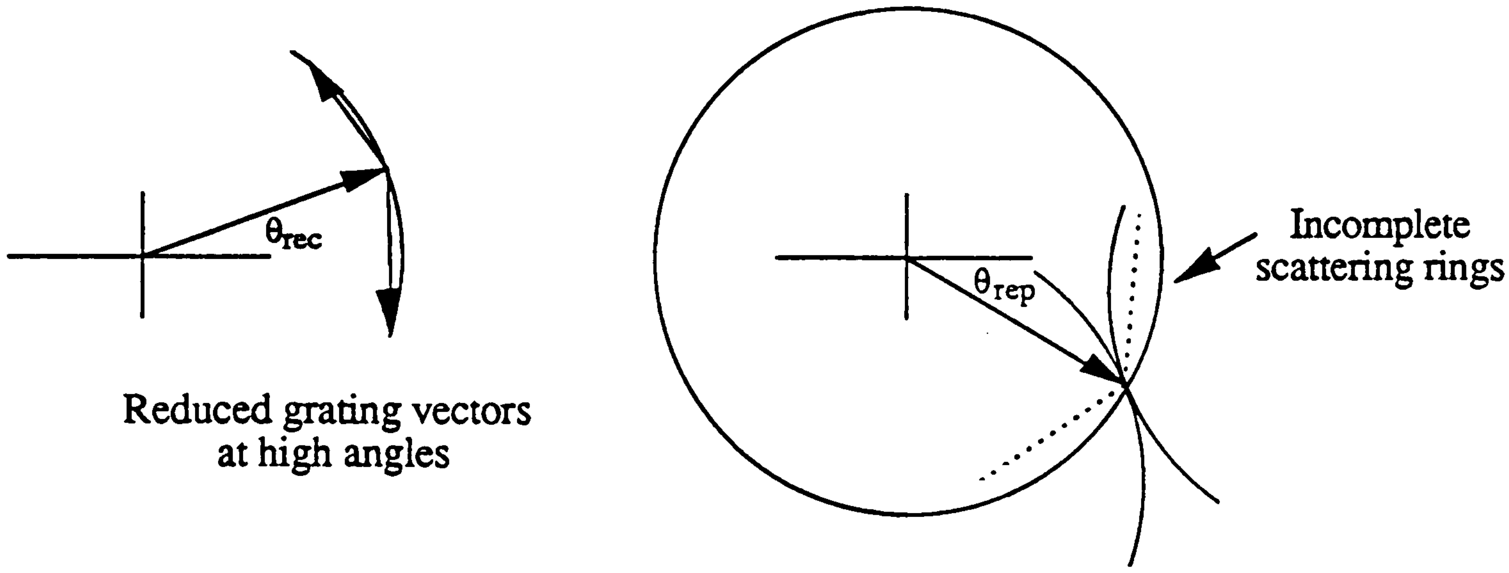


Figure 7.19 The effect of separation distance d upon the recording of noise gratings at high angles and the effect on scattering rings.

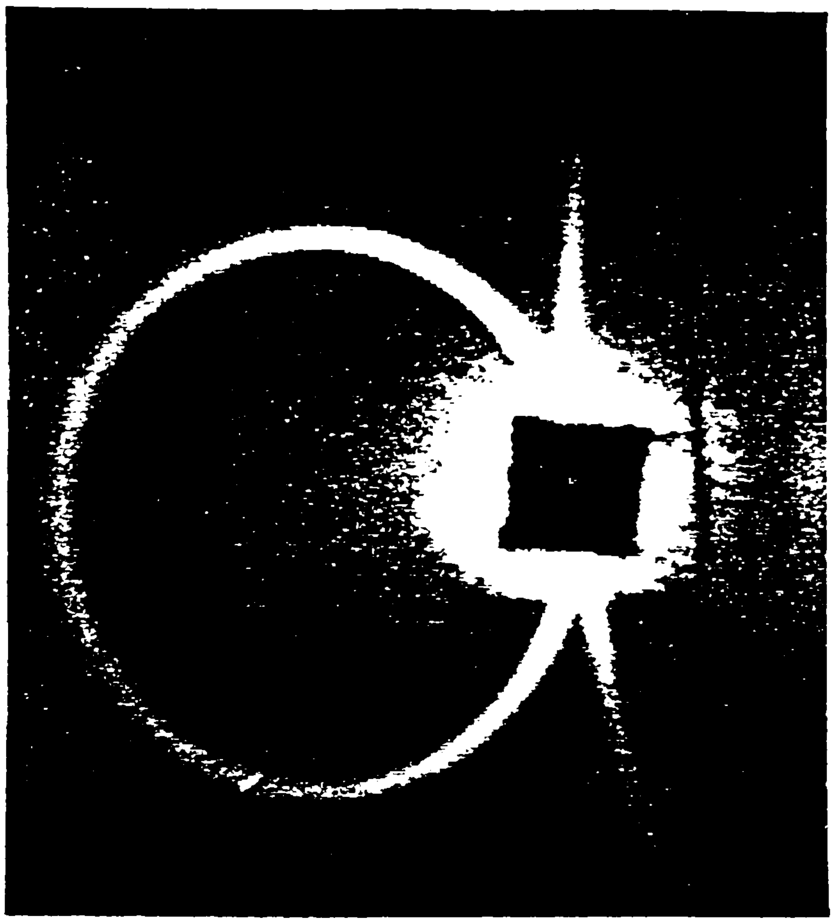

Figure 7.20 Scattering rings from low efficiency noise gratings recorded with separation $d = 0$ mm.

## 7.8 Reflected noise

Up to this point the recording of noise gratings in DCG has been made in transmission geometry. It is believed however, that reflected noise also exists. The aim of this small section is to record reflected noise gratings.

Newell [New87] previously tried to record reflection noise gratings in DCG but found little diffraction efficiency at the recording angle. He concluded that although the reflected noise may be weaker than the transmitted noise, in fact it was the high selectivity of the reflection gratings which made them difficult to observe in swollen DCG sensitised with 2% ammonium dichromate.

In order to reduce swelling, transmission and reflection noise gratings were recorded using an increased sensitisation (6% ammonium dichromate). The recording geometry used was the same as Figure 7.5 where $d = 0$ mm. For the reflection case, the DCG plate was placed before the $AgH^+$ emulsion instead of behind. Again, Agfa 8E56AH plates were used as the scattering source. An exposure energy of 1000 mJ / $cm^2$ was used at the recording angles of 0° and +20° (in the index matching tank) for both transmission and reflection geometries. Figure 7.21 shows the results.

At all recording angles we see optimum replay of the transmission noise gratings (solid line) occur around 460 nm. The 0° recording replayed at 0° and the 20° recording replayed at +17.5°. The reflected noise was replayed using the same replay wavelengths as found for optimum replay of the transmitted noise. These scans are represented by the dotted lines on each plot. Immediately we see reflected noise is recreated around the recording angle at the same place as the transmission dip but not at negative angles, making the scan asymmetric. The dips are much weaker than the transmitted dips and display lower angular selectivity. This is expected since reflection gratings are known to be less angularly selective than transmission gratings for holograms with the same thickness. Other symmetrical dips occur at higher angles due to the recording of a spurious, unslanted reflection grating caused by a reflection at the small boundary mismatch between the two plates. These do not effect the replay of the noise.

The plates were then reprocessed and swollen by introducing the swelling agent Ilfoshift discussed earlier in Chapter 2. A 20% concentration of Ilfoshift and a pH of 10 were used during the swelling stage at a temperature of 42°. This acted to swell the plates by around 19% from approximately 28.5 μm to 34.0 μm. The plates were rescanned and Figure 7.22 shows the results. Now we observe transmission dips with higher efficiencies and lower angular selectivity indicating an increase in modulation of the gratings. However, more significantly, we see a large increase in the efficiency of the reflected noise.

After processing, the refractive index of the gelatin is known to fall by approximately 10%. For transmission noise gratings (where swelling does not critically affect the replay conditions) we have found that this change in value causes optimum replay at a lower wavelength than recording. So, for simplicity we could assume that the refractive index is the main reason for a wavelength shift at replay.

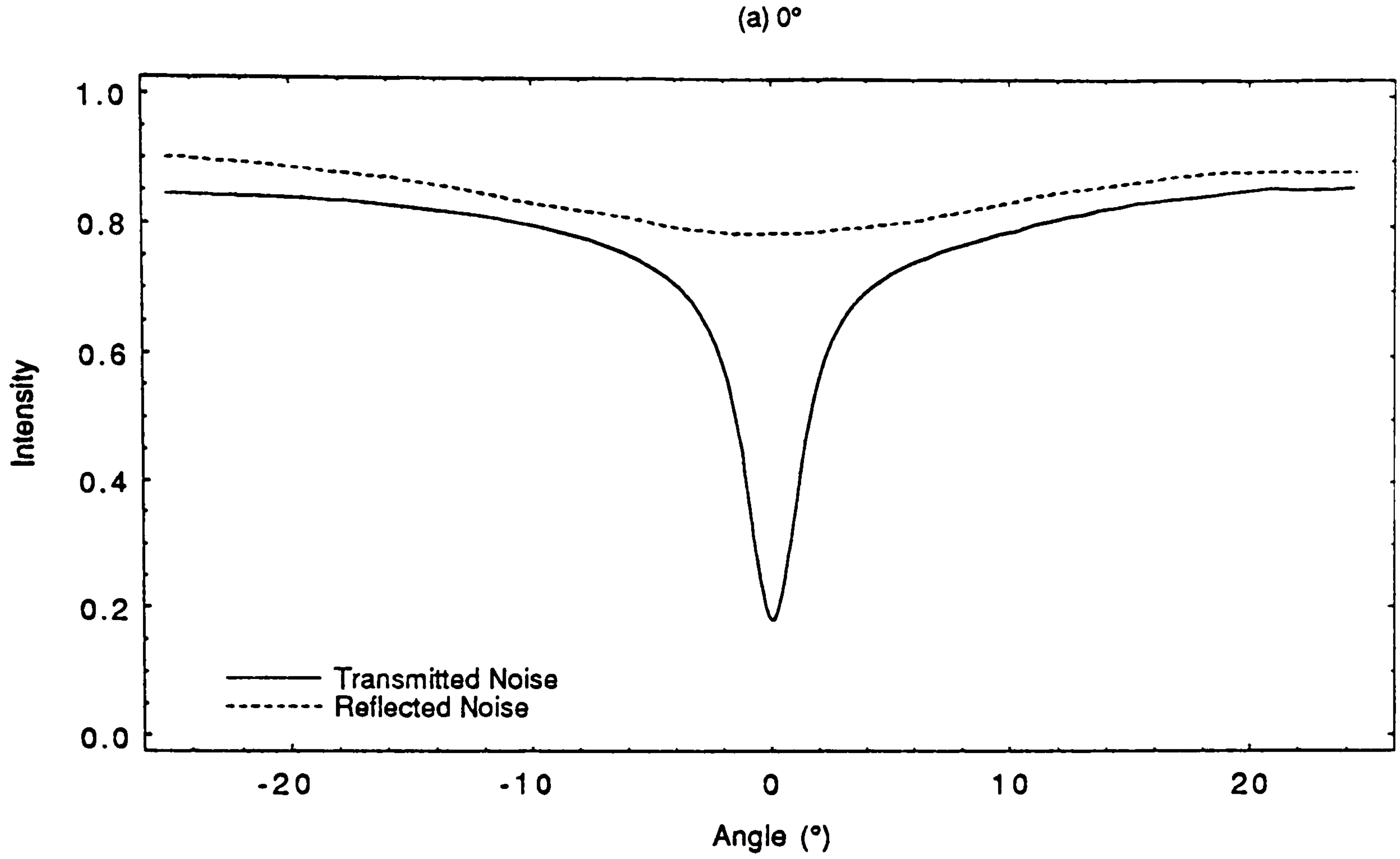


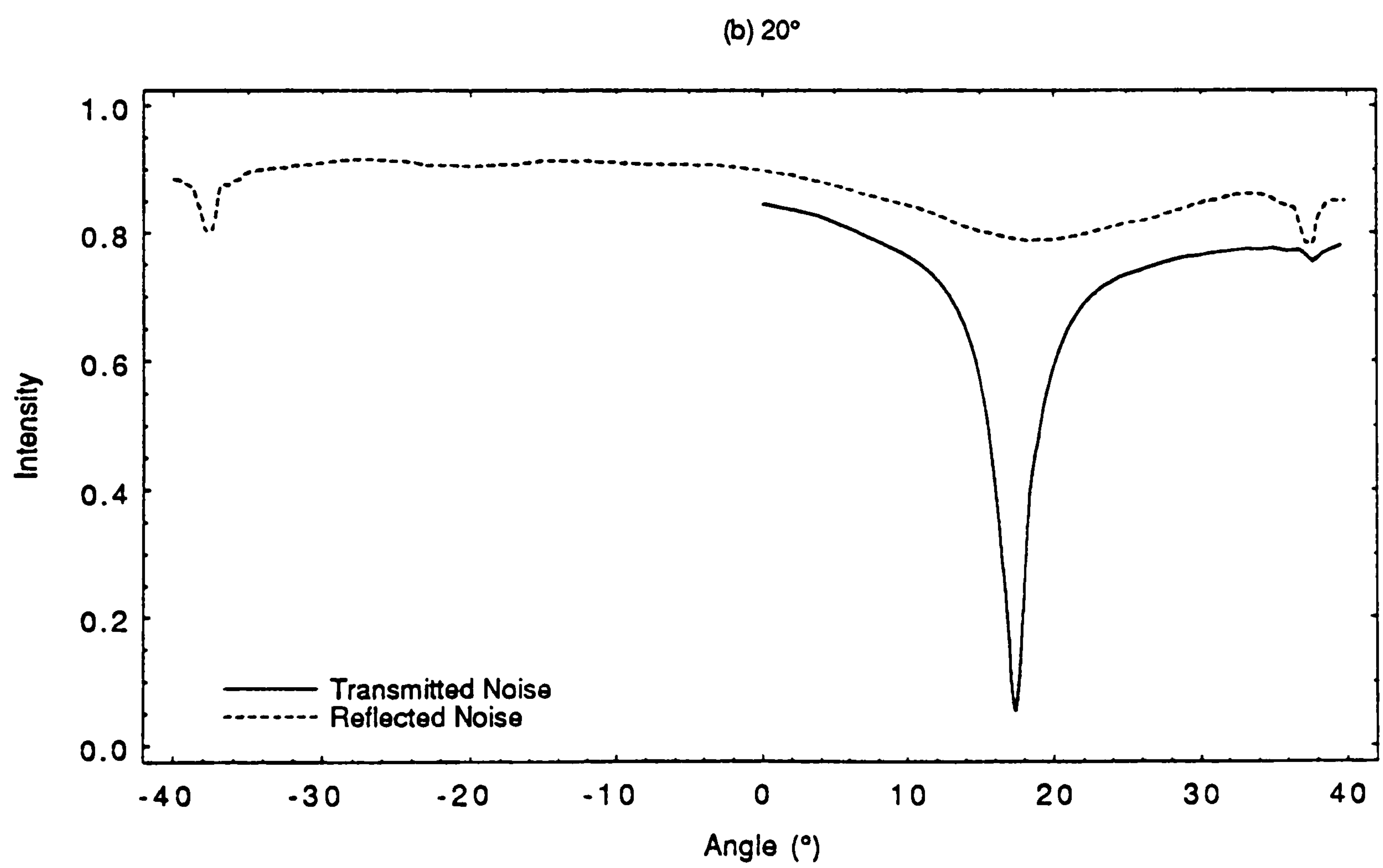


Figure 7.21 Reflection noise gratings copied into DCG compared with transmitted noise from the same scattering source (Agfa 8E56AH) recorded at (a) 0° and (b) 20°.

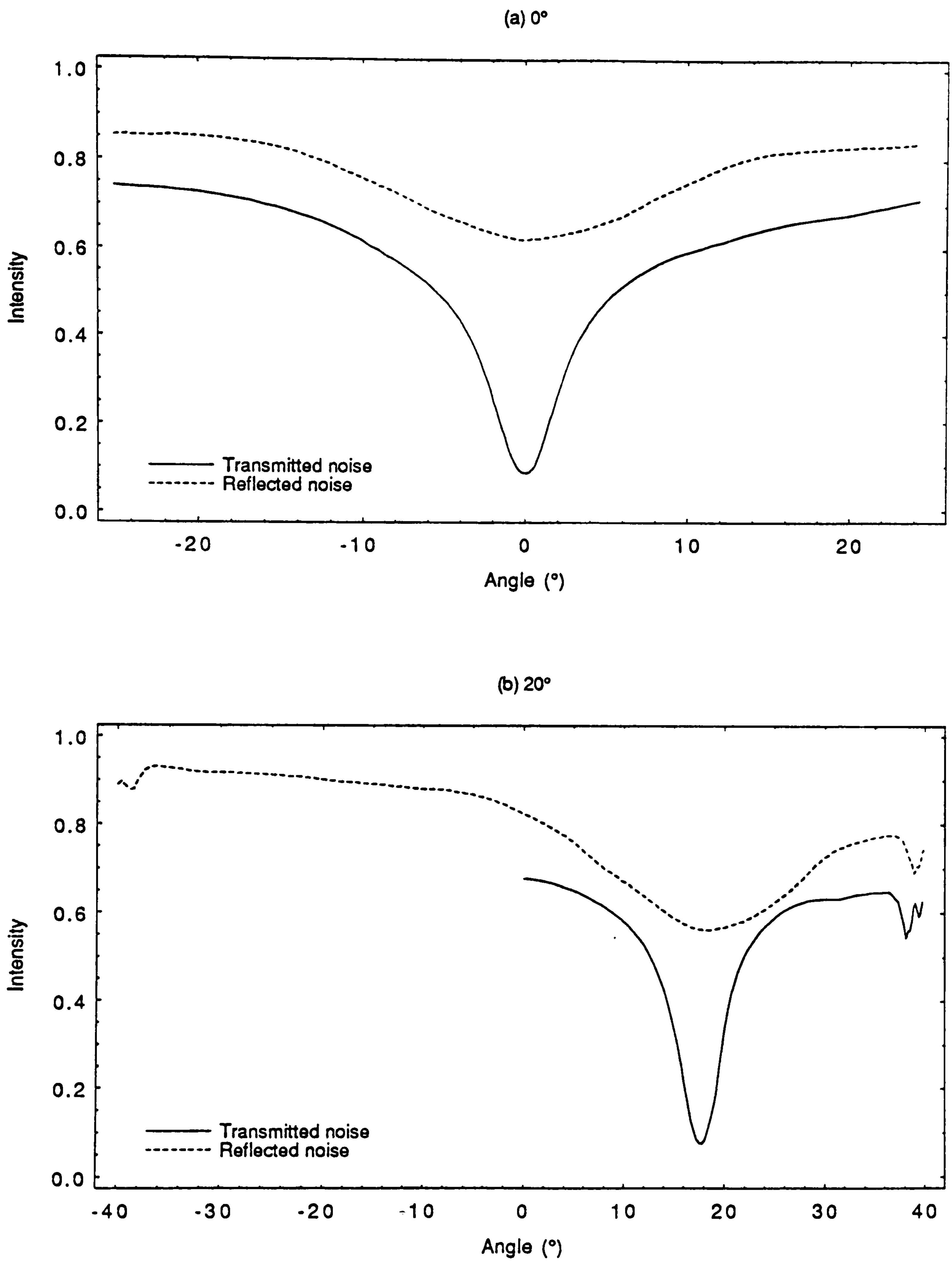


Figure 7.22 The reflection and transmission noise gratings shown in Figure 7.21 after reprocessing to swell the gelatin: (a) 0° and (b) 20°.

In the case of reflected noise however, the gratings are oriented in a direction perpendicular to the direction of swelling and are therefore greatly affected by any change in dimension. This leads to different gratings replaying on-Bragg under different conditions. In the first set of results (Figure 7.21) we saw weak reflected scatter. This corresponded to a small amount of swelling although not enough swelling to replay all the recorded reflection gratings (in particular the high frequency recordings with large K vectors) in an Ewald sphere which has been reduced in refractive index by 10%. However, in the second set of results (Figure 7.22) we saw substantial swelling which reduced the size of the K vectors and brings gratings with higher efficiency nearer to the Bragg condition. Thus, more reflection gratings are replayed causing the Bragg dip to becomes deeper. Unfortunately, due to the swelling, the gratings do not all replay at the Bragg condition simultaneously leading to a reduction in angular selectivity.

The exact mechanism of replay is still not clearly understood, since a large number of gratings are involved. It would therefore require a great deal of computer power [Rid88] to model these results and offer a more accurate quantitative explanation.

## 7.9 Summary

Silver halide noise gratings have been copied into dichromated gelatin using transmission and reflection geometries. The transmitted noise was found to exhibit greater selectivity and diffraction efficiency, however reflection noise gratings were successfully recorded for the first time and found to increase in diffraction efficiency as the thickness was increased. The forward scatter from three types of commercially available silver halide emulsions has been compared. The effect of reducing the significance of noise gratings recorded at high angles has been experimentally observed and has been found to agree with theoretical predictions.

# Chapter 8

# Conclusions and Future Work

The aim of the research described in this thesis was to study the use of dichromated gelatin (DCG) as a feasible recording material for holographic optical elements. In particular, to study the effects which are likely to limit the performance of these elements both at the recording and replay stages.

After a brief introductory chapter, which outlined the basic principles of holographic recording, we took a close look at the recording material, dichromated gelatin. In Chapter 2 we discussed the holographic properties of DCG and described the processing procedure in some detail. Two smaller investigations were also made. The first concerned the use of a chemical, called Ilfoshift, which was used to swell DCG during processing and allow replay at a longer wavelength. We saw that by increasing the concentration and pH of Ilfoshift we could record using a green wavelength (514.5 nm) and replay at red (620 nm). This is a particularly useful result considering the fact that DCG is normally insensitive to red wavelengths. The second investigation took a brief look at the effect of the substrate and coverplate upon the quality of a planar wavefront. Using interferometric techniques, we concluded that DCG is indeed capable of recreating a high quality wavefront on both float glass and optical flat substrates. However, this can be degraded by the improper choice of coverplate or irregularities in the gelatin.

In Chapter 3 we looked at a common, practical recording condition, i.e. the recording of a planar transmission grating in air. An investigation was made of specular reflections at the hologram / air boundaries at recording. Experiments were performed using recording polarisations perpendicular and parallel to the plane of incidence. We saw that, in addition to the primary transmission grating, we recorded a further five spurious gratings (one transmission type and four reflection type). By scanning the hologram through a series of replay angles at a wavelength shorter than that at recording, we were able to observe the individual incoherent replay of all six gratings. These were sufficiently separated in angle to allow the use of a simple linear superposition coupled wave model to describe replay. Thus, for the low modulation values involved in this case, the assumption of a linear recording characteristic was found to be reasonably valid.

In Chapter 4 we studied the nonlinear recording characteristics of DCG due to the increased exposure energy at recording. Both single and double exposure recordings were made. In each case spatial harmonic gratings were formed at high energy levels. For the double recordings we also noticed the existence of gratings with spatial frequencies equal to the sum and difference of integer values of the primary frequencies. The modulation values for each of these gratings were plotted against exposure energy. These were compared to a simple theory which assumes that the refractive index of DCG varies as a saturating exponential function with exposure and predicts the modulation values of both primary gratings and spatial harmonics. Good theoretical agreement was found with experimental results. An interesting result of the theory was that a $\pi$ phase shift may exist between certain harmonic gratings. The model was then used to describe theoretically the modulation profile of a single grating as a function of increasing exposure energy and beam ratio. As the exposure energy increased we observed the grating profile alter its shape as it became richer in spatial harmonic frequencies. For an overexposed grating an increase in beam ratio acted to maintain the sinusoidal characteristic, however this was at the expense of decreasing modulation. The effect of dispersion upon each grating was measured for both single and double exposure cases. All measurements showed a small drop in modulation with an increase in replay wavelength, but the difference grating ($G_1$ - $G_2$) was seen to increase in strength. This could not be explained using a simple coupled wave theory for a single grating recorded at a similar spatial frequency. From this chapter, it is clear that the saturating effects of DCG will introduce nonlinearities and hence the replay of spurious gratings.

Chapter 5 looked at the role of a varying beam ratio in both reflection and transmission geometries. Experimental results showed that an increase in sensitiser concentration can lead to high efficiency replay, in particular, for the case where a grating is recorded due to specular reflections. However, this efficiency is reduced as the recording angle decreases, i.e. the beam ratio increases. Experimental results of modulation versus exposure energy for reflection and transmission gratings were presented for varying beam ratios and compared with the nonlinear model presented earlier. Good agreement was found and showed a limitation in the maximum achievable modulation as the beam ratio is increased, due to an increase in bias exposure and hence bias hardness of the DCG.

In Chapter 6, we returned to look at the question of replaying a double exposure transmission hologram which has been recorded in the saturation region of the exposure characteristic. A coupled wave theory was developed to take account of two primary gratings and a third grating which is due to material nonlinearities and has a spatial frequency equal to the difference of the first two. A study was made of the replay of these gratings plus their interactions over a range of replay angles. The magnitude of the modulation of each grating was governed by the nonlinear theory described earlier. The theory was used to model experimental results at different separation angles between the two recording angles for the primary gratings, particularly when the angular difference between the two gratings is small. Results showed that the efficiency of the difference grating was depleted because of grating interactions between the two primary gratings which are of opposite phase. This phenomenon was used to explain the apparent rise in modulation for the dispersion result seen earlier.

Finally, DCG was used as a tool to investigate the recorded scatter observed in silver halide holograms. By changing the distance between a silver halide plate and the DCG at recording it was possible to record different angular spreads of noise gratings. This led to the conclusion that noise gratings with high angular components have high angular selectivity and are more efficient. A comparison of the transmitted scatter of three commercial holographic emulsions was made at high exposure energies. Both transmission and, for the first time, reflection type noise gratings have been independently recorded.

Much of the above work is still incomplete. A simple study was made of the nonlinear recording characteristic of dichromated gelatin and its effect on the sequential recording of two transmission gratings. However, much attention is being paid to the recording of holograms which have been simultaneously recorded for reasons of higher efficiency [LaM68b] for example. This case was not investigated and still requires attention, particularly when we realise that a nonlinear difference grating may compete with an intermodulation grating of opposite phase. It would also be interesting to extend the study of nonlinear recording further to look at the reflection case [Hea87] or indeed follow Chang and Case [Cha76b] in their use of nonlinear gratings for applications at infra-red or ultra violet wavelengths. With regards grating interactions, it is still necessary to optimise the recording conditions in order to minimise the replay of spurious waves. The study of noise gratings and, in particular, the copying of noise from silver halide emulsions to dichromated gelatin still requires a great deal of attention. The three dimensional dependence at replay needs to be studied before real quantitative analyses can be carried out. But, most importantly, it is necessary to control and attempt to minimise the transfer of scatter when copying holographic optical elements from silver halide to dichromated gelatin. Without this control we see that the noise is readily transferred and acts to limit the HOE's performance.

From these results, we can make several conclusions. Volume Holographic Optical Elements have their limitations. These may manifest themselves as the recording of spurious gratings at recording due to boundary reflections or material nonlinearities. At replay the interaction of multiple gratings leads to the replay of further 'spurious' waves. Together these effects paint a complex picture for holographic replay. Today much attention is being paid to the recording of complex systems such as holographic optical interconnects or display systems. These systems require the possible recording of many gratings in the one hologram and accurate replay with the minimisation of spurious noise. It is therefore important to minimise these spurious effects. At present DCG is the only high quality recording material available to record these components. In this thesis we have studied these effects and obtained a greater understanding of holographic recording in DCG. This information may now be used to minimise unwanted waves and increase quality in the design and fabrication of holographic optical elements.

# *Appendix I*

# *Coupled wave theory for multiple transmission and reflection gratings*

Here, generalised coupled wave equations based on Kogelnik's theory [Kog69] are derived to describe a hologram, recorded in dichromated gelatin (DCG), containing multiple transmission and reflection gratings [Bla89a].

It is assumed that the material recording response is linear and that the individual gratings are sufficiently angularly separated so that multiple grating interactions can be ignored. In this treatment we will also assume that the hologram is sufficiently thick and volume in nature (i.e. $\Omega \gg 20$) so as to neglect second and higher orders.

By assuming that the hologram is replayed with a wave polarised perpendicular to the plane of incidence, we can let the electric field $E$ within the hologram be a solution of the scalar wave equation as shown:-

$$\nabla^2 E + k^2 E = 0 \tag{I.1}$$

where
$$k^2 = \frac{\omega^2}{c^2}\varepsilon_r - j\omega\mu\sigma_o \tag{I.2}$$

$\omega$ is the angular frequency of replay, $c$ is the velocity of light in free space, $\varepsilon_r$ is a measure of the dielectric constant, $\mu$ is permeability and $\sigma_o$ indicates a constant conductivity. In order to use equation (I.2) we have neglected the existence of conductivity modulation, however we cannot assume that the effects of constant absorption ($\alpha$) will be negligible at replay. Therefore, by assuming that the absorption of DCG is small, we can let:-

$$\omega\mu\sigma_o = 2\alpha\beta$$

where $\beta = \dfrac{2\pi n_o}{\lambda}$ is the propagation constant, $n_0$ is the average refractive index of the medium and $\lambda$ is the replay wavelength.

Since we have stipulated that DCG only records as a variation in permitivity, we can let the dielectric constant ( $\varepsilon_r$ ) of the material vary as:-

$$\varepsilon_r = \varepsilon_{ro} + \sum_{l=1}^{L} \varepsilon_{rrl}\cos(\overline{K}_l.\bar{r}) + \sum_{n=1}^{N} \varepsilon_{rtn}\cos(\overline{M}_n.\bar{r}) \qquad (I.3)$$

where $L$ is the number of reflection gratings and $N$ is the number of transmission gratings recorded in the hologram, $\varepsilon_{ro}$ is the average dielectric constant , $\varepsilon_{rrl}$ and $\varepsilon_{rtn}$ are the modulations, and $\overline{K}_l$ and $\overline{M}_n$ are the grating vectors of the $l^{th}$ reflection and $n^{th}$ transmission gratings respectively.

We can now assume a solution to the wave equation as:-

$$E = R_o e^{-j\bar{\rho}_o.\bar{r}} + \sum_{l=1}^{L} S_l e^{-j\bar{\sigma}_l.\bar{r}} + \sum_{i=-1,1}\sum_{n=1}^{N} Q_n^{(i)} e^{-j\bar{\mu}_n^{(i)}.\bar{r}} \qquad (I.4)$$

where $R_o$ is the amplitude of the incident replay beam, $S_l$ and $Q_n{}^{(i)}$ are the amplitudes of the beams diffracted by the $l^{th}$ reflection and the $n^{th}$ transmission grating respectively. Note that for transmission gratings two output beams, both the -1 and +1 orders, are allowed. $\bar{\rho}_o$ , $\bar{\sigma}_l$ and $\bar{\mu}_n^{(i)}$ are the wave vectors of the replay beam, of the beams diffracted by the $l^{th}$ reflection, and of those diffracted by the $n^{th}$ transmission grating respectively.

We now substitute (I.4) in (I.1) and by conserving the component of the diffracted beam parallel to the hologram surface (i.e. the y axis), we will make the '$\beta$-valued' assumption that:-

$$|\bar{\rho}_o| = |\bar{\sigma}_l| = |\bar{\mu}_n^{(i)}| = \beta \tag{I.5}$$

Making this assumption we introduce the 'off-Bragg' parameters $\bar{\psi}_l$ and $\bar{\psi}_n^{(i)}$ for reflection and transmission gratings respectively. Figure I.1 shows their derivation for transmission gratings where:-

$$\bar{\rho}_o + (i)\overline{M}_n = \bar{\mu}_n^{(i)} + (i)\bar{\psi}_n^{(i)} \qquad i = 1, -1 \tag{I.6}$$

The 'off-Bragg' parameter is defined analogously for the reflection case where:-

$$\bar{\rho}_o - \overline{K}_l = \bar{\sigma}_l + \bar{\psi}_l \tag{I.7}$$

Now, by assuming that the energy exchange between the diffracted orders is slow we can neglect second order derivatives and obtain the expression:-

$$\begin{aligned}
&-2j\left\{\rho_o \nabla R_o e^{-j\bar{\rho}_o.\bar{r}} + \sum_{l=1}^{L} \sigma_l \nabla S_l e^{-j\bar{\sigma}_l.\bar{r}} + \sum_{i=-1,1}\sum_{n=1}^{N} \mu_n^{(i)} \nabla Q_n^{(i)} e^{-j\bar{\mu}_n^{(i)}.\bar{r}}\right\} \\
&= \frac{\beta^2}{2}\left\{R_o e^{-j\bar{\rho}_o.\bar{r}}\left[-j\frac{4\alpha}{\beta} + \sum_{l=1}^{L}\frac{\varepsilon_{rl}}{\varepsilon_{ro}}\left(e^{j\overline{K}_l.\bar{r}} + e^{-j\overline{K}_l.\bar{r}}\right) + \sum_{n=1}^{N}\frac{\varepsilon_{rn}}{\varepsilon_{ro}}\left(e^{j\overline{M}_n.\bar{r}} + e^{-j\overline{M}_n.\bar{r}}\right)\right]\right. \\
&+ \sum_{l=1}^{L} S_l e^{-j\bar{\sigma}_l.\bar{r}}\left[-j\frac{4\alpha}{\beta} + \sum_{l=1}^{L}\frac{\varepsilon_{rl}}{\varepsilon_{ro}}\left(e^{j\overline{K}_l.\bar{r}} + e^{-j\overline{K}_l.\bar{r}}\right) + \sum_{n=1}^{N}\frac{\varepsilon_{rn}}{\varepsilon_{ro}}\left(e^{j\overline{M}_n.\bar{r}} + e^{-j\overline{M}_n.\bar{r}}\right)\right] \\
&\left.+ \sum_{i=-1,1}\sum_{n=1}^{N} Q_n^{(i)} e^{-j\bar{\mu}_n^{(i)}.\bar{r}}\left[-j\frac{4\alpha}{\beta} + \sum_{l=1}^{L}\frac{\varepsilon_{rl}}{\varepsilon_{ro}}\left(e^{j\overline{K}_l.\bar{r}} + e^{-j\overline{K}_l.\bar{r}}\right) + \sum_{n=1}^{N}\frac{\varepsilon_{rn}}{\varepsilon_{ro}}\left(e^{j\overline{M}_n.\bar{r}} + e^{-j\overline{M}_n.\bar{r}}\right)\right]\right\}
\end{aligned} \tag{I.8}$$

We specify which waves we wish to consider at replay. Choosing only 1st order diffraction and no multiple grating interactions, we can drop the terms whose amplitude will be negligible. That is, we will assume that each grating is replayed individually with no cross coupling between diffracted beams. (I.8) simplifies to the following expression:-

$$-2j\left\{\rho_o \nabla R_o e^{-j\bar{\rho}_o.\bar{r}} + \sum_{l=1}^{L} \sigma_l \nabla S_l e^{-j\bar{\sigma}_l.\bar{r}} + \sum_{i=-1,1} \sum_{n=1}^{N} \mu_n^{(i)} \nabla Q_n^{(i)} e^{-j\bar{\mu}_n^{(i)}.\bar{r}}\right\}$$

$$= \frac{\beta^2}{2}\left\{-j\frac{4\alpha}{\beta_o} R_o e^{-j\bar{\rho}_o.\bar{r}} + R_o \sum_{l=1}^{L} \frac{\varepsilon_{rl}}{\varepsilon_{ro}} e^{-j(\bar{\rho}_o-\bar{K}_l).\bar{r}} + R_o \sum_{n=1}^{N} \frac{\varepsilon_{rn}}{\varepsilon_{ro}} \left[e^{-j(\bar{\rho}_o-\bar{M}_n).\bar{r}} + e^{-j(\bar{\rho}_o+\bar{M}_n).\bar{r}}\right]\right.$$

$$-j\frac{4\alpha}{\beta} \sum_{l=1}^{L} S_l e^{-j\bar{\sigma}_l.\bar{r}} + \sum_{l=1}^{L} \frac{\varepsilon_{rl}}{\varepsilon_{ro}} S_l e^{-j(\bar{\sigma}_l+\bar{K}_l).\bar{r}}$$

$$\left.-j\frac{4\alpha}{\beta} \sum_{i=-1,1} \sum_{n=1}^{N} Q_n^{(i)} e^{-j\bar{\mu}_n^{(i)}.\bar{r}} + \sum_{i=-1,1} \sum_{n=1}^{N} \frac{\varepsilon_{rn}}{\varepsilon_{ro}} Q_n^{(i)} e^{-j(\bar{\mu}_n^{(i)}+(i)\bar{M}_n).\bar{r}}\right\} \quad (I.9)$$

However, the wave vectors in the above equation may be expressed in terms of the 'off-Bragg' parameters shown in (I.6) and (I.7). The equation may then be simplified further to the following form:-

$$-2j\left\{\rho_o \nabla R_o e^{-j\bar{\rho}_o.\bar{r}} + \sum_{l=1}^{L} \sigma_l \nabla S_l e^{-j\bar{\sigma}_l.\bar{r}} + \sum_{i=-1,1} \sum_{n=1}^{N} \mu_n^{(i)} \nabla Q_n^{(i)} e^{-j\bar{\mu}_n^{(i)}.\bar{r}}\right\}$$

$$= \frac{\beta^2}{2}\left\{-j\frac{4\alpha}{\beta} R_o e^{-j\bar{\rho}_o.\bar{r}} + R_o \sum_{l=1}^{L} \frac{\varepsilon_{rl}}{\varepsilon_{ro}} e^{-j\bar{\sigma}_l.\bar{r}} e^{-j\bar{\psi}_l.\bar{r}} + R_o \sum_{i=-1,1} \sum_{n=1}^{N} \frac{\varepsilon_{rn}}{\varepsilon_{ro}} e^{-j\bar{\mu}_n^{(i)}.\bar{r}} e^{-j(i)\bar{\psi}_n^{(i)}.\bar{r}}\right.$$

$$-j\frac{4\alpha}{\beta} \sum_{l=1}^{L} S_l e^{-j\bar{\sigma}_l.\bar{r}} + \sum_{l=1}^{L} \frac{\varepsilon_{rl}}{\varepsilon_{ro}} S_l e^{-j\bar{\rho}_o.\bar{r}} e^{+j\bar{\psi}_l.\bar{r}}$$

$$\left.-j\frac{4\alpha}{\beta} \sum_{i=-1,1} \sum_{n=1}^{N} Q_n^{(i)} e^{-j\bar{\mu}_n^{(i)}.\bar{r}} + \sum_{i=-1,1} \sum_{n=1}^{N} \frac{\varepsilon_{rn}}{\varepsilon_{ro}} Q_n^{(i)} e^{-j\bar{\rho}_o.\bar{r}} e^{-j(i)\bar{\psi}_n^{(i)}.\bar{r}}\right\} \quad (I.10)$$

where, by comparing coefficients of the exponential terms, and simplifying in one dimension normal to the hologram surface, we may obtain the following set of coupled wave equations.:-

$$\sum_{l=1}^{L}\left\{\frac{dA_l}{dx}-\left(\frac{\alpha}{\cos\theta_l}+j\psi_l\right)A_l-j\frac{\kappa_l}{\cos\theta_l}R_o\right\}=0$$

$$\sum_{i=-1,1}\sum_{n=1}^{N}\left\{\frac{dB_n^{(i)}}{dx}-\left(\frac{\alpha}{\cos\phi_n^{(i)}}+j\psi_n^{(i)}\right)B_n^{(i)}-j\frac{\kappa_n}{\cos\phi_n^{(i)}}R_o\right\}=0$$

$$\cos\theta_o\frac{dR_o}{dx}-\alpha R_o-j\sum_{l=1}^{L}\kappa_l A_l-j\sum_{i=-1,1}\sum_{n=1}^{N}\kappa_n B_n^{(i)}=0 \tag{I.11}$$

where $\kappa_m=\dfrac{\varepsilon_m\beta}{4\varepsilon_o}$ $\qquad \cos\theta_o=\dfrac{\rho_{ox}}{\beta}$

$A_l=S_l e^{+j\psi_l.x}$ $\qquad \cos\theta_l=\dfrac{\sigma_{lx}}{\beta}$

$B_n^{(i)}=Q_n^{(i)}e^{+j\psi_n.x}$ $\qquad \cos\phi_n^{(i)}=\dfrac{\mu_{nx}^{(i)}}{\beta}$

The differential equations have constant coefficients so were solved by finding the eigenvalues numerically. The constants were determined from the boundary conditions, which state that the diffracted waves must be zero at the surfaces where they started to be generated, i.e. at the input surface for transmission gratings and at the output surface for reflection gratings.

The computer programme is an extension of work described by Heaton [Hea85b] in his study of reflection gratings. It also takes account of the change in average refractive index between the substrate and the gelatin and allows replay within a medium other than air.

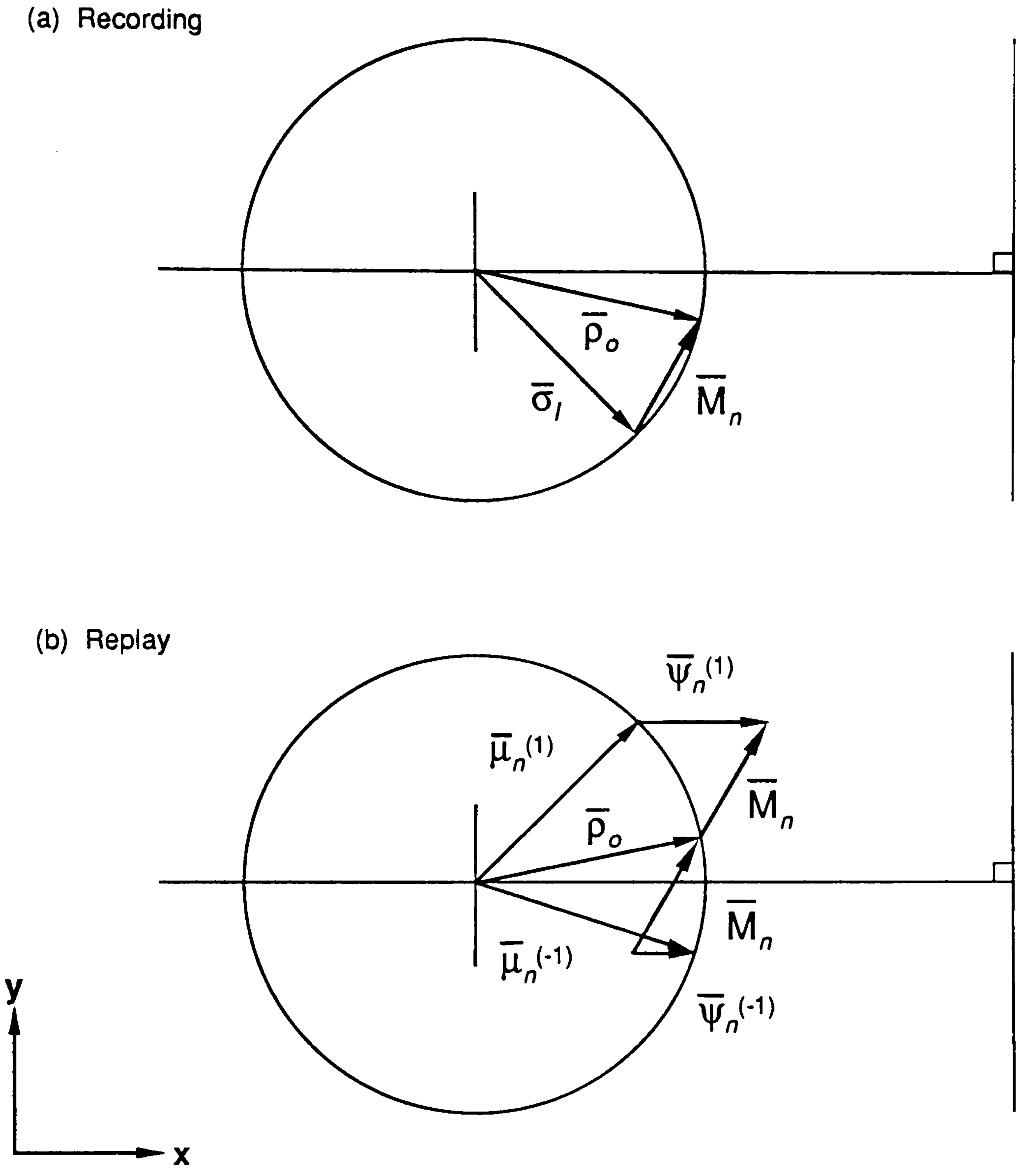


Figure I.1 Ewald circle representation of vector relationship between incident and first order diffracted waves for transmission gratings.

# Appendix II

# Coupled wave theory for double exposure transmission gratings

First, we will find solutions to the scalar wave equation:-

$$\nabla^2 E + k^2 E = 0 \tag{II.1}$$

where $E$ is the electric field and $k^2 = \frac{\omega^2}{c^2}\varepsilon_r - j2\alpha\beta$ , where $\beta$ is the propagation constant at replay and, since we have previously stated that we can neglect conductivity modulation, $\alpha$ is our measure of constant absorption. We shall let the permitivity $\varepsilon_r$ vary as:-

$$\varepsilon_r = \varepsilon_{ro} + \varepsilon_{r1}\cos(\overline{\mathrm{K}}_1 .\bar{\mathrm{r}}) + \varepsilon_{r2}\cos(\overline{\mathrm{K}}_2 .\bar{\mathrm{r}}) - \varepsilon_{r3}\cos(\overline{\mathrm{K}}_3 .\bar{\mathrm{r}}) \tag{II.2}$$

where $\overline{\mathrm{K}}_1$ and $\overline{\mathrm{K}}_2$ are the recorded grating vectors and $\overline{\mathrm{K}}_3$ is the vector corresponding to the difference grating $G_1$ - $G_2$.

From Figure 6.2 we assume that eleven waves will propagate within the hologram, so we will assume a solution to the wave equation as:-

$$E = \sum_{i=0}^{10} A_i e^{-j\bar{\sigma}_i .\bar{r}} \tag{II.3}$$

$A_i$ and $\overline{\sigma}_i$ are the amplitudes and wave vectors of the waves of interest and where $A_o\, e^{-j\,\overline{\sigma}_o\,.\overline{r}}$ represents the replay wave.

Placing (II.3) into (II.1) and making the '$\beta$-valued' assumption that:-

$$|\overline{\sigma}_i| = \beta \tag{II.4}$$

we can define our 'off-Bragg' vectors $\overline{\psi}_i$ as:-

$$\overline{\sigma}_o + l\mathrm{K}_i = \overline{\sigma}_i + \overline{\psi}_i \quad \text{where} \quad l = \pm 1 \tag{II.5}$$

We obtain the following expression:-

$$2j\sum_{i=0}^{10}\sigma_i\nabla A_i e^{-j\overline{\sigma}_i.\overline{r}} = \frac{\beta^2}{2}\sum_{i=0}^{10}A_i\left\{-j\frac{4\alpha}{\beta}\sum_{i=0}^{10}A_i e^{-j\overline{\sigma}_i.\overline{r}} + \frac{\varepsilon_{r1}}{\varepsilon_{ro}}\left[e^{-j(\overline{\sigma}_i-\overline{\mathrm{K}}_1).\overline{r}} + e^{-j(\overline{\sigma}_i+\overline{\mathrm{K}}_1).\overline{r}}\right]\right.$$
$$\left. + \frac{\varepsilon_{r2}}{\varepsilon_{ro}}\left[e^{-j(\overline{\sigma}_i-\overline{\mathrm{K}}_2).\overline{r}} + e^{-j(\overline{\sigma}_i+\overline{\mathrm{K}}_2).\overline{r}}\right] - \frac{\varepsilon_{r3}}{\varepsilon_{ro}}\left[e^{-j(\overline{\sigma}_i-\overline{\mathrm{K}}_3).\overline{r}} + e^{-j(\overline{\sigma}_i+\overline{\mathrm{K}}_3).\overline{r}}\right]\right\} \tag{II.6}$$

To obtain this, we have neglected second derivatives assuming that we are dealing with a slowly varying function.

This equation may be simplified by assuming only the existence of the following relevant terms, ie.those illustrated in Figure 6.2:-

$$2j\sum_{i=0}^{10}\sigma_i\nabla A_i e^{-j\overline{\sigma}_i.\overline{r}} = \frac{\beta^2}{2}\left\{-j\frac{4\alpha}{\beta}\sum_{i=0}^{10}A_i e^{-j\overline{\sigma}_i.\overline{r}}\right.$$
$$+A_o\frac{\varepsilon_{r1}}{\varepsilon_{ro}}\left[e^{-j(\overline{\sigma}_o-\overline{\mathrm{K}}_1).\overline{r}} + e^{-j(\overline{\sigma}_o+\overline{\mathrm{K}}_1).\overline{r}}\right] + A_o\frac{\varepsilon_{r2}}{\varepsilon_{ro}}\left[e^{-j(\overline{\sigma}_o-\overline{\mathrm{K}}_2).\overline{r}} + e^{-j(\overline{\sigma}_o+\overline{\mathrm{K}}_2).\overline{r}}\right]$$
$$-A_o\frac{\varepsilon_{r3}}{\varepsilon_{ro}}\left[e^{-j(\overline{\sigma}_o-\overline{\mathrm{K}}_3).\overline{r}} + e^{-j(\overline{\sigma}_o+\overline{\mathrm{K}}_3).\overline{r}}\right] + A_1\frac{\varepsilon_{r1}}{\varepsilon_{ro}}e^{-j(\overline{\sigma}_1-\overline{\mathrm{K}}_1).\overline{r}} + A_1\frac{\varepsilon_{r2}}{\varepsilon_{ro}}e^{-j(\overline{\sigma}_1-\overline{\mathrm{K}}_2).\overline{r}}$$
$$-A_1\frac{\varepsilon_{r3}}{\varepsilon_{ro}}\left[e^{-j(\overline{\sigma}_1-\overline{\mathrm{K}}_3).\overline{r}} + e^{-j(\overline{\sigma}_1+\overline{\mathrm{K}}_3).\overline{r}}\right] + A_2\frac{\varepsilon_{r1}}{\varepsilon_{ro}}e^{-j(\overline{\sigma}_2+\overline{\mathrm{K}}_1).\overline{r}} + A_2\frac{\varepsilon_{r2}}{\varepsilon_{ro}}e^{-j(\overline{\sigma}_2+\overline{\mathrm{K}}_2).\overline{r}}$$
$$-A_2\frac{\varepsilon_{r3}}{\varepsilon_{ro}}\left[e^{-j(\overline{\sigma}_2-\overline{\mathrm{K}}_3).\overline{r}} + e^{-j(\overline{\sigma}_2+\overline{\mathrm{K}}_3).\overline{r}}\right] + A_3\frac{\varepsilon_{r1}}{\varepsilon_{ro}}e^{-j(\overline{\sigma}_3-\overline{\mathrm{K}}_1).\overline{r}} + A_3\frac{\varepsilon_{r2}}{\varepsilon_{ro}}e^{-j(\overline{\sigma}_3-\overline{\mathrm{K}}_2).\overline{r}}$$

$$-A_3\frac{\varepsilon_{r3}}{\varepsilon_{ro}}\left[e^{-j(\bar{\sigma}_3-\bar{K}_3).\bar{r}}+e^{-j(\bar{\sigma}_3+\bar{K}_3).\bar{r}}\right]+A_4\frac{\varepsilon_{r1}}{\varepsilon_{ro}}e^{-j(\bar{\sigma}_4+\bar{K}_1).\bar{r}}+A_4\frac{\varepsilon_{r2}}{\varepsilon_{ro}}e^{-j(\bar{\sigma}_4+\bar{K}_2).\bar{r}}$$

$$-A_4\frac{\varepsilon_{r3}}{\varepsilon_{ro}}\left[e^{-j(\bar{\sigma}_4-\bar{K}_3).\bar{r}}+e^{-j(\bar{\sigma}_4+\bar{K}_3).\bar{r}}\right]+A_5\frac{\varepsilon_{r1}}{\varepsilon_{ro}}e^{-j(\bar{\sigma}_5-\bar{K}_1).\bar{r}}+A_5\frac{\varepsilon_{r2}}{\varepsilon_{ro}}e^{-j(\bar{\sigma}_3+\bar{K}_2).\bar{r}}$$

$$-A_5\frac{\varepsilon_{r3}}{\varepsilon_{ro}}e^{-j(\bar{\sigma}_5-\bar{K}_3).\bar{r}}+A_6\frac{\varepsilon_{r1}}{\varepsilon_{ro}}e^{-j(\bar{\sigma}_6+\bar{K}_1).\bar{r}}+A_6\frac{\varepsilon_{r2}}{\varepsilon_{ro}}e^{-j(\bar{\sigma}_6-\bar{K}_2).\bar{r}}-A_6\frac{\varepsilon_{r3}}{\varepsilon_{ro}}e^{-j(\bar{\sigma}_6+\bar{K}_3).\bar{r}}$$

$$\left.-A_7\frac{\varepsilon_{r3}}{\varepsilon_{ro}}e^{-j(\bar{\sigma}_7-\bar{K}_3).\bar{r}}-A_8\frac{\varepsilon_{r3}}{\varepsilon_{ro}}e^{-j(\bar{\sigma}_8+\bar{K}_3).\bar{r}}-A_9\frac{\varepsilon_{r3}}{\varepsilon_{ro}}e^{-j(\bar{\sigma}_9+\bar{K}_3).\bar{r}}-A_{10}\frac{\varepsilon_{r3}}{\varepsilon_{ro}}e^{-j(\bar{\sigma}_{10}-\bar{K}_3).\bar{r}}\right\} \qquad \text{(II.7)}$$

Equation (II.7) may now be re-written in terms of our 'off-Bragg' parameters found in Equations (II.5) :-

$$2j\sum_{i=0}^{10}\sigma_i\nabla A_i e^{-j\bar{\sigma}_i.\bar{r}}=\frac{\beta^2}{2}\left\{-j\frac{4\alpha}{\beta}\sum_{i=0}^{10}A_i e^{-j\bar{\sigma}_i.\bar{r}}\right.$$

$$+A_o\frac{\varepsilon_{r1}}{\varepsilon_{ro}}\left[e^{-j\bar{\sigma}_2.\bar{r}}e^{-j\bar{\psi}_2.\bar{r}}+e^{-j\bar{\sigma}_1.\bar{r}}e^{-j\bar{\psi}_1.\bar{r}}\right]+A_o\frac{\varepsilon_{r2}}{\varepsilon_{ro}}\left[e^{-j\bar{\sigma}_4.\bar{r}}e^{-j\bar{\psi}_4.\bar{r}}+e^{-j\bar{\sigma}_3.\bar{r}}e^{-j\bar{\psi}_3.\bar{r}}\right]$$

$$-A_o\frac{\varepsilon_{r3}}{\varepsilon_{ro}}\left[e^{-j\bar{\sigma}_6.\bar{r}}e^{-j\bar{\psi}_6.\bar{r}}+e^{-j\bar{\sigma}_5.\bar{r}}e^{-j\bar{\psi}_5.\bar{r}}\right]+A_1\frac{\varepsilon_{r1}}{\varepsilon_{ro}}e^{-j\bar{\sigma}_o.\bar{r}}e^{+j\bar{\psi}_1.\bar{r}}+A_1\frac{\varepsilon_{r2}}{\varepsilon_{ro}}e^{-j\bar{\sigma}_5.\bar{r}}e^{+j(\bar{\psi}_1-\bar{\psi}_5).\bar{r}}$$

$$-A_1\frac{\varepsilon_{r3}}{\varepsilon_{ro}}\left[e^{-j\bar{\sigma}_3.\bar{r}}e^{+j(\bar{\psi}_1-\bar{\psi}_3).\bar{r}}+e^{-j\bar{\sigma}_7.\bar{r}}e^{-j\bar{\psi}_7.\bar{r}}\right]+A_2\frac{\varepsilon_{r1}}{\varepsilon_{ro}}e^{-j\bar{\sigma}_o.\bar{r}}e^{+j\bar{\psi}_2.\bar{r}}+A_2\frac{\varepsilon_{r2}}{\varepsilon_{ro}}e^{-j\bar{\sigma}_6.\bar{r}}e^{+j(\bar{\psi}_2-\bar{\psi}_6).\bar{r}}$$

$$-A_2\frac{\varepsilon_{r3}}{\varepsilon_{ro}}\left[e^{-j\bar{\sigma}_8.\bar{r}}e^{-j\bar{\psi}_8.\bar{r}}+e^{-j\bar{\sigma}_4.\bar{r}}e^{+j(\bar{\psi}_2-\bar{\psi}_4).\bar{r}}\right]+A_3\frac{\varepsilon_{r1}}{\varepsilon_{ro}}e^{-j\bar{\sigma}_6.\bar{r}}e^{+j(\bar{\psi}_3-\bar{\psi}_6).\bar{r}}+A_3\frac{\varepsilon_{r2}}{\varepsilon_{ro}}e^{-j\bar{\sigma}_o.\bar{r}}e^{+j\bar{\psi}_3.\bar{r}}$$

$$-A_3\frac{\varepsilon_{r3}}{\varepsilon_{ro}}\left[e^{-j\bar{\sigma}_9.\bar{r}}e^{+j\bar{\psi}_9.\bar{r}}+e^{-j\bar{\sigma}_1.\bar{r}}e^{-j(\bar{\psi}_1-\bar{\psi}_3).\bar{r}}\right]+A_4\frac{\varepsilon_{r1}}{\varepsilon_{ro}}e^{-j\bar{\sigma}_5.\bar{r}}e^{+j(\bar{\psi}_4-\bar{\psi}_5).\bar{r}}+A_4\frac{\varepsilon_{r2}}{\varepsilon_{ro}}e^{-j\bar{\sigma}_o.\bar{r}}e^{+j\bar{\psi}_4.\bar{r}}$$

$$-A_4\frac{\varepsilon_{r3}}{\varepsilon_{ro}}\left[e^{-j\bar{\sigma}_2.\bar{r}}e^{-j(\bar{\psi}_2-\bar{\psi}_4).\bar{r}}+e^{-j\bar{\sigma}_{10}.\bar{r}}e^{+j\bar{\psi}_{10}.\bar{r}}\right]+A_5\frac{\varepsilon_{r1}}{\varepsilon_{ro}}e^{-j\bar{\sigma}_4.\bar{r}}e^{-j(\bar{\psi}_4-\bar{\psi}_5).\bar{r}}+A_5\frac{\varepsilon_{r2}}{\varepsilon_{ro}}e^{-j\bar{\sigma}_1.\bar{r}}e^{+j(\bar{\psi}_1-\bar{\psi}_5).\bar{r}}$$

$$-A_5\frac{\varepsilon_{r3}}{\varepsilon_{ro}}e^{-j\bar{\sigma}_o.\bar{r}}e^{+j\bar{\psi}_5.\bar{r}}+A_6\frac{\varepsilon_{r1}}{\varepsilon_{ro}}e^{-j\bar{\sigma}_3.\bar{r}}e^{-j(\bar{\psi}_3-\bar{\psi}_6).\bar{r}}+A_6\frac{\varepsilon_{r2}}{\varepsilon_{ro}}e^{-j\bar{\sigma}_2.\bar{r}}e^{-j(\bar{\psi}_2-\bar{\psi}_6).\bar{r}}-A_6\frac{\varepsilon_{r3}}{\varepsilon_{ro}}e^{-j\bar{\sigma}_o.\bar{r}}e^{+j\bar{\psi}_6.\bar{r}}$$

$$\left.-A_7\frac{\varepsilon_{r3}}{\varepsilon_{ro}}e^{-j\bar{\sigma}_1.\bar{r}}e^{+j\bar{\psi}_7.\bar{r}}-A_8\frac{\varepsilon_{r3}}{\varepsilon_{ro}}e^{-j\bar{\sigma}_2.\bar{r}}e^{+j\bar{\psi}_8.\bar{r}}-A_9\frac{\varepsilon_{r3}}{\varepsilon_{ro}}e^{-j\bar{\sigma}_3.\bar{r}}e^{-j\bar{\psi}_9.\bar{r}}-A_{10}\frac{\varepsilon_{r3}}{\varepsilon_{ro}}e^{-j\bar{\sigma}_4.\bar{r}}e^{-j\bar{\psi}_{10}.\bar{r}}\right\} \qquad \text{(II.8)}$$

and, by dividing both sides of (II.8) by $2j\beta$ and introducing our coupling constant $\kappa_i$ where $\kappa_i = \dfrac{\beta \varepsilon_{ri}}{4\varepsilon_{ro}}$ we obtain the following:-

$$\sum_{i=0}^{10} \frac{\sigma_i}{\beta} \nabla A_i e^{-j\bar{\sigma}_i.\bar{r}} =$$

$$-j\left\{-j\alpha A_o + \kappa_1\left[A_1 e^{+j\bar{\psi}_1.\bar{r}} + A_2 e^{+j\bar{\psi}_2.\bar{r}}\right] + \kappa_2\left[A_3 e^{+j\bar{\psi}_3.\bar{r}} + A_4 e^{+j\bar{\psi}_4.\bar{r}}\right] - \kappa_3\left[A_5 e^{+j\bar{\psi}_5.\bar{r}} + A_6 e^{+j\bar{\psi}_6.\bar{r}}\right]\right\} e^{-j\bar{\sigma}_o.\bar{r}}$$

$$-j\left\{-j\alpha A_1 + \kappa_1 A_o e^{-j\bar{\psi}_1.\bar{r}} + \kappa_2 A_5 e^{-j(\bar{\psi}_1-\bar{\psi}_5).\bar{r}} - \kappa_3\left[A_3 e^{-j(\bar{\psi}_1-\bar{\psi}_3).\bar{r}} + A_7 e^{+j\bar{\psi}_7.\bar{r}}\right]\right\} e^{-j\bar{\sigma}_1.\bar{r}}$$

$$-j\left\{-j\alpha A_2 + \kappa_1 A_o e^{-j\bar{\psi}_2.\bar{r}} + \kappa_2 A_6 e^{-j(\bar{\psi}_2-\bar{\psi}_6).\bar{r}} - \kappa_3\left[A_4 e^{-j(\bar{\psi}_2-\bar{\psi}_4).\bar{r}} + A_8 e^{+j\bar{\psi}_8.\bar{r}}\right]\right\} e^{-j\bar{\sigma}_2.\bar{r}}$$

$$-j\left\{-j\alpha A_3 + \kappa_1 A_6 e^{-j(\bar{\psi}_3-\bar{\psi}_6).\bar{r}} + \kappa_2 A_o e^{-j\bar{\psi}_3.\bar{r}} - \kappa_3\left[A_1 e^{+j(\bar{\psi}_1-\bar{\psi}_3).\bar{r}} + A_9 e^{-j\bar{\psi}_9.\bar{r}}\right]\right\} e^{-j\bar{\sigma}_3.\bar{r}}$$

$$-j\left\{-j\alpha A_4 + \kappa_1 A_5 e^{-j(\bar{\psi}_4-\bar{\psi}_5).\bar{r}} + \kappa_2 A_o e^{-j\bar{\psi}_4.\bar{r}} - \kappa_3\left[A_2 e^{+j(\bar{\psi}_2-\bar{\psi}_4).\bar{r}} + A_{10} e^{-j\bar{\psi}_{10}.\bar{r}}\right]\right\} e^{-j\bar{\sigma}_4.\bar{r}}$$

$$-j\left\{-j\alpha A_5 + \kappa_1 A_4 e^{+j(\bar{\psi}_4-\bar{\psi}_5).\bar{r}} + \kappa_2 A_1 e^{+j(\bar{\psi}_1-\bar{\psi}_5).\bar{r}} - \kappa_3 A_o e^{-j\bar{\psi}_5.\bar{r}}\right\} e^{-j\bar{\sigma}_5.\bar{r}}$$

$$-j\left\{-j\alpha A_6 + \kappa_1 A_3 e^{+j(\bar{\psi}_3-\bar{\psi}_6).\bar{r}} + \kappa_2 A_2 e^{+j(\bar{\psi}_2-\bar{\psi}_6).\bar{r}} - \kappa_3 A_o e^{-j\bar{\psi}_6.\bar{r}}\right\} e^{-j\bar{\sigma}_6.\bar{r}}$$

$$-j\left\{-j\alpha A_7 - \kappa_3 A_1 e^{-j\bar{\psi}_7.\bar{r}}\right\} e^{-j\bar{\sigma}_7.\bar{r}}$$

$$-j\left\{-j\alpha A_8 - \kappa_3 A_2 e^{-j\bar{\psi}_8.\bar{r}}\right\} e^{-j\bar{\sigma}_8.\bar{r}}$$

$$-j\left\{-j\alpha A_9 - \kappa_3 A_3 e^{+j\bar{\psi}_9.\bar{r}}\right\} e^{-j\bar{\sigma}_9.\bar{r}}$$

$$-j\left\{-j\alpha A_{10} - \kappa_3 A_4 e^{+j\bar{\psi}_{10}.\bar{r}}\right\} e^{-j\bar{\sigma}_{10}.\bar{r}} \qquad \text{(II.9)}$$

By equating terms of $e^{-j\bar{\sigma}_i.\bar{r}}$ and simplifying in one dimension perpendicular to the hologram surface, we can let $\dfrac{\sigma_{ix}}{\beta} = \cos\theta_i$ and obtain the following set of coupled differential equations with respect to x:-

$$\frac{dA_o}{dx} = -\frac{j}{\cos\theta_o}\left\{-j\alpha A_o + \kappa_1\left[A_1 e^{+j\psi_1.x} + A_2 e^{+j\psi_2.x}\right] + \kappa_2\left[A_3 e^{+j\psi_3.x} + A_4 e^{+j\psi_4.x}\right]\right.$$

$$\left. - \kappa_3\left[A_5 e^{+j\psi_5.x} + A_6 e^{+j\psi_6.x}\right]\right\}$$

$$\frac{dA_1}{dx} = -\frac{j}{\cos\theta_1}\left\{-j\alpha A_1 + \kappa_1 A_o e^{-j\psi_1.x} + \kappa_2 A_5 e^{-j(\psi_1-\psi_5).x} - \kappa_3\left[A_3 e^{-j(\psi_1-\psi_3).x} + A_7 e^{+j\psi_7.x}\right]\right\}$$

$$\frac{dA_2}{dx} = -\frac{j}{\cos\theta_2}\left\{-j\alpha A_2 + \kappa_1 A_o e^{-j\psi_2.x} + \kappa_2 A_6 e^{-j(\psi_2-\psi_6).x} - \kappa_3\left[A_4 e^{-j(\psi_2-\psi_4).x} + A_8 e^{+j\psi_8.x}\right]\right\}$$

$$\frac{dA_3}{dx} = -\frac{j}{\cos\theta_3}\left\{-j\alpha A_3 + \kappa_1 A_6 e^{-j(\psi_3-\psi_6).x} + \kappa_2 A_o e^{-j\psi_3.x} - \kappa_3\left[A_1 e^{+j(\psi_1-\psi_3).x} + A_9 e^{-j\psi_9.x}\right]\right\}$$

$$\frac{dA_4}{dx} = -\frac{j}{\cos\theta_4}\left\{-j\alpha A_4 + \kappa_1 A_5 e^{-j(\psi_4-\psi_5).x} + \kappa_2 A_o e^{-j\psi_4.x} - \kappa_3\left[A_2 e^{+j(\psi_2-\psi_4).x} + A_{10} e^{-j\psi_{10}.x}\right]\right\}$$

$$\frac{dA_5}{dx} = -\frac{j}{\cos\theta_5}\left\{-j\alpha A_5 + \kappa_1 A_4 e^{+j(\psi_4-\psi_5).x} + \kappa_2 A_1 e^{+j(\psi_1-\psi_5).x} - \kappa_3 A_o e^{-j\psi_5.x}\right\}$$

$$\frac{dA_6}{dx} = -\frac{j}{\cos\theta_6}\left\{-j\alpha A_6 + \kappa_1 A_3 e^{+j(\psi_3-\psi_6).x} + \kappa_2 A_2 e^{+j(\psi_2-\psi_6).x} - \kappa_3 A_o e^{-j\psi_6.x}\right\}$$

$$\frac{dA_7}{dx} = -\frac{j}{\cos\theta_7}\left\{-j\alpha A_7 - \kappa_3 A_1 e^{-j\psi_7.x}\right\}$$

$$\frac{dA_8}{dx} = -\frac{j}{\cos\theta_8}\left\{-j\alpha A_8 - \kappa_3 A_2 e^{-j\psi_8.x}\right\}$$

$$\frac{dA_9}{dx} = -\frac{j}{\cos\theta_9}\left\{-j\alpha A_9 - \kappa_3 A_3 e^{+j\psi_9.x}\right\}$$

$$\frac{dA_{10}}{dx} = -\frac{j}{\cos\theta_{10}}\left\{-j\alpha A_{10} - \kappa_3 A_4 e^{+j\psi_{10}.x}\right\} \tag{II.10}$$

These equations were solved using a numerical Runge-Kutta technique with boundary conditions which apply to transmission gratings, i.e. they state that the diffracted waves must be zero at the hologram input surface. An input power of one is assumed at the hologram boundary (x = 0) where no mismatch is assumed to occur. Therefore, values at x = d (where d is the hologram thickness) are direct indications of diffraction efficiency.

# Appendix III

## Useful parameters

**Typical value**

1. Average refractive index of DCG before sensitisation [1] .......................... ~ 1.55
2. Average refractive index of DCG after sensitisation [1,2] .......................... ~ 1.57
3. Average refractive index of DCG after processing [1,2] ............................. ~ 1.5
4. Thickness of DCG layer ........................................................ ~ 25 μm
5. Thickness of glass substrate ........................................................ 3 mm
6. Refractive index of glass substrate [1] ................................................ 1.515
7. Typical refractive index modulation for DCG [1,2] ................................ ~ 0.01
8. Optimum exposure energy at 514.5 nm [2] ......................... ~ 400 - 800 mJ / $cm^2$
9. Refractive index of Marcol 52 index matching oil [1] ............................. ~ 1.459
10. Refractive index of Xylene index matching oil [1] ................................ ~ 1.497
11. Refractive index of Di-n-butylephalate index matching oil [1] .................. ~ 1.497

---

1 This value is assumed at a replay wavelength of 514.5 nm.

2 This value assumes that the DCG has been sensitised with a 2% solution of ammonium dichromate.

# *Bibliography*


[Abu87] Y. S. Abu - Mostafa and D. Psaltis, "Optical neural computers", *Scientific American* **256**, 88-95, 1987.

[Aka71] H. Akahori and K. Sakurai, "Information search using superimposed holograms", *Appl. Opt.* **10**, 665-666, 1971.

[Alf75] R. Alferness, S. K. Case, "Coupling in doubly exposed, thick holographic gratings", *J. Opt. Soc. Am.* **65**, 730-739, 1975.

[Alf76] R. Alferness, "Analysis of propagation at the second-order Bragg angle of a thick holographic grating", *J. Opt. Soc. Am.* **66**, 353-362, 1976.

[Au87] L. B. Au, J. C. W. Newell and L. Solymar, "Non-uniformities in thick dichromated gelatin transmission gratings", *J. mod. Optics* **34**, 1987.

[Bar76] R. A. Bartolini, A. Bloom and J. S. Escher, "Multiple storage of holograms in an organic medium", *Appl. Phys. Lett.* **28**, 506-507, 1976.

[Ben72] C. R. Bendall, B. D. Guenther and R. L. Hartman, "Thick amplitude holograms: effect of nonlinear recording", *Appl. Opt.* **11**, 2992-2993, 1972.

[Bie70] K. Biedermann. "The scattered flux spectrum of photographic materials for holography", *Optik* **31**, 367-389, 1970.

[Bie75] K. Biedermann. "Information storage materials for holography and optical data processing", *Opt. Acta* **22**, 103-124, 1975.

[Bje89] H. I. Bjelkhagen and M. D. Friedman, "Applications of endoscopic holography through fiber optics", *Proc. S.P.I.E.* **1136**, 1989.

[Bla89a] L. T. Blair, J. Takacs and L. Solymar, "Spurious gratings due to internal reflections in dichromated gelatin", *J. mod. Optics* **36**, 83-93, 1989.

[Bla89b] L. T. Blair, L. Solymar and J. Takacs, "Nonlinear recording in dichromated gelatin", *Proc. S.P.I.E.* **1136**, 1989.

[Bla89c] L. T. Blair and P. M. Hubel, "Copying reflection gratings in silver halide and dichromated gelatin", *Proc. I.E.E.* **311**, 179-183, 1989.

[Bor80] M. Born and E. Wolf, "Principles of Optics", Pergamon Press, Oxford, 1980.

[Bra12] W. L. Bragg, "The diffraction of short electromagnetic waves by a crystal", *Proc. Camb. Phil. Soc.* **17**, 43-57, 1912.

[Bra69] R. G. Brandes, E. E. Francois and T. A. Shankoff, "Preparation of dichromated gelatin films for holography", *Appl. Opt.* **8**, 2346-2348, 1969.

[Cal84] S. Calixto and R. A. Lessard, "Real-time holography with undeveloped dichromated gelatin films", *Appl. Opt.* **23**, 1989-1994, 1984.

[Cas75] S. K. Case, "Coupled-wave theory for multiply exposed thick holographic gratings", *J. Opt. Soc. Am.* **65**, 724-729, 1975.

[Cas76] S. K. Case and R. Alferness, "Index modulation and spatial harmonic generation in dichromated gelatin films", *Appl. Phys.* **10**, 41-51, 1976.

[Cat65] W. T. Cathey, "Three-dimensional wavefront reconstruction using a phase hologram", *J. Opt. Soc. Am.* **55**, 457, 1965.

[Cau79] H. J. Caulfield, "Handbook of Optical Holography", Academic Press, New York, 1979.

[Cha68] E. B. Champagne, "Optical method for producing Fresnel zone plates", *Appl. Opt.* 7, 381-382, 1968.

[Cha71] M. Chang, "Dichromated gelatin of improved optical quality", *Appl. Opt.* **10**, 2550-2551, 1971.

[Cha76a] B. J. Chang, "Post-processing of developed dichromated gelatin holograms", *Opt. Comm.* **17**, 270-272, 1976.

[Cha76b] B. J. Chang and S. K. Case, "Nonlinear holographic waveguide coupler", *Appl. Opt.* **15**, 1800-1802, 1976.

[Cha79] B. J. Chang and C. D. Leonard, "Dichromated gelatin for the fabrication of holographic elements", *Appl. Opt.* **18**, 2407-2417, 1979.

[Cha80a] B. J. Chang, "Dichromated gelatin holograms and their applications", *Opt. Eng.* **19**, 642-648, 1980.

[Cha80b] B. J. Chang and K. Winick, "Silver halide gelatin holograms", *Proc. S.P.I.E.* **215**, 172-177, 1980.

[Cha86] R. Changkakoti and S. V. Pappu, "Study on the pH dependence of diffraction efficiency of phase holograms in dye sensitised dichromated gelatin", *Appl. Opt.* **25**, 798-801, 1986.

[Cha88] R. Changkakoti, S. S. C. Babu and S. V. Pappu, "Role of external electron donor in methylene blue sensitized dichromated gelatin holograms: an experimental study", *Appl. Opt.* **27**, 324-330, 1988.

[Che87] H. Chen, R. R. Hershey and E. N. Leith, "Design of a holographic lens for the infrared", *Appl. Opt.* **26**, 1983-1988, 1987.

[Che88] X. Y. Chen, "The beam ratio in holography", *J. mod. Optics* **35**, 1393-1398, 1988.

[Clo75] D. H. Close, "Holographic optical elements", *Opt. Eng.* **14**, 408-419, 1975.

[Col71a] W. S. Colburn and K. A. Haines, "Volume hologram formation in photopolymer materials", *Appl. Opt.* **10**, 1636-1641, 1971.

[Col71b] R. J. Collier, C. B. Burckhardt and L. H. Lin, "Optical Holography", Academic Press, New York, 1971.

[Col73] W. S. Colburn, R. G. Zech and L. M. Ralston, "Holographic Optical Elements", *Tech. Rep. AFAL TR 72409*, 1973.

[Col81] D. J. Coleman and J. Magariños, "Controlled shifting of the spectral response of reflection holograms", *Appl. Opt.* 20, 2600-2601, 1981.

[Coo84] D. J. Cooke and A. A. Ward, "Reflection hologram processing for high efficiency in silver halide emulsions", *Appl. Opt.* 23, 924-941, 1984.

[Cor75] W. D. Cornish and L. Young, "Influence of multiple internal reflections and thermal expansion on the effective diffraction efficiency of holograms stored in lithium niobate", *J. Appl. Phys.* **46**, 1252-1254, 1975.

[Cou84] J. J. A. Couture and R. A. Lessard, "Diffraction efficiency changes induced by coupling effects between gratings of transmission holograms", *Optik* **68**, 69-80, 1984.

[Cty76] J. Ctyroky, "Coupled-mode theory of Bragg diffraction in the presence of multiple internal reflections", *Opt. Comm.* **16**, 259-261, 1976.

[Cul82] R. A. Cullen, "Some characteristics of, and measurements on dichromated gelatin reflection holograms", *Proc. S.P.I.E.* **369**, 647-654, 1982.

[Cur70] R. K. Curran and T. A. Shankoff, "The mechanism of hologram formation in dichromated gelatin", *Appl. Opt.* 9, 1651-1657, 1970.

[Den62] Yu. N. Denisyuk, "Photographic reconstruction of the optical properties of an object in its own scattered radiation field", *Sov. Phys. Dok.* **7**, 543-545, 1962.

[Den63] Yu. N. Denisyuk, "On the reproduction of the optical properties of an object by the wave field of its scattered radiation", *Opt. Spectrosc.* **15**, 279-284, 1963.

[Den65] Yu. N. Denisyuk, "On the reproduction of the optical properties of an object by the wave field of its scattered radiation II", *Opt. Spectrosc.* **18**, 152-157, 1965.

[Dic89] L. Dickson, S. Fortenberry and S. Luerich, "Recent developments in holographic scanning", *Proc. S.P.I.E.* **1136**, 1989.

[Dun85] S. S. Duncan, J. A. McQuoid and D. J. McCartney, "Holographic filters in dichromated gelatin position tuned over the near-infrared region", *Opt. Eng.* **24**, 781-785, 1985.

[Eva89] R. W. Evans, A. P. Ramsbottom and D. W. Sheet, "Head-up displays in motor cars", *Proc. I.E.E.* **311**, 56 - 62, 1989.

[Ewb86] M. D. Ewbank, P. Yeh and J. Feinberg, "Photorefractive conical diffraction in $BaTiO_3$", *Opt. Comm.* **59**, 423-428, 1986.

[Fer84] R. A. Ferrante, "Silver halide gelatin spatial frequency response", *Appl. Opt.* **23**, 4180-4181, 1984.

[For73] M. R. B. Forshaw, "Explanation of the 'Venetian blind' effect in holography, using the Ewald sphere concept", *Opt. Comm.* **8**, 201-206, 1973.

[For74] M. R. B. Forshaw, "Explanation of the two ring diffraction phenomenon observed by Moran and Kaminow", *Appl. Opt.* **13**, 2, 1974.

[For75] M. R. B. Forshaw, "Explanation of the diffraction fine structure in overexposed thick hologhrams", *Opt. Comm.* **15**, 218-221, 1975.

[Fri67] A. A. Friesem and J. S. Zelenka, "Effects of film nonlinearities in holography", *Appl. Opt.* **6**, 1755-1759, 1967.

[Gab48] D. Gabor, "A new microscopic principle", *Nature* **161**, 777-778, 1948.

[Gab49] D. Gabor, "Microscopy by reconstructed wavefronts", *Proc. Roy. Soc.* A **197**, 454-487, 1949.

[Gay81] T. K. Gaylord and M. G. Moharam, "Thin and thick gratings: terminology clarification", *Appl. Opt.* **20**, 3271-3273, 1981.

[Gay82] T. K. Gaylord and M. G. Moharam, "Planar dielectric grating diffraction theories", *Appl. Phys. B* **28**, 1-4, 1982.

[Gay85] T. K. Gaylord and M. G. Moharam, "Analysis and applications of optical diffraction by gratings", *Proc. IEEE* **73**, 894-937, 1985.

[Geo87] T. G. Georgekutty and Hua-Kuang Liu, "Simplified dichromated gelatin hologram recording process", *Appl. Opt.* **26**, 372-376, 1987.

[Goo67] J. W. Goodman, "Film grain noise in wavefront-reconstruction imaging", *J. Opt. Soc. Am.* **57**, 493-502, 1967.

[Goo68] J. W. Goodman and G. R. Knight, "Effects of film nonlinearities on wavefront-reconstruction images of diffuse objects", *J. Opt. Soc. Am.* **58**, 1276-1283, 1968.

[Gra73] A. Graube, "Holograms recorded with red light in dye sensitised dichromated gelatin", *Opt. Comm.* **8**, 251-253, 1973.

[Gra80] W. R. Graver, J. W. Gladden and J. W. Eastes, "Phase holograms formed by silver halide (sensitised) gelatin processing", *Appl. Opt.* **19**, 1529-1536, 1980.

[Gro68] G. Groh, "Multiple imaging by means of point holograms", *Appl. Opt.* **7**, 1643-1644, 1968.

[Goo84] J. W. Goodman, F. J. Leonberger, S. Y. Kung and R. A. Athale, "Optical interconnections for VLSI systems", *Proc. IEEE* **72**, 850-866, 1984.

[Gue79] D. Guenther and C. D. Leonard, "A cookbook for dichromated gelatin holograms", Tech. Rep T - 79 - 17, 1979.

[Gün87] P. Günter, "Electro - optic effect and photorefractive materials", Springer Verlag, Berlin, 1987.

[Gup77] P. C. Gupta and A. K. Aggarwal, "Holographic stimulation of ellipsoid and hyperboloid mirrors", *Appl. Opt.* **16**, 1474-1476, 1977.

[Hai65] K. Haines and B. P. Hildebrand, "Contour generation by wavefront reconstruction", *Phys. Lett.* **19**, 10-11, 1965.

[Har84] P. Hariharan, "Optical Holography", Cambridge University Press, Cambridge, 1984.

[Har86] P. Hariharan, "Silver halide sensitized gelatin holograms: mechanism of hologram formation", *Appl. Opt.* **25**, 2040-2042, 1986.

[Hea85a] J. M. Heaton, "Wave interactions in static and dynamic volume holographic recording materials", D. Phil. Thesis, Oxford University, 1985.

[Hea85b] J. M. Heaton and L. Solymar, "Wavelength and angular selectivity of high diffraction efficiency reflection holograms in silver halide photographic emulsion", *Appl. Opt.* **24**, 2931-2936, 1985.

[Hea87] J. M. Heaton and L. Solymar, "Reflection holograms replayed at infrared and ultraviolet", *Opt. Comm.* **62**, 151-154, 1987.

[Hec87] E. Hecht, "Optics", Addison- Wesley, 1987.

[How72] A. M. Howatson, P. G. Lund and J. D. Todd, "Engineering Tables and Data", Chapman Hall, 1972.

[Hub89a] P. M. Hubel and A. A. Ward, "A comparison of silver halide emulsions for color reflection display holography", *Proc. Third Int. Symp. on Display Holography*, Lake Forest, Illinois, USA, 1989.

[Hub89b] P. M. Hubel and A. A. Ward, "Color reflection holography", *Proc. S.P.I.E.* **1051**, 18-24, 1989.

[Hut82] M. C. Hutley, "Diffraction Gratings", Academic Press, London, 1982.

[Jam48] R. W. James, "The optical principles of the diffraction of X-rays", Bell and sons, London, 1948.

[Jam77] T. H. James, "The Theory of the Photographic Process", Macmillan, 1977.

[Kas68] F. G. Kaspar, R. L. Lamberts and C. D. Edgett, "Comparison of experimental and theoretical holographic image radiance", *J. Opt. Soc. Am.* **58**, 1289-1295, 1968.
[Ker71] D. Kermisch, "Efficiency of photochromic gratings", *J. Opt. Soc. Am.* **61**, 1202-1206, 1971.
[Kle66] W. R. Klein, "Theoretical efficiency of Bragg devices", *Proc I.E.E.E.* **54**, 803-804, 1966.
[Kog67] H. Kogelnik, "Bragg diffraction in hologram gratings with multiple internal reflections", *J. Opt. Soc. Am.* **57**, 431-433, 1967.
[Kog69] H. Kogelnik, "Coupled wave theory for thick hologram gratings", *Bell Syst.Tech. J.* **48**, 2909-2947, 1969.
[Kon79] O. V. Konstantinov, M. M. Panakhov, Yu. F. Romanov and A. Yu. Tropchenko, "Difference in the widths of two Bragg peaks from three dimensional phase grating with inclined layers", *Opt. Spectrosc. (USSR)* **47**, 327-330, 1979.
[Kon82] O. V. Konstantinov, Yu. F. Romanov, A. F. Rykhlov and A. Yu. Tropchenko, "Secondary structures formed during the inscribing of diffractive three-dimensional phase gratings", *Sov. Phys. Tech. Phys.* **27**, 1134-1136, 1982.
[Kos65] J. Kosar, "Light sensitive systems", Wiley, New York, 1965.
[Kos86] R. K. Kostuk, J. W. Goodman and L. Hesselink, "Volume reflection holograms with multiple gratings: an experimental and theoretical evaluation", *Appl. Opt.* **25**, 4362-4368, 1986.
[Kos88] R. K. Kostuk and G. T. Sincerbox, "Polarization sensitivity of noise gratings recorded in silver halide volume holograms", *Appl. Opt.* **27**, 2993-2998, 1988.
[Kow78a] R. Kowarschik, "Diffraction efficiency of sequentially stored gratings in transmission volume holograms", *Optica Acta* **25**, 67-81, 1978.
[Kow78b] R. Kowarschik, "Diffraction efficiency of sequentially stored gratings in reflection volume holograms", *Opt. Quant. Elect.* **10**, 171-178, 1978.
[Kub76] T. Kubota, T. Ose, M. Sasaki and K.Honda, "Hologram formation with red light in methylene blue sensitised dichromated gelatin", *Appl. Opt.* **15**, 556, 1976.
[Kub79a] T. Kubota and T. Ose, "Lippmann colour holograms recorded in methylene-blue sensitised dichromated gelatin", *Opt. Lett.* **4**, 289-291, 1979.
[Kub79b] T. Kubota and T. Ose, "Methods of increasing the sensitivity of methylene-blue sensitised dichromated gelatin", *Appl. Opt.* **18**, 2538-2539, 1979.
[Kuk77] N. Kukhtarev, V. Markov and S. Odulov, "Transient energy transfer during hologram formation in $LiNbO_3$ in external electric field", *Opt. Comm.* **23**, 338-343, 1977.
[LaM68a] J. T. LaMacchia and D. L. White, "Coded multiple exposure holograms", *Appl. Opt.* **7**, 91-94, 1968.
[LaM68b] J. T. LaMacchia and C. J. Vincelette, "Comparison of the diffraction efficiency of multiple exposure and single exposure holograms", *Appl. Opt.* **7**, 1857-1858, 1968.
[Lam72] R. L. Lamberts, "Characterization of a bleached photographic material", *Appl. Opt.* **11**, 33-41, 1972.
[Lan78] M. J. Landry, G. S. Phipps and C. E. Robertson, "Measurement of diffraction efficiency, SNR, and resolution of single- and multiple-exposure amplitude and bleached holograms", *Appl. Opt.* **17**, 1764-1770, 1978.
[Lei62] E. M. Leith and J. Upatnieks, "Reconstucted wavefronts and communication theory", *J. Opt. Soc. Am.* **52**, 1123-1130, 1962.
[Lei63] E. M. Leith and J. Upatnieks, "Wavefront reconstruction with continuous-tone objects", *J. Opt. Soc. Am.* **53**, 1377-1381, 1963.
[Lei64] E. M. Leith and J. Upatnieks, "Wavefront reconstruction with diffused illumination and three-dimensional objects", *J. Opt. Soc. Am.* **54**, 1295-1301, 1964.
[Lew83] J. W. Lewis and L. Solymar, "Spurious waves in thick phase gratings", *Opt. Commun.* **47**, 23-26, 1983.
[Lie86] C. Liegeois, R. Piel and P. Meyrueis, "Dichromated gelatin holographic scanner", *Proc. S.P.I.E.* **673**, 439-445, 1986.
[Lin69] L. H. Lin, "Hologram formation in dichromated gelatin films", *Appl. Opt.* **8**, 963-966, 1969.
[Lip94] G. Lippmann, "Sur la Théorie de la photographie des couleures simples et composées par la methode interférentielle", *J. Physique* **3**, 97-107, 1894.
[McC73] D. G. McCauley, C. E. Simpson and W. J. Murbach, "Holographic optical element for visual display applications", *Appl. Opt.* **12**, 232-242, 1973.
[Mag85] J. R. Magariños and D. J. Coleman, "Holographic mirrors", *Optical Engineering* **24**, 769-780, 1985.
[Mag74] R. Magnusson and T. K. Gaylord, "Laser scattering induced holograms in lithium niobate", *Appl. Opt.* **13**, 1545-1548, 1974.

[Mag78] R. Magnusson and T. K. Gaylord, "Diffraction regimes of transmission gratings", *J. Opt. Soc. Am.* **68**, 809-814, 1978.

[Mal78] D. Malacara, "Optical Shop Testing", Wiley, 1978.

[Maz82a] M. Mazakova, M. Pancheva, P. Kandilarov and P. Sharlandjiev, "Dichromated gelatin for volume holographic recording with high sensitivity. Part I", *Opt. Quant. Electr.* **14**, 311-315, 1982.

[Maz82b] M. Mazakova, M. Pancheva, P. Kandilarov and P. Sharlandjiev, "Dichromated gelatin for volume holographic recording with high sensitivity. Part II", *Opt. Quant. Electr.* **14**, 317-320, 1982.

[Mey71] D. Meyerhofer, "Spatial resolution of relief holograms in dichromated gelatin", *Appl. Opt.* **10**, 416-421, 1971.

[Mey72] D. Meyerhofer, "Phase holograms in dichromated gelatin", *RCA Review* 33, 110-130, 1972.

[Mey73] D. Meyerhofer, "Holographic and interferometric viewing screens", *Appl. Opt.* 12, 2180-2184, 1973.

[Min75] G. D. Mintz, D .K. Morland and W. M. Boerner, Holographic simulation of parabolic mirrors", *Appl. Opt.* **14**, 564-565, 1975.

[Moh78] G. Moharam and L. Young, "Criterion for Bragg and Raman-Nath diffraction regimes", *Appl. Opt.* **17**, 1757-1759, 1978.

[Mol89] N. Molin, "Hologram interferometry as a tool to investigate transient waves in mechanics", *Proc. I.E.E.* **311**, 1-5, 1989.

[Mor73] J. M. Moran and I. P. Kaminow, "Properties of holographic diffraction gratings photoinduced in polymethyl methacrylate", *Appl. Opt.* 12, 1964-1970, 1973.

[New85] J. C. W Newell, L. Solymar and A. A. Ward, "Holograms in dichromated gelatin: real - time effects", *Appl. Opt.* 24, 4460-4466, 1985.

[New87] J. C. W. Newell, "Optical holography in dichromated gelatin", D. Phil. Thesis, Oxford University, 1987.

[New89] J. C. W. Newell and L. Solymar, "Nonuniformities in dichromated gelatin reflection gratings", *J. mod. Optics* 36, 751-767, 1989.

[Oli84] J. Oliva, P. G. Boj and M. Pardo, "Dichromated gelatin holograms derived from Agfa 8E75 HD plates", *Appl. Opt.* 23, 196-197, 1984.

[Owe83] M. P. Owen, A. A. Ward and L.Solymar, "Internal reflections in bleached reflection holograms", *Appl. Opt.* 22, 159-163, 1983.

[Pen71] K. S. Pennington, J. S. Harper and F. P. Laming, "New phototechnology suitable for recording phase holograms and similar information in hardened gelatin", *Appl. Phys. Lett.* 18, 80-83, 1971.

[Per85] J. C. Perrin, "Wide angle distortion free holographic head up display", *Proc. S.P.I.E.* **600**, 178-183, "Progress in Holographic Applications", 1985.

[Phi80] N. J. Phillips, A. A. Ward, R. Cullen and D. Porter, "Advances in holographic bleaches", *Photogr. Sci. Eng.* **24**, 120-124, 1980.

[Phi85] N. J. Phillips, "The role of $AgH^+$ materials in the formation of holographic images", *Proc. Soc. Photo. Instrum. Eng.* **532**, 29, 1985.

[Pow65] R. L. Powell and K. A. Stetson, "Interferometric vibration analysis of three-dimensional objects by wavwfront reconstruction", *J. Opt. Soc. Am.* **55**, 1593-1598, 1965.

[Rag78] S. I. Ragnarsson, "Scattering phenomena in volume holograms with strong coupling", *Appl. Opt.* **17**, 116-127, 1978.

[Ram35a] C. V. Raman and N. S. N. Nath, "The diffraction of light by high frequency sound waves. Parts I & II", *Proc. Ind. Acad. Sci.* 2, 406-412 (I); 413-420 (II), 1935.

[Ram35b] C. V. Raman and N. S. N. Nath, "The diffraction of light by high frequency sound waves. Parts III - V", *Proc. Ind. Acad. Sci.* 3, 75-84 (III); 119-125 (IV); 459-465 (V), 1935.

[Rao80] S. A. Rao and S. V. Pappu, "Holographic methods for the fabrication of various types of mirrors", *Rev. Sci. Instrum.* 51, 809-813, 1980.

[Ric74] A. K. Richter and F. P. Carlson, "Holographically generated lens", *Appl. Opt.* **13**, 2924-2930, 1974.

[Rid86] G. D. G. Riddy and L. Solymar, "Theoretical model of reconstructed scatter in volume holograms", *Electr. Lett.* 22, 1986.

[Rid88] G. D. G. Riddy, "The effect of light scattering on the recording and replay of holographic optical elements", D. Phil. Thesis, Oxford University, 1988.

[Sal82] O. Salminen and T. Keinonen, "On absorption and refractive index modulations of dichromated gelatin gratings", *Optica Acta* 29, 531-540, 1982.

[Sam80] D. M. Samollovich, A. Zeichner and A. A. Friesem, "The mechanism of volume hologram formation in dichromated gelatin", *Photogr. Sci. Eng.* **24**, 161-166, 1980.

[Sch67] M. J. R. Schwar, T. P. Pandya and F. J. Wienberg, "Point holograms as optical elements", *Nature* **215**, 239-241, 1967.

[Sch85] E. J. P. Schweicher, "Review of industrial applications of HOE-s in display systems", *Proc. S.P.I.E.* **600**, 66-80, "Progress in Holographic Applications", 1985.

[Sha68a] T. A. Shankoff, "Phase holograms in dichromated gelatin", *Appl. Opt.* **7**, 2101-2105, 1968.

[Sha68b] T. A. Shankoff and R. K. Curran, "Efficient, high resolution, phase diffraction gratings", *Appl. Phys. Lett.* **13**, 239-241, 1968.

[Sjö81] S. Sjölinder, "Dichromated gelatin and the mechanism of hologram formation", *Photogr. Sci. Eng.* **25**, 112-118, 1981.

[Sjö84] S. Sjöllnder, "Secondary holograms in dichromated gelatin filters", *Optica Acta* **31**, 1013-1015, 1984.

[Sjö86] S. Sjöllnder, "Dichromated gelatin and light sensitivity", *J. of Imaging Sci.* **30**, 151-154, 1986.

[Sko86] A. F. Skochilov and F. A. Sattarov, "Secondary gratings in 3-D phase holograms", *Opt. Spektrosk.* **60**, 1264-1268, 1986.

[Sli85a] C. W. Slinger, "Multiple holographic transmission gratings in silver halide emulsion", D. Phil. Thesis, Oxford University, 1985.

[Sli85b] C. W. Slinger, R. R. A. Syms and L. Solymar, "Non linear recording in silver halide planar volume holograms", *Appl. Phys. B* **36**, 217-224, 1985.

[Sli86] C. W. Slinger and L. Solymar, "Grating interactions in holograms recorded with two object waves", *Appl. Opt.* **25**, 3283-3287, 1986.

[Sli87] C. W. Slinger, R. R. A. Syms and L. Solymar, "Multiple holographic transmission gratings in silver halide emulsion", *Appl.Phys.B* **42**, 121-128, 1987.

[Smi77] H. M. Smith, "Holographic Recording Materials, Topics in Applied Physics Vol. 20", Springer-Verlag, Berlin, 1977.

[Smo89] W. K. Smothers, T. J. Trout, A. M. Weber and D. J. Mickish, "Hologram recording in Duponts new photopolymer materials", *Proc. I.E.E.* 311, 184-189, 1989.

[Sob87] G. A. Sobolev, "Recording holograms in gelatinous media", *Sov. Tech. Phys. Lett.* **13**, 300-301, 1987.

[Sol85] C. Solano, R. A. Lessard and P. C. Roberge, "Red sensitivity of dichromated gelatin films", *Appl. Opt.* **24**, 1189-1192, 1985.

[Sol76] L. Solymar, "Lectures on electromagnetic theory: a short course for engineers", Oxford University Press, 1976.

[Sol81] L. Solymar and D. J. Cooke, "Volume Holography and Volume Gratings", Academic Press, London, 1981.

[Sol89a] L. Solymar and J. C. W. Newell, "Silver halide noise gratings recorded in dichromated gelatin", *Opt. Comm.* **73**, 273-276, 1989.

[Sol89b] L. Solymar and G. D. G. Riddy, "Noise gratings for single and double beam exposures in silver halide emulsions", *To be published.*

[Sos70] T. P. Sosnowski and H. Kogelnik, "Ultraviolet hologram recording in dichromated gelatin", *Appl. Opt.* **9**, 2186-2187, 1970.

[Sta75] D. L. Staebler, W. J. Burke, W. Phillips and J. J. Amodei, "Multiple storage and erasure of fixed holograms in Fe-doped $LiNbO_3$", *Appl. Phys. Lett.* **26**, 182-184, 1975.

[Sto79] K. A. Stozharova, "Study of the noise diffraction spectra of photographic films", *Sov. J. Opt. Tech.* **46**, 192, 1979.

[Sto85] T. Stone and N. George, "Wavelength performance of holographic optical elements", *Appl. Opt.* **24**, 3797-3810, 1985.

[Str89] A. C. Strasser, E. S. Maniloff, K. M. Johnson and S. D. D. Goggin, "Procedure for recording multiple exposure holograms withequal diffraction efficiency in photorefractive media", *Opt. Lett.* **14**, 6-8, 1989.

[Sym82a] R. R. A. Syms, "Transmission holographic optical elements", D. Phil. Thesis, Oxford University, 1982.

[Sym82b] R. R. A. Syms and L. Solymar, "Noise gratings in photographic emulsion", *Opt. Commun.* **43**, 1982.

[Sym82c] R. R. A. Syms and L. Solymar, "Determination of material characteristics of bleached photographic emulsions used in volume phase holography", *Electron. Lett.* **18**, 249-250, 1982.

[Sym83a] R. R. A. Syms and L. Solymar, "Planar volume phase holograms formed in bleached photographic emulsions", *Appl. Opt.* 22, 1479-1496, 1983.
[Sym83b] R. R. A. Syms and L. Solymar, "Noise gratings in silver halide volume holograms", *Appl. Phys. B* 30, 177-182, 1983.
[Sym84] R. R. A. Syms and L. Solymar, "The effects of swelling on volume holograms formed in bleached photographic emulsion", *Optica Acta* 31, 149-157, 1984.
[Sym89] R. R. A. Syms, "Practical Volume Holography", Oxford University Press, Oxford, 1989.
[Tsu79] N. Tsukada, R. Tsujinishi and K. Tomishima, "Effects of the relative phase relationships of gratings on diffraction from thick hgolograms", *J. Opt. Soc. Am.* 69, 705-711, 1979.
[Uch73] N. Uchida, "Calculation of the diffraction efficiency in hologram gratings attenuated along the direction perpendicular to the grating vector", *J. Opt. Soc. Am.* 63, 280-287, 1973.
[Upa70] J. Upatnieks and C. Leonard, "Efficiency and image contrastof dielectric holograms", *J. Opt. Soc. Am.* 60, 297-305, 1970.
[Van63a] P. J. van Heerden, "A new optical method of storing and retrieving information", *Appl. Opt.* 2, 387-392, 1963.
[Van63b] P. J. van Heerden, "Theory of optical information storage in solids", *Appl. Opt.* 2, 393-400, 1963.
[Van64] A. Vander Lugt, "Signal detection by complex spatial filtering", *IEEE Trans. Inform. Theor.* **IT-10**, 139, 1964.
[Van78] V. A. Vanin, "Hologram copying (review)", *Sov. J. Quant. Electr.* 8, 809-818, 1978.
[Von86] G. von Bally, "Holography in biomedical sciences", *Proc S.P.I.E.* **673**, 327-336, 1986.
[Von88] G. von Bally, "Micro-optics and holography", *Proc. S.P.I.E.* **1014**, 1988.
[Vor80] V. V. Voronov, I. R. Dorush, Yu. S. Kuz'minov and N. V. Tkachenko, "Photoinduced light scattering in cerium-doped barium strontium niobate crystals", *Sov. J. Quant. Elect.* **10**, 1346-1349, 1980.
[Wan89] L. Wang and R. K. Kostuk, "Direct formation of planar holograms and noise gratings at 820 nm in bleached silver-halide emulsions", *Opt. Lett.* **14**, 919-921, 1989.
[War84] A. A. Ward, J. M. Heaton and L. Solymar, "Efficient noise gratings in silver halide emulsions", *Opt. Quant. Elect.* **16**, 365-367, 1984.
[War89] A. A. Ward and L. Solymar, "Diffraction efficiency limitations of holograms recorded in silver-halide emulsions", *Appl. Opt.* **28**, 1850-1855, 1989.
[Wel73a] W. T. Welford, "Isoplanatism and holography", *Opt. Comm.* **8**, 239-243, 1973.
[Wel73b] W. T. Welford, "Aplanatic hologram lenses on spherical surfaces", *Opt. Comm.* **9**, 268-269, 1973.
[Wie90] O. Wiener, "Stehende Lichtwellen und Sie Schwingungsrichtung Polarisirten Lichtes", *Ann. d. Phys.* **40**, 203-243, 1890.
[Woo83] B. H. Woodcock, "Volume phase holograms and their application to avionic displays", *Proc. S.P.I.E.* **399**, 333-338, 1983.
[Woo85] B. H. Woodcock and A. J. Kirkham, "The analysis and construction of powered reflection optical elements (HOEs)", *Proc. S.P.I.E.* **600**, "Progress in Holographic Applications", 1985.
[Wya69] J. C. Wyant and M. Parker Givens, "Effects of photographic gamma on hologram reconstructions", *J. Opt. Soc. Am.* **59**, 1650-1658, 1969.
[Zel80] B. Ya. Zel'dovich and T. V. Yakovleva, "Mode theory of volume holograms allowing for nonlinearity of the photographic process", *Sov. J. Quant. Elect.* **10**, 295-300,1980.

# *Publications arising from this thesis*

1. L. T. Blair, J. Takacs and L. Solymar, "Spurious gratings due to internal reflections in dichromated gelatin", *J. mod Optics* **36**, 83-93, 1989.

2. L. T. Blair, L. Solymar and J. Takacs, "Nonlinear recording in dichromated gelatin", *Proc. S.P.I.E.* **1136**, 1989.

3. L. T. Blair and P. M. Hubel, "Copying reflection gratings in silver halide and dichromated gelatin", *Proc. I.E.E.* **311**, 179-183, 1989.

4. L. T. Blair and L. Solymar, "Grating profiles in dichromated gelatin", Submitted for publication *Optics Communications* 1989.

5. L. T. Blair and L. Solymar, "Double exposure planar transmission holograms recorded in nonlinear dichromated gelatin", Submitted for publication *Applied Optics* 1989.

6. L. T. Blair and L. Solymar, "Silver halide reflection noise gratings recorded in dichromated gelatin", Submitted for publication *Opics Communications* 1989.

7. L. T. Blair and L. Solymar, "Angular selectivity of silver halide transmission noise gratings copied into dichromated gelatin", To be published.